

The large-scale structure of the Universe; environmental effects and relativistic corrections

Dissertation
zur
Erlangung des Doktorgrades (Dr. rer. nat.)
der
Mathematisch-Naturwissenschaftlichen Fakultät
der
Rheinischen Friedrich-Wilhelms-Universität Bonn

von
Mikolaj Ryszard Borzyszkowski
aus
Berent

Bonn, 04.05.2017

Dieser Forschungsbericht wurde als Dissertation von der Mathematisch-Naturwissenschaftlichen Fakultät der Universität Bonn angenommen und ist auf dem Hochschulschriftenserver der ULB Bonn http://hss.ulb.uni-bonn.de/diss_online elektronisch publiziert.

1. Gutachter: Prof. Dr. Cristiano Porciani
2. Gutachter: Prof. Dr. Peter Schneider

Tag der Promotion: 07.05.2018
Erscheinungsjahr: 2018

– To my grandparents

Abstract

In the current picture of the evolution of the Universe, gravity is primarily responsible for the agglomeration of matter, leading to the formation of galaxies, as our milky way. Thereby, the matter content is dominated by dark-matter, which is neither emitting nor absorbing light and only appears through its gravitational interaction. Regions of dark matter, which initially are slightly above the mean density, collapse under their own gravity into virialized, quasi-static structures (called haloes). These are the sites where galaxies form and it is, therefore, important to understand the evolution of haloes.

In this study, we use numerical simulations of structures developing in the universe under the action of gravity. We compare the resulting haloes from these simulations to the predictions of simplified models of halo formation. We further analyse the validity of the assumptions used to construct the models. Against the common wisdom we find that the growth of haloes in simulations can come to complete rest. We develop an estimator for the collapse time of haloes and show that early collapsing haloes preferentially live in prominent filaments of the cosmic web. The flow of matter inside the filament inhibits the halo from growing in mass. We present a simple criterion based on the ellipticity of the tidal field to predict the appearance of the filament and, thus, the collapse time and final mass of the halo.

Further, we show that the mechanism of quenched accretion is responsible for an effect called assembly bias. Assembly bias describes the fact that haloes of the same mass, but different age, are distributed differently in the cosmic web. Older haloes cluster more strongly together compared to younger haloes. In particular, we report that, as a characteristic imprint of the filament, in early collapsing haloes matter particles move on more tangential orbits compared to late collapsing haloes. This corroborates the recently found strong assembly bias with respect to the internal distribution of orbits, which is naturally and for the first time explained by our results.

Finally, we study the correlation of galaxies on very large scales, which only become observable with new upcoming surveys. We develop and implement a new method to calculate the observed distribution of galaxies starting from Newtonian simulations and taking into account leading-order general-relativistic corrections. The method is called `LIGER` and is important to make predictions for the clustering of galaxies on large scales and especially its expected uncertainty. We present two example applications of `LIGER` and demonstrate its usefulness for estimating observables that highlight the small effect of non-standard general-relativistic effects.

Contents

1	Introduction	1
1.1	The cosmological standard model	1
1.1.1	Baryonic and dark matter	5
1.1.2	Radiation and redshift	7
1.1.3	Dark energy	8
1.2	Structure formation in the cosmological model	8
1.2.1	Early linear evolution	9
1.2.2	Non-linear evolution: spherical collapse model	12
1.3	Numerical simulations	15
1.3.1	Initial conditions	17
1.3.2	Non-linear structures in simulations	17
1.4	Open questions addressed in this study	24
1.4.1	The formation and evolution of dark-matter haloes	24
1.4.2	Mock galaxy distributions from simulations in a perturbed FLRW metric	25
2	The formation of CDM haloes: collapse time and tides	27
2.1	Introduction	27
2.2	The Ellipsoidal Collapse Model	29
2.3	Numerical Methods	30
2.3.1	The Simulations	30
2.3.2	Halo Catalogues	31
2.3.3	Analysis Techniques	31
2.4	Results	33
2.4.1	Ellipsoidal collapse and density thresholds for CDM halo formation	33
2.4.2	The influence of external tides	35
2.4.3	Collapse times	36
2.4.4	The collapse threshold at collapse redshift z_c	40
2.5	Discussion	42
2.5.1	The mass dependence and scatter of δ_L	42
2.5.2	Implications for the extended Press-Schechter formalism	44
2.6	Summary	45
3	How the cosmic web inhibits halo growth and generates assembly bias	47
3.1	Introduction	47
3.2	Simulations and methods	49
3.2.1	Collapse time	49
3.2.2	The Dark-ZOMG simulation suite	52

3.3	Results	55
3.3.1	Collapse time and halo growth	55
3.3.2	Collapse time and accretion dynamics	57
3.3.3	The impact of the cosmic web on halo growth	59
3.3.4	The impact of the cosmic web on halo structure	63
3.3.5	Predicting halo masses with the excursion-set method	67
3.4	Summary & conclusions	71
4	LIGER: mock relativistic light-cones from Newtonian simulations	75
4.1	Introduction	75
4.2	The LIGER method	77
4.2.1	Theory	77
4.2.2	Light cones from simulations	80
4.2.3	Light cones based on dark-matter-only simulations	82
4.3	Examples	85
4.3.1	N-body simulations	85
4.3.2	Angular power spectra	85
4.3.3	Statistical analysis	87
4.3.4	Magnification bias in a Euclid-like survey	89
4.3.5	Estimating covariances with LIGER	93
4.3.6	Detectability of Doppler terms at low redshift	94
4.4	Summary & conclusions	98
5	Summary & conclusions	101
5.1	A new paradigm for the formation of dark-matter haloes	101
5.2	A piece in the puzzle of understanding assembly bias	102
5.3	The impact of General Relativity on the large-scale clustering of galaxies	102
5.4	Outlook	103
	Bibliography	105
	A Collapse thresholds for SO-haloes	119
	B Likelihood-ratio test	121
	List of Figures	123
	List of Tables	125

Introduction

“Nature is an infinite sphere whose center is everywhere and whose circumference is nowhere.”

– Blaise Pascal (17th century)

Since ages the night sky with its stars rises interest to humanity which always tried to understand the origin of the world. Already ancient cultures built models of the Universe, e.g. consisting of the central Earth enclosed by rigid spheres harbouring the Sun, the Moon and the stars. Together with deeper observations of the sky not only our knowledge and the ‘size’ of the Universe grew, but mankind had to realize that neither the Earth, nor the Sun, nor our Galaxy form the centre of the world. Even our solar system is not unique as was recently shown by the discovery of many other planets orbiting stars (roughly 3000 exoplanets have been catalogued in e.g. these archives: J. Schneider et al., 2011¹; Rein, 2012²; Han et al., 2014³). Today the ‘cosmological principle’, which states that no point in outer space is special, is one of the pillars of cosmology, the study of the Universe as a whole. According to the current perspective, the Universe has a well defined beginning, the Big Bang (e.g. Weinberg, 1993; Singh, 2004), where all matter is created. Afterwards, gravity is the main driver to form structures which in the end harbour galaxies and stars. This evolution is well described by Λ CDM, the present standard model of cosmology. In this work we study the formation of structures within the cosmological standard model. Although competing models have been developed, Λ CDM offers the best accord between simplicity and agreement with observational data. However, also Λ CDM postulates two poorly understood ingredients of the universe. We are going to introduce them along with the standard model in section 1.1, which describes a perfectly homogeneous universe. In section 1.2 we discuss the evolution of perturbations within this model. Further we motivate the utility of numerical simulations to study the evolution of structures in the universe and elucidate how they are performed in section 1.3. Finally, the main questions addressed in this thesis concerning the formation of structures in the universe and a method to estimate realistic full-sky maps of the galaxy distribution are presented in section 1.4.

1.1 The cosmological standard model

In the late 1920s it was realized that our Universe extends beyond the size of our Galaxy, the Milky Way. Back then, Edwin Hubble used a correlation between the periodicity of pulsating stars and their

¹ <http://www.exoplanet.eu/>

² <http://www.openexoplanetcatalogue.com/>

³ <http://exoplanets.org/>

luminosity, found by Henrietta Leavitt, to estimate the distance to objects called ‘nebulae’ at that time. Although the distance was underestimated, he showed that the nebulae are far away from our galaxy. Further, the intensity of the received light as a function of its wavelength has been measured by e.g. Humason (1927), which is called a spectrum. These spectra contain sharp peaks or dips which can be uniquely attributed to specific atoms (or molecules at low wavelength), where the locations of these ‘lines’ are shifted with respect to spectra obtained in laboratories on Earth (first noted by Slipher, 1913; Slipher, 1915). This deviation is denoted as ‘redshift’, since the spectra are usually shifted towards higher wavelength (redder colours). At the time of its detection, the redshift was explained invoking the Doppler effect, requiring a high relative receding velocity between the Earth and the nebulae to generate the shifted spectra. Hubble (1929) then highlighted a linear relation between the distance and velocity of the nebulae, where most of the nebulae are receding from the Milky Way. Overall, it turned out that these nebulae are actually galaxies themselves similar to our Milky Way.

Independent from each other Friedmann (1922) and Lemaître (1927) developed a model of the evolution of a homogeneous universe, based on general relativity proposed several years before. Together with the relation found by Hubble this implies that our Universe is currently expanding with a rate equal to the slope of Hubble’s relation. The Friedmann-Lemaître model describes the evolution of space homogeneously filled with a matter density $\rho(t)$, where the space is allowed to expand/contract only uniformly such that ρ stays homogeneous. To describe the evolution of the model it is convenient to introduce a coordinate system which is comoving with the general expansion of the universe. If the position of any target relative to any observer is denoted by $\mathbf{r}(t)$, we introduce the comoving coordinates $\mathbf{x}(t)$ and the scale factor $a(t)$, such that

$$\mathbf{r} = a\mathbf{x}, \quad (1.1)$$

$$\mathbf{u} = \dot{\mathbf{r}} = \dot{a}\mathbf{x} + a\dot{\mathbf{x}} = H\mathbf{r} + \mathbf{v}, \quad (1.2)$$

where t is the time passed since the big bang (for a comoving observer) and the dot denotes a derivative with respect to t . Hereby, the scale factor $a(t)$ captures the global evolution of the size of the universe and, as a convention, is set to unity $a(t_0) = 1$ at the time of today t_0 . In the following, \mathbf{r} is called the physical coordinate with the corresponding physical velocity \mathbf{u} . Further $\mathbf{v} = a\dot{\mathbf{x}}$ is the peculiar velocity and we define the Hubble parameter $H = \frac{\dot{a}}{a}$. If the peculiar velocities are small compared to $H|\mathbf{r}|$, eq. (1.2) predicts a linear relation between distance and receding velocity as found by Hubble (1929). The slope of this relation then highlights the present day value of the expansion rate of the universe H_0 .

Note that, in the homogeneous world model each matter element is following only the global expansion and hence \mathbf{x} is constant in time and $\mathbf{v} = 0$. Such a model is a simplified representation of our own Universe, although we observe accumulations of matter as e.g. galaxies. However, on larger spatial scales (or in larger volumes) we expect the Universe to be uniformly filled with matter (and galaxies), if the cosmological principle holds. Thus, the homogeneous world model is a valid approximation. To study the evolution of this simple model we resort to general relativity (GR). In GR, the geometry is described by the metric, which serves as a rule to estimate the infinitesimal distance ds between two neighbouring points in the four dimensional space-time. Photons, or light, travel at the finite speed c . Thus, two points which are separated in space and time such that a photon can pass both, have zero separation $ds = 0 \Rightarrow c dt = dr = a dx$. In turn, this means that light received from objects located at larger distances dates back to an earlier epoch in the cosmic history. Any massive particle can only travel at speeds lower than the speed of light, and any travelled distance in space-time must be space like $c dt > dr = a dx$. We use the convention which denotes space-like separations with negative values of ds . Accordingly, positive ds correspond to time-like paths, which cannot be travelled by any known particle and the connected points are not in causal contact. However, in GR, gravity is sourced by the distortion of space-time due

to matter, or energy. Therefore, the distances dt and dr are not simply measured employing Euclidean geometry. If we connect the time and three spatial dimensions into a single four-vector dx^μ , where time is the leading dimension denoted with the index zero⁴, we can write

$$ds^2 = g_{\mu\nu}dx^\mu dx^\nu. \quad (1.3)$$

Here we employ the Einstein summation convention, such that a sum is performed over each repeated index. The metric, $g_{\mu\nu}$, acts here as a ruler which indicates how distances are measured in space-time. Note that, if the metric has the diagonal elements $(-c^2, 1, 1, 1)$ and zeros elsewhere, it is called the Minkowski metric. In this case the distance estimate in the spatial dimensions only coincides with the usual Euclidean measure. Further, the metric depends on the position in space-time and is connected to the matter (or energy) content by Einstein's field equation. Since the photons follow the paths which are defined by $ds = 0$, eq. (1.3) implies that the distorted space also affects light rays. As a consequence light rays appear to bend around massive objects, an effect called 'gravitational lensing' (e.g. P. Schneider, 2003). Indeed, lensing is one of the first predictions of GR which has been tested with observations using the Sun as a lens to displace the apparent position of background stars. Dyson, Eddington and Davidson (1920) made use of a solar eclipse in 1919 and found evidence in favour of GR by measuring the shift of stars on the sky during the eclipse that matched the predictions well. Further, photons which fall into or climb up a potential well gain or lose energy, respectively, because time passes 'faster' the deeper the potential the photon resides in. This has first been shown by Pound and Rebka (1960) in an experiment on Earth, shooting high energy photons from the ground floor to the roof, about 20 m, and measuring the frequency shift. Although the effect is tiny, it could be estimated making use of nuclear transition lines, which are narrow due to the Mössbauer effect (occurring for certain atoms if they are confined within a lattice). This frequency shift can slightly modify also cosmological observables as shown by Sachs and Wolfe (1967), hence it is called 'Sachs-Wolfe' effect.

For the homogeneous world model H. P. Robertson (1935) and Walker (1937) showed that there exists an unique solution to the metric, if homogeneity is enforced on all scales. Thus, the metric is called Friedmann-Lemaître-Robertson-Walker (FLRW)⁵ metric:

$$ds^2 = -c^2 dt^2 + a^2(t) \left(d\chi^2 + f_K^2(\chi) d\Omega^2 \right), \quad (1.4)$$

$$f_K(\chi) = \begin{cases} K^{-1/2} \sin(K^{1/2}\chi) & (K > 0) \\ \chi & (K = 0) \\ |K|^{-1/2} \sinh(|K|^{1/2}\chi) & (K < 0). \end{cases} \quad (1.5)$$

Here, χ is the radial coordinate in a comoving spherical coordinate system and K describes the curvature in the spatial three-dimensional slice of space-time at constant coordinate time t . Solving the GR field equations using the FLRW metric reveals that the homogeneous world model can only contain a perfect fluid. A perfect fluid is fully described by its density ρ and an isotropic pressure \mathcal{P} . In this case, the

⁴ We follow the usual convention that Greek indices represent values between 0 and 3, while Latin indices run only over the spatial part of the four vector, i.e. (1-3).

⁵ It is also found under the name Friedmann-Robertson-Walker metric only (FRW).

different components of the field equations give two independent differential equations

$$\dot{a}^2 = \frac{8\pi G}{3}\rho a^2 - Kc^2, \quad (1.6)$$

$$\ddot{a} = -\frac{4\pi G}{3}\left(\rho + \frac{3\mathcal{P}}{c^2}\right)a, \quad (1.7)$$

where G is the gravitational constant. Due to the fact that matter and energy are equivalent in GR, the expansion history of the universe depends also on the pressure of its content as revealed by eq. (1.7). Also the curvature parameter K influences the evolution of the universe. In the special case of $K = 0$, space is ‘flat’ as in Euclidean space. Our understanding of geometry is based on flat space, e.g. initially parallel lines have a constant separation along the whole length of the lines. Instead, if space is curved (i.e. $K \neq 0$), parallel lines either converge ($K > 0$, spherical geometry) or diverge ($K < 0$, hyperbolic geometry) from each other. Setting $K = 0$ in eq. (1.6) we can estimate the characteristic (critical) density ρ_{crit} of a flat universe

$$\rho_{\text{crit}} = \frac{3H^2}{8\pi G}. \quad (1.8)$$

The critical density depends on the expansion rate of the universe. Hubble (1929) was the first to estimate the present day value of the expansion rate H_0 , from the slope of the relation between the distance and radial escape velocity of galaxies (as can be seen from eq. (1.2)). For a long time, H_0 was poorly constrained and, thus, parametrised with $H_0 = 100 h \text{ km s}^{-1} \text{ Mpc}^{-1}$. Today, h is known quite precisely to $h = 0.678 \pm 0.008$ (Planck Collaboration et al., 2014a) and there would be no need to parametrise it. However, to facilitate the comparison with previous work, we quote results usually using the parametrization, where dependencies on h will be given along with the units.

To simplify eqs. (1.6) and (1.7), we make some assumptions on the content of the universe, i.e. how pressure relates to density. One can distinguish three basic components of ρ : pressureless matter ρ_{m} , radiation ρ_{r} and a constant vacuum energy ρ_{Λ} . We can estimate how these components behave in an expanding space invoking the first law of thermodynamics. It relates the change in internal energy U of a closed system to the work done by the system, i.e. $dU = -\mathcal{P} dV$. It basically states that a hot cloud of gas, which has a high pressure and, therefore, expands (corresponding to the work $\mathcal{P} dV$), cools down because it loses internal energy. Restoring to special relativity, the internal energy of matter is given by $\rho c^2 V$. Note that V is a physical volume, such that, written in comoving coordinates $V_{\text{c}} = Va^{-3}$ and the first law of thermodynamics then is

$$d(\rho c^2 a^3) = -\mathcal{P} d(a^3) \quad (1.9)$$

Since pressureless matter has $\mathcal{P} = 0$ we find that $\rho_{\text{m}} = \rho_{\text{m},0} a^{-3}$, where $\rho_{i,0}$ denotes the density of the species i today. This corresponds to the intuitive result that the matter density decreases anti-proportional to the increase in volume. For radiation we can make use of the equation of state $\mathcal{P}_{\text{r}} = \rho_{\text{r}} c^2 / 3$, such that inserting this into eq. (1.9) we derive $\rho_{\text{r}} = \rho_{\text{r},0} a^{-4}$. Compared to matter, the radiation density decreases more rapidly. This is due to the effect of redshift, which we discuss later in more detail. The third ingredient, a vacuum energy density, is assumed to be constant in time. Hence, we can use the first law of thermodynamics to estimate its pressure. Setting $\rho = \rho_{\Lambda}$ to a constant in eq. (1.9) we find a negative pressure $\mathcal{P}_{\Lambda} = -\rho_{\Lambda} c^2$. In contrast to a hot ball of gas which loses internal energy while expanding (and therefore cools down), vacuum increases its internal energy during expansion (as ρ_{Λ} is fixed). Taking

everything together we can write the density and pressure of the universe as

$$\rho = \rho_m + \rho_r + \rho_\Lambda, \quad (1.10)$$

$$\mathcal{P} = \mathcal{P}_m + \mathcal{P}_r + \mathcal{P}_\Lambda = \frac{1}{3}\rho_r c^2 - \rho_\Lambda c^2. \quad (1.11)$$

Inserting this into eqs. (1.6) and (1.7) and defining the density parameters as $\Omega_i = \frac{\rho_{i,0}}{\rho_{\text{crit},0}}$ we obtain

$$Kc^2 = -H_0^2(1 - \Omega_r - \Omega_m - \Omega_\Lambda) = -H_0^2(1 - \Omega_{\text{tot}}) \quad (1.12)$$

$$H^2 = H_0^2 \left[\Omega_r a^{-4} + \Omega_m a^{-3} + (1 - \Omega_{\text{tot}}) a^{-2} + \Omega_\Lambda \right], \quad (1.13)$$

where Ω_{tot} is the sum of all density parameters Ω_i . The latter equation describes the expansion history of the universe depending on its content. The former equation relates the curvature parameter to Ω_{tot} . Hence, the total density in the universe determines the geometry of space. Densities above (below) ρ_{crit} lead to a spherical (hyperbolic) geometry of the universe. In the following, we further discuss the different contributions to Ω_{tot} in detail.

1.1.1 Baryonic and dark matter

We know that baryonic matter, which summarises all the matter we are made of (i.e. all massive particles of the standard model of particle physics except neutrinos), has a non-vanishing pressure. However, typically baryons move slowly compared to the speed of light. Thus, they contribute to pressureless matter. Since the dominant contribution of the energy density is given by the rest mass, the density of the pressureless component relates anti-proportional to the volume. Accordingly, the ρ_m decays like a^{-3} as the universe expands (see eq. 1.13).

However, baryonic matter is not the only contribution to Ω_m (see e.g. Del Popolo, 2014). Already Zwicky (1933) indicated that the visible baryonic matter is not sufficient to explain the motion of galaxies inside the nearby galaxy cluster Coma. Galaxy clusters are the most massive gravitationally bound objects in the Universe containing up to hundreds of galaxies. He estimated the baryonic matter content inside the cluster based on the apparent luminosity and calculated the relative radial velocities of the galaxies with respect to each other from the individual redshifts. He found that the amount of visible matter is not sufficient to keep the cluster bound, since the individual galaxies move fast enough to escape from the cluster, which in turn would dissolve within a short time. However, since Coma is assumed to be a stable structure, he speculated that it must contain a large amount of non-luminous matter (i.e. ‘dark matter’).

Further studies of galaxy clusters confirmed the discrepancy between luminous and dynamically inferred mass (e.g. Diaferio, Schindler and Dolag, 2008). In the 1970’s the Uhuru telescope made the first detection of a diffuse X-ray emission from galaxy clusters (Gursky et al., 1972). It turned out that the cluster medium is filled with very hot gas that is emitting X-rays via bremsstrahlung. Due to the high temperatures almost all atoms in the cluster gas are completely ionized, i.e. the electrons get stripped from the atomic nucleus. The free electrons are moving at high speeds and scatter off the stripped protons and nuclei, emitting high-energy bremsstrahlung-photons. The amount of the cluster gas exceeds the amount of baryonic matter in the galaxies of the cluster. Note that in the original argument of Zwicky (1933) the cluster gas is not considered, as it cannot be detected in optical images. Although, being the dominant baryonic matter component in a cluster, the amount of diffuse gas is not sufficient to compensate the discrepancy of the mass budget to the motion of the galaxies. Moreover, the potential induced by baryonic matter is not deep enough to hold the cluster gas at the observed temperatures (e.g. Fabricant,

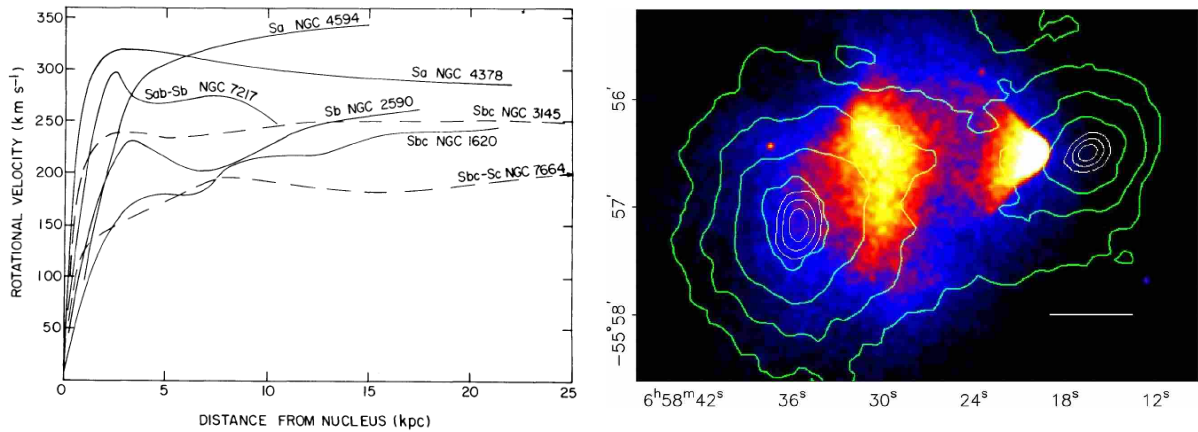


Figure 1.1: Observational evidence for dark matter. The left panel shows the rotational velocity of neutral hydrogen gas around the centres of spiral galaxies of different morphological types. The right panel displays the Bullet cluster. The coloured area depicts the intensity of X-ray radiation obtained with the *Chandra* satellite, highlighting the distribution of the cluster gas. The colour sequence from blue to red, yellow and white is indicating a raising X-ray flux. Note, the cone-like structure of the right emission peak, suggesting that the cluster run from left to right (through the other cluster) and, therefore, the gas experiences a shock. The green contours illustrate the distribution of the total mass in the system retrieved from weak gravitational lensing. (The left panel is taken from Rubin, Thonnard and Ford, 1978, while the right panel is from Clowe et al., 2006).

Lecar and Gorenstein, 1980). Without dark matter the diffuse gas would evaporate from the cluster.

As mentioned, GR predicts gravitational lensing, i.e. the bending of the path of light rays in a gravitational potential. Therefore, clusters can act as lenses that distort the image of background galaxies and even create multiple images of the same background source (see e.g. P. Schneider, 2003). The gravitational lensing effect of clusters has been observed and indicates a much higher mass than inferred by the cluster's luminosity (e.g. Squires et al., 1996). Furthermore, on galactic scales, dark matter is needed to explain the rotational speed of stars and gas around the centre of their host galaxy (e.g. Rubin, Thonnard and Ford, 1978; van der Kruit and Allen, 1978; Bosma, 1981, but also the review by Sofue and Rubin, 2001). The rotation velocity is not decreasing with increasing radius in the outskirts of the galaxy as expected, but stays constant instead (left panel of fig. 1.1). In summary, there are many different observations which show the need of an additional dark-matter component. The dark-matter component in the Universe is assumed to be massive but only weakly (or not at all) interacting. Thus, it only appears through its gravitational influence. This behaviour of dark matter can be observed in the Bullet cluster (e.g. Clowe et al., 2006): two merging clusters, that passed each other almost completely. Observing the cluster gas with X-ray telescopes shows that the gas of the smaller cluster is shocked presenting a typical cone in the intensity map (right panel of fig. 1.1). However, using gravitational lensing to map the total matter component in the system reveals that the total projected density peaks at a different place than the gas. The reason is that dark matter is weakly interacting and the two massive haloes just passed through each other. On the other hand, the gas is interacting with each other, leading to the shock and a deceleration of the gas. Hence, the gas stays behind the dark-matter component of the cluster. Recent data constrain $\Omega_m = 0.306 \pm 0.004$, where baryonic matter only accounts for a small part of the matter content of the Universe $\Omega_b = 0.0482 \pm 0.0005$ (Planck Collaboration et al., 2014a).

1.1.2 Radiation and redshift

In contrast to massive particles, photons travel with the speed of light. Therefore, their pressure is not negligible and their contribution to the evolution of the universe is different. Since $\mathcal{P}_r > 0$, a universe filled with radiation will decelerate faster compared to one filled with pressureless matter, as can be seen in eq. (1.7). This is closely related to the redshift, radiation is subject to. In addition to the Doppler effect, which shifts the wavelength of photons due to the relative velocity of emitter and receiver, the expansion of the universe induces a wavelength shift

$$z + 1 = \frac{1}{a}. \quad (1.14)$$

Here we assume that today we receive redshifted photons from a light source emitted when the Universe had a scale factor a . The frequency ν of the received light is shifted by $\Delta\nu/\nu = z$. This is called the cosmological redshift.

Note that the cosmological redshift depends on the time a photon was emitted and, since photons travel at a constant speed of light, it can be used to infer the distance to the source. We can deduce the relation between comoving distance and expansion factor (hence also redshift) from the metric eq. (1.4) by setting $ds = 0$

$$\chi = \int_a^1 da' \frac{c}{a'^2 H(a')}. \quad (1.15)$$

However, this is not a practical definition of distance. In general, two different definitions of distance are used: the luminosity and the angular-diameter distances. The latter defines distance by the apparent angle θ under which an extended object (of physical size s) is seen

$$d_{\text{ang}} = \frac{s}{\theta}. \quad (1.16)$$

Accordingly, the luminosity distance relates the intrinsic luminosity of a source L to the received flux f

$$d_{\text{lum}} = \sqrt{\frac{L}{4\pi f}}. \quad (1.17)$$

The metric (eq. 1.4) can be used to relate these distance estimators to the comoving distance χ . In case of a flat universe we obtain

$$d_{\text{ang}} = \frac{\chi}{1+z}, \quad (1.18)$$

$$d_{\text{lum}} = (1+z)\chi. \quad (1.19)$$

Based on Euclidean geometry we would expect that both measures of the distance give the same result. However, as shown in the latter equations this is not true in general.

As the energy density of radiation decays as a^{-4} (more rapid than pressureless matter), radiation is mostly important at early times. Today, the radiation energy density has a negligible contribution to the total energy content of the universe ($\Omega_r \sim 10^{-4}$). The majority of the present radiation energy has its origin in the early universe. Several minutes after the big bang the universe was filled with photons, electrons and atomic nuclei. Back then, the electrons and nuclei could not combine into neutral atoms, as any atom is dissociated immediately by the high energy photons. Furthermore, all these constituents

are tightly coupled due to the frequent elastic scattering of photons on the charged particles. But as the universe expands, the energy of the photons decreases due to redshift and, at $z \sim 1100$, the formation of neutral atoms could not be inhibited any more. Suddenly, the universe then became transparent to radiation as all charged particles combined into neutral atoms. Since then, the photons travel without any further interaction. Due to the action of star formation most of the baryons in the Universe are ionized again, but only a minority of the primordial photons have scattered on the charged particles. This primordial radiation has been redshifted further and is observed today in the microwave regime, called the cosmic microwave background (CMB). It has an almost perfect black-body spectrum with temperature of $\sim 2.7K$. Small inhomogeneities in the early Universe imprinted tiny μK fluctuations in the CMB. The statistical properties of the fluctuations are sensitive to the content of the universe, making the CMB one of the most important probes for the cosmological model (Dwek et al., 1998; Hinshaw et al., 2013; Planck Collaboration et al., 2014a).

1.1.3 Dark energy

The last term in eq. (1.13) describes a vacuum energy density that is constant in space and time. This is also called the cosmological constant Λ or ‘dark energy’.⁶ As we pointed out before, such an energy density has negative pressure, leading to a repelling force. Originally, Einstein (1917) realized that he was free to introduce the constant Λ into GR and used it to create a static model of the universe. A non-expanding universe only filled with matter would contract under its own gravity. Therefore a repelling force is necessary to keep such a universe static. The static universe is ruled out due to the measurement of Hubble’s relation, which indicates that the Universe is currently expanding. More recently, the observations of exploding stars of the particular type Ia revealed that the expansion of the Universe is currently accelerating (Riess et al., 1998; Perlmutter et al., 1999). Type Ia supernovae are believed to be exploding white dwarfs, which are remnants of medium sized stars like our Sun. In a binary system, the dwarfs can accrete material from their companion and explode as supernovas of type Ia, once they reach the critical mass above which a white dwarf is unstable. Since the mass of the exploding white dwarfs is always the same, their luminosity is known and their measured brightness can be used to infer the luminosity distance (eq. 1.17) to the supernova. Measuring their spectrum, the redshift z can be obtained, which constrains the expansion history of the universe. In this way Riess et al. (1998) and Perlmutter et al. (1999) revealed that the expansion of the Universe is currently accelerating. If the Universe just contains usual matter and radiation, such a behaviour cannot be explained, since self-gravity will always decelerate the expansion. Therefore, the cosmological constant Λ is introduced, which accelerates the expansion at late times ($z \lesssim 1$). Today, dark energy is the dominant contribution to the energy density budget of the universe $\Omega_\Lambda = 0.692 \pm 0.010$ (Planck Collaboration et al., 2014a).

The sum of all density parameters is very well constrained by recent observations and is consistent with unity with an uncertainty of 0.7 per cent (Planck Collaboration et al., 2014a). This implies, that the universe is flat and the third term in eq. (1.13) disappears ($\Omega_{\text{tot}} = 1$).

1.2 Structure formation in the cosmological model

Up to now, we discussed a universe which is perfectly homogeneous. Such a universe always stays homogeneous and, therefore, never harbours galaxies. A possibility to generate small fluctuations in the

⁶ Note that today many observational campaigns (e.g. the Euclid mission, Laureijs et al., 2011) aim to investigate whether the dark-energy density is constant in time and obeys the expected equation-of-state, i.e. the pressure-density relation. In this context, the term dark energy has been generalised to encompass also evolving dark-energy densities. Since there is yet no evidence for running dark energy, we only consider a constant Λ .

early universe is a period of exponential growth just after the big bang, called ‘inflation’ (e.g. Hawking, 1982; Bardeen, Steinhardt and M. S. Turner, 1983). During inflation microscopic quantum variations get stretched on macroscopic scales. Independently of how the fluctuations are seeded, the attractive nature of gravity amplifies them, leading to large density variations. It is convenient to describe the perturbed density field with the density contrast

$$\delta(\mathbf{x}, t) = \frac{\rho(\mathbf{x}, t) - \bar{\rho}(t)}{\bar{\rho}(t)}. \quad (1.20)$$

In general, we need to work in the framework of GR to study the evolution of δ . However, on small length scales GR reduces to the Newtonian description of gravity. Given the expansion rate of the universe H , we can define the Hubble radius

$$d_h = \frac{c}{H}. \quad (1.21)$$

For the evolution of spatially large perturbations, compared to d_h , the global expansion of the universe is important. On the other hand, for length scales much smaller than d_h , additional GR effects are negligible and we can restore to a Newtonian description of gravity. Furthermore, we adopt an approximate description of δ as a fluid. The fluid assumption is only valid as long as the velocity $\mathbf{v}(\mathbf{x})$ is uniquely defined in each point. The collisionless nature of dark matter allows different flows of matter to be present at the same spatial position, since they do not interact with each other. At this point the fluid approximation breaks down. However, at early times, when the perturbations are still small these multi-stream regions are unimportant. Then the fluid obeys the continuity, Euler and Poisson equations

$$\frac{\partial \delta}{\partial t} + \frac{1}{a} \nabla_{\mathbf{x}} \cdot [(1 + \delta)\mathbf{v}] = 0, \quad (1.22)$$

$$\frac{\partial \mathbf{v}}{\partial t} + H\mathbf{v} + \frac{1}{a}(\mathbf{v} \cdot \nabla_{\mathbf{x}})\mathbf{v} = -\frac{1}{a}\nabla_{\mathbf{x}}\phi, \quad (1.23)$$

$$\nabla_{\mathbf{x}}^2 \phi = \frac{3H_0^2 \Omega_m}{2a} \delta, \quad (1.24)$$

which are written here in comoving coordinates. We have defined the comoving potential $\phi(\mathbf{x}, t)$, which is related to the potential in physical coordinates $\phi_{\text{phy}}(\mathbf{x}, t)$ as

$$\phi(\mathbf{x}, t) = \phi_{\text{phy}}(\mathbf{x}, t) + \frac{\ddot{a}a}{2} |\mathbf{x}|^2. \quad (1.25)$$

Note that this system of equations is non-linear and has no known general solution. However, we can approximate these equations in the case of small perturbations $|\delta| \ll 1$.

1.2.1 Early linear evolution

In the early universe, density perturbations are thought to be small. Hence, the peculiar velocity \mathbf{v} is also small. This allows us to linearise eqs. (1.22) to (1.24), where we neglect any term of second order in the perturbations of peculiar velocity $\delta^2 \propto \mathbf{v}^2 \propto \delta \mathbf{v}$. Thus, for the continuity and Euler equation we obtain

$$\frac{\partial \delta}{\partial t} + \frac{1}{a} \nabla_{\mathbf{x}} \cdot \mathbf{v} = 0, \quad (1.26)$$

$$\frac{\partial \mathbf{v}}{\partial t} + H\mathbf{v} = -\frac{1}{a} \nabla_{\mathbf{x}} \phi. \quad (1.27)$$

The Poisson equation (eq. 1.24) remains unchanged since it is already linear. Now, we can combine all three equations, by applying a time derivative to eq. (1.26) and $a^{-1}\nabla_{\mathbf{x}}$ to eq. (1.27), to get

$$\frac{\partial^2 \delta}{\partial t^2} + 2H \frac{\partial \delta}{\partial t} - \frac{3H_0^2 \Omega_m}{2a^3} \delta = 0. \quad (1.28)$$

Interestingly, this differential equation for the density field does not contain any spatial derivative. Therefore, we can make a general ansatz to solve it

$$\delta(\mathbf{x}, t) = D_+(t)\Delta_+(\mathbf{x}) + D_-(t)\Delta_-(\mathbf{x}), \quad (1.29)$$

where we factorised δ into spatial and time dependent components. Equation (1.28) only constrains D_{\pm} , where D_- is decaying with time while D_+ is growing. Hence, only the solution connected with D_+ will be important for structure formation and its solution is given by

$$D_+(a) \propto \frac{5\Omega_m}{2} H(a) H_0^2 \int_0^a \frac{da'}{[a' H(a')]^3}. \quad (1.30)$$

We choose to normalize the growth factor D_+ to unity at the time of today. The density evolved up to today using eqs. (1.29) and (1.30) is called the linear density contrast δ_{Lin} .

As pointed out before, the solution we obtained is valid if the universe is matter dominated and the scale of the perturbation is small compared to the Hubble radius. However, since the radiation density decays faster than matter going back in time, radiation will eventually dominate. Compared to the matter dominated epoch of the universe, in the radiation dominated phase the expansion rate is enhanced (see eq. 1.13). In this case, H in eq. (1.28) is different, leads to the surprising result that matter perturbations do not grow during this time. In contrast to that, large-scale matter perturbations compared to the Hubble radius grow in amplitude during radiation domination. This is also valid in the matter dominated epoch and the perturbation amplitude grows even at the same rate as small perturbations.

To characterise the perturbations in the universe, we refer to statistical estimators like the two-point correlation function ξ . The correlation function describes the excess density compared to the mean and is defined as

$$\langle \rho(\mathbf{x})\rho(\mathbf{y}) \rangle = [1 + \xi(q)] \bar{\rho}^2, \quad (1.31)$$

where $q = |\mathbf{x} - \mathbf{y}|$. Equivalent to this, the power spectrum can be defined as the Fourier transform of ξ

$$P(|\mathbf{k}|) = \int d^3 \mathbf{q} e^{i\mathbf{q}\cdot\mathbf{k}} \xi(q). \quad (1.32)$$

Inserting the expression of ξ we obtain

$$(2\pi)^3 \delta_{\text{D}}(\mathbf{k} - \mathbf{k}') P(|\mathbf{k}|) = \langle \tilde{\delta}(\mathbf{k}) \tilde{\delta}^*(\mathbf{k}') \rangle. \quad (1.33)$$

where δ_{D} is the Dirac-distribution, $\tilde{\delta}$ and $\tilde{\delta}^*$ denote the Fourier transformed density contrast and its complex conjugate, respectively. The Fourier transform decomposes the density field into waves with wavenumber k (corresponding to a wavelength of $2\pi k^{-1}$) and the power spectrum gives the variance of the amplitude as a function of scale. The fact that P only depends on the magnitude of \mathbf{k} and not on its direction is a direct consequence of the assumed isotropy of the universe. If the probability distribution of δ is a Gaussian function and all Fourier modes of the density field are statistically independent, δ is called a Gaussian random field. A Gaussian random field is then fully characterised by either ξ or

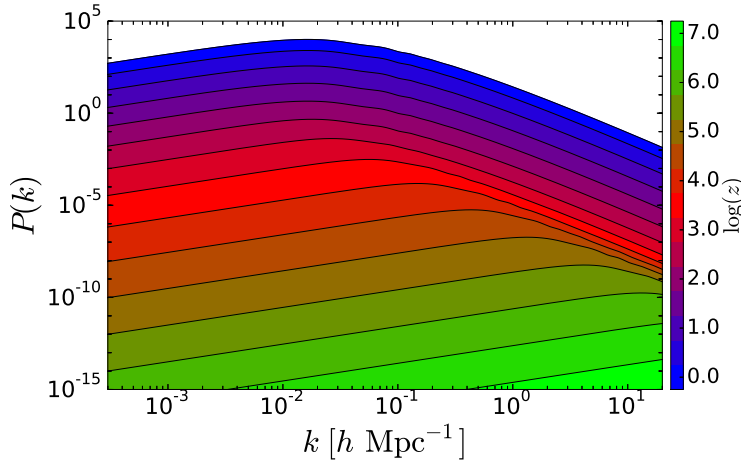


Figure 1.2: Linear power spectrum of perturbations in the density field. Black lines and coloured background show the evolution of $P(k)$ as a function of redshift. At early times the power spectrum is well described by a power law. During the radiation-dominated era in the evolution of the universe the growth of spatially small perturbations compared to d_H is strongly suppressed. Thus, $P(k)$ develops a peak which shifts with time to larger scales. At later times the universe becomes matter-dominated, then all scales grow at the same rate and the shape of the power spectrum is conserved. The linear power spectrum has been computed using the CAMB web interface⁷(Lewis and Challinor, 2011).

P . Up to now no evidence has been found that δ is non-Gaussian (Planck Collaboration et al., 2014b), hence, this assumptions is still justified. Note however, that non-linear gravitational growth will produce a non-Gaussian density field at later times.

Inflation is believed to produce a nearly scale free power spectrum $P \propto k^{n_{\text{tilt}}}$, with a slope n_{tilt} which is slightly lower than unity (see e.g. the review by Riotto, 2010). Recent observations of the CMB constrain the slope of the primordial power spectrum to $n_{\text{tilt}} = 0.961 \pm 0.005$ (Planck Collaboration et al., 2014a). The shape of the primordial power spectrum is then modified by the different growth rates of matter perturbations during the radiation dominated epoch. This is illustrated in fig. 1.2 where the linear power spectrum of perturbations is depicted at different times. In general, the amplitude of the power spectrum increases with time, hence lower curves correspond to earlier epochs. Since the Hubble radius at very early times ($z \sim 10^7$) is smaller than the range of spatial scales indicated in fig. 1.2, the power spectrum grows initially at the same rate. However, d_H increases with time, such that the growth of small scale perturbations (corresponding to high wavenumbers k) is suppressed, because the expansion of the universe is still dominated by radiation. Therefore, a peak appears in the power spectrum, which moves to lower wavenumbers with time, as the Hubble radius increases further. Later, the expansion rate of the universe changes from radiation to matter dominated. The expansion factor at the time when the radiation and matter density are equal is $a_{\text{eq}} = \Omega_r/\Omega_m \simeq 10^{-4}h^{-2}$. At times $a > a_{\text{eq}}$, perturbations grow at the same rate across all length scales. Accordingly, the scale of the power spectrum is unchanged and it only increases in amplitude $\propto D_+^2(a)$. The modified shape of $P(k)$ is usually captured by the transfer function $T(k)$, such that

$$P(k, a) = D_+^2(a) A k^{n_{\text{tilt}}} T^2(k), \quad (1.34)$$

where A is a normalisation constant. It is convenient to express the normalisation A in terms of the

⁷ https://lambda.gsfc.nasa.gov/toolbox/tb_camb_form.cfm

integrated power spectrum of the density field convolved with a smoothing kernel W_R . Usually, for W_R , a spatially spherical top-hat filter is adopted

$$W_R(\mathbf{x}) = \begin{cases} 0 & (|\mathbf{x}| > R) \\ \frac{3}{4\pi R^3} & (|\mathbf{x}| < R). \end{cases} \quad (1.35)$$

By convolving the linearly evolved density contrast δ_{Lin} with W_R we obtain its smoothed version

$$\delta_L(\mathbf{x}) = (\delta_{\text{Lin}} * W_R)(\mathbf{x}), \quad (1.36)$$

where perturbations of scale R or smaller are washed out. The standard deviation of the smoothed density σ_R can then be written as an integral over the power spectrum

$$\sigma_R^2 = \langle \delta_L(\mathbf{x})^2 \rangle = \int \frac{dk}{2\pi^2} P(k) \tilde{W}_R^2(k) k^2, \quad (1.37)$$

where \tilde{W}_R is the Fourier transform of the smoothing kernel. The amplitude of the power spectrum is then parametrised with a top-hat smoothing kernel of $R = 8 h^{-1}$ Mpc size and is constrained to be $\sigma_8 = 0.83 \pm 0.01$ (Planck Collaboration et al., 2014a). Note that, $P(k)$ in eq. (1.37) is the prediction from linear theory, which is presented also in fig. 1.2. Non-linear evolution will be important if $|\delta| \gtrsim 1$. Given the fact that σ_8 is of order unity, non-linear evolution will modify all scales $k \gtrsim 0.1 h \text{ Mpc}^{-1}$, i.e. on the right side of the peak.

1.2.2 Non-linear evolution: spherical collapse model

Since linear theory is only valid if $|\delta| \ll 1$, it is not suitable to describe the structures in the Universe observed today. Although there is no analytical solution for the general evolution of δ , some special cases can be studied. One particular case is the evolution of a homogeneous sphere with enhanced density in an otherwise uniform universe (Partridge and Peebles, 1967; Peebles, 1967; Gunn and Gott, 1972; Peebles, 1980). In the seek of simplicity we will review it within a matter dominated background universe ($\Omega_m = 1.0$, $\Omega_\Lambda = 0.0$), which is known as Einstein-de Sitter universe (EdS). The spherical perturbation has an extent r and contains a mass M . First we can study the evolution of a spherical patch of the background universe of the same mass M but enclosed within the radius r_{EdS} . According to our assumption, the volume of this patch always matches the critical density eq. (1.8), which we can rewrite as

$$\rho_{\text{crit}} = \frac{3M}{4\pi r_{\text{EdS}}^3} = \frac{3H^2}{8\pi G}, \quad (1.38)$$

$$r_{\text{EdS}} = \left(\frac{8\pi GM}{3H^2} \right)^{1/3}. \quad (1.39)$$

Further, we can use the relation between expansion factor and cosmic time

$$t(a) = \int_0^a dt = \int_0^a da' \frac{dt}{da'} = \int_0^a da' \frac{1}{a' H(a')}, \quad (1.40)$$

to replace H with t (using the fact that in an EdS universe $H = H_0 a^{-3/2}$), we then find

$$t = \frac{1}{H_0} \int_0^a da' \sqrt{a'} = \frac{1}{H_0} \frac{2}{3} a^{3/2} = \frac{2}{3} \frac{1}{H}, \quad (1.41)$$

$$r_{\text{EdS}} = \frac{1}{2} (GM)^{1/3} (6t)^{2/3}. \quad (1.42)$$

Now we can turn to the spherical perturbation, which initially is expanding along with the universe. The evolution of the sphere is entirely determined by its self-gravity and the Newtonian equation of motion

$$\ddot{r} = -\frac{GM}{r^2}. \quad (1.43)$$

Due to the attractive force of gravity, the initial expansion of the sphere is decelerated until the perturbation reaches a maximum extent. Then it will collapse again to a point. Hence, we can parametrise a possible solution with ω and express time and radius as

$$t(\omega) = \mathcal{B}(\omega - \sin(\omega)), \quad r(\omega) = \mathcal{A}(1 - \cos(\omega)). \quad (1.44)$$

In this parametrization the perturbation reaches its maximum extension r_{max} at $\omega = \pi$ and collapses back to a point at which $\omega = 2\pi$. Inserting this in eq. (1.43) yields

$$\frac{\mathcal{A}^3}{\mathcal{B}^2} = GM. \quad (1.45)$$

Thus, there exists a solution equal to our parametrization if \mathcal{A} and \mathcal{B} obey eq. (1.45). Combining this with the evolution of the EdS model we can calculate the density contrast inside the perturbation as a function of ω

$$\begin{aligned} \delta_{\text{NL}} &= \frac{r_{\text{EdS}}^3}{r^3} - 1 = \frac{GM(6t)^2}{2^3[\mathcal{A}(1 - \cos(\omega))]^3} - 1 \\ &= \frac{9GM\mathcal{B}^2(\omega - \sin(\omega))^2}{2[\mathcal{A}(1 - \cos(\omega))]^3} - 1 = \frac{9(\omega - \sin(\omega))^2}{2(1 - \cos(\omega))^3} - 1. \end{aligned} \quad (1.46)$$

Figure 1.3 shows the radius and density contrast as a function of time for some example cases. The solid line highlights a perturbation which exactly collapses today. Additionally, the case of higher (dashed line) and lower (dot-dashed line) initial density is depicted.

As shown by the above equation a homogeneous and perfectly spherical perturbation will collapse to a point and its density will diverge. However, realistic perturbations will not fulfill our assumption and thus form a virialized and stable object with finite extent r_{vir} . In this case we can calculate the final total energy per unit mass E of the perturbation using the virial theorem

$$E = \frac{E_{\text{Pot}}}{2} = -\frac{1}{2} \frac{GM}{r_{\text{vir}}}. \quad (1.47)$$

If we assume energy conservation during the collapse, we can estimate the virial size of the perturbation by calculating the energy at the point of the maximum extent

$$E = E_{\text{kin}} + E_{\text{Pot}} = 0 - \frac{GM}{r_{\text{max}}}. \quad (1.48)$$

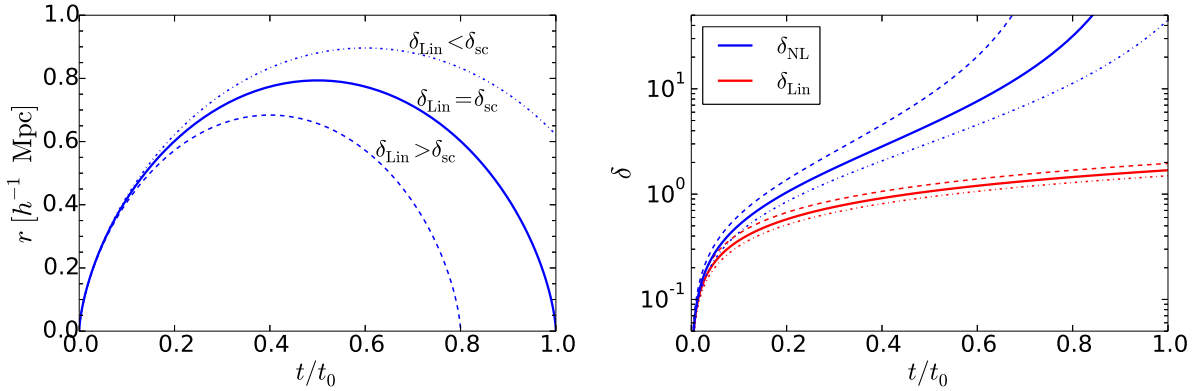


Figure 1.3: The left panel shows the evolution of the radius of a spherical symmetric and homogeneous density perturbation, for different values of the initial density but equal enclosed mass. The right panel highlights in blue the non-linear density contrast for the same perturbations presented in the left panel. The red lines indicate the linear approximation for the density evolution.

Thus, we obtain that the virial radius of a spherical perturbation is $r_{\max}/2$ and its final density contrast is

$$\frac{\rho_{\text{vir}}}{\rho_{\text{EdS}}} = \frac{r_{\text{EdS}}^3(\omega = 2\pi)}{(r_{\max}/2)^3} = 18\pi^2 \approx 178. \quad (1.49)$$

We can compare this result to the prediction of linear theory. Therefore, we approximate eq. (1.46) to linear order using a Taylor expansion

$$\begin{aligned} \delta_{\text{Lin}} &= \frac{9(\omega - \omega + \omega^3/6 - \omega^5/120)^2}{2(1 - 1 + \omega^2/2 - \omega^4/24)^3} - 1 \\ &= \frac{9 \cdot 2^3 \omega^6 (1 - \omega^2/20)^2}{2 \cdot 6^2 \omega^6 (1 - \omega^2/12)^3} - 1 \\ &\approx \left(1 + \frac{3}{20}\omega^2\right) - 1 = \frac{3}{20}\omega^2. \end{aligned} \quad (1.50)$$

Now we need to consider the linear time evolution with respect to ω , which we can obtain by truncating the series expansion of the sine

$$t(\omega) = \mathcal{B}\left(\omega - \omega + \frac{\omega^3}{6} \dots\right) \approx \frac{1}{6}\mathcal{B}\omega^3. \quad (1.51)$$

We substitute this in the linear density evolution and obtain

$$\delta_{\text{Lin}} = \frac{3}{20}\left(\frac{6t}{\mathcal{B}}\right)^{2/3}. \quad (1.52)$$

Note that the growth is proportional to $t^{2/3}$ and therefore scales exactly as the growth parameter D_+ for an EdS universe as can be computed from eq. (1.30). The predicted linear density contrast today of the

spherical patch is

$$\delta_{\text{sc}} = \frac{3}{20} \left(\frac{6t(\omega = 2\pi)}{\mathcal{B}} \right)^{2/3} = \frac{3}{20} (12\pi)^{2/3} \approx 1.686. \quad (1.53)$$

The red lines in the right panel of fig. 1.3 indicate the evolution of the linear density for the three cases shown in blue. Of course the result from linear theory for the late evolution of the spherical perturbation is wrong. But it is used to state that if linear theory predicts a density contrast of 1.686 the region of space should have collapse by now. Note that a small change in the linear density has a strong effect on the non-linear evolution of the perturbation. This model can be generalised to a spherical perturbation which is subject to an external gravitational tidal force. The external force can be driven by other collapsing, potentially more massive, perturbations and distorts the sphere into an ellipsoid. We will investigate this further in section 2.2 together with the possibility of an initially ellipsoidal perturbation.

1.3 Numerical simulations

Since there is no analytical solution to the fluid equations available, we solve them numerically. Therefore, we sample the density field with N_p particles and place them in a comoving box with side length L_{box} . In this work we use the code GADGET (Springel, 2005) to evolve this set of particles in time. In comoving coordinates this problem reduces to a Newtonian evolution of the particle system. The box has periodic boundary conditions, i.e. each particle leaving the box on one side will enter it on the opposite side again. This implements the cosmological principle. GADGET needs to evaluate the Newtonian force for each particle

$$\mathbf{F}_i = Gm_{p,i} \sum_{j=1, j \neq i}^{N_p} \frac{m_{p,j}}{|\mathbf{x}_i - \mathbf{x}_j|^3} (\mathbf{x}_i - \mathbf{x}_j). \quad (1.54)$$

In order to avoid strong two-body interactions a softening length ϵ is introduced such that the force is converging to the final value $-\frac{Gm_{p,i}m_{p,j}}{\epsilon^2}$ for two particles with vanishing separation. These strong two-body interactions are non-physical, since the particles originate from the discretisation of the smooth phase-space (i.e. the 6 dimensional space spanned by \mathbf{x} and \mathbf{v}) distribution of matter. With the introduced softening length, particles are assumed to be Plummer spheres of size ϵ .

For computational efficiency GADGET employs the so-called TreePM method which is a hybrid between two methods to approximate the sum in the force estimation. In the particle-mesh algorithm (PM) the density is computed on a grid using the cloud-in-cell (CIC) method (Hockney and Eastwood, 1988). The basic idea of the CIC method is to replace each particle with a cube of the same side length as the distance between two grid cells. The mass of each particle is then distributed to the neighbouring grid cells according to the fraction of intersecting volume with the grid cell. From the density the gravitational potential is evaluated in Fourier space solving the Poisson equation. This has the benefit that solving the differential equation reduces to a multiplication with the appropriate Green's function.

One shortcoming of the PM method is that the resolution is limited to the size of the grid. Therefore, GADGET also employs the Tree method for evaluating the sum in eq. (1.54). Here space is recursively subdivided and all particles contained within a subdivision are collected into a group, called node. One particle thereby contributes to many nodes, hence the nodes can be arranged in a tree-like structure. The force is then obtained by walking the tree from the root node, i.e. all particles in the full simulation box, downwards. Based on a parameter controlling the precision of the algorithm a decision is made whether

the combined force estimate of the total group is accurate enough or the eight daughter nodes should be considered. The contribution of a node to the force is estimated based on its monopole moment, i.e. a fictive particle with the total node mass at the position of the centre of mass. The benefit hereby is, that there is no intrinsic limiting scale as in the PM method.

The hybrid TreePM algorithm combines the Tree and the PM method to have the benefit of both. The Tree offers accurate short range force estimates and a high dynamical range. At the same time the long-range forces can be estimated accurately from the PM method with improvements in computational speed and memory consumption. For the TreePM method the potential calculated with the PM method ϕ_{PM} is smoothed with a Gaussian filter of size R_{TPM} . This corresponds to a exponential cut off in the Fourier transformed potential

$$\tilde{\phi}_{\text{L}} = \tilde{\phi}_{\text{PM}} e^{-k^2 R_{\text{TPM}}^2}. \quad (1.55)$$

Accordingly, the short range potential estimated from the Tree method ϕ_{Tree} is modulated by $(1 - e^{-k^2 R_{\text{TPM}}^2})$ in Fourier space to compensate for the smoothing of ϕ_{PM}

$$\tilde{\phi}_{\text{S}} = \tilde{\phi}_{\text{Tree}} (1 - e^{-k^2 R_{\text{TPM}}^2}), \quad \phi_{\text{S}} = -G \sum_{\text{i}} \frac{m_{\text{i}}}{x_{\text{i}}} \operatorname{erfc} \left(\frac{x_{\text{i}}}{2R_{\text{TPM}}} \right), \quad (1.56)$$

where we used the inverse Fourier transform and approximate the total potential as a superposition of potentials sourced by point particles. `GADGET` computes the forces from both estimates (eqs. 1.55 and 1.56) and adds them to arrive at the total particle acceleration.

Based on the estimated force `GADGET` evolves the velocities (called a Kick) and the positions of the particles set in time (called a Drift). From the Hamiltonian of the N -particle system the Kick and Drift operations for the time step Δt can be estimated (Quinn et al., 1997)

$$\mathbf{v} \xrightarrow{\mathcal{K}(\Delta t)} \mathbf{v} + \frac{\mathbf{F}}{m_{\text{p}}} \int_t^{t+\Delta t} dt \frac{1}{a} \quad (1.57)$$

$$\mathbf{x} \xrightarrow{\mathcal{D}(\Delta t)} \mathbf{x} + \mathbf{v} \int_t^{t+\Delta t} dt \frac{1}{a^2}. \quad (1.58)$$

In `GADGET` these integrations are performed as a function of $\log(a)$, which is related to t by eq. (1.40). As the system of N particles evolves, also the force acting on each particle changes. Thus, the force has to be recalculated after each time step. The long-range PM force update defines the global timestep of the simulation Δt_{PM} . This time step might be quite long, since the long-range potential is only evolving slowly. For the short-range force-estimate another advantage of the Tree algorithm can be used. To increase computational efficiency, the short-range force can only be calculated on a subset of particles. In the simulation each particle gets assigned its own timestep, depending on the strength of the force currently estimated. This timestep is a fraction of the global timestep $\Delta t_{\text{PM}}/2^n$ where $n \in \mathbb{N}$. Between two force estimates the particles are evolved in time with the operations

$$\mathcal{K} \left(\frac{\Delta t}{2} \right) \mathcal{D}(\Delta t) \mathcal{K} \left(\frac{\Delta t}{2} \right). \quad (1.59)$$

Usually in cosmological simulations all particles have the same mass, but `GADGET` does not rely on this assumption. Actually, in chapter 3 we will use so called zoom-in simulations, where in a small spatial region the number of particles is high and hence the particle mass is small. This region is then surrounded by particles with increasing mass further away from the high-resolution region in a number

of steps. This is particularly useful to study the evolution of single objects of interest in the simulation. The surrounding by low resolution particles is needed to guarantee a realistic environment.

1.3.1 Initial conditions

We use the code MUSIC (Hahn and Abel, 2011) to generate initial conditions, which are then further evolved with GADGET . In general, linear theory (see section 1.2.1) is used to estimate the density field at the initial redshift of the simulation z_{init} . Usually, $z_{\text{init}} \sim 100$ depending on the size of smallest scale which should be resolved. First, a grid is defined in Fourier space on which the (Fourier transformed) density is computed, given the linear power spectrum at z_{init} . Since we have a finite number of grid-cells, the density field can be represented by a finite number of Fourier-modes each representing some scale k . Following the definition of the power spectrum (eq. 1.32) for each available mode a random number is drawn from a Gaussian distribution with mean zero and variance equal to $P(k)$. Further the Poisson eq. (1.24) is solved to derive the potential ϕ from the density contrast. Changing the random seed for the estimation of the random numbers might completely change the appearance of the density field, therefore, one such field is called a realisation of δ . However, all realisations have by construction the same statistical properties. Second, a regular grid of particles is generated which are evolved according to the realisation to the potential ϕ . This is done with Lagrangian perturbation theory (LPT). The final position of each particle in the initial conditions is then given by a displacement $\mathbf{L}(\mathbf{q}, t)$ of each particle from its initial position \mathbf{q}

$$\mathbf{x}(t) = \mathbf{q} + \mathbf{L}(\mathbf{q}, t), \quad \mathbf{v}(t) = \frac{d}{dt} \mathbf{L}(\mathbf{q}, t). \quad (1.60)$$

We can now use LPT to approximate $\mathbf{L}(\mathbf{q}, t)$, since ϕ is small and so will be the displacement. To first order $\mathbf{L}(\mathbf{q}, t)$ can be written as a function to the spatial derivative of ϕ and D_+

$$\mathbf{L}_{1\text{LPT}}(\mathbf{q}) = -D_+(t) \nabla_{\mathbf{q}} \phi(\mathbf{q}, t). \quad (1.61)$$

The first order LPT is also called the Zel'dovich approximation. Note that particles move on straight paths in comoving coordinates. We will also use the second order LPT displacement which can be written as

$$\mathbf{L}_{2\text{LPT}}(\mathbf{q}) \simeq -D_+(t) \nabla_{\mathbf{q}} \phi(\mathbf{q}, t) + \left(\frac{3}{7} D_+(t) \right)^2 \nabla_{\mathbf{q}} \Psi(\mathbf{q}, t). \quad (1.62)$$

Here Ψ is a second order potential $\Delta_{\mathbf{q}} \Psi(\mathbf{q}, t) = \tau(\mathbf{q}, t)$ and

$$\tau(\mathbf{q}, t) = -\frac{1}{2} \sum_{i,j} \left[(\partial_{q_i} \partial_{q_j} \phi)^2 - (\partial_{q_i} \partial_{q_i} \phi) (\partial_{q_j} \partial_{q_j} \phi) \right]. \quad (1.63)$$

1.3.2 Non-linear structures in simulations

Starting from these initial conditions N-body simulations compute the non-linear density distribution. Here we review some basic aspects which have been found in simulations.

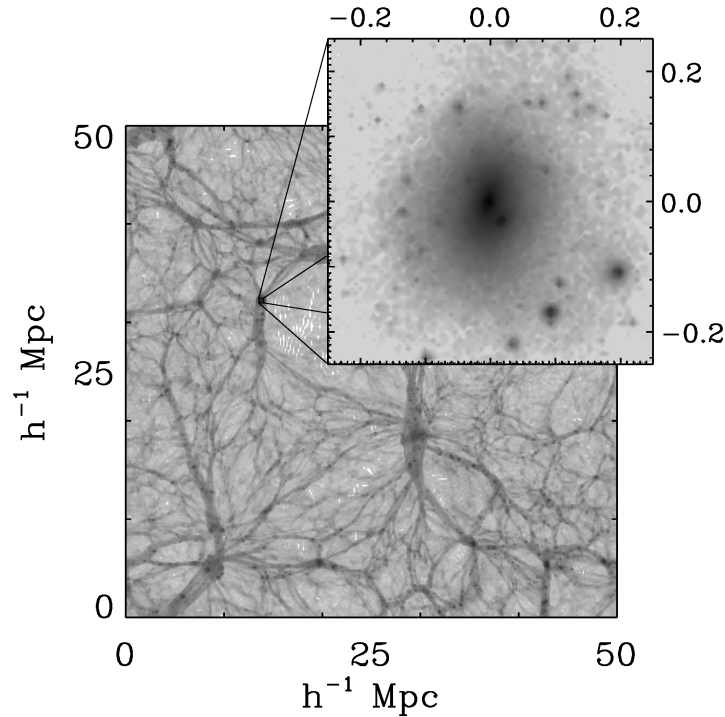


Figure 1.4: A density slice through a dark-matter simulation of $50 h^{-1} \text{Mpc}$ side length. The density is indicated with a grey colour scale, where darker colours highlight denser regions. The top-right panel shows a zoom-in on a halo situated in the node of the filamentary structure.

Dark-matter haloes

Figure 1.4 shows the density field in a slice through a simulation box, $50 h^{-1} \text{Mpc}$ in size, carried out with the `GADGET` code. The final ($z = 0$) particle distribution has been mapped onto a grid using the CIC method, where darker regions indicate higher densities. The density forms a web with linear structures (‘filaments’), where at their intersections very high mass concentrations are located. In fig. 1.4 the zoom in panel shows one of the concentrations in detail, referred to as dark-matter haloes. The particles in these haloes form a gravitationally bound structure. Usually individual particles follow eccentric orbits in the potential.

In general, the definition of a halo is ambiguous, since the transition to the embedding cosmic web is smooth. Most algorithms identifying haloes are therefore based on a cut in density contrast, inspired by the spherical collapse model (eq. 1.49). These algorithms can be classified into two broad categories: Spherical overdensity (SO) halo finders search for local density peaks in the particle distribution and grow spheres around them which enclose the density contrast Δ_{SO} . A common choice is $\Delta_{\text{SO}} = 200$, close to the value found for the spherical collapse model. Note, however, that the density contrast can be either computed relative to the mean matter or critical density. This always needs to be specified.

The drawback of SO halo finders is that they impose a spherical shape on the halo. However, haloes are not necessary spherical. An alternative approach is used by the friends-of-friends (FOF) algorithm (Davis, Efstathiou et al., 1985) which links particles with distance less than b_{FOF} times the mean inter-particle distance into groups. A commonly used value is $b_{\text{FOF}} = 0.2$ which gives consistent enclosed density contrasts to common values of Δ_{SO} . However, the FOF algorithm does not make any assumptions about the shape of the halo.

It is worth pointing out that both methods discussed so far depend on the mean density of the universe. Thus, even a completely static halo surrounded by a decreasing background density field will grow with time, independent which of the two algorithms is used to identify it (for a recent discussion see e.g. Zemp, 2014). For the SO-halo finder this is obvious, since it is directly linked to the mean (or critical) density of the universe. But this is also true for the FOF-halo finder, since the linking length of the particle pair is a fixed comoving separation. However, a halo of constant physical size shrinks in a comoving coordinate frame. Recently, a new way of defining the bound region of a halo was proposed, the ‘splashback’ radius (Diemer and Kravtsov, 2014; Adhikari, Dalal and Chamberlain, 2014; More, Diemer and Kravtsov, 2015). When matter accretes onto a halo it passes close to the halo centre (with some impact parameter) and orbits in usually very eccentric orbits. If the particle is bound the orbit has a well defined maximum distance to the halo centre, called the apocentre. The splashback radius follows the idea to identify the first apocenter of recently accreted matter. Thus, it should enclose all bound particles. We will discuss this in more detail and apply this definition to our haloes in section 3.2.2.

Apart from the fact that there is no unique dark-matter halo definition, haloes show an interesting property: Their average radial density profile follows a simple relation, known as the NFW profile, which fits haloes of various masses well (Navarro, Frenk and S. D. White, 1997)

$$\rho(r) = \frac{r_s^3 \rho_s}{r (r_s + r)^2}. \quad (1.64)$$

Here r_s and ρ_s are the characteristic radius and density of the profile and the only two free parameters. One can infer the circular velocity of particles in a halo of a NFW profile and find that the circular velocity is almost constant for a sufficiently large range in radius to explain observations. However, one should be careful with direct comparison of pure dark-matter profiles to observed galaxies. Since baryons radiate energy and cool, they fall deep in the potential of the halo and accumulate at the centre. Thus, the density of baryons can become very large in the centres of haloes, which leads to the formation of galaxies (S. D. White and Rees, 1978). All these processes, however, alter the properties of haloes especially on small scales.

Origin and growth of haloes

Due to the attractive nature of gravity, it is tempting to consider local peaks in the linear density field as origins of haloes. This has been explicitly studied using numerical simulations, where recent high-resolution simulations find a good correspondence of haloes to initial density peaks (Ludlow and Porciani, 2011). According to the spherical collapse model, a peak should have a linear density contrast of $\delta_{sc} = 1.686$ to form a halo today. Thus, it is illustrative to investigate the standard deviation of the smoothed density contrast σ_R (eq. 1.37) as function of the smoothing length as shown in fig. 1.5. Note that σ_R decreases with increasing size of the top-hat smoothing kernel R , indicating that the variance in δ_L is dominated by the smallest scales. The size of the top-hat can be related to a specific mass scale given by the enclosed mass of the sphere with radius R at mean density of the universe

$$M_s = \frac{4\pi}{3} R^3 \rho_{crit} \Omega_m. \quad (1.65)$$

Based on the spherical collapse model and fig. 1.5 we expect that small mass haloes form first, since on small scales the highest density peaks are expected. On the other hand, large haloes should be rare as only few regions of the linear density field reach δ_{sc} . Indeed this is found in simulations as well, the mass function of haloes (the number of haloes as a function of mass) extends to larger masses with

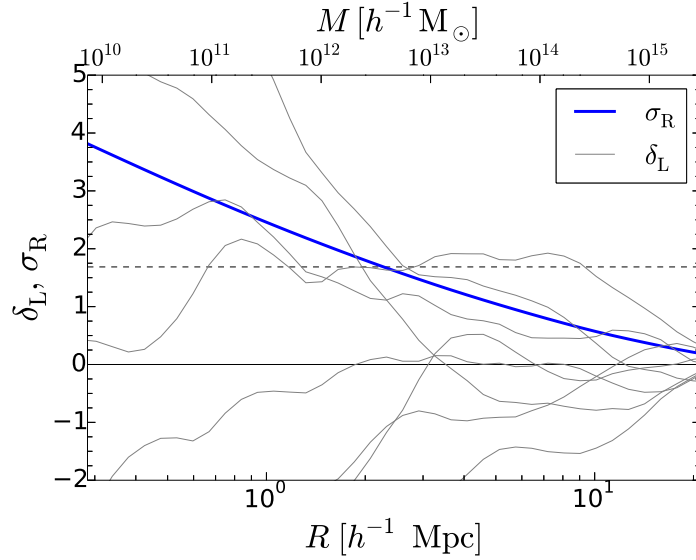


Figure 1.5: The blue thick line shows the standard deviation of the smoothed linear density contrast σ_R with a top-hat kernel as function of the top-hat radius R (solving eq. 1.37). The thin lines highlight the density contrast at a few fixed points in the smoothed linear density field. The horizontal dashed line indicates the spherical collapse barrier δ_{sc} . Top axis labels translates the size of the kernel into a mass-scale, computed as the enclosed mass of a sphere of radius R at mean density of the universe.

proceeding time (see e.g. Jenkins et al., 2001; Springel, S. D. White et al., 2005). Moreover, haloes show a hierarchical growth, where higher mass haloes are formed by subsequent mergers of lower mass haloes (e.g. Tormen, Bouchet and S. D. White, 1997). Beside mergers, haloes also increase their mass by accretion of material in their surrounding, called ‘smooth accretion’. If along the simulation several snapshots of the particle distribution at different times are saved we can follow the evolution of haloes identifying the progenitor of a halo in a snapshot at previous time. Thereby, the joint distribution of particles is estimated between a halo in snapshot n and all haloes in the previous snapshot $n - 1$ and the main progenitor is defined as the halo (in snapshot $n - 1$) with maximum number of common particles. In this way an accretion history of haloes is build, that features continues slow growth, and distinct jumps, due to smooth accretion and mergers, respectively. To characterise the growth history of haloes, it is convenient to estimate the time at which the halo had accumulated half its present day mass, termed ‘half-mass formation time’ or simply ‘age’.

Figure 1.5 further shows several realisations of the contrast δ_L as grey lines. Each realisation is obtained at a fixed position in the linear density field, which has been smoothed with a spherical top-hat filter of varying size R . Hence, these excursion-set trajectories encode the spherically averaged density profile around random points in the linear density field. According to the spherical collapse model, all these points in the initial density field should have collapsed to a halo, if δ_L exceeds the collapse barrier δ_{sc} . The mass then corresponds to the size of the highest filtering scale R for which $\delta_L \geq \delta_{sc}$. The spherical collapse threshold is computed for the case of a halo forming today. If we instead require the collapse of the sphere to occur at a different time, δ_{sc} has to be scaled with the inverse growth factor. Hence, by applying different thresholds for different times, the mass accretion history can be predicted from the initial density field. Moreover, the statistical count of trajectories and their highest mass-scale at which they cross the collapse barrier, yields a prediction of the halo mass function (Press and Schechter, 1974; Bond, Cole et al., 1991). The total mass in haloes in any infinitesimal mass range is then given by the

fraction of trajectories which up-cross the barrier in the same range of smoothing mass scales. Originally, Press and Schechter (1974) just counted the number of barrier crossings at each smoothing mass scale independently. However, the smoothed density contrast can cross the barrier several times as a function of R , which leads to a wrong normalisation of their predicted mass function. Later, Bond, Cole et al. (1991) argued that only the up-crossing at the largest smoothing mass scale should be counted, which is called the ‘extended Press-Schechter theory’ (EPS) and leads to a correctly normalized prediction. Still, the EPS mass function underestimates the number of high mass haloes and predicts too many low mass haloes (see e.g. Jenkins et al., 2001). (Bond and S. T. Myers, 1996, hereafter BM96) introduced an anisotropic gravitational field (tidal field) in the spherical collapse model, which is sourced by the gravitational influence of neighbouring haloes. Their extended model is named ‘ellipsoidal collapse model’, since the initial sphere is stretched into an ellipsoid due to the tidal field. In the presence of a significant tidal field, a higher initial density is required for spherical perturbations to collapse at the same time compared to δ_{sc} . Accordingly, Sheth, Mo and Tormen (2001) modified the collapse barrier in EPS to account statistically for the ellipsoidal collapse. However, they had to rescale their resulting mass function to achieve a precise fit of simulation results, which they attributed to the ambiguity in the halo definition. Until today theoretical predictions of the formation of haloes are not precise enough, such that simulations are still an important tool to predict the number of haloes, although the theoretical prediction of the shape of the mass function is used and fitted to simulation results (see e.g. Tinker et al., 2008).

Large-scale structure

In the following we turn from a single halo to the distribution of haloes in the simulation box. As already evident from fig. 1.4 haloes are not distributed randomly in the simulation, but are embedded in a web-like density field. Figure 1.6 shows in the top and left wedge (blue points) the distribution of observed galaxies from three different surveys. Each galaxy is plotted as a dot at the measured redshift and angular position on the sky. Note that due to the finite speed of light we observe distant galaxies at an earlier epoch. The comoving distance χ (eq. 1.15) corresponds to the cosmological redshift, however, what we measure is modulated by so-called redshift space distortions. One of the most prominent effects is the so-called ‘finger-of-god’ effect: Big dark-matter haloes can host many galaxies, which we observe as galaxy clusters. These galaxies are confined in a small region of space. Thus, their cosmological redshift and angular position on the sky is almost the same. However, the velocity dispersion of the individual galaxies is big and their peculiar velocity induces a Doppler shift of the emitted spectrum. This leads to a broadly distributed observed redshift, which produces elongated structures pointing towards the observer, hence the name.

In the right and bottom panel of fig. 1.6 (red dots) a numerical dark-matter only simulation was populated a posteriori with galaxies using a semi-analytical model (Springel, S. D. White et al., 2005; Springel, Frenk and S. D. White, 2006). In general semi-analytical models analyse the accretion history, i.e. the evolution of mass of a halo as function of time, to deduce the properties of the hosted galaxy. Here, Springel, Frenk and S. D. White (2006) used some observational motivated relations to estimate the amount of star formation during the quiescent accretion phase, which happens in a disk around the galaxy centre. In contrast to that, mergers of gas-rich haloes with similar mass lead to a starburst, i.e. high star formation rate for a short amount of time. However, major mergers in this model also destroy the disc and change the morphology of the galaxy to a spheroidal configuration. From the amount of stars and their age the luminosity of each galaxy is determined. Taking the sensitivity of a specific telescope into account a mock catalogue is constructed from the simulation and shown as red dots in fig. 1.6. The redshift hereby is computed from the cosmological distance as well as the contribution due to the peculiar velocity. As it is evident from fig. 1.6, there is qualitative agreement between the

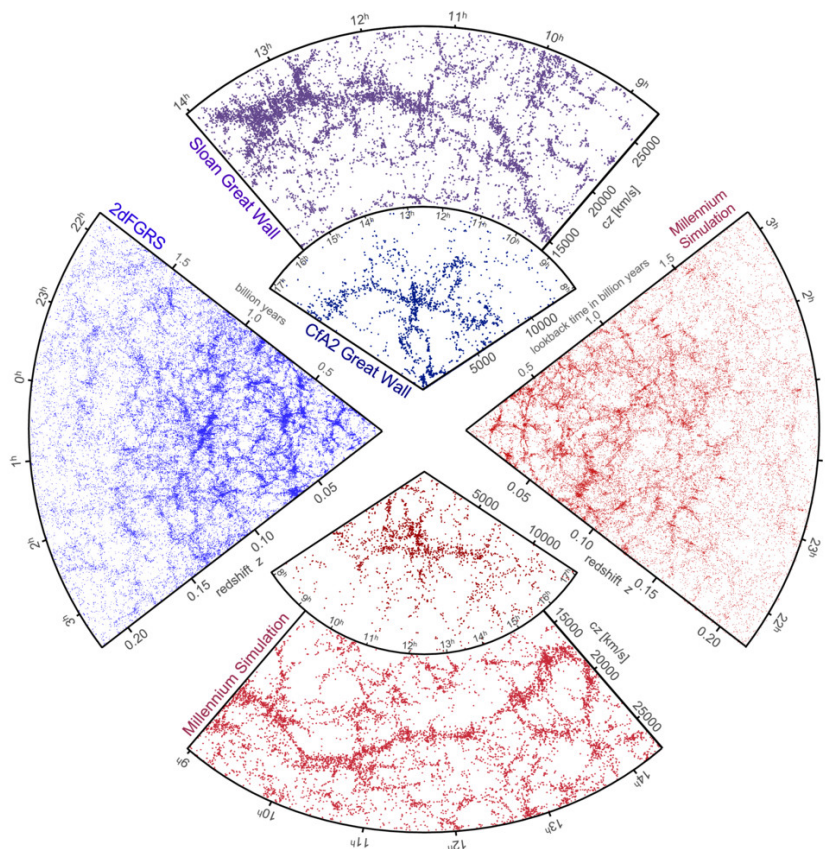


Figure 1.6: Top and left wedges show the measured galaxy sky position and redshift from three different surveys. Right and bottom wedges show the estimated galaxy distribution from a simulation. The simulation is dark matter only and galaxies were inserted using a semi-analytical approach. (Figure taken from Springel, Frenk and S. D. White, 2006).

web-like structure of observed galaxies and the numerical simulations. This correspondence has also been checked quantitatively by estimating the two-point correlation function of galaxies, which also matches the correlation function from simulations well (Springel, S. D. White et al., 2005; see also Davis, Huchra et al., 1982).

Halo Bias

Figure 1.6 also exemplifies the difficulty to compare the result of dark-matter only simulations to observations. N-body simulations give precise predictions for the distribution of dark matter, once the initial conditions are known. In contrast, observations can only detect objects which emit light, like galaxies. However, galaxies do not trace the dark-matter density uniformly, but are believed to populate haloes. Of course we can identify haloes in the simulation, although, it is not clear which kind of galaxy an individual halo hosts. Semi-analytical models or simulations which include baryons still rely on many assumptions and use empirical relations to convert gas into stars and estimate their feedback on the gas.

To be able to compare simulations with observations it is therefore important to study the statistics of biased tracers, in general called galaxy bias (for a recent review see Desjacques, Jeong and Schmidt, 2016). On large scales, where the matter density fluctuations are small $|\delta| < 1$, a perturbative approach

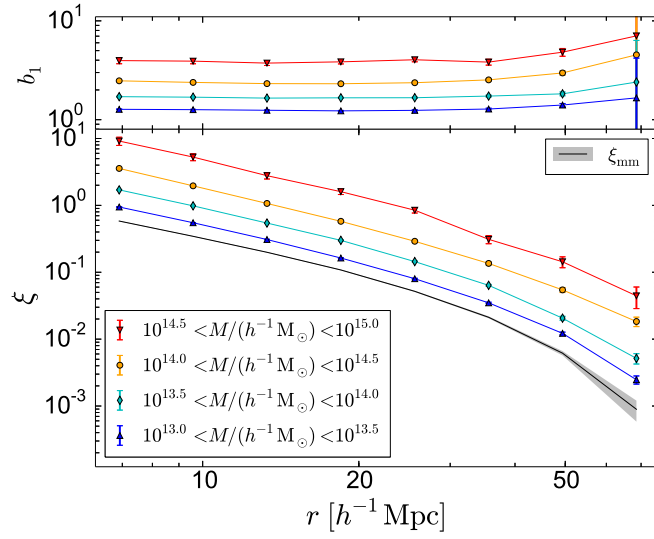


Figure 1.7: Points with error bars show the two-point correlation function for haloes in different mass ranges as indicated by the legend. The solid black line and the grey band highlight the matter correlation function and its uncertainty, respectively. Errors are estimated bootstrapping the distribution of the corresponding sample. The top panel shows the bias of the haloes, i.e. the square-root of the ratio of the halo and matter correlation functions.

can be applied and the galaxy number density contrast is expanded as

$$\delta_g = \sum_n b_n \delta^n. \quad (1.66)$$

This is known as the ‘local bias expansion’, since the galaxy density only depends on the local matter density contrast. Further, there have been more local contributions discussed to the sum, like the tidal field

$$K_{ij} = \partial_i \partial_j \phi - \delta_{ij} \frac{\delta}{3}. \quad (1.67)$$

The tidal field measures the stretching or compressing action, due to a gradient of the gravitational force. Although the tidal field is sourced by the surrounding structure, it is a local observable. However, such extensions to eq. (1.66) enter only at second order ($n = 2$) or higher. For our purpose it is enough to consider the first order only, where the galaxy density contrast is linearly related to the matter density contrast

$$\delta_g = b_1 \delta. \quad (1.68)$$

Following this assumption, the two-point correlation function of galaxies ξ_{gg} (eq. 1.31) is

$$\xi_{gg}(|\mathbf{x} - \mathbf{y}|) = \langle \delta_g(\mathbf{x}) \delta_g(\mathbf{y}) \rangle = b_1^2 \langle \delta(\mathbf{x}) \delta(\mathbf{y}) \rangle = b_1^2 \xi_{mm}(|\mathbf{x} - \mathbf{y}|). \quad (1.69)$$

Hence, the galaxy correlation function is enhanced by a factor of b_1^2 over the matter correlation function ξ_{mm} . Using dark-matter haloes instead of galaxies, which can also be used as tracers of the density field, this is shown in fig. 1.7. The coloured connected points indicate the halo correlation function for different halo mass ranges. These haloes are drawn from the larger of the two simulations introduced in section 2.3.

The solid black line highlights the matter correlation function computed for the same simulation. Clearly, the halo correlation function is biased with respect to ξ_m , where the bias value, estimated by the square root of the ratio of the correlation functions, is shown in the upper panel of fig. 1.7. Indeed, on large scales (several $h^{-1}\text{Mpc}$) the bias is constant, but changes with the mass of the haloes.

The concept of galaxy bias has already been introduced by Kaiser (1984). At that time the first galaxy redshift surveys have been compiled (e.g. CfA: Huchra et al., 1983). The estimated correlation amplitude from these galaxies was substantially smaller compared to the one of the Abel galaxy cluster sample. Since galaxy clusters are the most massive gravitationally bound objects in the Universe, they originate from exceptionally large initial density peaks. Kaiser (1984) showed that this would imply that galaxy clusters are biased tracers of the density field and estimated the amplification of the correlation function to be roughly an order of magnitude. Later, Davis, Efstathiou et al. (1985), using numerical simulations, argued that if galaxies would trace the matter density field uniformly this would imply a very dense universe with $\Omega_m > 1$. Since this is inconsistent with other observations it highlights the need of galaxy bias to compare galaxy statistics with simulations. Unfortunately, the precise galaxy bias depends on the specific tracer chosen. Figure 1.7 shows that in the case of haloes the bias depends strongly on mass, and in analogy to the high clustering of the Abel cluster sample, higher mass haloes cluster stronger. However, the precise connection between halo mass and inherited galaxy is unknown, so that precise predictions of galaxy bias cannot be made.

Following the EPS approach as discussed before, a prediction of the bias of dark-matter haloes can be obtained. It turns out that the bias depends only on how rare the high density regions are. The relevant parameter for the rarity is σ_R , which has a unique relation to halo mass. Hence, halo bias should be a function only of halo mass. Recent investigations from simulations surprisingly show that the bias is not only a function of the dark-matter halo mass, but also their age (Gao, Springel and S. D. White, 2005). This dependence becomes more important at haloes of smaller mass and is referred to as ‘assembly bias’. Since its discovery, it has been shown that many more halo properties correlate with the halo bias, like the concentration of the radial dark-matter density profile or internal distribution of particle velocities (Wechsler, Zentner et al., 2006; Jing, Suto and Mo, 2007; Gao and S. D. White, 2007; Bett et al., 2007; Angulo, Baugh and C. G. Lacey, 2008; Faltenbacher and S. D. White, 2010; R. Li et al., 2013).

1.4 Open questions addressed in this study

The aim of this study is twofold. First, we use numerical simulation to investigate the collapse and growth of dark-matter haloes. Second, a new method is developed to derive realistic mock observations from numerical simulations.

1.4.1 The formation and evolution of dark-matter haloes

In chapter 2 we compare the evolution of perturbations in idealised models to perturbations in cosmological simulations. Following the idea of the spherical collapse model (section 1.2.2) haloes should originate from local maxima in the linear density of height 1.686. In agreement with previous work, we show that haloes in simulations come from a large variety of initial densities $\delta \gtrsim 1.686$. There have been extensions to the spherical collapse model which we introduce in section 2.1 and lay out the relevant equations in section 2.2. As the spherical collapse model, the extended models predict a linear density contrast for the collapse of the perturbation. We use the simulations to measure the remaining parameters of the models and compare the predicted linear density contrast with the one measured in simulations. The aim is to either find a model which reproduces the collapse of perturbations in simulations well,

or, if this is not the case, which is shown in section 2.4, investigate why they fail. In general simplified collapse models underpredict the linear density contrast. Or in other words, we expect that simulations should contain more massive haloes than what is measured. We argue that growth of haloes is halted in numerical simulations. If one accounts for the prohibited growth in the models, the predicted linear density matches well with the simulation result.

The reason for haloes to halt accretion is further investigated in chapter 3. Here we use numerical zoom-in simulations to study some stalled haloes, as we call them, in detail and compare them to regular accreting ones. The simulations are explained in section 3.2, while the results are presented in section 3.3. We find that stalled and accreting haloes populate different regions of the cosmic web, which is the reason of their different growth rates. We show that this effect of inhibited halo growth is the reason for the assembly bias effect. Finally, we present a modification to the spherical collapse model which accounts for this effect and leads to accurate predictions for the collapsed final mass.

1.4.2 Mock galaxy distributions from simulations in a perturbed FLRW metric

In chapter 4 we turn to the implementation of a new method to derive realistic large-scale mock galaxy distributions from simulations. As discussed briefly in section 1.3.2, simulations can be used to produce mock observations (e.g. fig. 1.6). However, it is necessary to take redshift-space distortions into account, which modulate the redshift and angular position of a galaxy. The most prominent effect is the Doppler shift of the spectrum due to the peculiar velocity of each galaxy. This changes the estimated redshift and is routinely considered when mock observations are performed. Further, we shortly mentioned gravitational lensing, which also shifts the position of the galaxy on the sky. All these redshift-space distortions originate from the fact that we observe galaxies on our backward light cone. Thereby, the geometry of space-time is not exactly described by the FLRW metric (eq. 1.4). The density inhomogeneities in the universe also perturb the metric. In section 4.2 we lay out how the observed position of a galaxy changes when the disturbed metric is considered. These additional GR effects become important if the scale of the observed galaxy correlation approaches the Hubble radius. Current surveys do not cover enough volume to constrain such large scale signals. But upcoming surveys will map almost the full sky and deliver an unprecedented amount of data. Hence, new tools are necessary to model the expected signal, which include GR redshift-space distortions. We present the LIGER method in section 4.2 and how it can be used to produce mock galaxy distributions. Finally, we discuss two applications of LIGER at the example of the Euclid and SKA2 telescope in section 4.3.

The formation of CDM haloes: collapse time and tides¹

2.1 Introduction

The formation of dark-matter haloes through gravitational instability of small density perturbations is a formidable non-linear problem. Most of our current understanding of the process is based on N-body simulations, yet valuable theoretical insight can be gained through analytic models that attempt to approximate the growth of structure.

Most theoretical models are based on the assumption that haloes of mass M originate from compact Lagrangian patches of initial comoving size $R \propto M^{1/3}$ in which conditions are favorable for collapse. In the most simplistic picture, the collapse process can be approximated by following the evolution of a spherically symmetric perturbation with a top-hat density profile and vanishing initial peculiar velocities in a otherwise homogeneous and expanding background (Partridge and Peebles, 1967; Peebles, 1967; Gunn and Gott, 1972; Peebles, 1980). In this “spherical collapse model”, perturbations that are dense enough to form bound structures decouple from the background expansion, eventually reverse their motion and start collapsing at an increasingly faster rate. The mathematical solution of the equation of motion leads to a singularity, but the development of non-radial motions due to the imperfect symmetry of any realistic perturbation is expected to halt the collapse and form a stable structure in virial equilibrium. Energy conservation suggests that the final radius of the bound structure should be approximately one half of the maximum “turn-around” radius (Gott and Rees, 1975), or smaller in the presence of a cosmological constant (Lahav et al., 1991).

Based on the statistical properties of Gaussian random fields, Press and Schechter (1974) developed a model for the number density of dark-matter haloes as a function of their mass and redshift. The model assumes that all Lagrangian patches in which the linearly extrapolated density contrast at redshift z lies above a critical value δ_c (of order unity) have collapsed to form bound haloes by that redshift. For practical applications, one has to choose a specific value for δ_c that matches a given halo definition. In an Einstein-de Sitter universe, spherical collapse produces virialized haloes with a final mean overdensity of $\Delta_{\text{vir}} = 18\pi^2 \simeq 178$ which occurs when the linear density contrast is $\delta_c = (3/5)(3\pi/2)^{2/3} \simeq 1.686$ (Kaiser, 1984; Bardeen, Bond et al., 1986; Efstathiou et al., 1988). For different cosmological models, these quantities acquire a redshift dependence which, however, is very weak for δ_c (e.g. Eke, Cole and

¹ This chapter and appendix A have been published in Borzyszkowski, Ludlow and Porciani (2014). The notation has been adapted to match the remaining thesis.

Frenk, 1996).

Bond, Cole et al. (1991) provided a sounder theoretical basis for the Press-Schechter mass function using the theory of “excursion-sets”. A key assumption of their model is that a halo identified at redshift z_{id} should form by collecting all matter initially contained within the largest possible region over which the mean linear overdensity is $\delta_L(z_{\text{id}}) = \delta_c$. In other words, the Lagrangian boundary of a halo coincides with the outermost shell which is collapsing at redshift z_{id} . However, for $\delta_c \approx 1.686$, this method yields halo mass functions that agree only qualitatively with those extracted from N-body simulations; they exhibit systematic shifts from the numerical result at both low and high masses which can be eliminated by adopting an effective mass-dependent threshold for halo formation $\delta_c(M)$ (e.g. Sheth and Tormen, 1999).

One possible explanation for this discrepancy is that the spherical collapse model is too simplistic. For example, N-body simulations have shown that dark-matter haloes originate from elongated Lagrangian regions whose longest geometric axis aligns with the direction of maximum gravitational compression (Porciani, Dekel and Hoffman, 2002, see also Despali, Tormen and Sheth, 2013; Lee and Pen, 2000; Ludlow, Borzyszkowski and Porciani, 2014, hereafter LBP14) The collapse of an ellipsoidal top-hat overdensity amplifies any initial departure from sphericity whether perturbations are isolated (Lynden-Bell, 1964; C. C. Lin, Mestel and Shu, 1965) or embedded in a uniform and expanding background (Icke, 1973; S. D. White and Silk, 1979; Peebles, 1980). The presence of external tides generated by large-scale structure, however, is expected to influence the dynamics of collapsing ellipsoids (e.g. Hoffman, 1986; Bertschinger and Jain, 1994). These tides were incorporated into the EC model by Eisenstein and Loeb (1995) and BM96 in a way that recovers the Zel’dovich approximation (Zel’Dovich, 1970) in the linear regime. In the latter formulation, an initially spherical overdensity is sheared into a collapsing ellipsoid by the action of external tides. The perturbation first reaches zero extension along the direction of largest compression, at which point orbit crossing occurs and the single-stream fluid equations cease to be valid. This can be prevented, however, by artificially halting collapse once the axis has shrunk by a critical factor $(18\pi^2)^{-1/3} \approx 0.178$ with respect to the background expansion (BM96; Angrick and Bartelmann, 2010).

Using this model, and defining the collapse time of a perturbation to be the epoch at which its last principal axis freezes out, Sheth, Mo and Tormen (2001) showed that more strongly sheared perturbations require higher initial density contrasts to overcome the tidal stretching and collapse by a particular time. Approximating the locations of halo formation as random points in a Gaussian random field, this “ellipsoidal-collapse threshold”, B_{SMT} , can be expressed in terms of the rms amplitude of linear density perturbations, σ_R , or equivalently in terms of halo mass. The value of B_{SMT} typically increases towards lower masses in a way that resembles the measured mean linear overdensities of dark-matter “protohaloes” identified in the initial conditions of N-body simulations (B. E. Robertson et al., 2009; Elia, Ludlow and Porciani, 2012; LBP14); this is generally interpreted as a reflection of the stronger tides felt, on average, by less massive haloes.

Sheth, Mo and Tormen (2001) used the ellipsoidal-collapse threshold to predict the mass function and bias of dark-matter haloes in the excursion-set formalism. If B_{SMT} is rescaled by an ad-hoc factor, this solution offers better agreement with the results of numerical simulations than calculations based on the spherical collapse model. Sheth, Mo and Tormen (2001) justified the rescaling by noting that the halo finder that was used in the simulations did not necessarily match the final overdensity of the haloes produced by the EC model.

The EC model of BM96, however, cannot account for the considerable scatter in the measured linear overdensities, δ_L , of regions that later collapse to form haloes of a particular mass M , and additionally fails to explain why δ_L depends strongly on the characteristic half-mass formation time of the halo (LBP14). In that companion paper we showed that, although the average overdensity of dark-matter

protohaloes tends to scale with external tides as described by the ellipsoidal model of BM96, the majority of recently collapsed haloes fall systematically *below* the model-predicted threshold for collapse. Hahn and Paranjape (2014) reached similar conclusions using warm-dark-matter simulations and thus provided further evidence that the ellipsoidal model systematically over-predicts the collapse time of a perturbation.

These puzzling results can be explained by a modified EC model that allows for initial asymmetry in the shape of the linear perturbations. Changing the initial axis lengths alters their individual collapse times and therefore modulates the initial density contrast required for complete collapse by a particular redshift. In LBP14, we showed that a model tuned to match the Lagrangian shapes of dark-matter protohaloes in numerical simulations can accurately reproduce their linear overdensities as well as its dependence on the initial departure from sphericity. A nice feature of this model is that the three principal axes of the perturbation freeze out almost simultaneously, similar to the case of spherical collapse. There is one caveat, however: the predicted threshold for collapse at redshift z_{id} only traces the overdensities of recently collapsed haloes for a given external tidal field and lies below the mean value measured for fixed halo mass and identification redshift. This begs the question of why dark-matter protohaloes with linear overdensities substantially above the ellipsoidal-collapse threshold exist at all, when virtually none with lower initial densities are found in cosmological simulations. We address these questions here using different versions of the ellipsoidal collapse model combined with the same numerical simulations (and dark-matter halo catalogs) as in LBP14. We anticipate that our findings imply a major revision of the standard lore for halo formation and raise questions regarding the validity of the excursion-set ansatz.

This chapter is structured as follows. The dynamical model for ellipsoidal collapse is presented in section 2.2, while our simulations, halo catalogs and analysis techniques are discussed in section 2.3. Our main results are presented in section 2.4, with a discussion of the implications of our results in section 2.5. The conclusions are then summarized in section 2.6.

2.2 The Ellipsoidal Collapse Model

The dynamical equations for the collapse of a constant density ellipsoid in the presence of an external tidal field were derived in LBP14. We assume that the principal axes of the perturbation are aligned with the eigenvectors of the external tidal field (Porciani, Dekel and Hoffman, 2002), and that the background expansion is driven by a pressureless matter density and a cosmological constant (see Del Popolo, 2002 for a similar model).

In a Cartesian coordinate system that is aligned with the principal frame of the ellipsoid, the differential equation for the axis lengths, r_i , is (BM96)

$$\frac{\ddot{r}_i}{r_i} = \Omega_\Lambda H_0^2 - \frac{3}{2} \frac{\Omega_M H_0^2}{a^3} \left(\frac{1}{3} + \lambda_i^{\text{tot}} \right), \quad (2.1)$$

where the dots denote time derivatives; H_0 is the Hubble constant; a the expansion factor; and Ω_M and Ω_Λ are the present-day densities of matter and the cosmological constant, Λ , normalized to the critical density, $\rho_{\text{crit}} = 3 H_0^2 / 8 \pi G$, where G is Newton's gravitational constant. The tidal field, λ_i^{tot} , is given by

$$\lambda_i^{\text{tot}} = \lambda_i^{\text{ext}} + \frac{\delta}{3} + \frac{\zeta_i \delta}{2}, \quad (2.2)$$

where $\delta = \delta(a)$ is the time-dependent density contrast of the ellipsoid. Note that eq. (2.2) contains contributions from both external tides, λ_i^{ext} , as well as an internal component generated by the ellipsoid

itself. The latter can be calculated explicitly using elliptic integrals:

$$\zeta_i = r_1 r_2 r_3 \int_0^\infty \frac{d\tau}{(\tau + r_i^2) \prod_{k=1}^3 \sqrt{\tau + r_k^2}} - \frac{2}{3}, \quad (2.3)$$

where the $2/3$ guarantees $\sum_i \zeta_i = 0$. Note that for a spherical geometry, the integral in eq. (2.3) is equal to $2/3$ and internal tides vanish. Initial condition for eq. (2.1) are set at some early time, a_0 , using the Zel'dovich approximation.

The external tidal field, λ_i^{ext} , however, as well as its time evolution, must be explicitly specified. One common assumption is that λ_i^{ext} is generated by structure on large scales and evolves from its initial value according to linear theory; another possibility is that λ_i^{ext} is dominated by the (non-linear) tidal field generated by the perturbation itself (BM96). A model which interpolates between these two regimes was recently proposed by Angrick and Bartelmann (2010). In this approach, one adopts the non-linear model $\lambda_i^{\text{ext}}(t)$ until axis i turns around, at which point its corresponding eigenvalue continues to evolve linearly. In our model we will initially assume that external tides are generated by large-scale structure and grow with time according to the linear growth factor, $D(z)$; internal tides are calculated self-consistently using the time-dependent shape of the ellipsoid. In section 2.4.2 we will revisit the issue of external tides in more detail, in order to test the assumption made above regarding their time evolution.

The collapse and virialization of the perturbation is generally approximated in this model by freezing the individual axes when they reach a size $r_{f,i} = f q_i a$ (BM96). Here q_i is the *initial* comoving length of axis i , and the parameter f is usually set to 0.178. In the case of spherical collapse in an Einstein-de Sitter universe, this choice ensures that the perturbation has a density contrast of $\delta \approx 178$ at the moment of collapse. Note, however, that a particular choice of f has no fundamental physical motivation and may depend on the nature of collapse (e.g., whether spherical or ellipsoidal) or on the background cosmological model. A more general virialization condition based on the tensor virial theorem was suggested by Angrick and Bartelmann (2010). However, since the late stages of collapse generally occur quite rapidly, such modifications have only a minor effect on axis collapse times, from which density thresholds are inferred. For the sake of simplicity, and to ease comparison with previous work, we adopt the traditional freezing factor $f = 0.178$ for our EC model as well, but return this point in section 2.4.3.

2.3 Numerical Methods

2.3.1 The Simulations

Our analysis focuses on dark-matter haloes identified at $z_{\text{id}} = 0$ in two cosmological simulations of structure formation in the standard Λ CDM cosmology. These simulations are the same as those described in LBP14 (see also Pillepich, Porciani and Hahn, 2010). We therefore summarize here only their main aspects, and refer the reader to that work for further details.

Both runs followed the evolution of the dark-matter component using 1024^3 equal mass particles. The periodic boxes have side lengths equal to $150 h^{-1}\text{Mpc}$ and $1200 h^{-1}\text{Mpc}$. Each run was carried out with a lean version of the simulation code GADGET (Springel, Yoshida and S. D. White, 2001; Springel, 2005) and adopted the following cosmological parameters: $\Omega_M = 0.279$, $\Omega_\Lambda = 1 - \Omega_M = 0.721$, $n_{\text{tilt}} = 0.96$, $\sigma_8 = 0.817$, and $H_0 = 73 \text{ km s}^{-1} \text{ Mpc}^{-1}$. Here n_{tilt} is the spectral index of primordial density fluctuations; σ_8 is the rms density fluctuation measured in $8 h^{-1} \text{ Mpc}$ spheres, linearly extrapolated to $z = 0$. These values are consistent with the WMAP 5-year data release (Komatsu et al., 2009). The resulting particle masses are $m_p = 2.43 \times 10^8 h^{-1} M_\odot$ and $m_p = 1.24 \times 10^{11} h^{-1} M_\odot$ for the $150 h^{-1}\text{Mpc}$ and $1200 h^{-1}\text{Mpc}$

boxes.

Initial conditions for the simulations were produced using the Zel’Dovich approximation for a starting redshift of $z_{\text{start}} = 70$ and 50 for the small and large box, respectively. As discussed in detail by Pillepich, Porciani and Hahn (2010), these choices of z_{start} are sufficient to erase all transient artifacts in the halo mass function by $z = 0$. During each simulation, 30 snapshots were saved between $z = 10$ and 0 in logarithmically spaced intervals of $(1 + z)^{-1}$.

2.3.2 Halo Catalogues

We identified dark-matter haloes in each simulation output using a friends-of-friends (FOF) halo finder with a linking length equal to 0.2 times the mean nearest-neighbour distance. All haloes with at least $N_{\text{FOF}} = 32$ particles were included in the halo catalogues. Once all dark-matter haloes were identified, the formation histories of $z_{\text{id}} = 0$ haloes were constructed by tracing each halo’s most massive progenitor backwards through all previous simulation outputs. Accretion histories defined in this way can be used to provide simple estimates of halo formation times, such as the redshift z_{50} at which 50 per cent of the halo’s final mass had first assembled into one main progenitor.

We will also consider the Lagrangian “protohaloes” of each $z = 0$ halo, which can be easily identified by tracing all halo particles back to the initial conditions of the simulation. In this chapter we will only consider haloes that, at $z = 0$, are composed of at least $N_{\text{FOF}} = 1000$ particles, unless explicitly stated otherwise.

In order to test the sensitivity of our results to the adopted halo definition, we have also built halo catalogues using a spherical overdensity (SO) halo finder. This algorithm grows spheres around local density maxima until they reach a density contrast of Δ_{SO} times the mean matter density. We adopted $\Delta_{\text{SO}} = 100, 200$ and 500, and repeated all aspects of the analysis using these alternative halo definitions. We will distinguish the characteristics of haloes identified by the FOF or SO algorithms using subscripts. The FOF halo mass, for example, will be denoted M_{FOF} , whereas M_{200} defines the SO mass based on an overdensity of $\Delta_{\text{SO}} = 200$. The main results of our work will be presented for the FOF halo definition; the results for SO haloes are summarized in appendix A.

2.3.3 Analysis Techniques

The EC model described in section 2.2 depends explicitly on the initial axis ratios of the collapsing overdensity. Since in practice these are free parameters, we will constrain their values using the shapes of protohaloes identified in the initial conditions of our simulation.

We characterize the shapes of dark-matter haloes and protohaloes using the inertia tensor, defined

$$I_{ij} = m_p \sum_k x_{k,i} x_{k,j}, \quad (2.4)$$

where \mathbf{x}_k is the distance vector between particle k and the halo’s center-of-mass; the i and j are the projected lengths of \mathbf{x}_k along each coordinate direction. This matrix can be diagonalized to obtain the principal axis lengths of the ellipsoid, $q_1 \geq q_2 \geq q_3$, which can be used to characterize halo shapes in terms of their ratios: q_2/q_1 and q_3/q_1 , for example, are the intermediate-to-major and minor-to-major axis ratios. The eigenvectors of the inertia tensor define the principal axis frame, and will be denoted \hat{i}_i .

As discussed in LBP14, the shapes of protohalo boundaries are closely related to the external tidal field acting upon them. Protohaloes have strongly triaxial shapes whose principal directions align closely with those of the surrounding tides. When estimating the tides acting upon a given protohalo, it is therefore

desirable to move beyond simple spherical filtering of the tidal field, and attempt to incorporate additional information on the shape of the protohalo as well.

Here we propose a novel method to estimate the *average* tidal field acting upon a protohalo as it collapses to form a non-linear object. We start by calculating the density contrast field on a 1024^3 grid that covers the entire simulation volume. Densities are assigned to each grid element using cloud-in-cell interpolation (Hockney and Eastwood, 1988). Within each grid element, we also calculate the tidal deformation tensor,

$$D_{ij} = \frac{\partial^2 \Phi}{\partial x_i \partial x_j}, \quad (2.5)$$

using standard Fourier techniques. Here Φ is the peculiar gravitational potential, which is related to the density contrast by Poisson's equation: $\nabla^2 \Phi = \delta$. This field can be used to compute the total strength and orientation of the tidal field over an arbitrary volume, V (for example, a protohalo), in the following way. We first compute the magnitude of D_{ij} along the direction $\boldsymbol{\vartheta}$ using

$$\lambda = \sum_V \boldsymbol{\vartheta} \cdot \mathbf{D} \cdot \boldsymbol{\vartheta}, \quad (2.6)$$

where the sum is over all grid cells contained within the volume. We then iteratively determine the orientation of $\boldsymbol{\vartheta}$ that minimizes λ ; this defines the direction \mathbf{d}_3 and its magnitude λ_3 . In the plane perpendicular to \mathbf{d}_3 , we then search for the direction $\boldsymbol{\vartheta} = \mathbf{d}_1$ that maximizes eq. (2.6), which also determines λ_1 . This constrains the direction \mathbf{d}_2 since it is, by definition, perpendicular to both \mathbf{d}_1 and \mathbf{d}_3 ; λ_2 is then determined using eq. (2.6) along the direction $\boldsymbol{\vartheta} = \mathbf{d}_2$. In this way we estimate the total tidal tensor, described by the λ_i s and \mathbf{d}_i s, acting on the volume V without invoking a spherical filter function. For protohaloes, we assume that V can be approximated by an ellipsoid whose axis lengths and orientations are derived from its inertia tensor.

Once the linear tidal field has been measured in this way, we define the Lagrangian overdensity of each protohalo as $\delta_L = \sum_i \lambda_i$. Both the tides and the density contrast of the protohaloes are therefore evaluated within an ellipsoidal (rather than spherical) aperture whose shape and orientation is tailored to match each individual protohalo. Relative to spherical filtering, this results in per cent-level corrections to δ_L over the range of masses we study here.

Applying this procedure to FOF haloes with ≥ 1000 particles ensures that even the lowest mass haloes are, on average, resolved with at least 20 grid cells. We have explicitly verified that this is sufficient to yield robust estimates of the λ_i s and \mathbf{d}_i s.

Note that the tidal field can be alternatively characterized in terms of its ellipticity, e , and prolateness, p . These are defined

$$e = \frac{\lambda_1 - \lambda_3}{2 \delta_L} \quad (2.7)$$

and

$$p = \frac{\lambda_1 - 2\lambda_2 + \lambda_3}{2 \delta_L}. \quad (2.8)$$

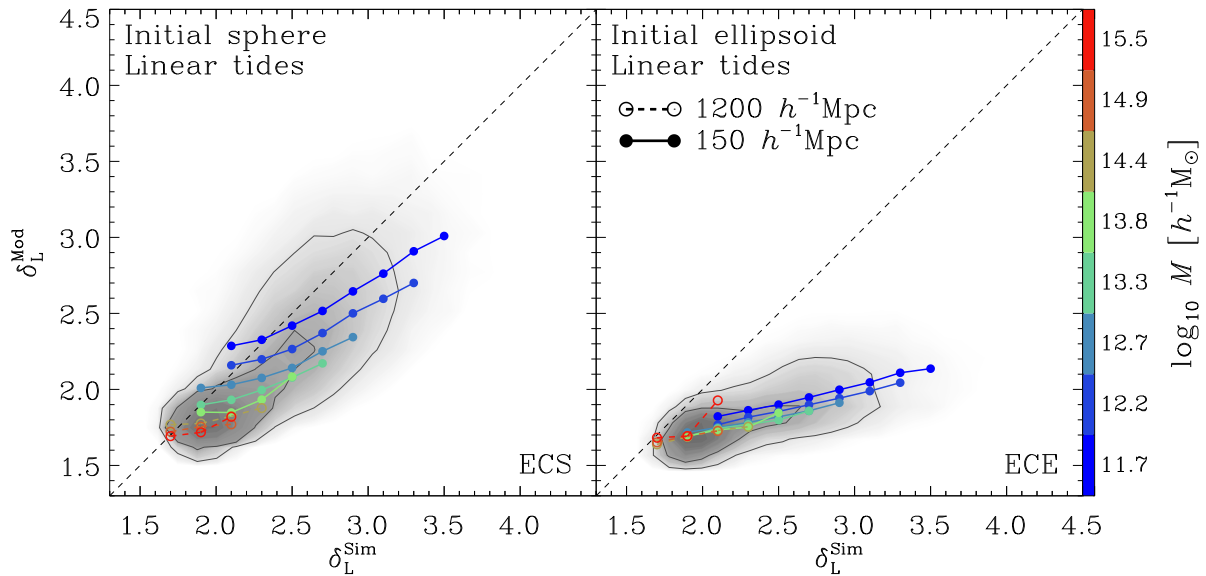


Figure 2.1: Lagrangian overdensities of dark-matter protohaloes predicted by the ellipsoidal collapse model plotted versus their overdensities measured in the initial conditions of our simulations. Model predictions assume that the Lagrangian tidal field measured at each protohalo’s center evolves according to linear theory. The left-hand panel corresponds to the EC model of BM96, which assumes that each protohalo’s initial shape can be approximated by a sphere; the right-hand panel explicitly accounts for each protohalo’s initially non-spherical shape, which we measure in the simulation initial conditions. Shaded regions highlight the density of points in the $\delta - \delta$ plane; contours enclose 50 per cent and 80 per cent of the data. Connected points show the median values of δ_L^{Mod} at fixed δ_L^{Sim} measured in separate mass bins (shown using different colored lines), equally spaced in $\log M$. Solid circles are used for haloes in our $150 h^{-1}$ Mpc box; open squares for those in the $1200 h^{-1}$ Mpc box

2.4 Results

2.4.1 Ellipsoidal collapse and density thresholds for CDM halo formation

Given estimates of the tidal field acting upon a given protohalo, we can use the EC model described in section 2.2 to *predict* the linear density contrast required for collapse to occur at $z_{\text{id}} = 0$. We will discriminate “predicted” and “measured” values of δ_L using superscripts: δ_L^{Sim} , for example, refers to its value measured in the initial conditions of our simulations; δ_L^{Mod} to the model-predicted value. Protohalo overdensities predicted by the EC model are shown in fig. 2.1, and are compared directly with the linear overdensities δ_L^{Sim} obtained by the method described above. We will use these “ $\delta - \delta$ ” relations as a diagnostic for the ability of the EC model to describe the dynamics of individual dark-matter haloes.

In fig. 2.1 we plot, for each protohalo, the linear density contrast for collapse at $z = 0$ predicted by the EC model versus their measured overdensities. The left hand panel shows the predictions of the EC model of BM96, which assumes that each protohalo occupies a spherical Lagrangian volume². We will hereafter refer to this as the ECS model (for Ellipsoidal Collapse of Spherical perturbations); density contrasts predicted by this model will be denoted δ_L^{ECS} . On the right, we have included the influence of each protohalo’s shape on the predicted collapse threshold (hereafter referred to as the ECE model, for Ellipsoidal Collapse of Ellipsoidal perturbations). Note that, in this case, the non-spherical perturbation itself contributes to the initial tidal field. We therefore modify the external component such that the

² Note that an equivalent plot was provided in Figure 3 of Sheth, Mo and Tormen (2001).

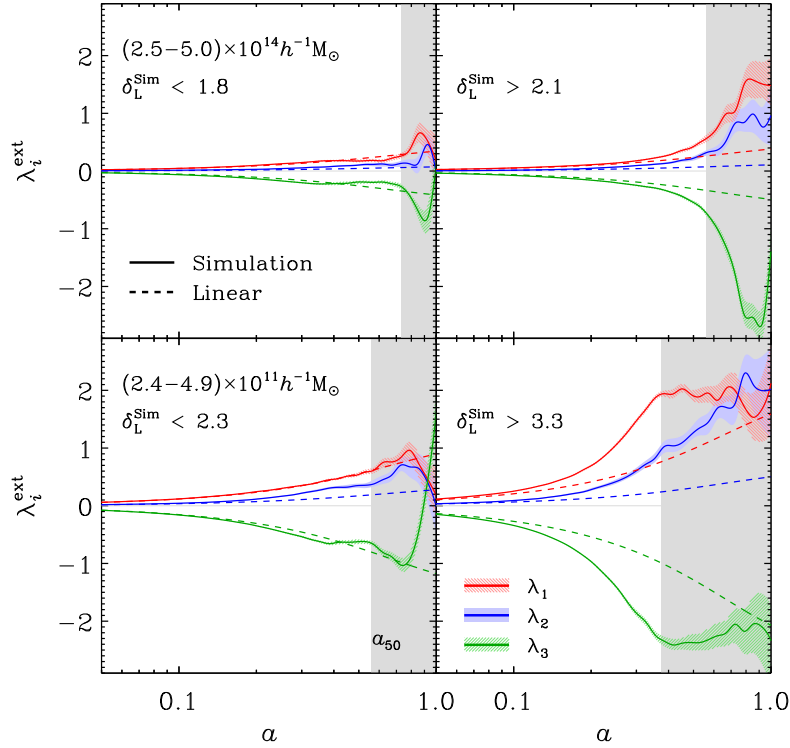


Figure 2.2: Evolution of the median external tidal field (solid lines) for haloes in two separate mass bins. Upper panels correspond to haloes in the mass range $2.5 < M_{\text{FOF}}/(10^{14} h^{-1} M_{\odot}) < 5$, lower panels to those with $2.4 < M_{\text{FOF}}/(10^{11} h^{-1} M_{\odot}) < 4.9$. Left- and right-hand panels split haloes in each mass bin according to their initial density contrast, $\delta_{\text{L}}^{\text{Sim}}$: those of the left include only haloes that rank in the lowest 15 per cent of the $\delta_{\text{L}}^{\text{Sim}}$ distribution, and those on the right only those in the highest 15 per cent. In each case, hatched regions correspond to the 90 per cent confidence interval on the median $\lambda_i^{\text{ext}}(z)$ obtained by bootstrapping. For comparison, we also show the linear evolution of the median Lagrangian tidal fields measured at each halo center using dashed lines. Grey shaded regions correspond to redshifts $z < z_{50}$, where z_{50} is the median half-mass formation redshift of each halo sample.

total tidal field in the model initially matches the linear tidal field measured for each protohalo in the simulation. In each panel connected symbols show the median values of $\delta_{\text{L}}^{\text{Mod}}$ measured in fixed bins of $\delta_{\text{L}}^{\text{Sim}}$; different colored lines plot the relations for equally spaced logarithmic mass bins (indicated in the legend).

Note that, in both cases, the model-predicted overdensities correlate rather well with those measured directly in the initial conditions of the simulations, albeit with considerable scatter. The median trends, however, are noticeably shallower than one would expect if the ellipsoidal model truly captures the dynamics of halo collapse. Note also that the ECS model predicts a strong mass dependence to the median $\delta - \delta$ relations. This results from the fact that the collapse barrier (at fixed p) depends entirely on the ellipticity of the tidal field e , growing monotonically with increasing e . Because, for random points, e scales with mass as $e = (\sigma_{\text{R}}/\delta)/\sqrt{5}$ (Doroshkevich, 1970), the ECS model predicts systematically higher collapse thresholds for lower mass haloes, resulting in a segregation of the average $\delta_{\text{L}}^{\text{Mod}}$ s predicted for haloes of different mass.

Intriguingly, the mass dependence disappears when individual protohalo shapes are included in the

model prediction. This is because toward lower masses, protohaloes become increasingly triaxial, which lowers the density threshold required for collapse to occur in spite of the increasing tidal field strength (see LBP14). None the less, both models fail to reproduce the measured distribution of protohalo overdensities, and it is worthwhile exploring what aspects or assumptions of the EC model may result in the discrepancy.

2.4.2 The influence of external tides

One common assumption of the EC model – and indeed our assumption in constructing fig. 2.1 – is that the external tidal field, assumed to be generated by structure on very large scales, remains linear at all times. All ingredients needed to solve eq. (2.1) are therefore already present in the linear density field. In reality, a growing dark-matter halo may be subjected to interactions with nearby neighbours which may result in strongly non-linear tidal forces that act to suppress its growth and alter its collapse time (Hahn, Porciani, Dekel et al., 2009; H. Wang et al., 2011). It is therefore important to assess whether the assumption of linearly evolving tides remains valid during the evolution of simulated haloes, in order to make a more meaningful comparison between their measured and predicted overdensities.

To do so, we trace all particles belonging to each protohalo through each simulation output, and use eq. (2.4) to characterize the redshift dependence of the shape and orientation of each collapsing region. We approximate the geometry of this region as an ellipsoid and fix its volume, V , such that it encloses the protohalo mass at all subsequent times. The total tidal field acting upon the collapsing region is then estimated using the procedure outlined in section 2.3.3. This method has two distinct advantages over using the particles themselves to define V : 1) it ensures that we follow a region with constant enclosed mass, even though the individual particles within it may change with time; 2) it allows for a simple decomposition of the total tidal field into its internal and external components.

We apply this procedure to each $z_{\text{id}} = 0$ FOF halo (containing at least 1000 particles) and in all simulations outputs in order to explicitly measure the time evolution of the tidal field, $\lambda_i^{\text{tot}}(z)$, acting upon each halo. The shape of the ellipsoid can be used to approximate the contribution of internal tides, $\zeta_i \delta/2$, using eqs. (2.2) and (2.3), in order to estimate $\lambda_i^{\text{ext}}(z)$. Note that calculating the internal tides this way assumes a homogeneous density inside the ellipsoid, which may be inaccurate at late times.

The evolution of the external tidal field calculated in this way is shown in fig. 2.2 for haloes in two separate mass bins. Upper panels correspond to haloes that fall in the mass range $2.5 < M_{\text{FOF}}/(10^{14} h^{-1} M_{\odot}) < 5$; the lower to those with $2.4 < M_{\text{FOF}}/(10^{11} h^{-1} M_{\odot}) < 4.9$. Panels on the left show haloes in each mass bin that rank in the lowest 15 per cent of δ_L^{Sim} , whereas those on the right rank in the highest 15 per cent. (The threshold values of δ_L^{Sim} for each sample are provided in each panel.) Grey shaded regions indicate redshifts below the median half-mass formation redshift for each sample, after which the assumption of a homogeneous density inside the ellipsoid is likely inaccurate. The measured $\lambda_i^{\text{ext}}(z)$ s are shown using solid lines, as indicated in the legend, while the dashed lines show the linear extrapolation of the average Lagrangian tides measured for each halo sample.

Massive haloes tend to evolve in environments where the tidal field scales approximately as expected from linear theory. This is not surprising given that these haloes dominate their environments and the external tides are therefore generated by long-range modes that have not yet collapsed. The same is true for low-mass haloes in low-density regions. Protohaloes with low values of δ_L^{Sim} tend to be less clustered than those of higher δ_L^{Sim} , with the latter forming in regions where tidal fields clearly grow more strongly than expected from a simple linear extrapolation of the Lagrangian values.

What implications do these non-linear tides have for the collapse thresholds of dark-matter haloes inferred from the EC model? Having calculated the evolution of the tidal field explicitly for each individual halo, we can insert it directly into eq. (2.1) in order to assess the impact of non-linear tides on

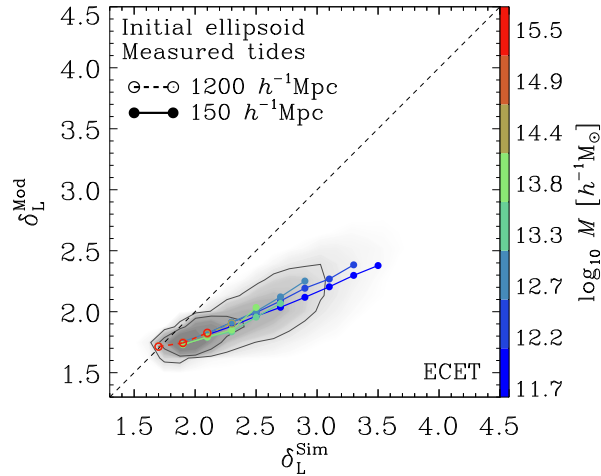


Figure 2.3: Linear density contrast predicted by the ECET model plotted against the measured Lagrangian overdensities of dark-matter protohaloes. The ECET model explicitly accounts for the non-spherical shape of each individual protohalo as well as the evolution of their external tidal fields, without resorting to the common assumption of linearly evolving tides. As in fig. 2.1, shaded regions indicate the density of haloes in the $\delta - \delta$ plane; contours enclose 50 per cent and 80 per cent of the data points. Connected points show the median values of δ_L^{Sim} at fixed δ_L^{Mod} measured in separate mass bins, as indicated in the legend.

the collapse thresholds inferred from the ellipsoidal collapse model. The resulting $\delta - \delta$ relation for the ECE model is shown in fig. 2.3 (hereafter the ECET model) where, again, the connected points highlight medians in logarithmic mass bins.

As expected, massive haloes, and those with $\delta_L^{\text{Sim}} \approx \delta_{\text{sc}}$, are largely unaffected by the inclusion of explicitly measured external tides. Those with higher δ_L^{Sim} , however, live in more clustered environments and are affected by tides that clearly evolve non-linearly. These tides act to inhibit the collapse of the density perturbations, increasing the initial density contrast required for collapse to occur at $z = 0$. The effect, however, is weak. For example, haloes in the lower right panel of fig. 2.2 are subject to external tides that deviate from the linear theory extrapolation by roughly a factor of ~ 2.2 at the halo's half-mass formation time (shaded regions indicate redshifts below the median value of z_{50} for all haloes in each sample). This effect delays full collapse (in the ECE case) by roughly $1.4 h^{-1} \text{Myr}$, or, equivalently, requires an enhancement of only 12 per cent in the initial density contrast for collapse at $z = 0$. This is clearly not sufficient to bring the predictions of the ECE model into agreement with the simulation data, suggesting that other factors may be at play. We turn our attention to these next.

2.4.3 Collapse times

There is a clear mismatch between the predictions of the EC model and the true properties of dark-matter protohaloes when applied on a object-by-object basis. As discussed in LBP14, these differences may be related to the details of each halo's unique evolutionary history. For example, in the EC or SC model, collapse occurring at redshift $z_c > z_{\text{id}}$ requires an initial density contrast a factor of $D(z_{\text{id}})/D(z_c)$ larger than what would be needed for collapse at z_{id} under the same environmental conditions. Because, at a given mass scale, haloes with higher δ_L typically form earlier than those of lower δ_L (LBP14), correcting the model predictions for $z_c > 0$ may explain the discrepancy between the measured overdensities of protohaloes and the model-predicted values.

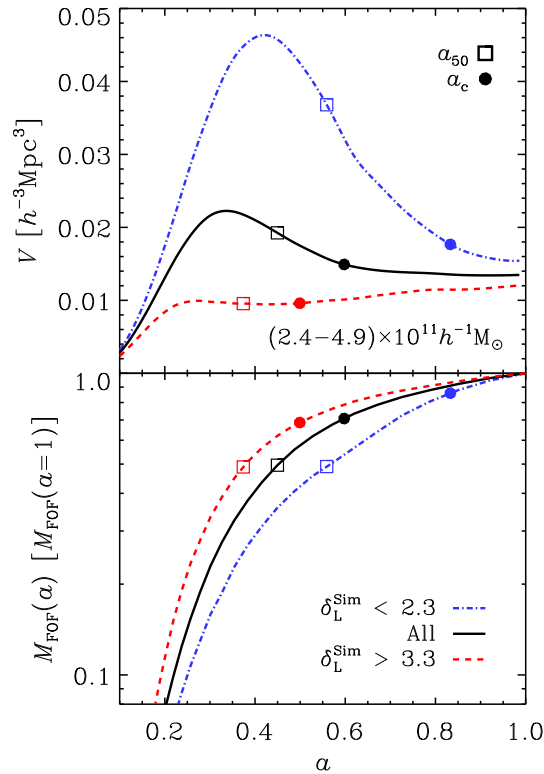


Figure 2.4: *Upper panel:* Evolution of the median volume of the ellipsoid, centred on each collapsing protohalo, that, at any z , encloses the final mass of the descendant halo at $z = 0$ (see section 2.4.3 for details). All haloes are selected to lie in a narrow mass bin, as indicated in the legend. The black solid line corresponds to the median $V(a)$ for all haloes in that mass bin. Dashed (red) and dot-dashed (blue) lines show the evolution for the subsamples of haloes that lie in the upper-most and lower-most 15 per cent of δ_L^{Sim} . *Lower panel:* Evolution of the median FOF mass of the most massive progenitor for the same samples of haloes. In both panels, solid circles highlight the “collapse redshift”, z_c , defined in section 2.4.3, whereas open squares indicate the half-mass formation time, z_{50} , at which each haloes main progenitor first assembled half of its present-day mass.

As discussed in LBP14, simple estimates of halo formation times based on the growth of their most massive progenitors fail to account for the scatter in their linear overdensities. However, unlike our simulated haloes, which grow through a sequence of mergers and smooth accretion, perturbations in the EC model remain homogeneous throughout their evolution and the collapse redshift is therefore unambiguously defined as the time at which the last axis reaches the radius $r_{f,i} = f q_i a$. Once collapse has occurred, the model assumes that the volume of the ellipsoid remains constant thereafter. Is there an analogous definition of “collapse” that can be easily applied to cosmological haloes?

For a dark-matter halo identified at $z_{\text{id}} = 0$, one can approximate the evolution of its outermost mass shell by tracking the volume $V(a)$ of the same best-fitting ellipsoid used to calculate the external tidal field (described in section 2.4.2). Its size can be used to provide a simple and intuitive estimate of the time at which its *entire* $z = 0$ mass had first assembled into a single, dispersion-supported non-linear system.

In the upper panel of fig. 2.4 we plot the evolution of the volume of three such ellipsoids after averaging

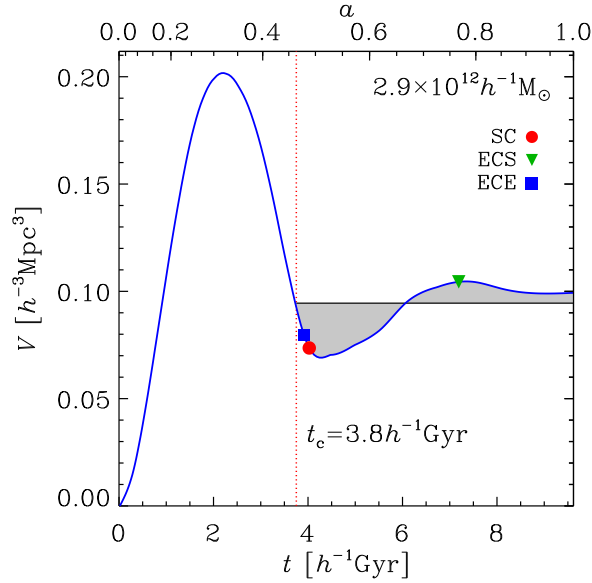


Figure 2.5: Evolution of the volume of an ellipsoid centred on the progenitor of a ($z = 0$) $2.8 \times 10^{12} h^{-1} M_{\odot}$ halo that, at each redshift, encloses the present day halo mass. The shape and orientation of the best-fitting ellipsoid is explicitly calculated using the full set of particles that, at $z = 0$, belong to the FOF group. The evolution of the volume, $V(z)$, is used to estimate the “collapse redshift” of the halo, $z_c = 1.2$ (dotted-dashed vertical line), using the condition specified in eq. (2.9). This definition of z_c estimates the time at which the entire $z = 0$ halo mass had first assembled into a stable configuration, and accounts for oscillations in the volume that occur during the system’s approach toward equilibrium. The coloured symbols plotted along the blue line highlight the collapse times predicted by the different versions of the EC model discussed in this chapter.

over subsamples of haloes in the mass range $(2.4 - 2.9) \times 10^{11} h^{-1} M_{\odot}$. The solid (black) curve shows the evolution of the median $V(a)$ computed for all haloes in the quoted mass bin; dashed (red) and dot-dashed (blue) lines show the corresponding result for haloes that rank in the maximum and minimum 15 per cent of δ_L^{Sim} , respectively.

On average, the present-day mass of these haloes was already in place at $z \approx 0.7$. More extreme examples can be found in the sample with the highest initial density contrasts, whose present-day masses reached a stable volume at $z \approx 2$, when the Universe was only ~ 15 per cent of its current age. Attempting to predict the collapse dynamics of these haloes with models tuned for collapse at $z = 0$ is therefore prone to systematic errors. On the other hand, haloes with the lowest value of δ_L^{Sim} appear to have accreted their outer-most mass shells only very recently. This implies that, on average, haloes with $\delta_L^{\text{Sim}} > \delta_L^{\text{ECE}}$ have $z_c > 0$: strictly speaking, *these haloes collapsed before they were identified*.

This may seem to conflict with the mass accretion histories of the same haloes, shown in the bottom panel of fig. 2.4. These curves trace the median evolution of the FOF mass of each halo’s main progenitor, and suggest that halo masses increase at all redshifts. However, as already noted by Diemand, Kuhlen and Madau (2007), this “pseudo-growth” results from the fact that halo boundaries are defined, at any time, relative to a fixed (or slowly varying) overdensity threshold. The decrease in the cosmic background density with time therefore results in an artificial increase of halo boundaries, and hence masses (see also, Cuesta et al., 2008; Diemer, More and Kravtsov, 2013; Zemp, 2014). Halo finders based on fixed *physical* densities may therefore result in more realistic estimates of their masses and sizes.

None the less, we can use the trajectories of $V(a)$ to estimate an appropriate “freezing” or collapse

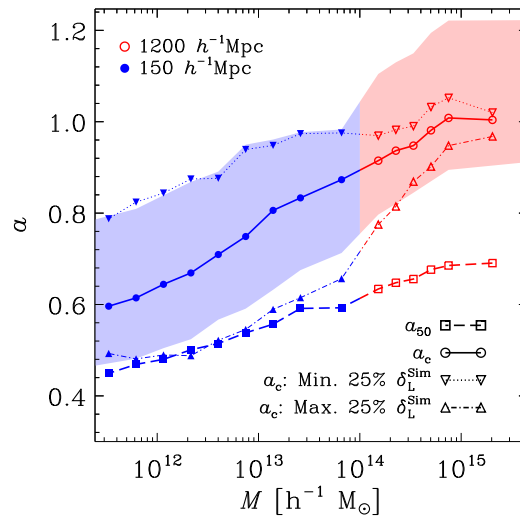


Figure 2.6: Mass dependence of halo collapse and formation times. Circles connected by solid lines show the median “collapse redshift”, z_c (defined in eq. 2.9); squares connected by dashed lines show the the median half-mass formation time, z_{50} , at which each halo’s main progenitor had first assembled half of its present-day mass. Triangles connected by dotted and dot-dashed lines show the medians values of z_c for haloes that rank in the highest and lowest quartile of δ_L^{Sim} . Filled and open symbols are used to distinguish haloes identified in our $150 h^{-1} \text{ Mpc}$ box from those in the $1200 h^{-1} \text{ Mpc}$ box, respectively. Shaded regions (shown only for z_c) indicate the 25th and 75th percentiles of the scatter.

time, z_c , for each individual halo. This estimate of z_c can then be used to halt collapse in the EC model in order to make a more appropriate comparison between the model’s predictions and measured Lagrangian overdensities of dark-matter protohaloes.

We define z_c as earliest redshift at which the following condition is satisfied:

$$\int_{t_c}^{t_{\text{max}}} [V(t) - V(t_c)] dt = 0, \quad (2.9)$$

where t_c and t_{max} are the cosmological times corresponding to the collapse redshift, z_c , and the end of the simulation, z_{max} . In fig. 2.5 we provide an example of the evolution of $V(a)$ (solid blue curve) for a single halo of ($z = 0$) mass $M_{\text{FOF}} \sim 2.9 \times 10^{12} h^{-1} M_{\odot}$. The evolution mimics the expectations of simple collapse models: after an initial phase of expansion the system turns around, begins collapsing and eventually reaches a stable quasi-equilibrium configuration. The first “dip” after turnaround corresponds to a state of maximal compression in which the halo’s entire $z = 0$ mass is briefly confined within a compact volume smaller than the present-day virial volume of the halo. This is followed by a phase of expansion, and a second (very slight) phase of contraction as the system moves toward equilibrium. These “dips” and “peaks” clearly occur *after* collapse, but before virialization. Our definition of z_c allows for these oscillations as the system relaxes to a state of equilibrium. The grey shaded region in fig. 2.5 highlights the integrand of eq. (2.9). Note that areas above and below the horizontal line cancel so that the integral vanishes. The corresponding collapse time, $z_c \approx 1.2$, is indicated with a vertical (red) dotted line.

In fig. 2.6 we plot the mass dependence of $a_c = (1 + z_c)^{-1}$ for all $z_{\text{id}} = 0$ haloes in each simulation. Note that we have verified that our estimates of z_c are insensitive to the snapshot output sequence by skipping even-numbered outputs and repeating the analysis. Connected, filled (blue) circles show the

Table 2.1: Values obtained from fitting eq. (2.10) to the median collapse redshift as a function of halo mass.

Haloes	c_1	c_0
FOF	0.13	-0.88
SO ($\Delta = 100$)	0.13	-0.81
SO ($\Delta = 200$)	0.12	-0.79
SO ($\Delta = 500$)	0.11	-0.66

median trend for all haloes in our $150 h^{-1}$ Mpc box; open (red) circles correspond to haloes in our $1200 h^{-1}$ Mpc box. Shaded regions in each case indicate the 25th and 75th percentiles of the scatter³. As expected, the most massive haloes (those above a few $\times 10^{14} h^{-1} M_{\odot}$) have typical collapse times of $z_c \approx 0$, whereas $z_c > 0$ for lower mass haloes. The median mass dependence to a_c can be approximated by a simple linear function:

$$a_c = c_1 \log_{10}(M/[h^{-1}M_{\odot}]) + c_0. \quad (2.10)$$

The values of the best-fitting parameters are provided in table 2.1 for several different halo definitions.

2.4.4 The collapse threshold at collapse redshift z_c

Adopting separate collapse and identification redshifts has a subtle implication for comparing the predictions of the EC model to the outcome of simulations. FOF haloes defined at $z_{\text{id}} = 0$ are bounded by mass (and resolution) dependent isodensity contours. Our definition of z_c , however, defines the time at which the entire $z = 0$ mass was first confined within approximately the same *physical* volume. As a result, the (comoving) overdensity of the halo at z_c will be lower than its $z = 0$ value by a factor of $(1 + z_c)^3$. To account for the different density contrast at collapse we multiply the radial freezing factor, f , used in the EC model by $(1 + z_c)$.

Additional corrections to f can be made in order to account for the mass-dependence of FOF halo overdensities. For example, we find that haloes in our $150 h^{-1}$ Mpc box have, on average, $\Delta \approx 325$, whereas $\Delta \approx 270$ for those in our $1200 h^{-1}$ Mpc run (see More, Kravtsov et al., 2011, for a more detailed discussion of the overdensities of FOF groups). Since $f = 0.178$ sets the $z = 0$ virial overdensity in the spherical collapse model, we modify the radial freezing factors in the EC model to match the mean overdensities of haloes in each of our simulations. This results in $f = 0.145$ for haloes in our $150 h^{-1}$ Mpc box, and $f = 0.155$ for those in the $1200 h^{-1}$ Mpc box.

Based on the results presented in fig. 2.6, the vast majority of dark-matter haloes (apart from the most massive ones) are expected to have reached stable configurations at $z_c \geq 0$. This implies that most haloes, at the moment they are identified, are experiencing little, if any, net mass accretion. We examine this point further in fig. 2.7, where we plot the average radial-velocity profiles measured in spherical bins surrounding each $z_{\text{id}} = 0$ dark-matter halo. Note that the radial coordinates have been scaled to the characteristic radius $R_{\text{FOF}} = (3 V_{\text{FOF}}(z = 0)/4\pi)^{1/3}$; median values of the radii enclosing fixed overdensities of $\Delta = 100, 200,$ and 500 are also shown as solid, dashed and dot-dashed vertical lines, respectively. Panels correspond to two separate mass bins: $(2.5 - 5.0) \times 10^{14} h^{-1} M_{\odot}$ (top) and $(2.4 - 4.9) \times 10^{11} h^{-1} M_{\odot}$ (bottom). Within each mass bin separate curves show the median $v_r(r)$ profiles

³ Because many massive haloes at $z = 0$ are expected to be in a state of rapid growth, the use of eq. (2.9) to estimate z_c may not be justified. In order to obtain a reasonable estimate of the collapse times of massive systems we decided to extend our $1200 h^{-1}$ Mpc box run to $z = -0.27$, which allowed us to track the collapse phase of even the most massive haloes identified at $z_{\text{id}} = 0$.

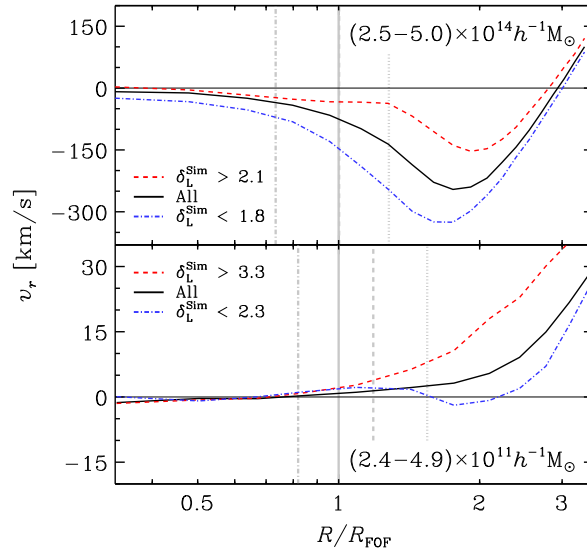


Figure 2.7: Solid black lines show the median radial velocity profiles of FOF haloes at $z_{\text{id}} = 0$ in two separate mass bins. Dashed (red) and dot-dashed (blue) lines show the median $v_r(r)$ for haloes that rank in the highest and lowest 15 per cent of δ_L^{Sim} . In all cases, the radial coordinate is expressed in units of the mean size of the FOF haloes. Vertical grey lines indicate the typical size of the haloes when identified with the SO-algorithm, using an overdensity threshold of $\Delta = 100$ (dotted), 200 (dashed) and 500 (dot-dashed), respectively. Note the different scale of the velocity axis in the upper and lower panels.

for all haloes (solid curve) as well as for the upper and lower-most 15 per cent of the δ_L^{Sim} distribution.

Independent of their initial overdensity, the majority of massive haloes exhibit a strong pattern of infall in the regions surrounding the halo. The radius at which infall becomes substantial, however, is a function of δ_L (and hence, z_c). This suggests, that these systems are still accreting, and have not yet reached their final quasi-equilibrium state. Lower-mass haloes, on the other hand, display very little infall and are therefore not accreting mass (see also Prada et al., 2006).

The physics that determines the collapse redshift of a particular halo, or the moment at which infall is suppressed, is not well understood. None the less, practical estimates of z_c , such as that defined by eq. (2.9), can be used to rescale the collapse redshifts in the EC model in order to make a more meaningful prediction of the density threshold required for the perturbation to collapse. We plot the predicted density contrast for collapse at z_c , linearly extrapolated to $z_{\text{id}} = 0$, versus the measured protohalo overdensities (also linearly extrapolated to $z = 0$) in fig. 2.8. For completeness, we include the results for all variants of the ellipsoidal model that we have considered, and show the median trends in the same halo-mass bins as before. In all cases, correcting for $z_c > 0$ significantly improves the correlation between the predicted and measured protohalo overdensities.

Note that the mass dependence of the $\delta - \delta$ relation predicted by the ECS model (seen already in fig. 2.1) remains after correcting for z_c . This is a result of the fact that z_c increases with decreasing mass, and therefore corrects the predicted overdensities of low-mass haloes more than those of massive ones. Haloes of $\sim 10^{12} h^{-1} M_\odot$, for example, have $\langle z_c \rangle \sim 0.58$, rather than $z_c = 0$. Within the ECS model, this shift in collapse time is achieved by enhancing the linear density contrast of the perturbation by roughly 35 per cent. Massive haloes ($\gtrsim 10^{14} h^{-1} M_\odot$), on the other hand, have $z_c \sim 0$ and therefore remain unchanged in this $\delta - \delta$ plot.

Note also that the overdensities predicted by the ECE and ECET models now follow closely the

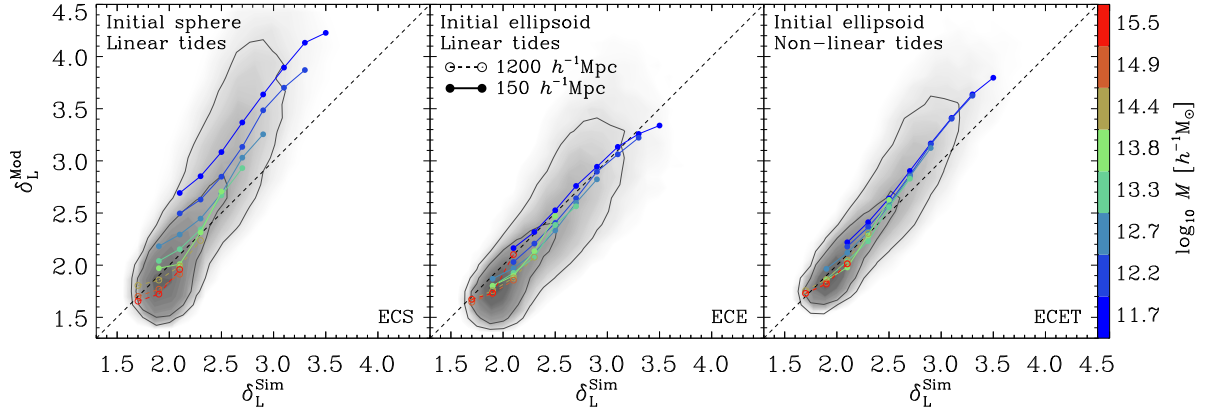


Figure 2.8: Predicted linear overdensities of dark-matter protohaloes calculated from the EC model plotted versus their measured overdensities. Predicted overdensities are calculated for collapse at $z_c > 0$ (z_c is the collapse redshift defined by eq. (2.9), and is explicitly calculated for each individual halo). The left-hand panel corresponds to the predictions of the BM96 ECS model, which assumes that each protohalo occupies a spherical Lagrangian volume, and that external tidal forces evolve from their initial values according to linear theory. Predictions in the middle panel explicitly account for the non-spherical shapes of dark-matter protohaloes, as measured in the initial conditions of our simulations, but retains the linear evolution of their tidal fields (this model is referred to in the text as the ECE model). Finally, the right-most panel shows the predictions of the EC model after fully accounting for the triaxial shapes of dark-matter protohaloes, as well as the evolution of their non-linear external tidal fields (referred to as ECET). As in similar figures, the connected symbols show, for various mass bins, the median values of δ_L^{Mod} in bins of δ_L^{Sim} .

one-to-one line (shown in each panel as a dashed line), with the median trend differing by, at most, 10 per cent for all halo masses and the full range of linear overdensities. The median relations for these models are also independent of halo mass: all individual lines in the middle and right-hand panels of fig. 2.8 neatly overlap. The fit of a linear function, $\delta_L^{\text{Mod}} = A \delta_L^{\text{Sim}} + B$, to individual points in the $\delta - \delta$ plane reveals that the ECE model is consistent with a one-to-one line, while the ECS model is not.

The correction to the slope of the $\delta - \delta$ relation results from the fact that, at any given mass scale, δ_L^{Sim} and z_c are strongly correlated. The dotted and dot-dashed lines in fig. 2.6 make this point clear. These curves highlight the median mass-dependence of z_c for haloes that, in each mass bin, rank in the highest and lowest 25 per cent of δ_L^{Sim} . Clearly haloes that are initially denser tend to collapse earlier, resulting in a larger correction to their model-predicted overdensities.

2.5 Discussion

2.5.1 The mass dependence and scatter of δ_L

The dependence of z_c on δ_L can also be seen in the lower-right panel of fig. 2.9. Here we plot the mass-dependence of δ_L for all haloes in both of our simulations, and color points by Δa_c , defined by the offset between each halo's collapse time, a_c , and the median value for haloes of the same mass. The mean trends are shown using solid and open points for haloes in our $150 h^{-1} \text{Mpc}$ box and our $1200 h^{-1} \text{Mpc}$ box, respectively; the error bars indicate standard deviation.

For comparison, we also plot the *predicted* $\delta_L(M)$ relations in the other three panels, adopting the same color-coding for each. Data in the upper-left panel show the mass-dependence of protohalo overdensities

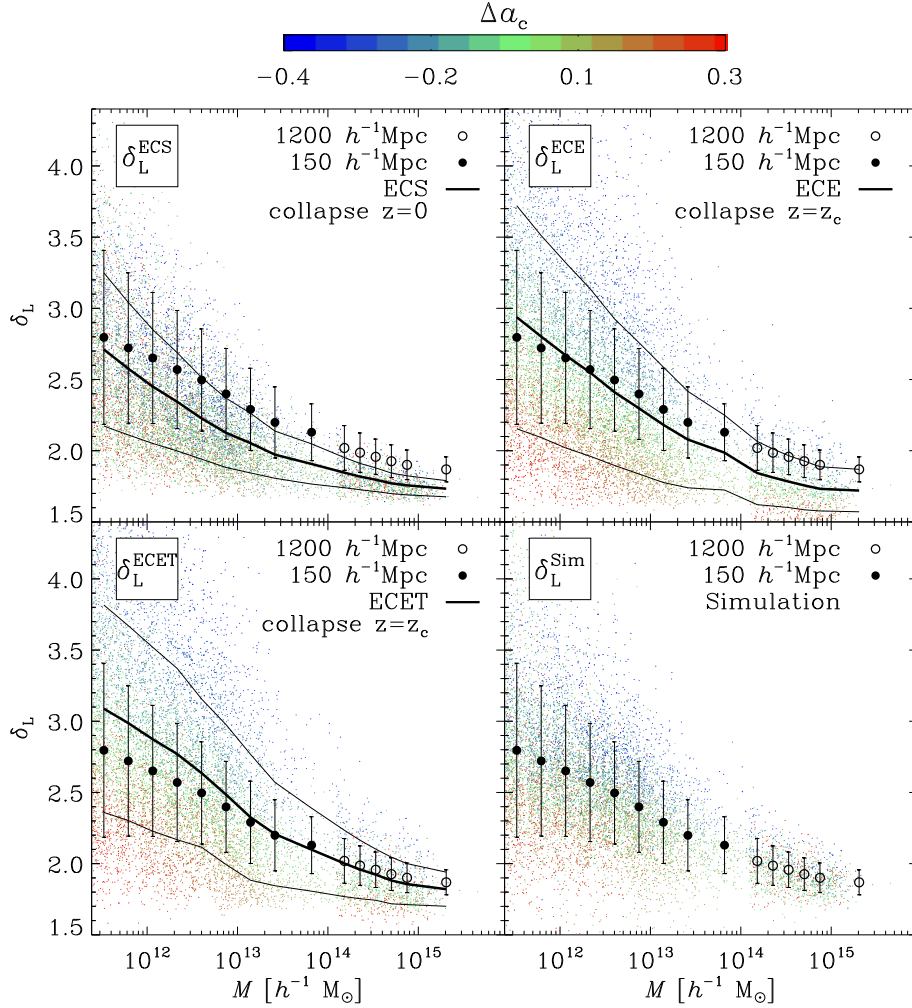


Figure 2.9: Linear density contrast as a function of mass. Points show the predicted value of the ECS model in the upper left panel, the ECE model including collapse times in the right upper panel and the ECET model including collapse times in the lower left panel. The lower right panel shows the values measured directly in the simulation. The points are coloured according to Δa_c , the offset between the expansion factor at collapse and the corresponding mean value for haloes of the same mass (note that this colour coding is different from what is used in figure 1 of LBP14). Heavy points with error bars show the mean and standard deviation of the *measured* density contrast in bins of mass. Heavy lines show the mean of the predicted density contrast in each panel, while thin lines indicate the standard deviation. For clarity, we have randomly down-sampled points in mass bins with ≥ 1000 haloes.

predicted by the ellipsoidal model of BM96, tuned for $z = 0$; the upper-right and lower-left panels correspond to the ECE and ECET-model predictions (both tuned for collapse at z_c). In all cases, the mean trends at fixed mass are shown using thick solid lines, with thinner lines indicating the standard deviation at fixed M . These trends can be compared to the points with error bars, which reproduce the measured $\delta_L(M)$ relation plotted in the lower-right panel.

Note that, while the standard ECS model systematically under-predicts the linear collapse threshold, the ECE and ECET models fare much better. Both models reproduce the mass and collapse time-dependence of δ_L rather well; the average trends deviate by at most ~ 10 per cent over roughly five orders of magnitude

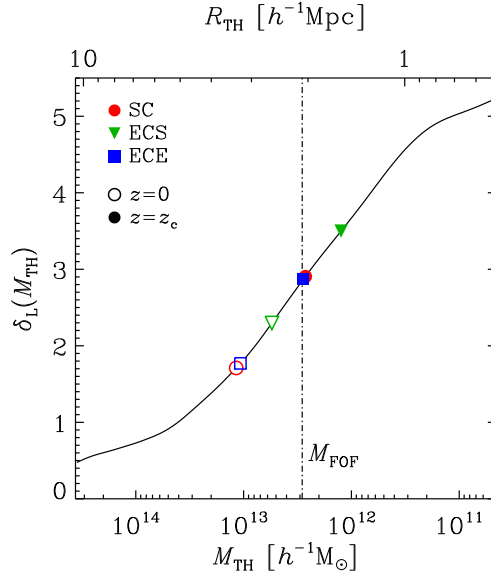


Figure 2.10: Excursion-set trajectory associated with the protohalo shown in fig. 2.5. $\delta_L(M_{\text{TH}})$ is the linear density contrast extrapolated to $z = 0$ after averaging within a sphere of radius R_{TH} (corresponding to the mass scale $M_{\text{TH}} = 4\pi\rho_{\text{crit}}\Omega_M R_{\text{TH}}^3/3$) extending around the protohalo center of mass. Open symbols highlight the points at which the trajectory crosses the threshold for halo formation at $z = z_{\text{id}} = 0$ evaluated using different collapse models. In all cases, the EPS theory substantially overestimates the halo mass measured in the simulation at z_{id} (indicated by the vertical dot-dashed line). On the other hand, when the SC and ECE models are tuned for collapse at z_c (solid symbols), the predicted halo masses are in excellent agreement with the numerical results.

in mass. This is remarkable given the simplicity of the ellipsoidal model, which overlooks entirely the complex hierarchical growth of dark-matter haloes. Note also that these models predict a scatter in δ_L that decreases with increasing mass, which is qualitatively consistent with the variance of measured protohalo overdensities. However, all models typically over-predict the scatter in δ_L at a given mass, and it is unclear whether different estimates of halo collapse times will perform better in this regard.

2.5.2 Implications for the extended Press-Schechter formalism

Our results raise questions concerning the validity of the extended Press-Schechter (EPS) formalism (Bond, Cole et al., 1991), particularly for low-mass haloes identified at late times (i.e. those with $\sigma(M) \gg \delta_c$). In the EPS theory, the outer boundary of a protohalo coincides with the initial location of a spherical mass shell that should collapse at z_{id} . However, our results demonstrate that most haloes stop accreting matter at $z_c > z_{\text{id}}$ and are essentially immutable thereafter. For redshifts $z < z_c$, the use of halo finding algorithms based on density contrasts results in the (small) pseudo-growth of the halo mass due to the decreasing background density.

We present an illustrative (and typical) example in fig. 2.10, where we plot the excursion-set trajectory at the Lagrangian location of the same halo used in fig. 2.5. The solid line shows the linear density contrast (extrapolated to $z = 0$) smoothed with a spherical top-hat filter of radius R_{TH} and mass M_{TH} . The open symbols indicate the points where the trajectory crosses the threshold for collapse at $z = z_{\text{id}} = 0$ computed using the SC (circle), ECS (triangle) and ECE (square) models. In all cases, the EPS model substantially overestimates the halo mass measured in the simulation at z_{id} (dot-dashed line). This is because, contrary to the model assumption, no mass shells were accreted onto the halo after $z_c = 1.2$. On

the other hand, the EPS predictions are rather accurate at z_c (cf. the solid symbols and the dot-dashed line), when the ECE (or SC) model is adopted to predict the collapse threshold. This can also be seen in fig. 2.5, where the same symbols mark the collapse times predicted by the different models.

We therefore disagree with the interpretation given by Sheth, Mo and Tormen (2001) that the mass dependence of the halo formation threshold δ_c is due to the fact that denser linear perturbations are necessary to overcome stronger tides in order to guarantee collapse at z_{id} . Rather, we attribute the mass scaling to the fact that, on average, low-mass haloes collapse and stop accreting at higher redshifts than haloes of higher mass. Future work will focus on understanding the physical mechanisms that prevent the collapse of the outer material shells. Non-linear tidal interactions (e.g. Hahn, Porciani, Dekel et al., 2009) and the geometrical overlap of the outer Lagrangian boundaries of neighbouring haloes (LBP14) likely play a key role.

Finally, we note that the phenomenon known as “assembly bias” (see e.g. Gao, Springel and S. D. White, 2005) simply reflects the dependence of the collapse threshold on z_c at fixed halo mass and identification redshift: “old” haloes ($z_c \gg z_{id}$) are more biased tracers of the underlying matter distribution than “young” haloes ($z_c \approx z_{id}$).

2.6 Summary

We used two high-resolution simulations of structure formation in the Λ CDM cosmology to test how well the EC model describes the linear density contrasts in regions that collapse to form haloes identified at $z_{id} = 0$. Our analysis focused on EC models of increasing complexity. The first (ECS) assumes that each protohalo can be approximated by a spherical Lagrangian tophat perturbation acted upon by linearly evolving external tidal forces, as described in BM96. The second model (ECE) allows for initially non-spherical perturbations, but retains the linear evolution of external tides (this model was described in detail in LBP14). Finally, we consider a model (ECET) which accounts for both the non-spherical initial shape of protohaloes, as well as the fact that their external tidal fields evolve non-linearly. Our main results can be summarized as follows.

1. The ECS model fails to describe the linear density contrasts measured at the sites of halo collapse in the initial conditions of our simulations. In this model, the required density contrast for collapse (at fixed z_c) is determined entirely by the surrounding tidal field, i.e. by e and p . Because the average tidal field strength decreases with mass, the ECS prediction is strongly mass-dependent, and is unable to reproduce the measured density contrasts of haloes on an object-by-object basis, as evident in fig. 2.1. For example, protohaloes with the same linear density contrast, but with final masses of 10^{12} and $10^{14} h^{-1} M_\odot$, have predicted δ_L^{ECS} values that differ systematically by ~ 30 per cent.
2. The mass dependence of the predicted protohalo overdensity disappears completely when their measured initial shapes are properly accounted for in the model calculation. This is because initially triaxial perturbations that align with the eigenvectors of their external tidal field typically collapse at lower overdensities than their spherical brethren when acted upon by strong external tides (LBP14). The mass dependence of protohalo shapes (in which lower mass haloes are systematically less spherical) therefore balances the higher initial density contrasts needed for low-mass systems to overcome the strong tidal forces in the ECS model. Nevertheless, when tuned for collapse at $z = 0$, the model still fails to predict the observed range of Lagrangian overdensities measured in our simulations, succeeding only for very massive haloes and those with low initial density contrasts.

3. In order to better understand these results, we developed an accurate method to measure the time evolution of the strength and orientation of the external tidal field acting upon a collapsing halo. This method reproduces the linear evolution of external tides for massive haloes, and for those forming in low density regions, but shows a clear non-linear evolution for highly clustered haloes in the initial density field. Although non-linear tides act to inhibit the collapse of dense protohaloes (and therefore increase the model-predicted density contrasts for collapse at $z = 0$), incorporating these effects into the EC model only slightly improves the agreement between the model prediction the measured Lagrangian overdensities of protohaloes.
4. The main discrepancy between the predicted and measured protohalo overdensities can be accurately accounted for if one drops the assumption that haloes are collapsing *today*. For a given tidal ellipticity, e , and prolaticity, p , the barrier height for collapse at redshift $z_c > z_{id}$ predicted by the EC model is larger by factor of $D(z_{id})/D(z_c) > 1$. We devised a simple method of calculating z_c : it does not depend on halo merger histories or on the growth of the main progenitor, but approximately estimates the earliest time at which the entire $z = 0$ mass of the halo first reached a stable volume. Using this, we showed that a modified EC model that accounts for both the triaxial nature of protohaloes as well as the collapse times of their descendants, can predict the Lagrangian density contrast of protohaloes in an unbiased way.
5. Although the ECE and ECET models provide a more faithful description of the density thresholds required for gravitational collapse, they rely heavily on input from the simulations. This substantially reduces the predictability of these models, but illuminates possible avenues for future progress. For example, a deeper understanding of the connection between the overdensities of protohaloes and their collapse times, z_c , would undoubtedly result in a much more powerful analytic model for halo formation. This would have important implications for theoretical modeling of, among other things, large-scale structure, the halo mass function, and the merger trees of dark matter halos.

Our results suggest that the Lagrangian overdensity of regions that collapse to form haloes by $z = 0$ increase toward lower halo masses (see also B. E. Robertson et al., 2009; Elia, Ludlow and Porciani, 2012). Within the context of the standard model for ellipsoidal collapse (referred to here as the ECS model) this behavior results from the fact that lower-mass haloes are subject to stronger tidal distortion and therefore require larger initial overdensities to collapse by a particular time (Sheth, Mo and Tormen, 2001). Our results suggest a different interpretation. One difference results from the much weaker dependence of B_{SMT} on external tides when protohaloes are modeled as triaxial ellipsoids rather than spheres. This substantially reduces the model-predicted density threshold required for the collapse of low-mass (or strongly sheared) perturbations by $z = 0$. On the other hand, the vast majority of low-mass haloes had already assembled their total $z = 0$ masses at $z_c > 0$, suggesting that model barriers tuned for collapse *today* are underestimating the true barrier height. In this interpretation, the shape of the $\delta_L(M)$ relation simply reflects the mass-dependence of halo collapse times: low-mass haloes collapse, on average, earlier than more massive ones, and therefore have higher initial density contrasts. This interpretation is supported by the fact that, at fixed halo mass, δ_L depends strongly on z_c but not on the shape or strength of the surrounding tidal field.

How the cosmic web inhibits halo growth and generates assembly bias¹

3.1 Introduction

In the standard model of cosmology, galaxies are surrounded by extended haloes made of cold dark matter (CDM). These CDM clumps are generated by primordial density perturbations that are gravitationally unstable. The power spectral density of the fluctuations is such that haloes form hierarchically in a bottom-up fashion. The first generation of haloes comes into being at redshift $z \sim 60$ with Earth masses (Diemand, Moore and Stadel, 2005). Larger and larger objects are then progressively assembled through halo mergers and accretion of loose material. N-body simulations are the ideal tool to study this highly non-linear process. They show that the host haloes of present-day bright galaxies start forming at a redshift of a few and become a prominent population around $z \sim 1$.

Galaxies and their host haloes are embedded in the large-scale structure of the Universe. Matter is organised in a vast network of knots, filaments and sheets known as the ‘cosmic web’ (Bond, Kofman and Pogosyan, 1996). Distinct halo populations trace the various elements of the web in different ways and thus show dissimilar clustering properties (Hahn, Porciani, Carollo et al., 2007; Hahn, Carollo et al., 2007; Aragón-Calvo et al., 2007; Cautun et al., 2014). For a long time, numerical studies have focussed on determining the clustering amplitude (e.g. the amplitude of the two-point correlation function) as a function of halo mass (see also section 3.3.5 for a more theoretical perspective). More recently, however, it has been shown that, at fixed mass, halo clustering depends on the formation time (Gao, Springel and S. D. White, 2005; Wechsler, Zentner et al., 2006; Zhu et al., 2006; Y. Li, Mo and Gao, 2008; J. Wang et al., 2011; Sunayama et al., 2016) and other correlated variables (Wechsler, Zentner et al., 2006; Jing, Suto and Mo, 2007; Gao and S. D. White, 2007; Bett et al., 2007; Angulo, Baugh and C. G. Lacey, 2008; Faltenbacher and S. D. White, 2010; R. Li et al., 2013). For galaxy-sized objects (the subject of this chapter), haloes that formed earlier cluster more strongly than their ‘younger’ counterparts. In other words, older haloes tend to reside in denser environments (Sheth and Tormen, 2004; Harker et al., 2006). This set of phenomena is known under the collective name of ‘halo assembly bias’. It is an intriguing open question whether also ‘galaxy assembly bias’ exists, i.e. to what extent the assembly history of the host haloes influences galaxy properties and imprints detectable signatures in the galaxy-clustering pattern (e.g. Jung, Lee and Yi, 2014; Hearin, Watson and van den Bosch, 2015; Hearin, Zentner et al.,

¹ This chapter has been published in Borzyszkowski, Porciani et al. (2016). The notation has been adapted to match the remaining thesis.

2016; Y.-T. Lin et al., 2016).

This chapter is the first in a series of three articles describing a numerical project named Zooming On a Mob of Galaxies (ZOMG). The aim of the ZOMG simulations is to study how cosmic environment regulates the growth and the structure of dark-matter haloes and of their central and satellite galaxies, hence to investigate the physical origin of halo and (possibly) galaxy assembly bias. Here we focus on the formation of dark-matter haloes and therefore use high-resolution N-body simulations. In the companion papers, instead, we also consider the baryonic component and use hydrodynamic simulations including star formation and feedback. In particular, in paper II (Romano-Díaz et al., 2017), we investigate how environment regulates the gas supply and the properties of the central galaxies while, in paper III (Garaldi et al., 2017), we shift our attention to the satellite galaxies.

In this work, we study the formation and evolution of the host haloes of present-day L_* galaxies. These haloes are of particular interest because they are the sites where star formation is most efficient and the stellar-to-halo mass ratio peaks (Moster, Naab and S. D. White, 2013; Behroozi, Wechsler and Conroy, 2013). In N-body simulations, they also present a number of puzzling properties which are interconnected. First, they show a strong assembly bias. Second, the bulk of them seem to have assembled early on (chapter 2) and, consistently, do not present signs of mass growth at later times (Diemand, Kuhlen and Madau, 2007 and chapter 2). Third, the region within which they are dynamically stable (i.e. where the mean radial velocity of matter vanishes) appears to be significantly more extended than expected from simple theoretical considerations (Prada et al., 2006). Fourth, given the linear overdensity and the tides in the Lagrangian patch from which they originate, they form much earlier than predicted by popular collapse models (LBP14; Hahn and Paranjape, 2014 and chapter 2). The main motivation for our work is to verify these results and provide a comprehensive and coherent explanation for all of them.

Several studies indicate that halo assembly bias can be explained in terms of a population of haloes that stop accreting matter once they find themselves in dense environments (H. Y. Wang, Mo and Jing, 2007; Dalal et al., 2008; Hahn, Porciani, Dekel et al., 2009; J. Wang et al., 2011). However, the detailed physical origin of this phenomenon has not been clarified yet. Although older haloes lie closer to more massive objects (H. Y. Wang, Mo and Jing, 2007), mass loss due to tidal stripping during fly-bys does not seem to play any relevant role in establishing the bias (H. Y. Wang, Mo and Jing, 2007; Hahn, Porciani, Dekel et al., 2009; J. Wang et al., 2011). H. Y. Wang, Mo and Jing (2007) note that the dark-matter flow surrounding the older haloes is hotter and might escape capture from the halo potential well. Hahn, Porciani, Dekel et al. (2009) provide evidence in favour of tidally suppressed accretion driven by the strong velocity shear within marked filaments of the large-scale structure. Consistently, J. Wang et al. (2011) find that halo formation time at fixed mass correlates with the strength of the local tidal field. All these valuable investigations are based on fairly large cosmological N-body simulations providing substantial statistical samples but with relatively poor spatial and mass resolution. For this reason they are ideal for spotting correlations in the data although they give little insight into the physics of assembly bias. In fact, there are questions that cannot be addressed with simulations in which galaxy-sized haloes are resolved with $10^2 - 10^4$ particles leading to a very poor sampling of the phase-space configuration of the halo and its surroundings. Information on the internal structure of the haloes as well as the precise geometry with which matter accretes onto them can only be inferred stacking thousands of objects with similar apparent characteristics. In this way, one always ends up mixing information coming from different objects in more or less disparate dynamical states. The precise outcome of this procedure relies on assumptions (for instance a stacking criterion) and can provide only generic indications or trends. Actually, the corresponding results cannot be treated as facts at the level of individual haloes until they are corroborated with further, direct evidence. Complementary to this line of research, we use the zoom technique to study a small sample of representative haloes at very high resolution. This enables us to investigate the accretion-pattern of individual haloes in great detail and identify the series of events

leading to halted growth. Furthermore, our simulations allow us to make a connection between matter accretion from the environment and the dynamical structure of the haloes. This is particularly interesting since assembly bias has been found to be surprisingly strong when haloes are split based on the velocity anisotropy parameter (Faltenbacher and S. D. White, 2010). Our study reveals the unknown origin of this signal and its connection with the halted halo growth.

This chapter is structured as follows. In section 3.2 we introduce our numerical simulations and lay out the methods we use to analyse them. In section 3.3 we present our results and clarify the origin of halo assembly bias. We show that there is a tight link between halo assembly and the cosmic web: the accretion rate of matter onto galaxy-sized haloes is regulated by the environment. In particular, mass growth is inhibited for haloes embedded in prominent filaments due to the strongly sheared velocity field. Furthermore, the characteristic accretion pattern determines the internal dynamics of the haloes quantified in terms of the velocity anisotropy profile. In section 3.3.5 we discuss the mass-accretion history of our haloes in the context of the excursion-set model (Bond, Cole et al., 1991; Zentner, 2007). We show that the most common implementations of this theoretical framework fail to capture the effects of the inhibited mass growth in filaments. Hence we propose a simple extension to the model that nicely accounts for them. Finally, we draw our conclusions in section 3.4. :

3.2 Simulations and methods

We use the tree-PM N-body code `PGADGET-3` (Springel, 2005) to simulate the formation and evolution of dark-matter haloes in the Λ CDM cosmology. Consistently with the most recent observations (Planck Collaboration et al., 2014a), we assume the cosmological parameters $\Omega_\Lambda = 0.692$, $\Omega_m = 0.308$, $\Omega_b = 0.0481$ and $H_0 = 100 h \text{ km s}^{-1} \text{ Mpc}^{-1} = 67.8 \text{ km s}^{-1} \text{ Mpc}^{-1}$. Initial conditions are set at $z = 99$ using second-order Lagrangian perturbation theory with the `MUSIC` code (Hahn and Abel, 2011). The linear power spectrum of the density fluctuations (Eisenstein and Hu, 1998) is characterised by the scalar spectral index $n_{\text{tilt}} = 0.9608$ and the normalisation amplitude $\sigma_8 = 0.826$.

We first carry out a simulation within a periodic cube of side $50 h^{-1} \text{ Mpc}$ at a uniform initial resolution in which the matter distribution is sampled with 512^3 equal mass particles (hereafter U512). This box forms the parent run from which we select sub-volumes to sample at higher resolution using the multimass zoom technique (section 3.2.2). To study the stability of our results with respect to numerical discretization, we run a second simulation with uniform initial resolution starting from the same initial conditions but containing only 256^3 identical particles (U256).

Using the `AMIGA HALO FINDER` (Gill, Knebe and Gibson, 2004; Knollmann and Knebe, 2009), we conventionally identify dark-matter haloes as spherical regions enclosing a mean matter density equal to 200 times the critical density of the universe (the consequences of adopting this common definition will be discussed later). Additionally, we apply an unbinding procedure which iteratively purges the halo of the particles that move faster than 1.5 times the escape velocity. We define the halo radius R_h as the radius of the smallest sphere enclosing the bound particles and the halo mass M_h as their total mass.

3.2.1 Collapse time

Halo formation can be discussed either in terms of the growing mass of the most massive progenitor or as the coherent collapse of a single perturbation with the final halo mass. The first approach is popular in numerical studies while the second one characterises many analytical models. In this work, we follow both methods and make use of a particular definition of halo collapse time first introduced in chapter 2 in order to establish a direct correspondence between the predictions of theoretical models and N-body

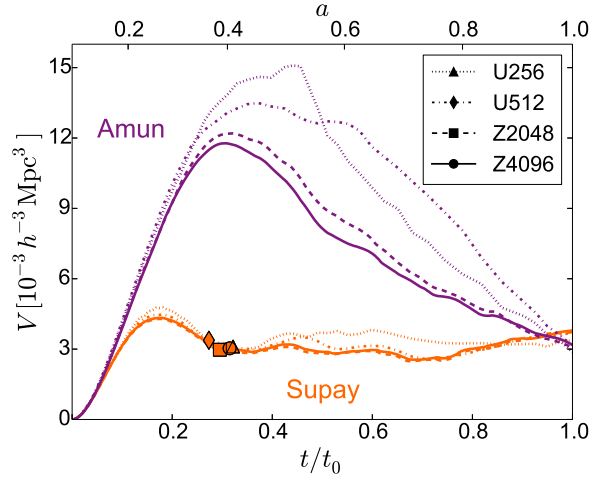


Figure 3.1: The volume of the collapsing patch that ends up forming a dark-matter halo is plotted as a function of time. Results are shown for two haloes with approximately the same mass $M_h \sim 4 \times 10^{11} h^{-1} M_\odot$. Different line styles correspond to N-body simulations with different mass and force resolution and the solid symbols indicate the collapse time, t_c , defined as in eq. (3.1). The top series of curves refers to Amun, a halo whose outer shells are still contracting at the present time and that represents the prototypical ‘accreting’ halo. On the other hand, the bottom set shows results for Supay, a representative of the class of ‘stalled’ haloes. Supay turned around earlier than Amun and reached a much lower maximum volume. Although Supay has been identified at the present time, its volume has been stable for ~ 70 per cent of the life of the universe. Note that the measurement of t_c is very robust with respect to the numerical resolution of the simulations.

simulations.

To begin with, we compute the (time-dependent) physical volume of the collapsing patch out of which a halo forms. This goal is achieved implementing the following procedure (for further details see chapter 2): (i) a halo is identified at some epoch (we use the present time, t_0); (ii) the halo particles are tagged and their inertia tensor is evaluated for every snapshot of the simulation (with respect to their centre of mass); (iii) an ellipsoid with principal axes oriented as the eigenvectors of the inertia tensor and shape determined by the ratios of the square roots of the eigenvalues is located at the centre of mass of the particle set; (iv) the ellipsoid is rigidly rescaled until it encloses the final mass of the halo. The volume of the ellipsoid defines the volume of the collapsing patch, $V(t)$.

In fig. 3.1 we show results obtained for two haloes with approximately the same mass named Amun and Supay (various line styles correspond to simulations with different mass resolutions). Qualitatively the time evolution of V conforms to the predictions of the spherical-collapse model. The volume first increases in a decelerated fashion due to the combined action of cosmic expansion and self gravity. At a certain point the perturbation turns around and from this moment onwards V decreases until ‘virialization’ is achieved (meaning that V stabilizes around a constant value). However, in spite of these similarities, the patches that give origin to Amun and Supay show very different evolutionary paths. Supay turns around earlier (when its mean physical density is comparable with the present-day one) and virializes shortly after turnaround. On the other hand, Amun has a much lower density at turn around² and has not yet reached a stable configuration by the present time. Note, that the final volume is determined by the fixed density threshold with which haloes have been defined.

² For both Amun and Supay, the ratio between the maximum of $V(t)$ and $V(t_0)$ is much lower than the factor of eight one would expect based on the spherical collapse model and simple descriptions of the virialisation process (similar findings have been presented by Diemand, Kuhlen and Madau, 2007).

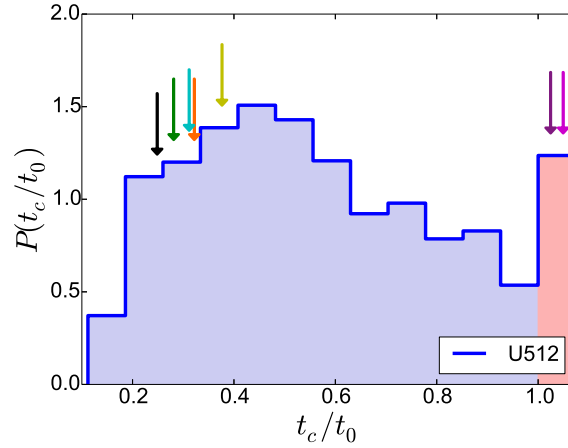


Figure 3.2: Probability distribution of collapse times for haloes with $2.0 < M_h/(10^{11} h^{-1} M_{\odot}) < 20.0$ extracted from the U512 simulation. The spike in the rightmost bin (painted red) represents the total contribution of haloes with $t_c \gtrsim t_0$. The vertical arrows indicate the collapse time of the haloes selected for re-simulation.

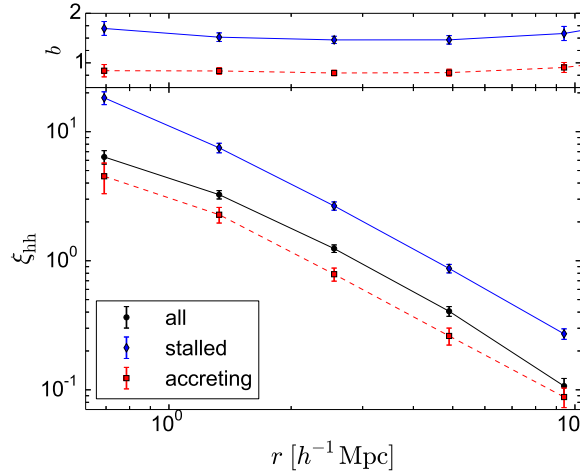


Figure 3.3: Bottom: datapoints show the two-point correlation function of haloes with mass $2.0 < M_h/(10^{11} h^{-1} M_{\odot}) < 20.0$ and that populate the lower (red) and upper (blue) 20 per cent tails of the collapse-time distribution. For comparison, the correlation function of all haloes in the mass bin is shown in black. All data come from the U512 simulation. Error bars are obtained bootstrapping the halo positions. Top: Halo assembly bias defined as the square root of the ratio between the two-point correlations of a sub-population and of the full sample.

It is tempting to classify haloes based on these marked differences. We thus define the collapse time of a halo, t_c , as the moment in which $V(t)$ becomes stable. In order to account for the late-time oscillations of $V(t)$, we determine t_c as the earliest epoch for which

$$\int_{t_c}^{t_{\max}} [V(t) - V(t_c)] dt = 0, \quad (3.1)$$

with $t_{\max} = t_0$ (i.e. the final time of our simulations although, in principle, it would make sense to take the limit $t_{\max} \rightarrow +\infty$). Solving this equation, for Supay we find that $t_c \simeq 0.31 t_0$ (or, equivalently, $a_c \simeq 0.4$ in terms of the cosmic expansion factor normalized to unity at the present time). For haloes like Amun that

have not yet collapsed, instead, we can only provide a lower limit $t_c > t_0$ [although a precise value for t_c could be determined by running the simulations into the future this would not influence our results].

Figure 3.2 shows the probability distribution of t_c for haloes of mass $2.0 < M_h / (10^{11} h^{-1} M_\odot) < 20.0$ in the U512 simulation. The median value is $0.54 t_0$ and the scatter around it is quite large. The distribution is skewed towards large values of t_c . The earliest-forming object collapsed at $t_c = 0.11 t_0$ while approximately 9 per cent of the haloes have not collapsed by the present time.

Halo assembly bias can be clearly detected after partitioning objects of a given mass in different classes based on t_c . The red and blue lines in fig. 3.3 show the two-point correlation functions of the haloes with the 20 per cent earliest ($t_c < 0.33 t_0$) and latest ($t_c > 0.85 t_0$) collapse times, respectively. For comparison, the black line indicates the autocorrelation function of all haloes in the same mass range. The size of the bias is comparable with (if not larger than) that obtained after separating the haloes based on the half-mass formation time, t_{50} (see e.g. Gao, Springel and S. D. White, 2005) although t_c correlates poorly with t_{50} (see also sections 3.2.2 and 3.3.1).

3.2.2 The Dark-ZOMG simulation suite

We employ high-resolution zoom simulations to pin down the physical mechanism leading to the different collapse histories presented in fig. 3.1. At the level of single objects, the zoom technique provides several advantages over standard cosmological simulations in which galaxy-sized haloes are typically resolved with only a few thousand computational elements. Zooming allows a much closer look at the geometry of matter accretion and provides a detailed picture of the phase-space structure. In particular, we use this information to make a connection between the halo environment and its internal structure. On the other hand, the heavier computational requirements of zoom simulations limit our analysis to a small number of representative cases. The concept is to provide clear templates and extract regularities from them that serve as a model to explain what happens in general. Our investigation is thus complementary to statistical studies analysing thousands of low-resolution haloes. In particular, we build upon Hahn, Porciani, Dekel et al. (2009) and chapter 2.

Target haloes for re-simulation are selected from the U512 run based on M_h , t_c , and applying an isolation criterion. We consider haloes with mass $M_h \approx$ a few $\times 10^{11} h^{-1} M_\odot$ (i.e. the hosts of present-day L_* galaxies, Moster, Naab and S. D. White, 2013; Behroozi, Wechsler and Conroy, 2013) that are not closely surrounded by more massive neighbours (i.e. no particles belonging to a more massive halo must be found within three R_h from the halo centre). The latter condition is necessary to limit the size of the high-resolution region and thus the computational costs while fully benefiting from the zoom-in method. Admittedly, introducing the seclusion criterion might bias our sample. However, there are good reasons why the bias should be very small. In the parent run, only 4.8 per cent of the haloes with the selected mass violate our isolation criterion. Moreover, it has been shown that close encounters and fly-bys cannot generate the assembly bias (H. Y. Wang, Mo and Jing, 2007; Hahn, Porciani, Dekel et al., 2009; J. Wang et al., 2011). Therefore, we are confident that our sample is adequate for this study and mostly representative of the halo population.

Among the haloes that satisfy the selection criteria, we randomly pick five objects that collapsed very early on (at $a_c \leq 0.4$) and two that have not collapsed by today. This set forms the Dark-ZOMG simulation suite (D-ZOMG). To facilitate distinguishing between the different haloes, we name each of them after an ancient god (and also associate them with individual colours in figures, see table 3.1). We use names starting with the letter A (standing for ‘accreting’) for the haloes with $t_c \geq t_0$ and with the letter S (standing for ‘stalled’) for the remaining ones. Although the meaning of our labels can be intuited from fig. 3.1, it will become clearer in section 3.3.1.

For each halo, we use the music code (Hahn and Abel, 2011) to generate zoom initial conditions in

Table 3.1: Properties of the haloes in the D-ZOMG simulation suite (Z4096). The columns give the halo name and the colour we associate with it in all plots, the $z = 0$ mass (M_h) and radius (R_h), the splashback radius (R_{spl}), the minimal Hill radius R_H , the concentration (c_{NFW}) of the radial mass-density profile fitted with the Navarro-Frenk-White (NFW) formula (Navarro, Frenk and S. D. White, 1997), the major to minor axis ratio (d_1/d_3) derived from the inertia tensor of the halo particles in the initial conditions and at the present time as well as the angle between the shortest principal axes at these two epochs (θ_{33}), the cosmic expansion factor at formation time defined in terms of the first appearance of a progenitor with 30 and 50 per cent of the final halo mass (a_{30} and a_{50}), the expansion factor at collapse time (a_c) defined as in section 3.2.1, and, finally, the spin parameter (\mathcal{S}) (as defined by Peebles, 1969).

Halo	M_h $10^{11} h^{-1} M_\odot$	R_h $h^{-1} \text{kpc}$	R_{spl} $h^{-1} \text{kpc}$	R_H $h^{-1} \text{kpc}$	c_{NFW}	d_1/d_3 $z = 99$	d_1/d_3 $z = 0$	$\cos(\theta_{33})$	a_{30}	a_{50}	a_c	\mathcal{S} 10^{-2}
Abu	4.5	156	261	1528	8.0	1.39	1.23	0.71	0.44	0.46	0.97	2.4
Amun	4.3	153	304	1697	9.3	1.58	1.56	0.90	0.50	0.51	1.00	3.4
Seth	7.4	184	228	1478	6.0	3.45	1.10	0.70	0.32	0.49	0.39	3.7
Supay	4.7	158	337	922	8.7	3.01	1.30	0.07	0.32	0.45	0.40	1.8
Sobek	4.3	153	201	653	10.7	2.40	1.10	0.07	0.34	0.38	0.38	2.1
Sedna	4.2	152	306	854	11.2	2.36	1.36	0.17	0.27	0.50	0.40	1.6
Siris	2.6	129	195	724	15.4	1.79	1.16	0.35	0.25	0.45	0.33	0.7

which the mass resolution varies within the simulation box. The high-resolution region coincides with the Lagrangian convex hull of the particles that in the parent simulation are found within $3R_h$ from the halo centre of mass at $z = 0$. Within this patch, matter is sampled with a large number of elements and, during the evolution, gravitational forces are computed at high resolution. Outside this volume, we place a number of buffer regions in which the simulation particles become progressively more massive (and forces less accurate) with increasing distance from the high-resolution region. This method allows us to simulate the haloes and their immediate surroundings at high resolution while keeping into account the tidal influence of the large-scale structure in a reasonable computational time. In the D-ZOMG simulations, the coarsest mass resolution in the box corresponds to that of a uniform grid sampled with 128^3 particles while we simulate each halo twice at different maximum resolutions. In our production runs (Z4096), the dark-matter particles in the high-resolution region have a mass of $1.6 \times 10^5 h^{-1} M_\odot$ corresponding to a uniform grid with 4096^3 elements. In order to test the robustness of our results with respect to numerical errors, we repeat the simulations using a particle mass of $1.3 \times 10^6 h^{-1} M_\odot$ corresponding to a 2048^3 grid (Z2048). The Plummer equivalent softening lengths adopted in the high-resolution region are 0.24 and $0.49 h^{-1} \text{kpc}$ for Z4096 and Z2048, respectively.

During each run, we save eight snapshots between $z = 90$ and $z = 30$ uniformly sampled in redshift, and twelve between $z = 30$ and $z = 9$. Subsequently, we save an output every 20 Myr, for a total of 682 snapshots. We identify haloes in all snapshots (using the method previously described) and find their main progenitor by maximizing the merit function $N_{i \cap j}^2 / (N_i N_j)$ where N_i and N_j denote the number of particles in the descendant halo and in the candidate progenitor halo (defined at the previous snapshot with respect to the descendant), respectively, and $N_{i \cap j}$ is the number of particles they have in common (Knollmann and Knebe, 2009). Iterating this procedure, we build mass-accretion histories moving along the so-called ‘main branch’ of the halo merger tree (e.g. Y. Li, Mo and Gao, 2008). We tag the earliest time at which a main-branch progenitor with a mass of $M_h/2$ appears as t_{50} and we refer to this quantity as the half-mass formation time (C. Lacey and Cole, 1993). Similarly, we use the symbol t_{30} to indicate the time at which a progenitor with 30 per cent of the final mass first comes into existence.

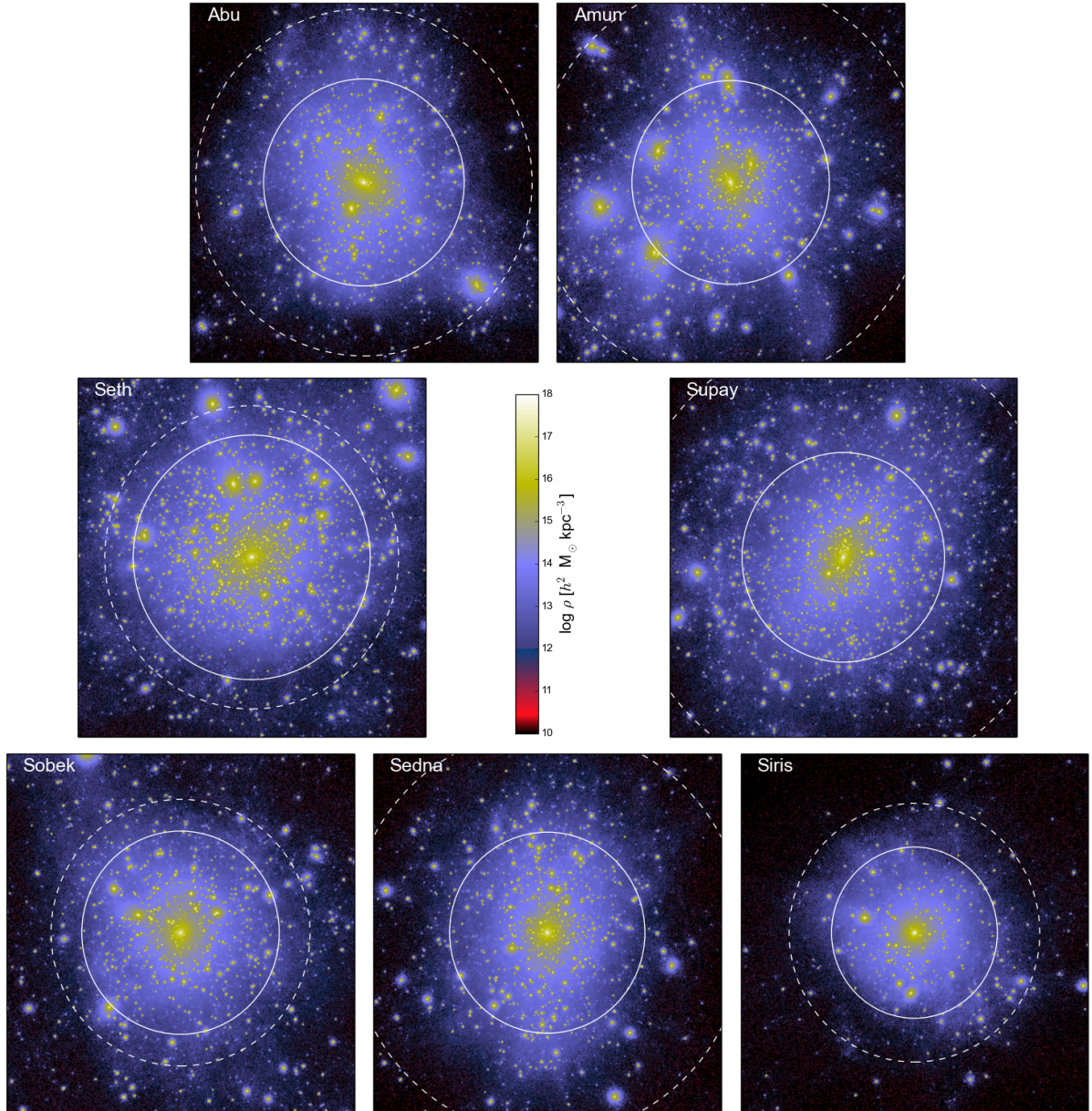


Figure 3.4: Matter distribution in the D-ZOMG haloes. N-body particles are coloured based on the local mass density computed with a standard smoothed-particle-hydrodynamic kernel including 64 neighbours. Each panel refers to a cube with side length of $540 h^{-1}$ kpc projected along one of the axes and centred on a resimulated halo. The solid circle shows R_h while the dashed one indicates R_{spl} .

A particular, parameter-free, halo definition has been recently discussed in the literature (Diemer and Kravtsov 2014; Adhikari, Dalal and Chamberlain 2014; More, Diemer and Kravtsov 2015). In this case, the halo boundary is defined in terms of the so-called ‘splashback’ radius, R_{spl} , which corresponds to a sudden steepening of the radial mass-density profile and is attributed to a caustic (intended as the accumulation of particle trajectories) located near the first apocenter of recently accreted matter. We determine the splashback radius for our re-simulated haloes (at all time steps) by measuring the density profile in spherical shells around the halo centre and locating the global minimum of its slope. Since

substructures introduce spikes in the profile, we preventively exclude their particles from the calculation. [Substructures are associated with local density peaks within haloes and their edge coincides with the radius of the smallest sphere enclosing all their gravitationally bound particles.] The mass enclosed within the splashback radius is denoted by M_{spl} and we track its growth along the main branch of the merger tree.

Before moving further with our study, it is imperative to test that our definition of t_c is robust with respect to numerical resolution. Figure 3.1 shows that the U256, U512, Z2048 and Z4096 simulations give perfectly consistent values for the collapse times of Amun and Supay. The same conclusion applies to the other re-simulated haloes (not shown in the figure). The only discrepancy which is worth mentioning is found for Abu. In this case, we measure $a_c > 1$ in the U256 and U512 (fig. 3.2) runs as well as $a_c = 0.96$ and 0.97 in Z2048 and Z4096, respectively (table 3.1). The difference is caused by a merger with a sizeable mass ratio that takes place at $a \sim 0.9$. The outward motion of the recently accreted subhalo after the first pericenter passage causes a small upturn in the $V(t)$ plot (we remind the reader that all our ellipsoids are drawn around the centre of mass) which basically determines the collapse time. In fact, the integral in eq. (3.1) is sensitive to fluctuations in $V(t)$ when $t_c \simeq t_{\text{max}}$ while it is very robust when $t_c \ll t_{\text{max}}$ so that the interval of integration is larger. The net effect is that small temporary increases in $V(t)$ at late times can artificially give values of t_c which are very close to t_{max} in high-resolution runs. This issue is irrelevant if one wants to distinguish early and late collapsing haloes and can be easily solved by using a larger value for t_{max} (i.e. by running the simulations longer). Inspection of the mass shells immediately surrounding Abu reveals that they are coherently infalling at $z = 0$ as expected for an accreting halo. It follows from this test that large-volume cosmological simulations with uniform sampling of the initial conditions are well suited for measuring t_c and performing statistical studies based on this quantity.

3.3 Results

A synopsis of the D-ZOMG haloes is given in fig. 3.4 and table 3.1 where we report several halo properties measured from the Z4096 simulations. A prominent feature can be noticed at first glance: stalled haloes originate from much more aspherical patches in the initial conditions than the accreting ones (while the final shape of the haloes does not seem to be different between the two classes). In the remainder of this chapter we will investigate the origin of this characteristic pattern and delve into the physical processes that generate it.

3.3.1 Collapse time and halo growth

At this point, it is interesting to compare our definition of collapse time with other related quantities that are commonly used in the literature to define halo ages. From table 3.1 we note that, while accreting and stalled haloes neatly separate based on t_c , they are not so clearly distinct using the half-mass formation time. As a matter of fact, many of our re-simulated haloes have very similar formation times. On the other hand, using t_{30} gives results more in line with those obtained with t_c . This suggests that t_c contains information on the early phases of halo formation.

The mass-accretion histories of our re-simulated haloes are shown in fig. 3.5. Abu and Amun experience a major merger at $a \sim 0.4$ - 0.5 , steadily grow in mass afterwards and undergo a minor merger at late times. In parallel, the stalled haloes assemble a significant fraction of their mass early on through major mergers and subsequently show a positive net mass-increment rate. From this perspective, it appears that the difference between stalled and accreting haloes is just the timing at which an adequately sized

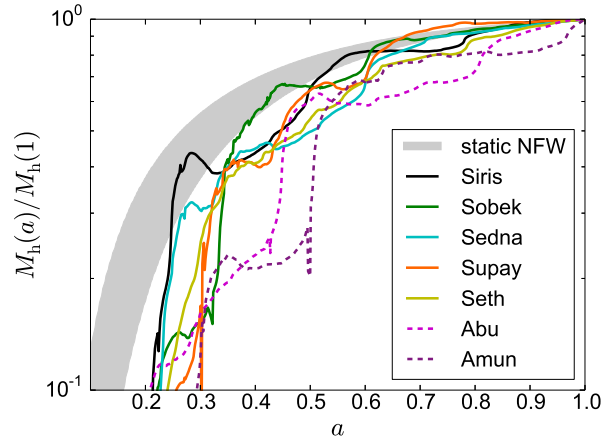


Figure 3.5: Mass accretion histories of the resimulated haloes in the highest resolution simulation. The grey shaded area shows the pseudo-evolution of a static NFW profile due to the changing background density in the range of concentrations of our simulated haloes $6 < c_{\text{NFW}} < 16$. See text for details.

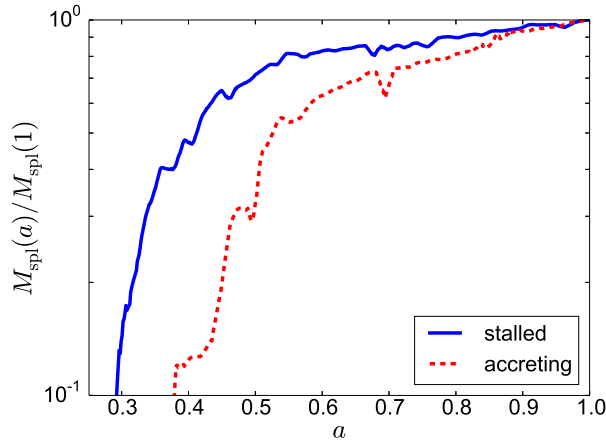


Figure 3.6: The mass enclosed within the splashback radius is plotted as a function of the cosmic expansion factor. Haloes are followed along the main branch of their merger tree. To reduce noise, the curves have been obtained averaging over our accreting (dashed red) and stalled (solid blue) haloes. The time evolution has also been coarse-grained with a resolution of 200 Myr. Stalled haloes assemble most of their final mass early on compared to accreting haloes which, on the other hand, grow more rapidly at the present time.

progenitor is assembled. No other evident dissimilarity emerges from fig. 3.5. We are going to show that this mental picture is simplistic and does not capture a number of fundamental features that distinguish the two classes of haloes.

The first thing to consider is that haloes are conventionally cut out of their environment adopting a somewhat arbitrary criterion that defines their outer boundary. Following a standard practice, we use a density threshold which decreases with time. As a consequence of this choice, the halo mass is subject to pseudo-evolution, meaning that the very same immutable object would be assigned different masses at different epochs just because its conventional boundary moves outwards (see e.g. Diemer, More and Kravtsov, 2013; Zemp, 2014). The grey band in fig. 3.5 highlights the pseudo-evolution of a stationary NFW density profile and its thickness reflects the range of concentrations covered by our stalled haloes ($6 < c_{\text{NFW}} < 16$). For $a > 0.6$, the mass-accretion histories of Sedna, Sobek and Supay closely match

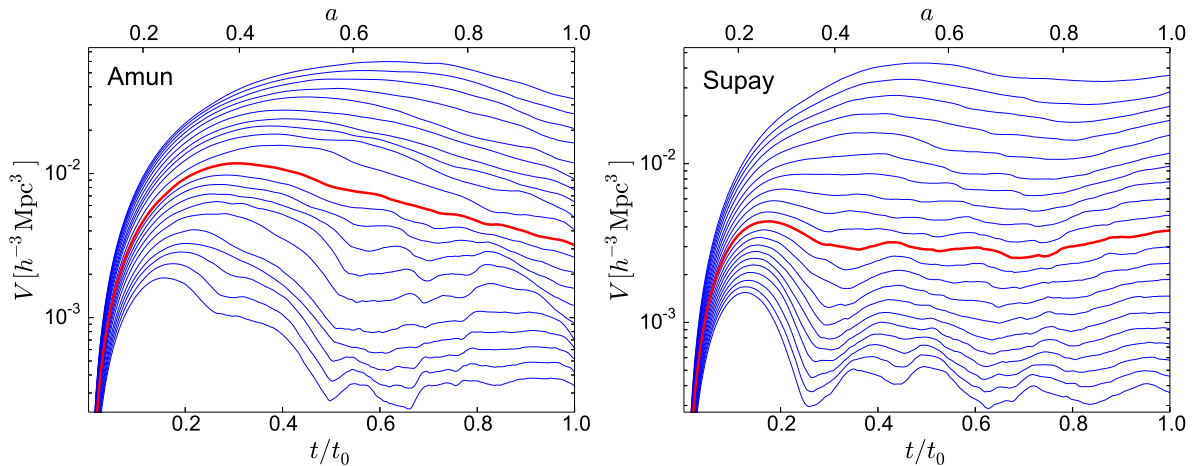


Figure 3.7: The red curves reproduce the volume evolution shown in Fig. 1 for Amun (left-hand panel) and Supay (right-hand panel). The same analysis is repeated considering different volumes (blue curves) that enclose a mass ranging from $0.1M_h$ to $10M_h$ in logarithmic steps. To improve readability and place equal emphasis on all shells, a logarithmic scale is used for V . Note that the outer mass shells are infalling onto Amun and receding from Supay.

the pseudo-evolution of a stationary NFW profile while this is not true for the accreting haloes. In fact, Abu and Amun grow faster than that mainly because they both undergo a merger with approximately 1:6 mass ratio. Finally, Seth and Siris show an intermediate behaviour as they also experience a merging event at $a \sim 0.77$ (with a substantially smaller mass ratio) and follow pseudo-evolution afterwards.

In fig. 3.6 we show the evolution of M_{spl} which is not affected by changes in the critical density of the universe. Since measurements of M_{spl} are quite noisy for individual haloes, we report results averaged over our re-simulated objects and smoothed over ten snapshots. These curves are well fit by an exponential function of redshift (Wechsler, Bullock et al., 2002) only for $z < 1$. At earlier times the evolution is much more rapid than the simple analytical approximation. Two things are worth noticing here. (i) The haloes with low t_c assemble any given fraction of their final mass earlier with respect to the others. (ii) These haloes do not grow much at late times: on average, M_{spl} only increases by 17 per cent since $a = 0.6$. On the other hand, the haloes with high t_c increase their mass by 34 per cent during the same period. All this points to t_c as a discriminator between haloes that assemble at early times and then undergo little changes and those that gathered most of their mass later on and are still growing at the present time.

3.3.2 Collapse time and accretion dynamics

Although parameter free, our definition of collapse time is sensitive to the halo definition. In fact, the halo finder identifies the particle set and thus the Lagrangian patch whose volume evolution determines t_c . Let us imagine for a moment that our halo definition just picks the innermost virialized core of the halo and excludes more recently accreted shells [haloes are known to form from the inside out (Salvador-Solé, Solanes and Manrique 1998; Wechsler, Bullock et al. 2002; Zhao et al. 2003; J. Wang et al. 2011)]. In this case, we would severely underestimate the collapse time for the more extended halo. To investigate the stability of t_c with respect to the operational halo definition, we repeat the study of the volume evolution for many shells that enclose from ten per cent up to ten times the final halo mass (in logarithmic steps). Our results for Amun and Supay are plotted in fig. 3.7 [we find consistent results also for all the other re-simulated haloes]. It is straightforward to note that the innermost core of Amun reaches a stable

configuration at approximately $t = t_0/2$ while all the outer shells are still contracting towards the halo centre at the present time (hence the appellation ‘accreting’). This conforms to the common idea that haloes constantly grow in mass due to the infall of outer shells (e.g. Press and Schechter, 1974; Bond, Cole et al., 1991). In this case, it would make sense to define the boundary of the halo as the location of the outermost shell that stabilized by $z = 0$. For Amun, this criterion gives a mass of $\sim 0.5 M_h$. Switching our attention to Supay, we immediately note that there are no infalling shells at the present time. The material surrounding what we conventionally call the halo is actually receding from its centre. Even some of the internal shells show the same feature. The net outward motion kicks in at $t > 0.8 t_0$ following a long period in which the shells have been loitering at nearly constant volume. Based on this information it is unclear how to draw a physically motivated boundary for Supay. Anyway, our analysis suggests that Supay, as a physical object, should not be able to grow in mass at late times (hence the appellation ‘stalled’).

Haloes are objects with a complex dynamics and continuously interact with their surroundings. To capture the details that might have been lost in the study of the different mass shells, in the top-panels of fig. 3.8 we investigate the radial phase-space distribution of matter at $z = 0$ within and around Amun and Supay [consistent results are found for all the other re-simulated haloes]. Colour coding reflects the phase-space density while the vertical lines indicate R_h (dashed) and R_{spl} (dot-dashed). The halo cores are characterized by a large velocity dispersion reflecting the depth of the gravitational-potential well. Substructures and external haloes can also be easily identified as patches with high density and increased velocity dispersion. Infalling material ($v_r < 0$) moves faster and faster while approaching the halo core and, after reaching the pericenter, suddenly reverses its motion ($v_r > 0$). Particles that are bound to the halo describe particular trajectories in the radial phase-space diagram. The needle-shaped configurations with positive radial velocity correspond to the remnants of substructures after their first pericenter passage. Note that these streams of matter stretch far beyond R_{spl} which has been computed in terms of a spherically averaged mass-density profile. Defining the halo boundary in terms of the apocenter of the material ‘ejected’ with high speed would thus require tracing the positions of the caustics in three dimensions. The thick white curve in fig. 3.8 shows the mean radial velocity as a function of the distance, r , from the halo centre. Amun shows a net radial inflow of matter over a large range of r . This flow is rather cold and coherent. Basically the phase-space diagram can be decomposed into three elements: the halo, an accretion flow and the outward streams (although it is not obvious how to separate them). The corresponding diagram for Supay shows striking differences. For instance, the outward streams are much less pronounced than in Amun. Moreover, for Supay there is no net inflow of matter: the mean radial velocity is zero in the innermost regions and positive in the outer regions. This does not mean that no material is infalling, rather that the mass outflow through any spherical surface exactly matches the inflow up to distances of several times R_h (consistent with Prada et al., 2006). All this suggests that some sort of dynamical equilibrium is established between the halo and the surrounding environment which is characterized by a rather large velocity dispersion.

The bottom panels of fig. 3.8 show the mass-density profile of the two haloes at $z = 0$ and of their progenitors at $z = 1.5$ (which corresponds to the collapse time of Supay). The matter distribution in Amun has evolved a lot between these two epochs. Only the very central and dense core appears not to have changed while the outskirts have developed later. On the contrary, Supay shows exactly the same profile at $z = 1.5$ and at $z = 0$ within the innermost $250 h^{-1}$ kpc ($\approx 1.6 R_h$) while the evolution in the outer regions just reflects the drop in the mean density of the universe.

We have now collected sufficient factual evidence to support the claim that there exists a large population of dark-matter haloes that: (i) are in place since early times with essentially unchanged structure; (ii) do not grow in mass although they experience some matter infall which is however balanced by outflows. These stalled haloes form the bulk of galaxy-sized haloes at the present time (fig. 3.2).

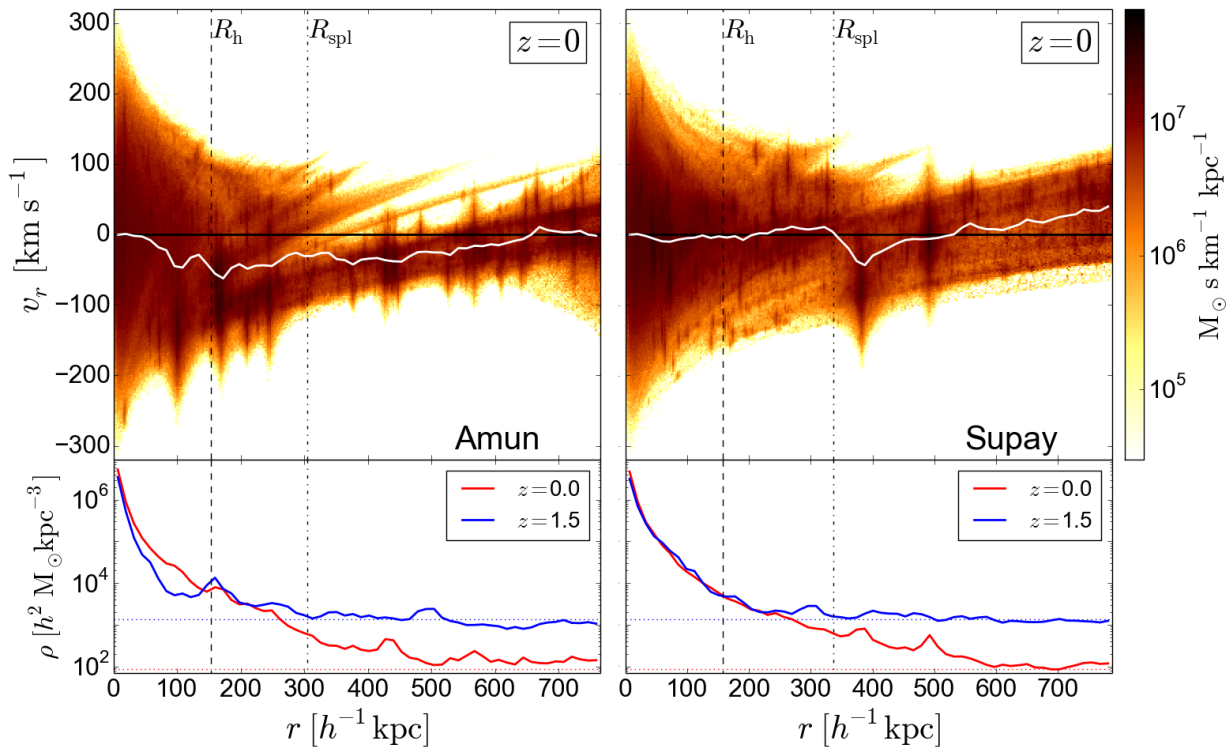


Figure 3.8: Top: radial phase-space diagram for Amun (left-hand panel) and Supay (right-hand panel) at $z = 0$. The colour coding indicates the matter density in phase space while the white curve shows the mean velocity as a function of the distance from the halo centre. The vertical lines refer to the halo radius (dashed) and the splashback radius (dot-dashed). Bottom: the radial mass density profiles of the haloes at $z = 0$ (red) and 1.5 (blue). The dotted horizontal lines indicate the mean matter density of the universe at the corresponding epochs.

Our findings challenge the common wisdom about halo formation according to which the halo mass constantly grows with time due to infalling material. Only a small minority of the haloes shows this behaviour on galaxy scales. Conversely, the vast majority of cluster-sized haloes are of the accreting type (chapter 2). What remains to be identified is the physical process that prevents accretion to the stalled haloes. This is the subject of the following section.

3.3.3 The impact of the cosmic web on halo growth

We want to study how accreting and stalled haloes are assembled and connect this process with the properties of their Lagrangian patches and final environments. To achieve this goal, we use Amun and Supay as templates representing the two classes of haloes [the other haloes behave identically]. The cyan area in the left-hand panels of fig. 3.9 marks the distribution of the halo particles in the initial conditions that from now on we call the ‘protohalo’. We use physical coordinates and project the particle positions onto the image plane. The Cartesian axes of the plot are aligned with the longest and the shortest principal axes of inertia of the halo particles and the blue ellipse shows the projection of the inertia ellipsoid. The greyscale in the background highlights the nested mass resolution levels of the re-simulations and is not relevant to our analysis. It is worth noticing, however, that the central light-grey area indicates the high-resolution region of the re-simulations which corresponds to the Lagrangian patch occupied by the particles that are found within $3R_h$ from the halo centre at $z = 0$. For Supay, this volume is very well

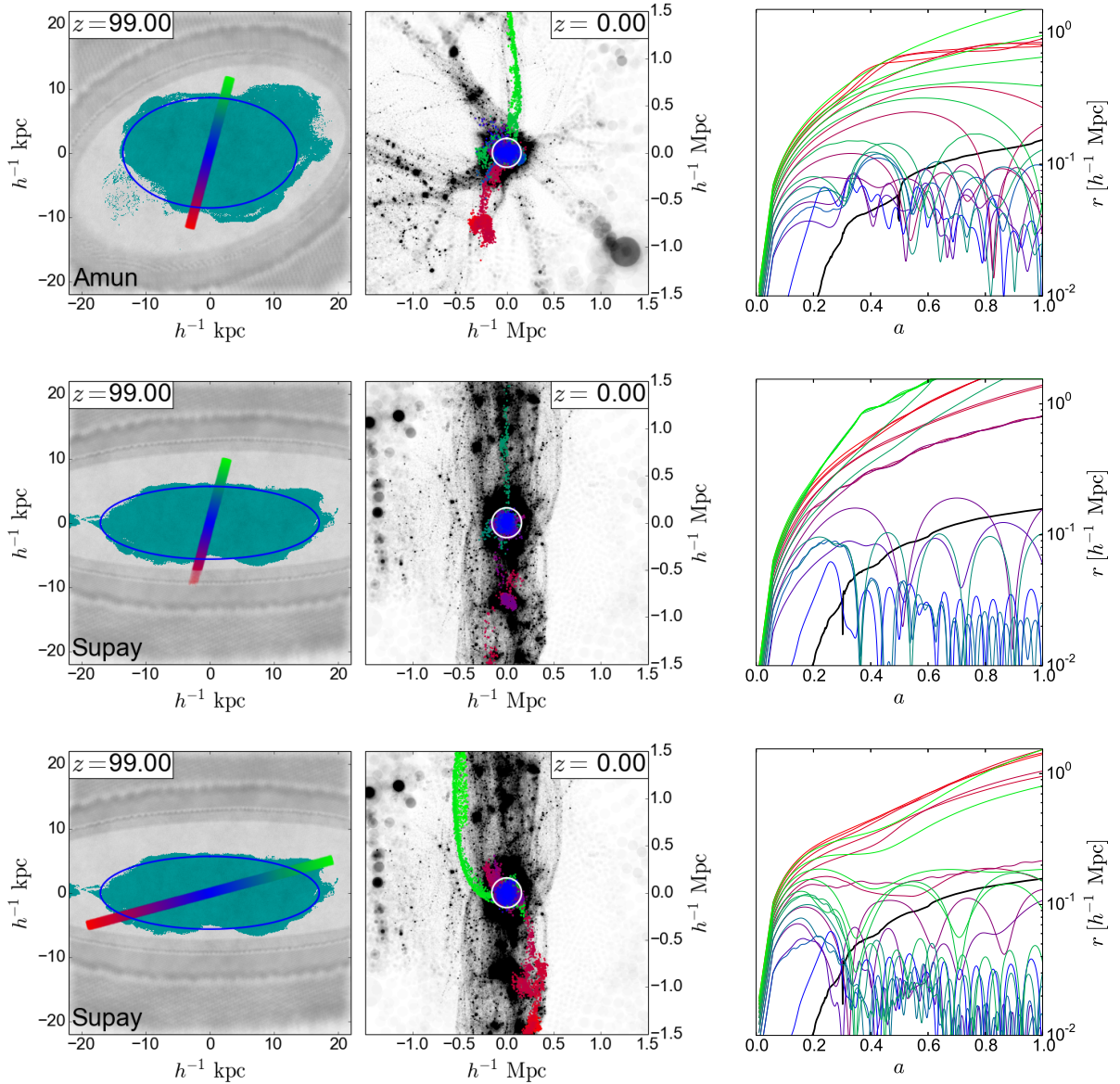


Figure 3.9: Particle positions and orbits for Amun (top) and Supay (middle and bottom). The left-hand panels show the halo particles in the initial conditions (cyan points). The x and y axes are oriented parallel to the longest and the shortest principal axes of inertia of the halo particles at $z = 99$, respectively. The blue ellipse shows the projection of the inertia ellipsoid on this plane. The underlying grey scale reveals the multi-mass sampling of the initial conditions. The central light grey area denotes the high-resolution region. We select particles within a thin cylinder and colour them according to their distance from the centre of mass of the protohalo. The projection of the cylinder onto the plane of the figure produces the central coloured rectangle. The middle panels show the particle distribution at $z = 0$ using the same orientation of the axes as in the left-hand panels (the size of the represented region is different though). All the particles within $\pm 100 h^{-1}$ kpc from the plane of the page are rendered using grey circles with size proportional to the particle mass and fixed transparency. Note that the middle and bottom row only differ by the orientation of the thin cylinder used to define the coloured particles. The white circumference indicates the conventional halo boundary, R_h . The final positions of the particles that initially lie within the cylinder shown in the left-hand panel are highlighted using the colour coding introduced above. The right-hand panels show how the distance to the halo centre of 21 particles selected within the cylinder evolves with time (coloured curves). Also indicated is the evolution of the halo radius (thicker black curve). The halo position and size are computed considering the main progenitor at every snapshot.

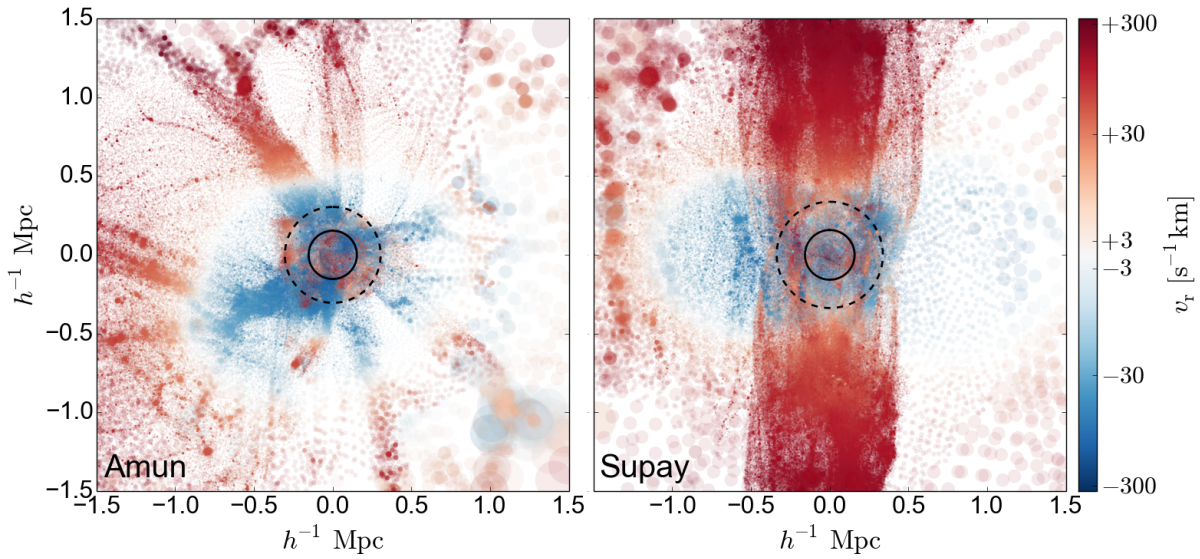


Figure 3.10: As in the middle panels of fig. 3.9 but colouring the simulation particles according to their radial velocity with respect to the halo center. Note that separate logarithmic scales are used for infalling and receding matter connected with a linear scale in the range from -3 to $+3$ km s^{-1} . The solid and dashed circles indicate the halo and the splashback radius, respectively.

aligned with the cyan patch while a substantial misalignment is noticeable for Amun. This fact suggests that concentric Lagrangian shells follow a more consistent dynamics in Supay than in Amun.

In the central panels of fig. 3.9, we plot the particle distribution at $z = 0$. The orientation of the axes is the same as in the left-hand panels but the comoving area shown here is a bit smaller. The white circumference indicates R_h and all the non-halo particles within $\pm 100 h^{-1}$ kpc in the direction perpendicular to the page have been rendered using grey circles with size proportional to the particle mass and fixed transparency. These plots show that Amun forms a node in the cosmic web and is connected to a series of thin filaments. Some of these are more prominent than others but there is clearly no dominant structure surrounding the halo. On the contrary, Supay is embedded in a very pronounced filament which is much thicker than R_h . Note that the filament is perfectly aligned with the shortest principal axis of the protohalo and perpendicular to the longest one. The entire high-resolution region has been compressed into the filament. Similar visual examples of the connection between halo assembly and the cosmic web have been published by Hahn, Porciani, Dekel et al. (2009, see their fig. 2). Their statistical study based on large cosmological simulations shows that the halo mass-assembly rate correlates most strongly with the largest eigenvalue of the rate-of-strain tensor (a measure of velocity shear) which reflects the integrated effect of gravitational tides over time. What is still missing, however, is a detailed study of a few examples that help establishing physical links between these correlated variables: how does matter accretion respond to the more or less sheared dark-matter flows surrounding haloes? We address this issue below by analysing our zoom simulations.

To study how matter accretes to the haloes, we hand-pick a set of particles based on their Lagrangian coordinates and follow their trajectories. In particular, we consider the material that is initially contained within a right circular cylinder symmetrically located around the protohalo centre of mass. The radius of the cylinder is small compared to its height which is comparable with the size of the protohalo. In fig. 3.9 we highlight the material in the cylinder with colours indicating its distance from the protohalo centre (left-hand panels) and also show its final Eulerian position at $z = 0$ (middle panels). We finally

select 21 individual particles initially located within the cylinder (and equally spaced in \sqrt{r} to put more emphasis on the halo boundary) and plot the time evolution of their distance to the centre of the halo main progenitor using the same colour coding (right-hand panels). As a reference, we also show R_h as a function of time as black line. For Amun (top row), we orient the cylinder with a slight tilt (15 deg inclination) with respect to the shortest principal axis of inertia of the protohalo. Of course, the particles that initially are found close to the centre of the cylinder end up forming the halo. Those that originally are in the outskirts, instead, still form a continuous sequence at $z = 0$ which is aligned with the short principal axis of inertia of the protohalo. This implies that the particles follow nearly radial orbits with respect to the halo centre. The top right-hand panel of fig. 3.9 shows that the most distant particles are approaching or have just experienced turn around at the present time. They will then accrete to the halo in the future. In the left-hand panel of fig. 3.10, we colour the simulation particles at $z = 0$ according to their radial velocity: blue tones indicate infall while red ones correspond to outflows. The thin white cloud marks the locus of the particles that are turning around. Matter flows towards Amun along a few preferential directions which are isotropically distributed around the halo. To first approximation, the collapsing patch can be described as an ellipsoid (as in many theoretical models for halo collapse, see section 3.3.5) although the distance of the particles that are turning around is always substantially larger than $2R_h$ (which is what is generally assumed).

We now repeat the analysis for Supay (middle row of fig. 3.9), once again considering a cylinder which is slightly tilted with respect to the short principal axis of inertia of the protohalo. In this case, this direction also coincides with the orientation of the thick filament embedding the halo at $z = 0$. All the particles that are not part of the halo form a thin plume of matter lying at the centre of the filament at the present time. Most of them, however, are found at very large distances from the halo (i.e. outside the range of $\pm 1.5 h^{-1}$ Mpc shown in the figure). This is a consequence of the fact that the velocity field in the filament has a very strong shear and matter recedes from the halo as clearly demonstrated in the right-hand panel of fig. 3.10. Further evidence is provided by the radial trajectories of the particles that show a clear separation between those that are orbiting within Supay and those that are receding from it (middle-right panel in fig. 3.9). We conclude that matter cannot accrete to the halo along the filament.

Since the protohalo of Supay is very asymmetric and elongated, it is interesting to replicate our analysis using a different set of particles. We thus consider a narrow cylinder which is slightly tilted with respect to the first principal axis of inertia of the protohalo and perpendicular to the final filament (bottom panels in fig. 3.9). At $z = 0$ this material is stretched into a thin strip of matter that runs along the filament. Particles that initially were lying on the left-hand side of the protohalo are now found on the right-hand side of the filament and vice versa. This phenomenon reveals that the material originally contained in the cylinder underwent orbit crossing during the formation on the thick filament which is a fully non-linear structure. Examining the radial trajectories of the particles we notice that also in this case there is a clear gap in the final position between the particles bound to the halo and those dispersed along the filament. Material that immediately surrounds the protohalo in the initial conditions is now receding from the halo (sometimes after having experienced turn around followed by an episode of positive acceleration). We also note that some particles found initially at the boundary of the protohalo, nowadays follow orbits that loiter at approximately fixed distance from the halo centre with a dominant velocity component in the tangential direction. They form the outermost shell of matter that can accrete to the halo.

Hahn, Porciani, Dekel et al. (2009) have shown that the velocity shear of the dark-matter flow surrounding a halo correlates with the tides due to the dominant neighbour halo. These authors used the restricted three-body problem to quantify the tidal influence of larger haloes. Consider two bodies of mass M (the primary mass) and $m \ll M$ (the secondary mass) orbiting each other at distance d . The gravitational region of influence of the secondary mass is approximately bounded by the Hill radius, $R_H \simeq d [m/(3M)]^{1/3}$, i.e. the maximum distance at which a test particle can stably orbit the secondary

without being pulled away by the primary (this is a proxy for the size of the complex Roche lobes). To extend the applicability of this concept in the presence of multiple neighbours, Hahn, Porciani, Dekel et al. (2009) considered a given halo as the secondary body and determined the corresponding minimal Hill radius by varying the primary among all more massive objects. They found that the mass flux into the minimal Hill sphere is reduced for the least accreting halos which provides a hint towards tidally suppressed mass growth. Repeating this analysis, we find that the minimal Hill radii of the stalled haloes are substantially smaller than for the accreting ones (see table 3.1) which is not surprising as they cluster much stronger. In all cases, however, the minimal Hill radius is much larger than R_h and R_{sp} showing that the tidally dominant neighbour is not directly responsible for the stalled accretion (nor it causes any mass loss). Hahn, Porciani, Dekel et al. (2009) envisaged that stalled haloes can accrete material lying within their minimal Hill radii as long as it does not move with too large relative velocities. In the right-hand panel of fig. 3.10, we plot the radial-velocity map for the matter surrounding Supay at $z = 0$. Infall takes place within a donut shaped region that extends till the turnaround radius (which is comparable with R_H) while strong and coherent outflows are present within the filamentary structure that hosts Supay. In this case, the tidally dominant halo has a mass of $5.41 \times 10^{12} h^{-1} M_\odot$ and lies at a distance of $3.01 h^{-1}$ Mpc from Supay mostly in the direction of the filament. This halo is actually receding from Supay: both objects are flowing towards a very large mass concentration located at one extreme of the filament but Supay, which is more distant from it, moves more slowly. The second and third most dominant haloes are two much more distant cluster-sized objects ($M_h \simeq 10^{14} h^{-1} M_\odot$, $d \simeq 15 h^{-1}$ Mpc) which lie in opposite directions with respect to Supay and, substantially, define the filament. In general, our high-resolution simulations reveal that reasoning in terms of the minimal Hill sphere provides a poor description of the dark-matter flow around stalled haloes mainly because of the strong geometrical asymmetry due to the presence of elongated large-scale structures.

3.3.4 The impact of the cosmic web on halo structure

We now focus on the material that forms the haloes at the present time and explore differences in the internal structure of accreting and stalled haloes.

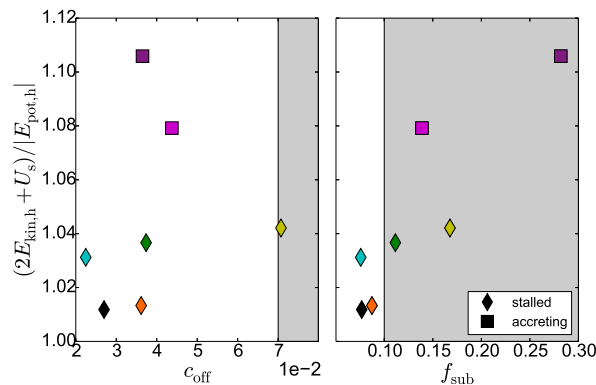


Figure 3.11: Indicators of the dynamical state of the resimulated haloes at $z = 0$: the virial ratio $(2E_{\text{kin,h}} + U_s)/|E_{\text{pot,h}}|$ (see the main text for details), the offset between the centre of mass and the location of the potential minimum in units of R_h , c_{off} , and the mass fraction in resolved substructures, f_{sub} . The unshaded area indicates the region of parameter space occupied by dynamically relaxed haloes ($(2E_{\text{kin,h}} + U_s)/|E_{\text{pot,h}}| < 1.35$, $c_{\text{off}} < 0.07$, $f_{\text{sub}} < 0.1$) according to the study by Neto et al. (2007) which is based on large cosmological simulations with a lower mass resolution than ours and thus provides smaller values for f_{sub} . Overall, stalled haloes appear to be more relaxed (i.e. closer to dynamical equilibrium) with respect to the accreting ones.

We first consider halo shapes both at the initial and final times. As evidenced in table 3.1, fig. 3.9, and briefly described at the beginning of section 3.3, the Lagrangian patches of stalled haloes show a characteristic elongated shape in which the shortest principal axis of inertia aligns with the filament (see also Porciani, Dekel and Hoffman 2002; LBP14). This phenomenon reflects the fact that halo growth is inhibited along the filament by a strong velocity shear while material can more easily flow in along the perpendicular directions (this is the way the filament itself is formed, actually). As already mentioned, at $z = 0$, no obvious difference can be noticed in the halo shapes between stalled and accreting haloes (see table 3.1). However, the minor axis of stalled haloes retains a ‘memory’ of the halo-assembly process and is preferentially oriented in the perpendicular direction to the filament. The mass-density profiles of the resimulated haloes at $z = 0$ are well approximated by the NFW formula. With the exception of Seth, stalled haloes tend to be slightly more concentrated.

Three quantities are often used to infer whether a halo is dynamically relaxed or not: the offset between the centre of mass and the minimum of the gravitational potential measured in units of the halo radius, c_{off} , the fraction of mass in resolved substructures, f_{sub} , and the virial ratio, $(2E_{\text{kin,h}} + U_s)/|E_{\text{pot,h}}|$. [Here $E_{\text{kin,h}}$ and $E_{\text{pot,h}}$ denote the kinetic and the potential energy of the halo, respectively, while U_s is the correction due to the surface pressure of the particles crossing the halo boundary.] In fig. 3.11, we contrast the accreting haloes (squares) with the stalled ones (diamonds) in terms of these quantities. Accreting haloes show a systematically higher virial ratio and a tendency towards having larger f_{sub} while no significant difference in c_{off} is seen. Seth distinguishes itself from the other stalled haloes by showing the largest values of the virial ratio, f_{sub} and, in particular, c_{off} . This is because it contains a massive substructure (with mass ratio 1:17) that just had its first pericenter passage.

The internal dynamics of the haloes can be conveniently described in terms of the velocity anisotropy parameter,

$$\beta = 1 - \frac{\sigma_t^2}{2\sigma_r^2}, \quad (3.2)$$

where σ_r and $\sigma_t = (\sigma_\theta^2 + \sigma_\phi^2)^{1/2}$ denote the radial and tangential velocity dispersions, respectively. An isotropic velocity distribution has $\beta = 0$, while $\beta < 0$ indicates a bias towards tangential motions. Faltenbacher and S. D. White (2010) showed that classifying haloes in terms of β leads to a very strong assembly bias. Stacking thousands of haloes from a large cosmological simulation, they also found a systematic difference between the radial β profiles of halo subpopulations split based on some other halo properties (e.g. shape or spin) at fixed halo mass. These unexplained results suggest that the halo velocity structure correlates with the large-scale environment and provide us with the motivation to analyse what happens in single objects using our zoom runs. In the left-hand panel of Figure 3.12, we report the individual and averaged radial β profiles extracted from our re-simulations. Stalled and accreting haloes show consistent dynamics only in their innermost cores (i.e. for $r/R_h < 0.15$ where $\beta \simeq 0.2$). Further out, their orbital structure is very different. Within R_h , β increases with r for the accreting haloes while it decreases and even turns negative for the stalled ones that are therefore dominated by tangential motions in their outer regions. The origin of this phenomenon can be schematically understood as follows. To first approximation, matter falls towards accreting haloes following radial orbits as it is assumed in the spherical or ellipsoidal collapse models. However, this is not the case for the stalled haloes. In fact, the presence of the host filament has a dramatic influence on the orbits of the surrounding material particles that get deflected from the radial direction and accrete to the halo with a significant tangential-velocity component. Due to the approximate symmetry around the filament axis, both senses of rotation are possible for the accreting particles and stalled haloes do not spin up substantially (see table 3.1). Small asymmetries in the accretion flow, however, could potentially generate a spin component parallel to the

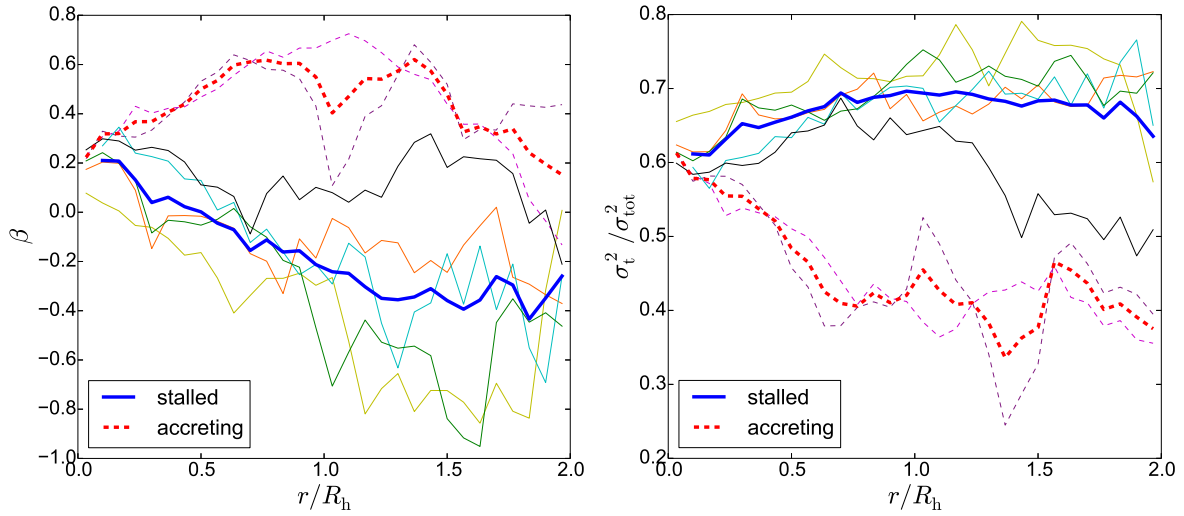


Figure 3.12: The present-day velocity anisotropy parameter β (left-hand panel) and the ratio of tangential to total velocity variance (right-hand panel) measured in thin spherical shells at distance r from the centre of our resimulated haloes. The thick solid and dashed lines show averages taken over all the stalled and accreting haloes, respectively. The thin lines refer to the individual haloes (with the usual colour coding). Circular orbits play a much more important role in the stalled haloes due to the impact of the host filament on halo assembly.

filament. For our six re-simulated stalled haloes this component is always subdominant (the mean and standard deviation of the angle between the spin and the filament direction are 66° and 17° , respectively). The velocity anisotropy also reflects changes in the radial velocity dispersion which is slightly higher for the accreting haloes due to the contribution of their radially infalling streams. In order to get a more complete picture, we show the tangential contribution to the total velocity variance in the right-hand panel of fig. 3.12. Once again the differences between stalled and accreting haloes are striking and consistent with our previous findings. We conclude that the dynamical effects due to the gravitational attraction of the filament are already noticeable deep inside the haloes where stalled haloes are dominated by tangential orbits and accreting haloes by radial ones. This intimate link between the velocity anisotropy parameter and the formation history of the haloes elucidates the results by Faltenbacher and S. D. White (2010). Our results complement (and are consistent with) several recent studies on the complex interplay between the cosmic-web dynamics and the spins of galaxy-sized haloes (independently of their assembly histories). Orbit-crossing generates vortical flows within multi-stream regions (Pichon and Bernardeau, 1999; Puelbas and Scoccimarro, 2009; Libeskind, Hoffman and Gottlöber, 2014; X. Wang et al., 2014) and the resulting vorticity is preferentially perpendicular to the axis along which gravitational collapse proceeds faster (Libeskind, Hoffman, Steinmetz et al., 2013; Laigle et al., 2015). In the plane perpendicular to a filament, vorticity shows a characteristic quadrupolar pattern (Laigle et al., 2015) originated by the winding of the matter flows (Pichon, Pogosyan et al., 2011; Codis et al., 2012). Halo spins are thus influenced by secondary anisotropic infall of matter from the vortical filaments (Aubert, Pichon and Colombi, 2004; Bailin and Steinmetz, 2005; Codis et al., 2012; Libeskind, Hoffman, Steinmetz et al., 2013). As a consequence, the angular momentum of low-mass haloes ($M_h < 5 \times 10^{12} M_\odot$ at $z = 0$) tends to be preferentially aligned (in a statistical sense) with the cosmic-web filaments in which they reside whereas the spin of larger objects lies in the perpendicular direction (Hahn, Porciani, Carollo et al., 2007; Aragón-Calvo et al., 2007; Sousbie, Pichon et al., 2008; Paz, Stasyszyn and Padilla, 2008; Zhang et al., 2009; Codis et al., 2012; Aragon-Calvo and Yang, 2014). Laigle et al. (2015) make the conjecture that these correlations reflect the Lagrangian size of the haloes compared with the Lagrangian stretch of the

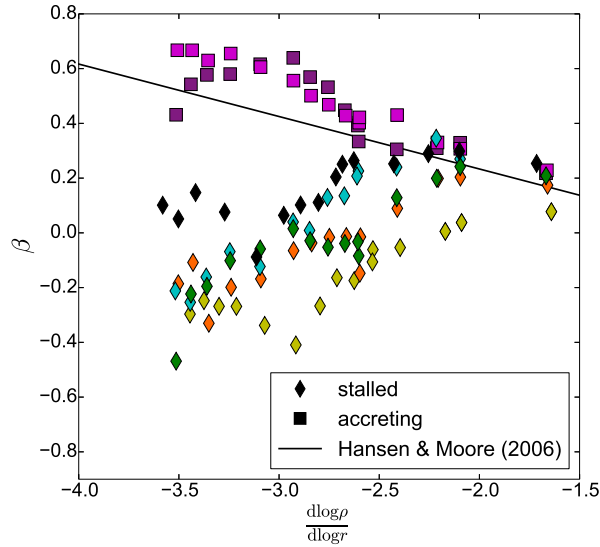


Figure 3.13: The velocity anisotropy parameter measured in thin radial shells for our resimulated haloes at $z = 0$ is plotted against the corresponding slope of the mass-density profile. Only shells contained within R_h are considered. The solid line indicates the universal relation proposed by Hansen and Moore, 2006.

vorticity quadrants forming within the filament. Small haloes feel only one polarity and get an important spin component along the filament. On the other hand, more extended objects overlap with quadrants of opposite polarity and do not develop a net angular-momentum component parallel to the filament, L_{\parallel} . In order to clarify what happens in our simulations, we compute the specific L_{\parallel} per unit mass for the particles immediately surrounding the stalled haloes (i.e. lying between R_h and R_{spl}). The spatial distribution of the specific L_{\parallel} in the plane perpendicular to the filament presents a complicated pattern (approximately quadrupolar with superimposed small-scale fluctuations), while its azimuthally averaged probability density is broad and approximately symmetric for the two senses of rotation. The mean value corresponds to 20-30 per cent of the mean specific angular momentum of the halo particles. The same result is found considering only infalling material. This suggests that, in the mass range we consider, accretion from the filament should not alter the halo spin significantly. The kinematic structure of the filament mostly imprints a tangential velocity dispersion in the halo as a characteristic signature.

Early studies suggested that β follows a universal radial profile in relaxed haloes (e.g. Cole and C. Lacey, 1996; Carlberg et al., 1997; Rasia, Tormen and Moscardini, 2004). More recently, Hansen and Moore (2006) provided evidence for a universal relation between β and the slope of the radial mass-density profile (both evaluated at the same position). Our simulations are inconsistent with such a relation. In fact, while the density profiles of all haloes are monotonically decreasing, the β profiles increase with r for accreting haloes and decrease with r for stalled haloes. The velocity anisotropy and the logarithmic slope of the density profile for different radial shells (all with $r < R_h$) of our re-simulated haloes are shown in fig. 3.13. The solid line highlights the fit derived by Hansen and Moore (2006). Accreting haloes approximately follow the assumedly universal relation while stalled haloes violate it. In both cases, better agreement with the fit is found for the innermost shells which are displayed on the right-hand side of the figure. We deduce that the universal relation proposed by Hansen and Moore (2006) holds true only in the halo core ($r < 0.2R_h$) where no difference is found between accreting and stalled haloes. Several authors have reached similar conclusions following different approaches (e.g. Navarro, Ludlow et al., 2010; Ludlow, Navarro et al., 2011; Lemze et al., 2012) even in the presence of a

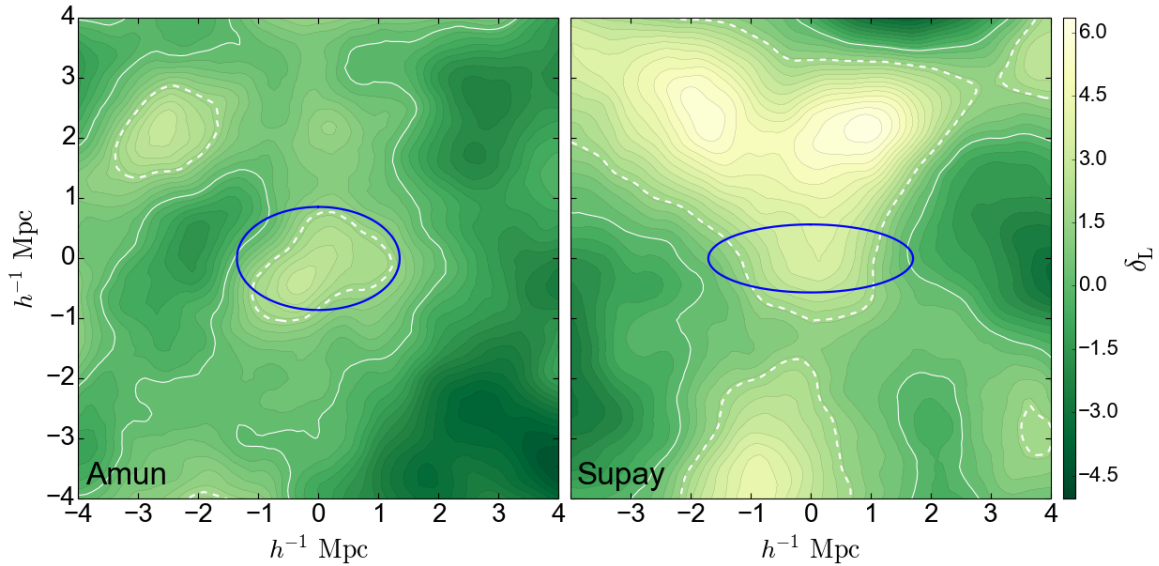


Figure 3.14: Map of the linear density field at $z = 0$ on a slice passing through the protohalo centres of Amun (left) and Supay (right). The orientation of the axes is as in fig. 3.9. The solid white contour lines indicates the mean density of the universe while the dashed one corresponds to the spherical-collapse threshold $\delta_L = 1.686$. The blue ellipse is the projection of the inertia ellipsoid of the protohalo as in fig. 3.9. The density contrast is smoothed with a top-hat filter in configuration space with mass resolution $M_s = M_h$.

baryonic-matter component (Tissera et al., 2010). The reason why Hansen and Moore (2006) could not notice any departure from a universal relation is that they considered a special set of simulations: single overdensities undergoing spherical collapse, two colliding objects, and a very massive halo extracted from a cosmological simulation. All these systems show a continuous radial infall of matter at late times and would be tagged as accreting in our classification scheme.

3.3.5 Predicting halo masses with the excursion-set method

Analytical methods that establish a link between dark-matter haloes and the properties of their Lagrangian patches in the linear density field are extremely useful in cosmology as they provide the tools to make predictions for the halo mass function and clustering properties. In principle, the rarity and biasing of density peaks in different environments of the cosmic web follows directly from the statistics of Gaussian random fields (Doroshkevich, 1970). However, for any practical application, it is necessary to express the results as a function of the final halo properties (rather than the initial peak height, etc.). The challenge is to create a mapping from the initial to the final configurations in terms of a collapse model (e.g. Peebles 1980; BM96; LBP14) and deal with the multi-scale nature of the density field. The most successful algorithm is certainly the excursion-set method (Bond, Cole et al., 1991; Zentner, 2007). In this section we test it against our high-resolution simulations.

We extract the linear density field from the initial conditions of the parent U512 simulations and use the linear growth factor of matter perturbations to evaluate the linear density contrast at the present time. We convolve this field with a top-hat kernel in configuration space and obtain the smoothed linear density contrast, δ_L . We vary the smoothing radius, R_s and associate it with the mass scale $M_s = \frac{4\pi}{3} R_s^3 \bar{\rho}_m$ where $\bar{\rho}_m$ denotes the mean matter density in the universe. For example, in fig. 3.14 we draw maps of δ_L for Amun and Supay with resolution M_h (we use a plane passing through the protohalo center of mass with

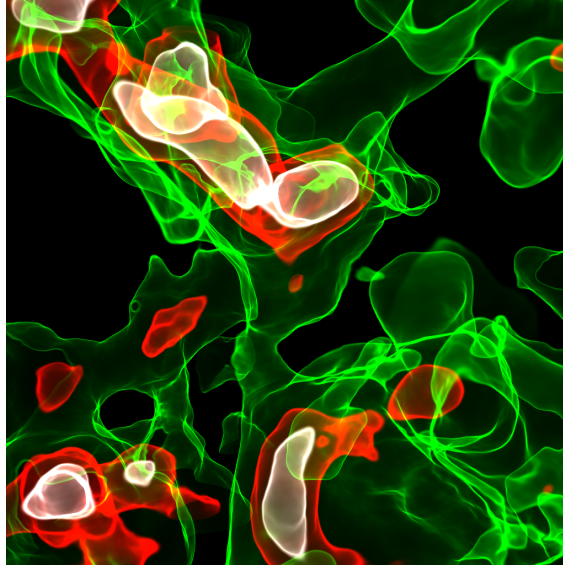


Figure 3.15: Volume rendered image of the linear density field presented in the right-hand panel of fig. 3.14. Selected isodensity surfaces with $\delta_L = 1.68, 3.9$ and 4.9 are drawn in green, red and white, respectively. Supay originates from the small red peak located at the centre of the figure.

the same orientation as in fig. 3.9). To facilitate understanding, in fig. 3.15 we also present a volume rendering of the linear density field for Supay. Both haloes originate from a density peak (although, for Supay, this is not noticeable in fig. 3.14 as the local maximum is slightly off the plane of the image). However, while Amun emerges from a rather isolated peak, the protohalo of Supay lies in between two extended and very dense structures (its large-scale layout closely reminds that of a saddle point with a superimposed small-scale peak). Only such particular configurations in the linear density field lead to the formation of strong filaments. What is necessary is the presence of two rare high-density peaks that are not too distant from each other and whose tidal tensors are sufficiently well aligned (Bond, Kofman and Pogosyan, 1996). This layout evolves into two massive haloes joint by a thick filament. Consistently with this concept, our stalled haloes always lie within $2 - 3 h^{-1}\text{Mpc}$ from a more massive object and move along the filament. The relative velocities indicate that merging might only happen in some distant future thus confirming that stalled haloes are long lived objects.

Excursion-set trajectories are obtained by plotting δ_L evaluated at the Lagrangian positions of the haloes versus M_s . In fig. 3.16, we show the trajectories for the D-ZOMG haloes and compare them with the collapse threshold derived from the spherical collapse model (horizontal grey line). We first note that the slopes of the excursion-set trajectories are pretty similar for accreting and stalled haloes (with the only exception of Siris) thus indicating that their protohaloes have similar radial density profiles. We attempt to predict the final halo masses by identifying the mass scale at which the trajectories first up-cross the threshold level $B_{SC} = 1.686$. This corresponds to requiring that the outermost mass shell collapses at the present time according to the spherical collapse model (Peebles, 1980). Such a guess overestimates M_h by a factor of ~ 3 for the stalled haloes while it gives better results (offset by nearly 25 per cent) for the accreting ones. In addition, fig. 3.16 shows a tight correlation between the linear density contrast smoothed on the halo mass scale (highlighted by a vertical grey line) and the collapse time as already evidenced by LBP14 and in chapter 2 using large cosmological simulations. Therefore it is not possible to accurately predict the halo masses using the same threshold for all the trajectories.

We now consider additional variables to account for the effect of tides that we quantify in terms of the

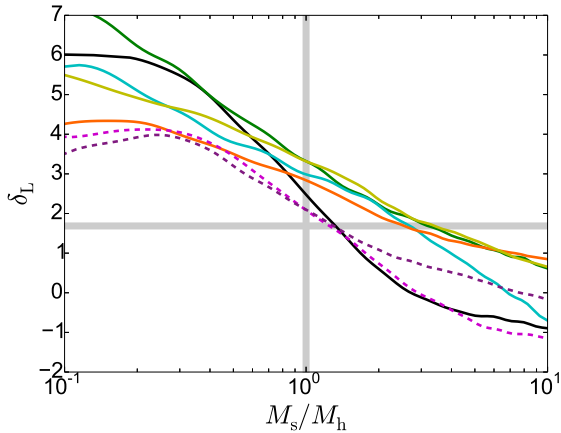


Figure 3.16: The linear density contrast evaluated at the centre of the D-ZOMG protohaloes is plotted as a function of the smoothing mass scale for a spherical top-hat filter in configuration space. The vertical and horizontal grey lines mark the mass of the haloes in the N-body simulations and the spherical-collapse threshold, respectively. Note that collapse time correlates very well with the linear density contrast measured on the halo-mass scale, M_h .

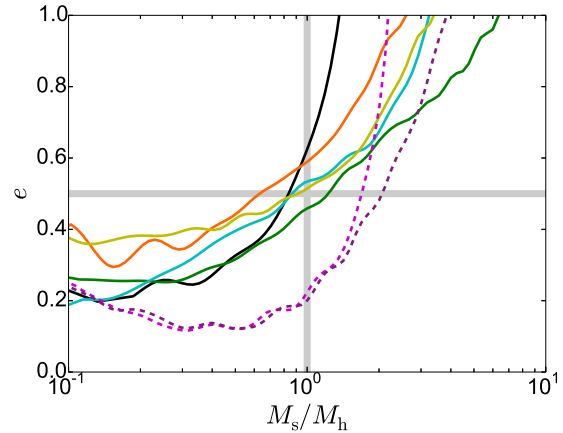


Figure 3.17: As in fig. 3.16 but for the ellipticity of the linear tidal field instead of the density contrast. The vertical and horizontal grey lines indicate the mass of the haloes in the N-body simulations and the value $e = 0.5$, respectively. Note that the environment of stalled haloes produces stronger tides.

linear deformation tensor, $D_{ij} = \partial_i \partial_j \phi$, where ϕ is the gravitational potential obtained solving $\nabla^2 \phi = \delta_L$. After computing the eigenvalues of the deformation tensor, $\lambda_1 \geq \lambda_2 \geq \lambda_3$, we define the ellipticity of the tidal field as

$$e = \frac{\lambda_1 - \lambda_3}{2\delta_L} \quad (3.3)$$

(we recall that $\lambda_1 + \lambda_2 + \lambda_3 = \delta_L$). This quantity measures the degree of anisotropy between the most compressing and stretching components of the linear tidal field (or of the linear velocity shear). In fig. 3.17, we show how e (evaluated at our protohalo centres) changes as a function of the smoothing scale. For $M_s \simeq M_h$, stalled haloes experience significantly stronger tides than accreting ones. Information on the formation of a filament in their surroundings is therefore already encoded in the linear density field.

The ellipsoidal model by BM96 is commonly used to describe gravitational collapse in the presence of tides. In this case, an initially spherical patch is distorted into an ellipsoid by the action of linear tides and collapse takes place at different times along the different principal axes. As a matter of fact, collapse along all the three axes corresponds to an excursion-set threshold, B_{BM} , that depends on λ_1 , λ_2 and λ_3 . We apply this model to our protohaloes and we show the resulting mass-accretion histories in the left-hand panel of fig. 3.18 (sharp variations are due to the oscillations in e seen in fig. 3.17). Predictions for the halo mass at $z = 0$ are quite accurate for the accreting haloes but severely underestimate M_h for the stalled haloes. The latter class of objects, in fact, shows very elongated protohaloes that cannot be well approximated with spheres.

Sheth, Mo and Tormen (2001) combined the ellipsoidal collapse model with the statistics of Gaussian random fields and derived an effective threshold for halo formation which is a function of M_s only. The

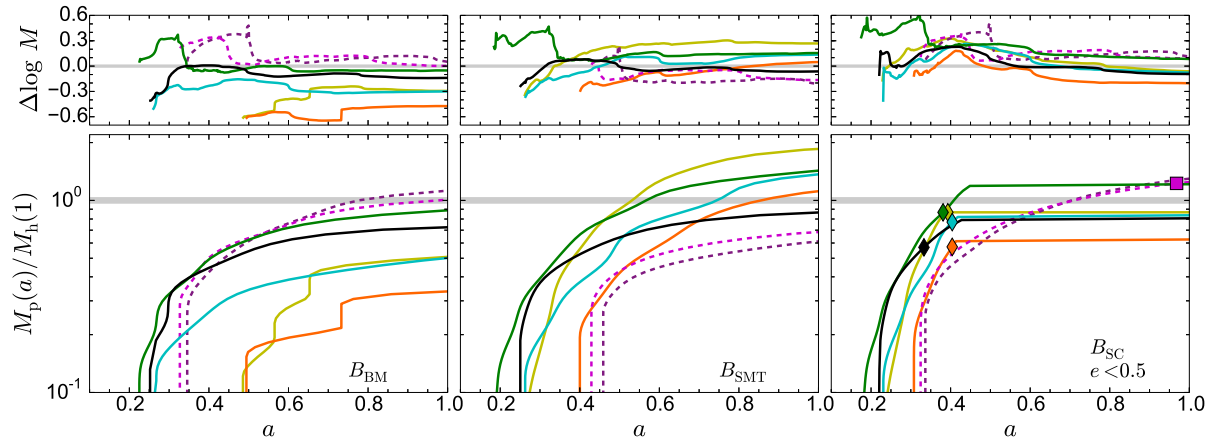


Figure 3.18: Mass accretion histories for the D-ZOMG haloes predicted using the excursion-set method with different collapse thresholds normalized to the individual measured halo present mass. The left-hand panel shows results derived with the ellipsoidal collapse model by BM96. The middle panel is based on the fit by Sheth, Mo and Tormen (2001). Finally, in the right-hand panel we combine the spherical-collapse threshold with the additional condition $e < 0.5$ for a shell to collapse. The horizontal band highlights the halo mass measured in the Z4096 simulations at $z = 0$ while the symbols in the right-hand panel indicate the collapse time of the haloes estimated from the same runs. The smaller panels on the top show the logarithm of the ratio between the different excursion-set predictions and the mass accretion histories measured in the simulations (see fig. 3.5).

underlying idea is that lower-mass objects experience stronger tides (on average) and thus need higher initial densities to overcome the tidal forces and collapse by a given time. Once obtained a functional form for the threshold, Sheth, Mo and Tormen (2001) arbitrarily rescaled some of its coefficients in order to fit the halo mass function and linear bias parameters extracted from N-body simulations, the justification being the freedom in the definition of the halo boundary. The resulting threshold, B_{SMT} , accurately describes the mean protohalo densities found in simulations as a function of halo mass (B. E. Robertson et al., 2009; Elia, Ludlow and Porciani, 2012) although, contrary to expectations, the scatter around the mean correlates with the halo collapse or formation time (LBP14, chapter 2) and does not depend on the tidal prolateness (Hahn and Paranjape, 2014). In the middle panel of fig. 3.18, we show the mass accretion histories deriving from the excursion-set method combined with B_{SMT} . On average the model predicts the correct halo masses at $z = 0$ but the individual estimates are not accurate. This method tends to underestimate the mass of accreting haloes and to overestimate that of stalled haloes. Furthermore, stalled haloes grow at a slightly faster pace in the model compared to the simulations (top-centre panel).

N-body simulations show that protohaloes are strongly aspherical and their inertia tensors are closely aligned with the tidal shear (Lee and Pen 2000; Porciani, Dekel and Hoffman 2002; Despali, Tormen and Sheth 2013; LBP14). Supay provides a clear example of this phenomenon (see figs. 3.9 and 3.14). A modified ellipsoidal collapse model that follows the evolution of ellipsoidal Lagrangian regions aligned with the linear velocity shear has been introduced in LBP14 and further discussed in chapter 2. This model provides a better match to simulations. Also in this case, however, the linear density required for perturbations to collapse by the present time underestimates the values measured for protohaloes in N-body experiments. Dropping the assumption that haloes are forming today and imposing that their outermost shell collapsed at t_c nicely reconciles model predictions and simulations and provides a consistent picture chapter 2. This works well even when the constant threshold of the spherical collapse model is adopted in the excursion-set calculations. The key idea is that haloes grow (in approximate

agreement with the spherical collapse model) until the gravitational effect of surrounding structures inhibits further growth. The problem is that one needs to estimate t_c based on the linear field in order to make the model predictive. Useful indications can be extracted from fig. 3.17: stalled haloes are associated with values of $e \sim 0.5$ for $M_s \simeq M_h$ while accreting haloes present much smaller values of e . This suggests the following condition for halo growth:

$$e < 0.5 \quad \Rightarrow \quad \delta_L > \lambda_1 - \lambda_3 . \quad (3.4)$$

This equation requires that the spherical part of the linear tidal tensor dominates over the anisotropic part. Note that this condition is independent of λ_1 . In fact, substituting δ_L with the sum of the eigenvalues of the deformation tensor, it can be re-written as $\lambda_2 > -2\lambda_3$. It basically states that, in the presence of one-dimensional dilating deformations (i.e. when $\lambda_2 > 0$ and $\lambda_3 < 0$), $|\lambda_3|$ cannot be too large for accretion to take place. Moreover, halo growth is always inhibited if λ_2 is negative (i.e. when dilation happens along two or more principal axes). The latter case should be tested against numerical simulations as all our stalled haloes have $\lambda_2 > 0$ for $M_s = M_h$ (as expected in the presence of a filament). It might be possible that an additional condition on the tidal prolateness is necessary to describe the most general configuration.

To develop an efficient algorithm that correctly identifies the halo masses given the initial conditions, we implement eq. (3.4) within the excursion-set model as follows: (i) we build two trajectories for each halo: δ_L versus M_s and e versus M_s ; (ii) we look for the first up-crossing of the spherical-collapse threshold (linearly rescaled with the growth factor for matter perturbations at each time) and label the corresponding smoothing mass with M_{up} ; (iii) if $e < 0.5$ on the scale M_{up} we say that the halo mass is M_{up} , otherwise we keep the halo mass unchanged compared with the previous time step. [Note that if the e trajectory crosses the value 0.5 several times, the halo will experience a series of accreting and stalled phases.] The resulting mass-accretion histories are shown in the right-hand panel of fig. 3.18. Both the collapse time and the final masses of the stalled haloes are nicely reproduced by this very simple scheme (within 11 per cent for a_c and 19 per cent for M_h). The ratio between the predicted and measured masses is approximately constant over a large period of time (top-right panel). Stalled haloes, however, show a slight decrease of the mass ratio, which can be attributed to pseudo-evolution in the simulation.

3.4 Summary & conclusions

We have investigated the origin of halo assembly bias using a suite of N-body simulations including a cosmological box and seven zoom runs. Our analysis focuses on haloes with a mass of a few $\times 10^{11} h^{-1} M_\odot$. These are the haloes in which star formation is most efficient and that host L_* galaxies at the present time.

Target haloes for re-simulation have been selected based on the collapse time, t_c , introduced in chapter 2. This quantity measures the time at which the physical volume occupied by the forming haloes becomes stable and virialization can be established. Partitioning haloes of a fixed mass based on t_c generates a strong assembly bias. We sampled the tails of the distribution of t_c by picking (for re-simulation) five isolated haloes that form very early on (at redshift $z > 1$) and two that have not yet collapsed by $z = 0$ in the parent run. This set forms the D-ZOMG simulation suite. We have checked that our sample is mostly representative of the full halo population (less than 5 per cent of the haloes in the parent run do not satisfy the isolation criterion).

We studied the formation process and the internal structure of the resimulated haloes as well as the properties of the Lagrangian patches from which they originate. Our conclusions are as follows.

1. Matter steadily accretes to late-collapsing haloes which grow in mass. These ‘accreting’ haloes

coincide with nodes of the cosmic web and are fed by the radial infall of matter along thin filaments. Substructures and their associated tidal streams orbit the haloes following eccentric trajectories that extend up to very large distances.

2. The radial mass-density profile of early-collapsing haloes does not evolve since t_c . These ‘stalled’ haloes are embedded in prominent filaments of the large-scale structure which are thicker than the halo radius. Matter recedes from the halo along the filament and infall is only possible from the perpendicular directions (see the right-hand panel in fig. 3.10 for an illustrative example). Although some matter always accretes to the halo, the inflow is balanced by outflows along the direction of the filament so that there is no net mass growth. Stalled haloes form the bulk of the halo population with a few $\times 10^{11} h^{-1} M_\odot$ at $z = 0$ (see fig. 3.2).
3. Halo assembly bias reflects the fact that accreting and stalled haloes populate different regions of the cosmic web.
4. Stalled haloes are more dynamically relaxed, their radial density profiles are slightly more concentrated, and a smaller fraction of their mass is in substructures with respect to the accreting haloes.
5. Excluding their core, accreting and stalled haloes are characterized by different internal motions. The velocity anisotropy is biased towards radial orbits in accreting haloes and towards tangential orbits in stalled haloes. This is a consequence of the different mass-accretion modes. While matter impinges on the accreting haloes along nearly radial orbits, the gravitational influence of the filament imparts the infalling particles a substantial tangential component for the stalled haloes. Due to the approximate axial symmetry of the filament, little net angular momentum is generated by this process because both senses of rotation are almost equally likely. No obvious trend is noticeable between the collapse time and the spin parameter \mathcal{S} in our (small) halo sample (table 3.1). The strongest signature imprinted by the filament on the halo is an enhanced tangential velocity dispersion. Our results reveal why classifying haloes in terms of their velocity anisotropy produces a strong assembly bias (Faltenbacher and S. D. White, 2010).
6. The supposedly universal relation between the velocity anisotropy and the slope of the radial mass-density profile found by Hansen and Moore (2006) holds only in the innermost parts of the haloes. Accreting and stalled haloes show very different trends in the outer regions.
7. Accreting haloes are invariably associated with isolated density peaks in the initial conditions and their Lagrangian patches are close to spherical. Stalled haloes, instead, form in between two prominent peaks. The shape of their protohaloes is very elongated along the directions perpendicular to the final filament. This is a consequence of the strong compressional deformation that leads to the formation of the filament.
8. The excursion-set method based on the classical spherical or ellipsoidal collapse models cannot reproduce the formation of the stalled haloes while it makes good predictions for the accreting ones (see also chapter 2). We have presented a very simple extension of the model that accurately predicts the collapse time and the final mass of both accreting and stalled haloes. The key concept is that the accretion of new mass shells is inhibited whenever the asymmetric part of the tides dominates over the spherical part.
9. It is common wisdom that new shells of matter continuously accrete to dark-matter haloes so that they grow in mass. For this reason, in the calculation of the mass function (Press and Schechter,

1974) or in the excursion-set model, one requires that the Lagrangian patches collapse at the same redshift at which haloes are identified, z_{id} (although some more general formulations that release this assumption have appeared, e.g. Mo and S. D. White, 1996; Catelan et al., 1998). Furthermore, N-body simulations show that the linear overdensity of protohaloes increases towards lower halo masses (this is why the halo mass function departs from the Press and Schechter (1974) form). The standard explanation is that lower mass haloes feel stronger tides and therefore need larger initial overdensities to collapse by z_{id} (Sheth, Mo and Tormen, 2001). Our results do not support this conjecture and provide the following alternative explanation. Once galaxy-sized haloes are embedded in non-linear filaments of the cosmic web (a manifestation of strongly anisotropic tides), they cannot grow any longer. These objects must therefore assemble all their mass early on (at $z \gg z_{\text{id}}$) which can only happen starting from large overdensities (see also chapter 2).

In the next two papers of this series, we will use zoom hydrodynamic simulations including star formation and feedback to investigate the impact of the dichotomy between accreting and stalled haloes on galaxy formation and the properties of substructures.

LIGER: mock relativistic light-cones from Newtonian simulations¹

4.1 Introduction

The advent of galaxy redshift surveys has revolutionised our understanding of the large-scale structure of the Universe and provided us with multiple ways to constrain the cosmological model. Mock catalogues of synthetic galaxies play a threefold role in the analysis of these datasets (Cole, Hatton et al., 1998; Blaizot et al., 2005; Kitzbichler and S. D. White, 2007; Sousbie, Courtois et al., 2008; Carlson and M. White, 2010; Merson et al., 2013). (i) They shape theoretical predictions into structures that closely match observations. (ii) They form a straightforward tool to derive biases and covariance matrices of estimators for statistical descriptions of the large-scale structure (e.g. correlation functions or their Fourier analogues). (iii) Related to that, as forecasting tools, they provide key information to designing new surveys by minimising the impact of statistical errors and systematic effects on selected observables.

Since the 1970s, the size of galaxy catalogues has constantly increased in terms of solid-angle and redshift coverage as well as in sampling rate. The next generation of surveys will provide us with the possibility to measure galaxy clustering on scales comparable with the Hubble radius (e.g. Laureijs et al., 2011; Levi et al., 2013; R. Maartens et al., 2015). Theoretical studies suggest that a number of general relativistic effects might be detectable on these scales. In order to fully exploit the potential of the new datasets, it is therefore imperative to develop analysis tools (and thus mock catalogues) that include these effects. In this chapter, we present a method to create mock galaxy catalogues that incorporate relativistic corrections and are built upon the output of either common Newtonian simulations of galaxy formation or semi-analytic models based on standard N-body simulations.

Relativistic effects arise from the fact that we observe galaxies on our past lightcone. The presence of perturbations superimposed to a Friedmann-Robertson-Walker (FRW) background alters the null geodesics of the photons emitted by distant galaxies. In consequence, all the direct observables for a galaxy are different than in a smooth universe: its redshift, angular position on the sky and the flux in any given waveband. Galaxy peculiar velocities, for instance, distort the radial pattern of the galaxy distribution (Kaiser, 1987; Hamilton, 1998). Similarly, magnification due to gravitational lensing modifies the observed number counts in flux-limited samples (E. L. Turner, 1980; E. L. Turner, Ostriker and Gott, 1984; Sasaki, 1987; Matsubara, 2000). Many recent studies have demonstrated the existence of several

¹ This chapter and appendix B have been published in Borzyszkowski, Bertacca and Porciani (2017). The notation has been adapted to match the remaining thesis.

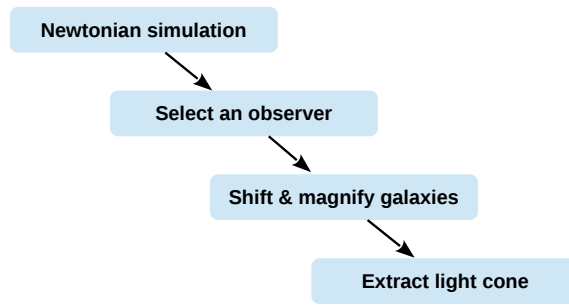


Figure 4.1: Schematic diagram illustrating the sequence of main processing steps in the LIGER method.

additional corrections that, although suppressed on smaller scales, might generate observable signals on distances comparable with the Hubble radius (e.g. McDonald, 2009; Yoo, 2009; Yoo, Fitzpatrick and Zaldarriaga, 2009; Bonvin and Durrer, 2011; Challinor and Lewis, 2011; Bertacca et al., 2012; Jeong, Schmidt and Hirata, 2012; Yoo, Hamaus et al., 2012; Di Dio, Montanari, Lesgourgues et al., 2013; Di Dio, Montanari, Durrer et al., 2014; Bonvin, Hui and Gaztañaga, 2014; Montanari and Durrer, 2015; Yoo and Seljak, 2015; Bonvin, Hui and Gaztañaga, 2016; Cardona et al., 2016; Di Dio, Montanari, Raccanelli et al., 2016; Raccanelli, Bertacca, Jeong et al., 2016; Raccanelli, Bertacca, R. Maartens et al., 2016; Raccanelli, Montanari et al., 2016; Gaztañaga, Bonvin and Hui, 2017). At linear order in the perturbations, these additional corrections include Doppler terms plus Sachs-Wolfe (standard and integrated, see Sachs and Wolfe, 1967; Rees and Sciama, 1968) and (Shapiro) time-delay contributions. Robust models of galaxy clustering on large scales should thus include these modifications that, most likely, will be key to extracting unbiased information on the dark sector of the Universe (i.e. on the nature of dark energy and dark matter) and to improve constraints on primordial non-Gaussianity. This can be done following different approaches. One possibility is to study structure formation using N-body simulations that include dynamical space-time variables in the weak-field approximation (Adamek et al., 2013; Adamek, Durrer and Kunz, 2014; Adamek et al., 2016a; Adamek et al., 2016b), within a post-Friedmann framework (Milillo et al., 2015; Bruni, Thomas and Wands, 2014; Thomas, Bruni and Wands, 2015), or by employing full numerical relativity (Bentivegna and Bruni, 2016; Giblin, Mertens and Starkman, 2016). Alternatively, one can correct a posteriori the results of Newtonian simulations to account for lightcone effects (Chisari and Zaldarriaga, 2011). This is feasible because, at linear order in the perturbations, the mathematical description of a pressureless fluid can be formulated so that there is agreement between general relativity and its Newtonian approximation (Haugg, Hofmann and Kopp, 2012; Rigopoulos and Valkenburg, 2015; Fidler, Rampf et al., 2015; Fidler, Tram et al., 2016)

In this chapter, we follow the latter approach to develop the LIGER (light cones using general relativity) method. As illustrated in fig. 4.1, schematically, LIGER takes a Newtonian simulation as an input and, after selecting an observer, outputs the distribution of galaxies in ‘comoving redshift space’ (i.e. as it would be inferred by applying the background metric to the observed galaxy properties). The algorithm combines the original snapshots of the simulation at constant background time to produce the galaxy distribution on the perturbed light cone. This is achieved by using a coordinate transformation that includes local terms and contributions that are integrated along the line of sight.

Multiple efforts have been made in the literature to investigate the detectability of subtle relativistic effects from forthcoming survey data. Generally, these studies are based on the Fisher-information matrix, use idealised survey characteristics and neglect systematics. The ultimate test to discern which relativistic effects will be observable is to apply the very same estimators that are used for the data to the LIGER mocks. This exciting perspective provides the main motivation for our work. The numerical implementation of

the LIGER method is publicly available at www.astro.uni-bonn.de/~porciani/LIGER.

The chapter is structured as follows. In section 4.2, we introduce the LIGER method and describe its numerical implementation. In section 4.3, we present two straightforward applications of our code. As an illustration of LIGER’s functionality, we first re-analyse a result which has already been discussed in the literature, namely, the impact of magnification bias in the observed cross-correlation of galaxy samples at substantially different redshifts. Subsequently, we discuss the more challenging detection of Doppler terms in the galaxy angular power spectrum at low redshift. Finally, in section 4.4, we conclude. Throughout, we adopt units in which the speed of light is one and define the space-time metric tensor to have signature $(-, +, +, +)$. Greek indices indicate space-time components (i.e. run from 0 to 3) while Latin indices label spatial components (i.e. run from 1 to 3). The Einstein summation convention is adopted.

4.2 The LIGER method

4.2.1 Theory

Redshift-space distortions

We observe galaxies as they are at the time in which their worldline intersects our past light cone. The comoving location of a galaxy can be inferred from two basic observables: its position on the sky, \mathbf{n}_s (a unit vector defined in terms of two angles), and its redshift, z . In fact, these data are sufficient to build three-dimensional maps of the galaxy distribution provided that we assume to live in an unperturbed FRW universe with a fixed set of cosmological parameters. In reality, such a ‘redshift-space’ map gives a

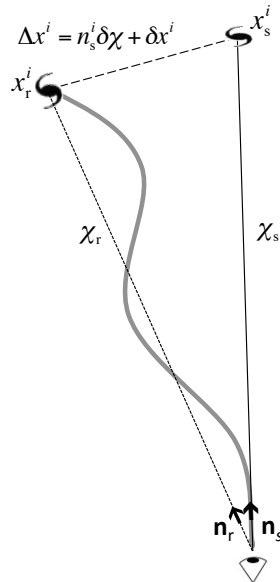


Figure 4.2: Real- and redshift-space perspectives. A galaxy with real-space position x_r^i (top left), located at distance χ_r from the observer (bottom), is assigned an apparent position x_s^i in redshift space (top right) at distance χ_s . Since the photon path to the observer in real space is not straight, the observed position of the galaxy on the sky, \mathbf{n}_s does not coincide with its actual one, \mathbf{n}_r .

distorted portrayal of the cosmic web due to the presence of inhomogeneities (Jackson, 1972; Sargent and E. L. Turner, 1977). Galaxies are artificially shifted both in the radial and tangential directions due to their peculiar motions and the bending of the light they emit. These effects are collectively known under the name of redshift-space distortions.

In mathematical terms, redshift-space is characterized by a set of coordinates that ‘flatten’ our past light cone (e.g. Bertacca, 2015). For instance, the null geodesic from an observed galaxy to us can be described in terms of the following conformal space-time coordinates:

$$x_s^\mu = (\eta_s, \mathbf{x}_s) = (\eta_0 - \chi_s, \chi_s \mathbf{n}_s), \quad (4.1)$$

where η_0 is the present-day value of conformal time (i.e. at observation), χ_s denotes the comoving distance (from the observer) of events located along the geodesic in the unperturbed model universe and $n_s^i = x_s^i/\chi_s$. The full distance to the galaxy corresponds to the observed redshift z , in compact notation $\chi_s(z)$.

For a given photon path (see fig. 4.2), we want to define a mapping from real to redshift space,

$$x_r^\mu[\chi_r(\chi_s)] = x_s^\mu(\chi_s) + \Delta x^\mu(\chi_s), \quad (4.2)$$

where x_r^i denotes the actual comoving position located at distance χ_r along the direction $n_r^i = x_r^i/\chi_r$. [In general, we use the subscripts ‘s’ and ‘r’ to distinguish redshift-space quantities from their real-space counterparts.] Perturbing x_r^μ around x_s^μ and writing $\chi_r = \chi_s + \delta\chi$, we obtain, at linear order,

$$x_r^\mu(\chi_r) = x_s^\mu(\chi_r) + \delta x^\mu(\chi_r) = x_s^\mu(\chi_s) + \frac{dx_s^\mu}{d\chi_s} \delta\chi + \delta x^\mu(\chi_s). \quad (4.3)$$

By using χ_s as the affine parameter for the null geodesic, we write the total derivative along the past light cone as $d/d\chi_s = -\partial/\partial\eta_s + n_s^i \partial/\partial x_s^i$. Since $dx_s^i/d\chi_s = n_s^i$ [to zero order], linear redshift-space distortions can be written as

$$\Delta x^0(\chi_s) = -\delta\chi + \delta x^0(\chi_s) \quad (4.4)$$

$$\Delta x^i(\chi_s) = n_s^i \delta\chi + \delta x^i(\chi_s). \quad (4.5)$$

The first term on the right-hand side of eq. (4.5) corresponds to the change in the affine parameter while the second one derives from the perturbation of the photon path and has both tangential and radial components. Note that the real-space distance to the galaxy does not coincide with $\chi_s(z)$.

Perturbations of the past light cone

In order to compute explicitly all the terms in eqs. (4.4) and (4.5), we need to work out how metric perturbations alter null geodesics. In what follows, we model the matter content of the universe as a collisionless fluid in the single-stream regime. This common assumption provides a suitable approximation on the large scales we are interested in. We use the subscripts ‘e’ and ‘o’ to denote the fluid properties evaluated at the position of the light source (the galaxy) when the photons were emitted and at the location of the observer when the photons were received, respectively. For linear scalar perturbations

in the Poisson gauge², the space-time metric can be expressed as

$$ds^2 = a^2(\eta) \left[-(1 + 2\psi) d\eta^2 + (1 - 2\varphi) \delta_{ij} dx_r^i dx_r^j \right], \quad (4.6)$$

where a denotes the scale factor of the expanding universe while ψ and φ indicate the Bardeen potentials of the inhomogeneities. In this framework, the redshift of a galaxy measured by an observer is

$$1 + z = \frac{(u_\mu p^\mu)|_e}{(u_\mu p^\mu)|_o}, \quad (4.7)$$

where u^μ denotes the four-velocity of the matter fluid (we assume there is no velocity bias) and p^μ is the photon four-momentum. By perturbing the photon geodesic around the FRW solution, we derive expressions for δx^μ and $\delta\chi$. The final result for the galaxy shift is (see also Yoo, 2009; Yoo, Fitzpatrick and Zaldarriaga, 2009; Bonvin and Durrer, 2011; Challinor and Lewis, 2011; Jeong, Schmidt and Hirata, 2012)

$$\begin{aligned} \delta\chi = & - \left(\chi_s + \frac{1}{\mathcal{H}} \right) \left[\psi_o - (n_s^i v_i)_o \right] + \frac{1}{\mathcal{H}} \left[\psi_e - (n_s^i v_i)_e \right] + \int_0^{\chi_s} [2\psi + (\chi_s - \chi) \partial_0 (\varphi + \psi)] d\chi \\ & + \frac{1}{\mathcal{H}} \int_0^{\chi_s} \partial_0 (\varphi + \psi) d\chi, \end{aligned} \quad (4.8)$$

$$\delta x^0 = -\chi_s \left[\psi_o - (n_s^i v_i)_o \right] + 2 \int_0^{\chi_s} \psi d\chi + \int_0^{\chi_s} (\chi_s - \chi) \partial_0 (\varphi + \psi) d\chi, \quad (4.9)$$

$$\delta x^i = - (v_o^i + \varphi_o n_s^i) \chi_s + 2n_s^i \int_0^{\chi_s} \varphi d\chi - \int_0^{\chi_s} (\chi_s - \chi) \delta^{ij} \partial_j (\varphi + \psi) d\chi, \quad (4.10)$$

where $\mathcal{H} = \partial_0 \ln a$ and χ_s are evaluated at the observed redshift of the galaxy while v^i is the peculiar velocity. Here, local corrections express the Sachs-Wolfe and the Doppler effects. Those integrated along the line of sight derive from gravitational lensing, the Shapiro time-delay and the integrated Sachs-Wolfe effect.

Magnification

Metric perturbations also alter the solid angle under which galaxies are seen by distant observers thereby enhancing or decreasing their apparent flux. In terms of the luminosity distance, D_L , the magnification of a galaxy is defined as

$$\mathcal{M} = \left(\frac{d_{\text{lum}}}{\bar{d}_{\text{lum}}} \right)^{-2}, \quad (4.11)$$

where \bar{D}_L denotes the luminosity distance in the background model universe evaluated at the observed redshift of the galaxy.

² The restricted Poisson gauge containing only scalar perturbations is also known as the longitudinal or conformal Newtonian gauge.

At linear order in the perturbations, we can write (e.g. Challinor and Lewis, 2011; Bertacca, 2015)

$$\begin{aligned} \mathcal{M} = & 1 - 2 \left(1 - \frac{1}{\mathcal{H}\chi_s} \right) \left[\psi_o - (n_s^i v_i)_o \right] + 2 \left(1 - \frac{1}{\mathcal{H}\chi_s} \right) \left[\int_0^{\chi_s} \partial_0(\varphi + \psi) d\chi + \psi_e - (n_s^i v_i)_e \right] \\ & + 2\varphi_e - \frac{2}{\chi_s} \int_0^{\chi_s} (\varphi + \psi) d\chi + 2\kappa, \end{aligned} \quad (4.12)$$

where

$$\kappa = \frac{1}{2} \int_0^{\chi_s} (\chi_s - \chi) \frac{\chi}{\chi_s} \nabla_{\perp}^2 (\varphi + \psi) d\chi \quad (4.13)$$

corresponds to the classical convergence and the differential operator ∇_{\perp}^2 is defined as

$$\nabla_{\perp}^2 = \nabla^2 - (n_s^i \partial_i)^2 - \frac{2}{\chi} n_s^i \partial_i. \quad (4.14)$$

Note that the magnification includes contributions from different physical effects. We refer to the term proportional to $n_s^i v_i$ as ‘Doppler lensing’. In order to model statistical observables (e.g. correlation functions) on small-scales, it is acceptable to replace the two-dimensional Laplacian ∇_{\perp}^2 with the three-dimensional one ∇^2 , so that κ can be expressed in terms of the matter overdensity using the Poisson align. In fact, the effective lensing weight, $(\chi_s - \chi)\chi/\chi_s$, varies on scales comparable to the Hubble radius and the line-of-sight integral that defines κ heavily suppresses the contribution of radial Fourier modes with smaller wavelengths (e.g. Kaiser, 1992). Although this approximation has been implemented to produce full-sky mock catalogues (e.g. Fosalba, Gaztañaga, Castander and Manera, 2008; Fosalba, Gaztañaga, Castander and Crocce, 2015), we do not use it since we want to study galaxy clustering at wide angular separations.

Link with N-body simulations

To evaluate δx^t , $\delta\chi$ and \mathcal{M} , we need to compute the gravitational potentials appearing in eq. (4.6) as a function of space and time. Since we want to apply our results to simulations, we need to derive the potentials starting from the particle distribution in the computer models. This corresponds to using the matter density contrast in the synchronous comoving gauge, i.e. $\delta_{\text{sim}} \equiv \delta_{\text{syn}}$. Fortunately, to linear order in the perturbations and for a pressureless fluid in a universe with Λ CDM background, the source align for ψ in the Poisson gauge can be re-written in terms of δ_{syn} as the standard Poisson align (e.g. Chisari and Zaldarriaga, 2011; Green and Wald, 2012). Therefore, the complete dictionary we use to translate from the simulations to the Poisson gauge is:

$$\varphi = \psi = \phi, \quad \nabla^2 \phi = 4\pi G a^2 \bar{\rho}_m \delta_{\text{sim}}, \quad \text{and } v^i = v_{\text{sim}}^i, \quad (4.15)$$

where G denotes Newton’s gravitational constant and $\bar{\rho}_m$ is the matter density in the FRW background.

4.2.2 Light cones from simulations

In this section we explain the numerical methods we use to implement the theory discussed above and build mock light cones starting from the output of a simulation. We begin with the calculation of the gravitational potential. Following a standard procedure, we use the particle distribution in each snapshot to compute the matter density contrast on a regular Cartesian grid with the cloud-in-cell method (e.g.

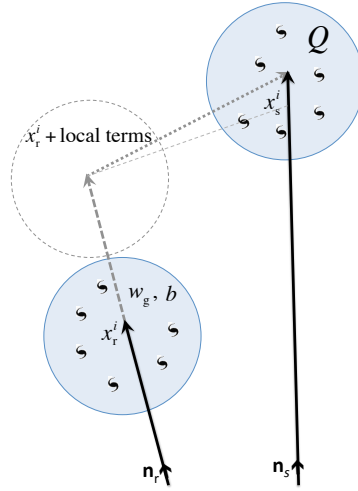


Figure 4.3: Schematic summarising how galaxies (section 4.2.2) or N-body particles (section 4.2.3) are shifted to build the light cones. We first apply the correction due to local terms (dashed arrow) and then compute the shift produced by the non-local contributions (dotted arrow). In runs with low mass resolution, each particle ‘contains’ w_g galaxies. The linear bias coefficient b_1 and w_g are calculated at the real-space position x_r^i while the magnification bias Q is computed at the redshift-space position x_s^i .

Hockney and Eastwood, 1988). We then solve the Poisson equation using a fast Fourier transform and obtain $\phi(\mathbf{x}_r, t)$ as well as its spatial derivatives (by spectral differentiation). Partial time derivatives of the potential are computed with a finite-difference method that combines several consecutive snapshots at fixed comoving position \mathbf{x}_r .

There are a few subtleties at play in the calculation of the galaxy shift and the magnification given in eqs. (4.8), (4.9) and (4.12). All these quantities include local terms evaluated at a specific position and non-local parts that are expressed as integrals along the line of sight to the observer. The integrals should be taken in redshift-space where the photon path is a straight line. Since $|\phi| \ll 1$ and deflections are generally small, we take the integrals in real space which is correct to linear order in the perturbations as in the Born approximation in quantum mechanics. We use the fast voxel traversal algorithm by Amanatides and Woo (1987) to perform the integrals within the grid over which the gravitational potential is evaluated. All functions appearing in the integrands are interpolated in time (here converted into the line-of-sight distance to make sure that everything is computed on the backward light cone of the observer) such that their first derivatives are continuous. Note that the integration path starts at the observer and ends at a fixed redshift-space position which is unknown for all the simulated galaxies. Although to linear accuracy we could use the real-space position of the galaxies, we implement the following procedure which is slightly more accurate (see also fig. 4.3). (i) We evaluate all local terms in eqs. (4.8) and (4.9) and shift the galaxies accordingly. (ii) The non-local terms are estimated with integrals that run from the observer to the position of the galaxy shifted by the local terms. (iii) An additional shift due to the non-local terms is imposed to obtain the final redshift-space position. In principle, steps (ii) and (iii) could be iterated until numerical convergence is achieved. However, this is not necessary in practice since the local terms generate much larger shifts than the non-local ones. This is fortunate because the integration along the line of sight is by far the slowest element of the LIGER code. Magnification is computed along the same lines (similar line-of-sight integrations have been used by M. White and Hu, 2000; Kiessling et al., 2011; Fosalba, Gaztañaga, Castander and Manera, 2008; Fosalba, Gaztañaga, Castander and Croce, 2015, for weak-lensing studies).

Of course we do not shift all the galaxies at all times as this would significantly slow down the code

and also be useless. We first identify the snapshots within which a given galaxy would cross the backward light cone of the observer in the absence of metric perturbations. We then calculate and apply the redshift-space displacements considering a few outputs surrounding this time. Finally, we compute the intersection of the world line of the galaxy with the straight light cone of the observer in redshift space and we save this position and the corresponding magnification.

Each light cone identifies a sub-region in space-time corresponding to a three-dimensional ball in comoving redshift space. Its radius is limited by the box size of the underlying simulation. To avoid replications or spurious correlations due to the periodic boundary conditions applied in cosmological simulations, we limit the radius of the balls to one third of the box size. This way each light cone covers nearly 15 per cent of the simulation volume and we can place five different observers from a single run avoiding intersections.

Galaxy mocks with LIGER

Whenever galaxy positions, velocities and luminosities are available (from either a hydrodynamic simulation or a semi-analytic model based on an N-body run), we modify the worldlines of the galaxies according to eqs. (4.4) and (4.5). The different components of the shift in space-time are given in eqs. (4.8) to (4.10) where $(n_s^i v_i)_e$ coincides with the radial peculiar velocity of the galaxy in the simulation and the gravitational potential ϕ is generated by the total matter content. Eventually, we determine the coordinates of the event at which the modified worldline of the galaxy crosses the light cone of the observer. The main differences between LIGER and the standard method used to build mock catalogues in redshift space are twofold. First of all, LIGER considers four dimensional distortions affecting both space and time. Furthermore, it includes several additional terms beyond the usual radial displacement $\mathcal{H}^{-1}(n_s^i v_i)_e$.

4.2.3 Light cones based on dark-matter-only simulations

The LIGER method is general and can be used with all kinds of cosmological simulations. However, the transverse size of the light cones rapidly increases with redshift so that very large simulation boxes are required to cover wide opening angles. In this case, running simulations with sufficient spatial and mass resolution to follow galaxy formation is computationally challenging. A popular method to avoid this problem is to tile replicate the simulation box to cover the light cone up to larger redshifts. Although this technique could be applied to LIGER, we decide not to implement it. Tile replications introduce spurious artefacts and alter clustering statistics on large scales (e.g. Blaizot et al., 2005). This would be a major drawback for a code which includes linear relativistic effects and aims at exploiting the very large scales that will be surveyed by the observational facilities of the next generation. Instead, we use dark-matter only simulations with very large computational boxes. For this reason, LIGER has the option to shift the dark-matter particles themselves and create the galaxy density field a posteriori. The problematic step is to account for galaxy biasing. We illustrate how our implementation works by reasoning in terms of continuous densities.

To linear order in the perturbations, we can write the matter density contrast in redshift space as

$$\delta_s = \delta_{\text{sim}} + \delta_{\text{RSD}} , \quad (4.16)$$

where we have conveniently collected the corrections due to the metric distortions into the term (Yoo, 2009; Yoo, Fitzpatrick and Zaldarriaga, 2009; Bonvin and Durrer, 2011; Challinor and Lewis, 2011;

Jeong, Schmidt and Hirata, 2012)

$$\delta_{\text{RSD}} = -\left(\frac{\partial_0 \mathcal{H}}{\mathcal{H}^2} + \frac{2}{\chi_s \mathcal{H}}\right) \delta \ln a + \psi_e - 2\varphi_e + \frac{(\partial_0 \varphi)_e}{\mathcal{H}} + 3\mathcal{H}\phi_v - \frac{1}{\mathcal{H}} \left[n_s^i \partial_i (n_s^j v_j) \right]_e + \frac{2}{\chi_s} \int_0^{\chi_s} (\varphi + \psi) d\chi - 2\kappa, \quad (4.17)$$

in which ϕ_v is the linear velocity potential³ at the galaxy position (i.e. $v_i = \partial_i \phi_v$) and the apparent redshift change $\delta \ln a = \delta z / (1 + z)$ due to the perturbations is

$$\delta \ln a = \psi_o - (n_s^i v_i)_o - \psi_e + (n_s^i v_i)_e - \int_0^{\chi_s} \partial_0 (\varphi + \psi) d\chi. \quad (4.18)$$

To the same accuracy, galaxy clustering in redshift space can be modelled in terms of three redshift-dependent bias parameters, b_1 , Q and \mathcal{E} , encoding information about different properties of the galaxy population under study, namely (Challinor and Lewis, 2011; Jeong, Schmidt and Hirata, 2012)

$$\delta_{\text{g},s} = b_1 \delta_{\text{sim}} + Q(\mathcal{M} - 1) + \mathcal{E}(\delta \ln a - \mathcal{H}\phi_v) + \delta_{\text{RSD}}. \quad (4.19)$$

The expression above assumes that the intrinsic perturbation in the galaxy number density is $\delta_{\text{g},r} = b_1 \delta_{\text{sim}}$ with b_1 the linear bias parameter. It also considers that lensing magnification alters the observed number density of galaxies. This effect is quantified by the magnification-bias parameter

$$Q = -\left. \frac{\partial \ln \bar{n}_g}{\partial \ln L} \right|_{L=L_{\text{lim}}}, \quad (4.20)$$

where $\bar{n}_g(> L)$ denotes the comoving number density of galaxies with luminosity larger than L and the derivative is evaluated at the (redshift-dependent) limiting luminosity of the survey.⁴ Finally, eq. (4.19) takes into account that the comoving number density of galaxies in the sample might change with redshift. This phenomenon is described by the ‘evolutionary bias’ parameter

$$\mathcal{E} = -\frac{\partial \ln \bar{n}_g}{\partial \ln(1+z)}. \quad (4.21)$$

Our goal is to connect $\delta_{\text{g},s}$ with the particle density in the N-body simulations. For simplicity, we assume that $|\mathcal{H}\phi_v| \ll |\delta \ln a|$ and neglect the velocity potential which could influence galaxy clustering only on scales comparable with the Hubble radius. Then eqs. (4.16) and (4.19) give

$$\delta_{\text{g},s} = (b_1 - 1)\delta_{\text{sim}} + \delta_s + \mathcal{E} \delta \ln a + Q(\mathcal{M} - 1), \quad (4.22)$$

which can be used to derive the local galaxy number density $n_{\text{g},s} = \bar{n}_g (1 + \delta_{\text{g},s})$. By expressing the matter fields in terms of the density of N-body particles, i.e. $\delta_{\text{sim}} + 1 = n_{\text{sim},r} / \bar{n}_{\text{sim}}$ and $\delta_s + 1 = n_{\text{sim},s} / \bar{n}_{\text{sim}}$, we can write

$$n_{\text{g},s} = (b_1 - 1) (w_g n_{\text{sim},r} - \bar{n}_g) + w_g n_{\text{sim},s} + \bar{n}_g \mathcal{E} \delta \ln a + \bar{n}_g Q(\mathcal{M} - 1), \quad (4.23)$$

where $w_g = \bar{n}_g / \bar{n}_{\text{sim}}$ denotes the mean number of galaxies per simulation particle at a given redshift.

³ This term originates because δ_{sim} is defined in the synchronous comoving gauge while all the rest is set in the Poisson gauge.

⁴ For simplicity, we assume that the list of targets for spectroscopic observations is flux limited. In case also a size cut is applied, another redshift-dependent function should be added to Q since gravitational lensing also alters the size of galaxy images (Schmidt et al., 2009).

The products $w_g n_{\text{sim},r}$ and $w_g n_{\text{sim},s}$ rescale the unbiased density fluctuations in the simulations to the galaxy mean density. The magnification term in eq. (4.23) reflects the relative change of the galaxy counts per particle which is proportional to $w_Q = \mathcal{M}^Q$. For $|\mathcal{M} - 1| \ll 1$, we can thus write $w_g w_Q n_{\text{sim},s} = w_g [\mathcal{Q}(\mathcal{M} - 1) + 1] n_{\text{sim},s}$, so that

$$n_{g,s} = (b_1 - 1) (w_g n_{\text{sim},r} - \bar{n}_g) + w_g w_Q n_{\text{sim},s} + \bar{n}_g \mathcal{E} \delta \ln a. \quad (4.24)$$

By using the definition of \mathcal{E} and linearising, $w_g(z) w_Q(\hat{\mathbf{n}}_s, z) n_{\text{sim},s}(\hat{\mathbf{n}}_s, z) + \bar{n}_g(z) \mathcal{E} \delta \ln a$ coincides with $w_g(\bar{z}) w_Q(\hat{\mathbf{n}}_s, \bar{z}) n_{\text{sim},s}(\hat{\mathbf{n}}_s, \bar{z})$ where $\bar{z} = z - \delta z$ is the redshift in absence of perturbations (note that to first order it is equivalent to evaluate w_Q at z or \bar{z}). Eventually, making explicit the arguments of all functions, we obtain

$$n_{g,s}(\hat{\mathbf{n}}_s, z) = [b_1(\bar{z}) - 1] [w_g(\bar{z}) n_{\text{sim},r}(\hat{\mathbf{n}}_r, \bar{z}) - \bar{n}_g(z)] + w_g(\bar{z}) w_Q(\hat{\mathbf{n}}_s, \bar{z}) n_{\text{sim},s}(\hat{\mathbf{n}}_s, \bar{z}). \quad (4.25)$$

We use this expression to compute $n_{g,s}$ from the simulations (see fig. 4.3 for a schematic representation). In practice, we weigh the shifted and unshifted dark-matter particles according to eq. (4.25). Once the light cone for the matter has been constructed, it is very fast to build the galaxy mocks for many different galaxy populations. This corresponds to changing the functions $w_g(z)$, $b_1(z)$ and $\mathcal{Q}(z)$.

Doppler terms

Isolating the terms proportional to the velocity field in the right-hand side of eq. (4.19) we obtain

$$\delta_{g,v} = -\frac{1}{\mathcal{H}} \left(\frac{\partial n_s^i v_i}{\partial \chi_s} \right)_e - \frac{\alpha(\chi_s)}{\mathcal{H} \chi_s} \left[(n_s^i v_i)_e - (n_s^i v_i)_o \right], \quad (4.26)$$

where $\partial/\partial \chi_s = n^i \partial_i$,

$$\alpha(\chi_s) = \gamma_0 + \gamma_1 \mathcal{H} \chi_s \quad (4.27)$$

and, assuming a flat Λ CDM universe,

$$\gamma_0 = 2(1 - \mathcal{Q}) \quad \text{and} \quad \gamma_1 = 1 - \frac{3}{2} \Omega_m(z) - \mathcal{E} + 2\mathcal{Q}. \quad (4.28)$$

Equation (4.26) coincides with the seminal result for the linear redshift-space distortions derived by Kaiser (1987). In the classical literature, the function α is often written as $\alpha = 2 + \partial \ln \bar{n}_g / \partial \ln \chi_s$ (Kaiser, 1987; Zaroubi and Hoffman, 1996; Hamilton, 1998). Taking into account that we observe galaxies on our past light-cone reveals that several physical effects influence α (see also McDonald, 2009; Yoo, 2009; Bertacca et al., 2012; Raccanelli, Bertacca, Jeong et al., 2016). Equation (4.28), get contributions from geometric distortions, redshift evolution (or redshift-dependent selection effects), Doppler magnification and cosmic acceleration.

Following a standard practice in cosmology, we label the expression proportional to α in eq. (4.26) with the collective name of Doppler terms. Their contribution is usually neglected in clustering studies. In fact, for an ideal galaxy sample with $\alpha \simeq 2$ and if the depth of a galaxy redshift survey is much larger than the comoving wavelength of interest, the Doppler induced $\delta_{g,v}$ is heavily suppressed (due to the χ_s^{-1} scaling) with respect to the signal generated by the radial velocity gradient which is always comparable to density perturbations (Kaiser, 1987). This reasoning relies upon the distant-observer approximation. However, it has been shown that the Doppler corrections can alter the galaxy autocorrelation function

at large angular separations in a significant way (Pápai and Szapudi, 2008; Raccanelli, Samushia and Percival, 2010). In this case, the two terms on the right-hand side of eq. (4.26) can be of comparable sizes. Moreover, Q and \mathcal{E} can drive α sensibly away from 2 and thus enhance the chance of detecting the Doppler terms from observational data. We will return to this issue in section 4.3.6.

4.3 Examples

We present two sample applications of LIGER: first, we estimate the importance of magnification bias in an Euclid-like survey and then we investigate the detectability of Doppler terms in a low-redshift galaxy catalogue based on the concept of the Square Kilometre Array (SKA). To begin with, we introduce the numerical simulations and the statistical methods we use. We then describe the specifications for the surveys and discuss our results in sections 4.3.4 and 4.3.6.

4.3.1 N-body simulations

We run a large number of cosmological N-body simulations using the L-PICOLA code (Howlett, Manera and Percival, 2015) and subsequently apply LIGER to their outputs. L-PICOLA is an implementation of the COLA method (Tassev, Zaldarriaga and Eisenstein, 2013) in which the large-scale dynamics is solved using second-order Lagrangian perturbation theory while a particle-mesh algorithm is used for the small scales. This technique is orders of magnitude faster than standard N-body codes and accurately simulates the clustering of matter on large scales. This makes it an ideal tool to build large mock catalogues for studying galaxy clustering although it does not resolve the internal dynamics of dark-matter haloes.

Our simulations include 1024^3 particles in a periodic cube with side length L . In order to cover the relevant volumes, we use very large values of L_{box} , namely $12h^{-1}$ Gpc for our first application and $5h^{-1}$ Gpc for the second one. This way we obtain 165 light cones extending to redshift 2.3 for the Euclid-like mocks and 125 light cones extending to redshift 0.6 for the more local mocks. In all cases, the gravitational potential in LIGER is evaluated on a grid with 512^3 cells.

An illustrative example is presented in fig. 4.4 (using the 'total' galaxy sample introduced in section 4.3.6). In the upper part, we show wedge maps of the galaxy distribution in real- (top-left) and redshift-space (top-right) colour coded according to the density contrast. The figures at the bottom isolate different effects. On the left-hand side, we show the redshift-space distortions due to the Doppler terms. This signal is dominated by the squashing of the density contours due to the coherent infall of matter onto large-scale structures. On the right-hand side, we map the remaining distortions, $\delta_{g,s} - b_1\delta_{\text{sim}} - \delta_{g,v}$. The resulting signal is patchy but the integrated terms in eq. (4.17) produce correlations along the line of sight. Note that the maps on the bottom show very different patterns and characteristic amplitudes.

It is worth stressing that LIGER is completely general and can be applied to the output of any N-body code. Here we use L-PICOLA because it is ideal for our purposes. Note that we do not make use of the built-in feature to build light cones on the fly implemented in L-PICOLA. However LIGER could be merged with it in the future.

4.3.2 Angular power spectra

Our examples focus on large-scale galaxy clustering that we quantify in terms of the angular power spectrum. We first divide our mock light cones into multiple redshift bins and measure the projected galaxy number density contrast on the sky, $\sigma_g^{(i)}(\theta)$, for each of them (labelled by the index i). We then

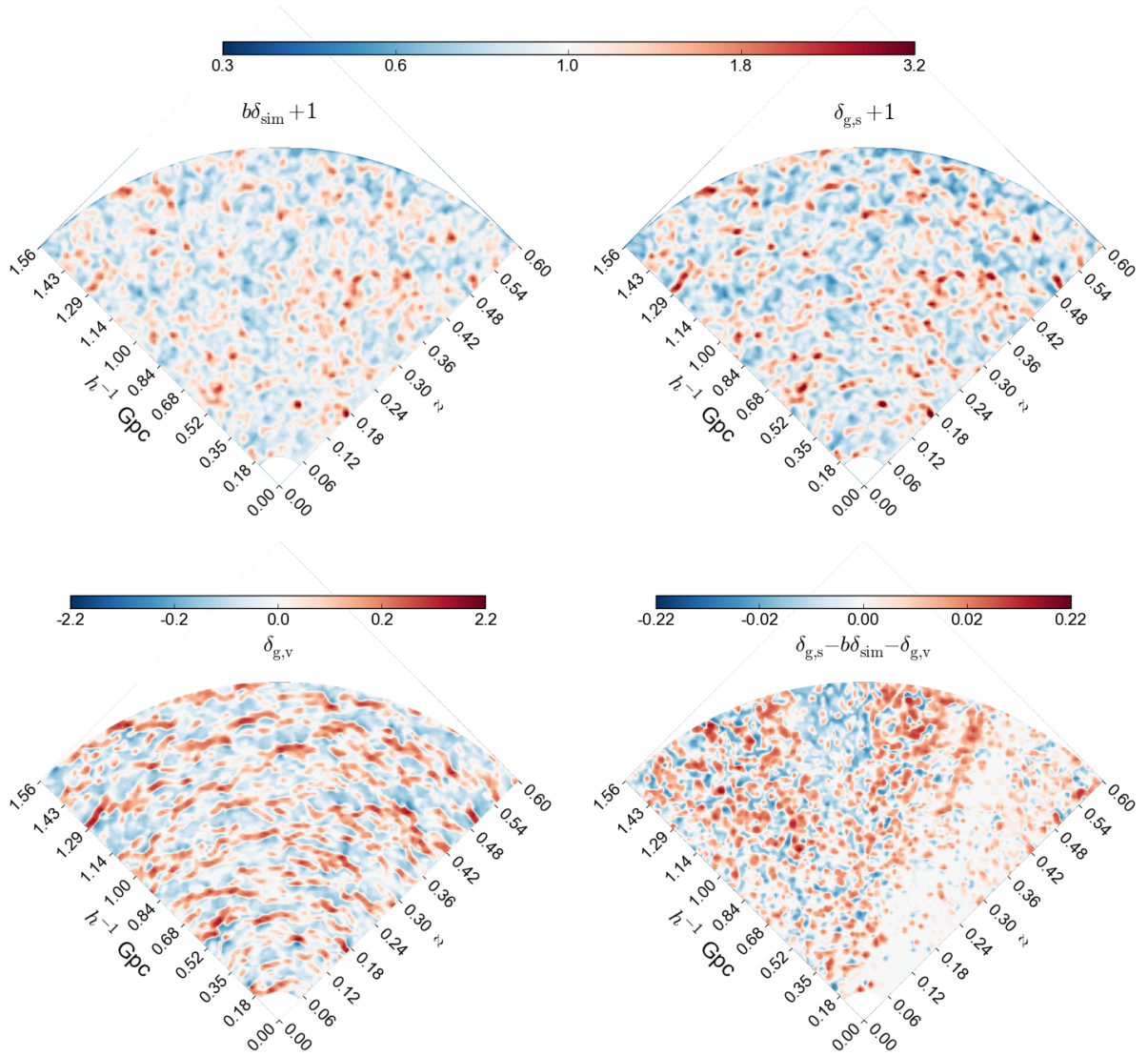


Figure 4.4: Wedge plots extracted from a sample like cone. The top images show $b_1\delta_{\text{sim}}$ and $\delta_{g,s}$. In all cases, the maps show the galaxy density contrast projected onto the plane of the page within a slice of 5 arcmin thickness. The observer is located at the vertex of the wedge and the labels indicate redshift and comoving distance. The bottom panels highlight different contributions to the redshift-space distortions as described in detail in the main text (note the symmetric log-scale).

decompose $\sigma_g^{(i)}(\boldsymbol{\theta})$ in spherical harmonics, $\sigma_g^{(i)}(\boldsymbol{\theta}) = a_{lm}^{(i)} Y_{lm}(\boldsymbol{\theta})$, with

$$a_{lm}^{(i)} = \int d^2\boldsymbol{\theta} \sigma_g^{(i)}(\boldsymbol{\theta}) Y_{lm}^*(\boldsymbol{\theta}), \quad (4.29)$$

and measure the angular auto- and cross-spectra between all redshift bins using

$$C_l^{(ij)} = \frac{1}{2l+1} \sum_{m=-l}^l a_{lm}^{(i)} a_{lm}^{(j)*}. \quad (4.30)$$

In practice, we use the Healpix algorithm (Górski et al., 2005) to build digitized maps of $\sigma_g^{(i)}(\theta)$ from which we calculate the power spectra. In all cases, we make sure that the pixel size does not affect our results in the range of scales of interest. The galaxy density in a pixel is computed from the distribution of the N-body particles as described in section 4.2.3. Since our particles are rather massive ($1.2 \times 10^{14} h^{-1} M_\odot$ for the $12 h^{-1}$ Gpc boxes and $8.8 \times 10^{13} h^{-1} M_\odot$ for the $5 h^{-1}$ Gpc ones), each of them ‘contains’ multiple galaxies (i.e. $w_g \sim 10$). This is unavoidable given the extremely large volumes covered by our simulations and the obvious limitations in computing time and memory usage. Although the resulting overdensity field has increased shot noise with respect to the actual galaxy distribution, our statistical analysis is not influenced by it. In fact, we never attempt to subtract shot noise from the power spectra as our study is based on the comparison of different sets of mock catalogues. Even more importantly, in all cases, shot noise is by far subdominant with respect to the sample and cosmic variance of the clustering signal we are interested in (note that our main results are based on the analysis of cross statistics between galaxy samples at different redshift).

We also take into account that most survey geometries do not cover the full sky and exclude wide regions surrounding the galactic plane. In order to simulate a realistic setting, we mask an appropriate amount of the sky around the equator of the observer and consider two distinct regions around the poles covering a fraction f_{sky} of the celestial sphere. Spherical harmonics are not orthogonal over finite solid angles and the pseudo power spectrum $\tilde{C}_l^{(ij)}$ measured from the cut sky does not coincide with $\hat{C}_l^{(ij)}$ (Peebles, 1973; Wandelt, Hivon and Górski, 2001). We use the standard method by Hivon et al. (2002) to construct an unbiased estimate of the full-sky spectra $\hat{C}_l^{(ij)}$ which is obtained multiplying $\tilde{C}_l^{(ij)}$ by the inverse of a mode-mode coupling matrix that depends on the survey mask.

4.3.3 Statistical analysis

Our sample applications aim at quantifying the detectability of some specific redshift-space effects from measurements of two-point statistics. We assume that we can perfectly model the different contributions to the clustering signal and check whether including or excluding some of them improves or worsen the fit to the mock data including the full physics. In particular, we proceed as follows. We isolate a particular effect (say, e.g., magnification bias) and denote its expected partial contribution to the model galaxy power spectrum as $C_l^{(A)}$ so that its complementary part is $C_l^{(B)} = C_l - C_l^{(A)}$ (here the superscripts (ij) indicating the redshift bins are understood to simplify notation). We then fit the power spectra extracted from our mock catalogues with the model $M_l = \epsilon C_l^{(A)} + C_l^{(B)} = C_l + (\epsilon - 1)C_l^{(A)}$ where the coefficient ϵ can only assume the values zero or one. The question we want to address is to what statistical significance the data favour $\epsilon = 1$, i.e. how necessary it is to add $C_l^{(A)}$ to the model in order to fit the data \hat{C}_l . All this boils down to comparing the quality of the fit obtained using $\epsilon = 0$ and $\epsilon = 1$. This exercise can be performed following different statistical procedures which give very similar results.

Frequentist approach: simple hypotheses (SH)

We want to test the null hypothesis $H_0 : \epsilon = 0$ against the alternative hypothesis $H_1 : \epsilon = 1$. Let \mathcal{L}_0 and \mathcal{L}_1 denote the likelihood of the data under H_0 and H_1 , respectively. Based on the Neyman-Pearson lemma, the likelihood-ratio statistic $\Gamma = \mathcal{L}_0/\mathcal{L}_1$ provides the most powerful test for two simple hypotheses. If the data do not support H_0 , then the likelihood ratio should be small. Thus, we reject the null hypothesis with confidence level ς , if $\Gamma \leq \omega$, where ω is a constant such that the probability $P(\Gamma \leq \omega|H_0) = \varsigma$. In order to determine ς it is thus necessary to determine the probability distribution of the test statistic under H_0 . Working with the log-likelihood $\chi^2 = -2 \ln \mathcal{L}$, the rejection condition becomes $\Delta\chi^2 = \chi_1^2 - \chi_0^2 > \ln \omega$. Assuming Gaussian errors for the angular power spectrum with covariance matrix

$\Sigma_{lm} = \langle \hat{C}_l \hat{C}_m \rangle - \langle \hat{C}_l \rangle \langle \hat{C}_m \rangle$, we find that, under H_0 , $\Delta\chi^2$ follows a Gaussian distribution with mean

$$\mu = C_l^{(A)} \Sigma_{lm}^{-1} C_m^{(A)} \quad (4.31)$$

and variance 4μ (see appendix B). Therefore, we reject H_0 at the 95 per cent confidence level if $\Delta\chi^2 > \mu + 3.29 \sqrt{\mu}$. The coefficient 3.29 should be replaced with 4.652 to get a 99 per cent confidence level. A formal 5σ rejection is obtained for $\Delta\chi^2 > \mu + 10 \sqrt{\mu}$.

It is worth noticing that, if the covariance matrix of the measurements does not depend on ϵ , then the expected value of Γ under H_1 is $E(\Gamma|H_1) = -E(\Gamma|H_0) = -\mu$. Therefore, the mean values $E(\Gamma|H_1)$ and $E(\Gamma|H_0)$ will be separated by more than \mathcal{N} standard deviations of the Γ distribution only if $\sqrt{\mu} > \mathcal{N}$. This is why $\sqrt{\mu}$ is often denoted as the signal-to-noise ratio, S/N , of $C_l^{(A)}$. On the other hand, if the covariance depends on ϵ , then $E(\Gamma|H_1) \neq -E(\Gamma|H_0)$ and the dispersions around the mean of Γ under H_0 and H_1 will be different (see appendix B).

Frequentist approach: composite hypothesis (CH)

We also consider a generalized likelihood-ratio test with a compound alternative hypothesis. In this case we contrast the null hypothesis $H_0 : \epsilon = 0$ with $H_1 : \epsilon \neq 0$. Let \mathcal{L}_{\max} be the maximum value of the likelihood of the data when ϵ is varied (between 0 and 1) and \mathcal{L}_0 the corresponding likelihood under the null hypothesis. We form the ratio $\Gamma = \mathcal{L}_0 / \mathcal{L}_{\max}$ which is always between 0 and 1. We assess the statistical significance of the test by comparing $\Delta\chi^2 = -2 \ln \Gamma$ to the chi-square distribution with one degree of freedom (as we only tuned one parameter to determine \mathcal{L}_{\max}). Basically we convert $\Delta\chi^2$ into the corresponding percentile of the chi-square distribution. This is the confidence level at which the null hypothesis can be rejected. In this case, 95 (99) per cent confidence corresponds to a critical value of $\Delta\chi^2 = 3.84$ (6.64).

Fisher information

An alternative approach consists of quantifying the Fisher information that the angular power spectrum carries about ϵ (which, in this case, is assumed to be a real number). Assuming Gaussian errors, we obtain that the Fisher ‘matrix’ for ϵ is

$$F = \partial_\epsilon M_l \Sigma_{lm}^{-1} \partial_\epsilon M_m = C_l^{(A)} \Sigma_{lm}^{-1} C_m^{(A)} \equiv \mu \quad (4.32)$$

(we adopt the ‘field’ perspective as in Carron, 2013). It follows from the Cramèr-Rao inequality that $\mu^{-1/2}$ gives a lower bound for the expected uncertainty on ϵ (i.e. the mean curvature of the likelihood function $\mathcal{L}(\epsilon)$ at its peak). Therefore, $\sqrt{\mu}$ corresponds to the signal-to-noise ratio with which ϵ can be measured.

Bayesian approach (BA)

Assuming a flat prior for ϵ , the posterior probabilities for $\epsilon = 0$ and $\epsilon = 1$ are $P_0 = \frac{\mathcal{L}_0}{\mathcal{L}_0 + \mathcal{L}_1}$ and $P_1 = \frac{\mathcal{L}_1}{\mathcal{L}_0 + \mathcal{L}_1}$, respectively. The Bayes factor, $K = P_0 / P_1$, thus corresponds to the likelihood ratio $\mathcal{L}_0 / \mathcal{L}_1$. According to the Jeffrey scale, there is strong (decisive) evidence against H_0 if $K > 10$ (100) which gives $\Delta\chi^2 > 4.605$ (9.21). Using the alternative scale by Kass and Raftery gives very strong evidence for $\Delta\chi^2 > 10$.

Likelihood estimation

All the statistical methods listed above require the calculation of the likelihood function for ϵ in each mock realisation. To do this, we need a model and the covariance matrix for the power spectra (we assume Gaussian measurement errors). We build an ‘exact’ and unbiased model by averaging the angular power spectra obtained for all our mock light cones. Since there are no particularly deviant realizations, the average spectra are smooth. In parallel, we use the maximum-likelihood estimator to get a first approximation for the covariance matrix, $\hat{\Sigma}_{lm}$. It is well known that the precision matrix obtained by inverting $\hat{\Sigma}_{lm}$ is not very accurate. Although we make sure to consider enough mock skies so that the covariance matrix of our data vector is invertible, it still contains considerable noise. We thus use the shrinkage method (Schäfer and Strimmer, 2005) to reduce the noise in $\hat{\Sigma}_{lm}$. As a target we use a diagonal matrix which is always compatible with our estimates.

4.3.4 Magnification bias in a Euclid-like survey

As a simple application of the LIGER method, we discuss the detectability of magnification bias in a Euclid-like survey. Related work has been presented by Di Dio, Durrer et al. (2014) and Montanari and Durrer (2015). These authors focused on the Fisher information matrix as a forecasting tool, while we base our study on the statistical analysis of a large number of mock catalogues.

Euclid spectroscopic sample

Euclid is a medium-class mission of the European Space Agency planned for launch in 2020. It will map the distribution of star-forming galaxies through their redshifted H α emission in the regions with galactic

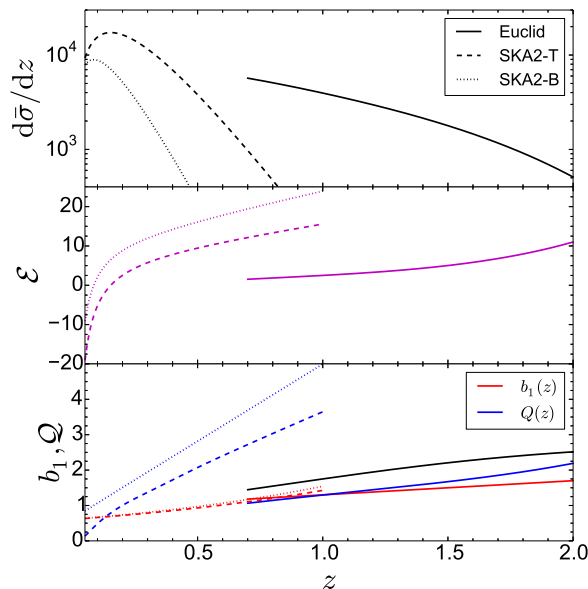


Figure 4.5: Expected characteristics of the Euclid (solid) and SKA2 redshift surveys. In the latter case we consider two flux sensitivities: 23 (dashed) and 60 μ Jy (dotted). The mean galaxy number counts per square-degree and redshift (top), the evolutionary bias (middle), and the linear and magnification bias parameters (bottom) are shown as a function of redshift.

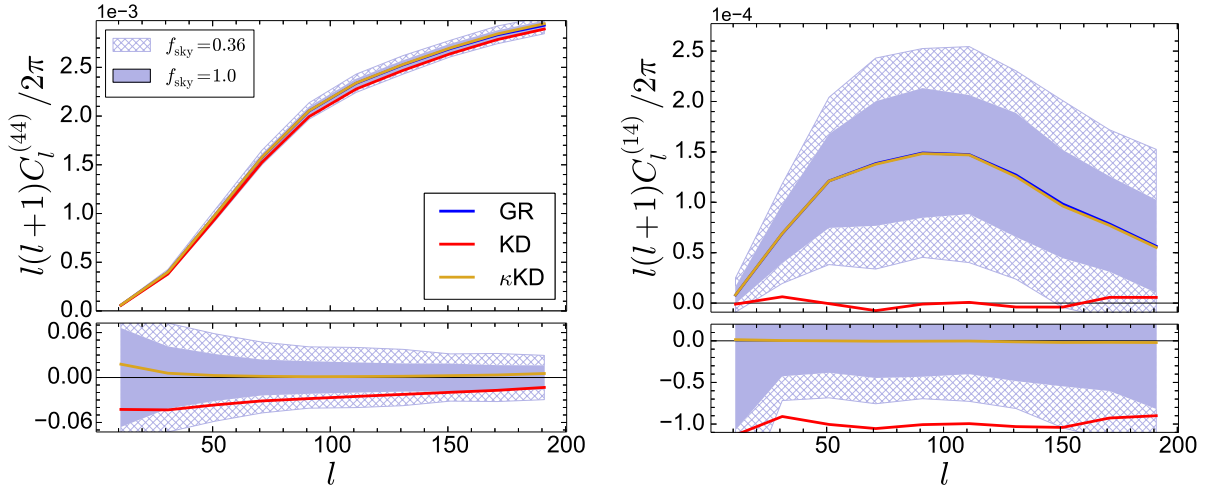


Figure 4.6: Angular power spectra for the galaxy distribution in an Euclid-like survey split into four equally populated redshift bins. The left-hand panel refers to the auto-spectrum of the highest-redshift bin while the right-hand panel shows the cross-spectrum between the lowest-and the highest-redshift bins. The blue curves show the signal averaged over 165 mock catalogues that include relativistic effects to linear order in the perturbations (GR). The shaded regions surrounding them indicate the standard deviation of the measurements for full-sky (light blue) and Euclid-like (cross pattern) mocks. The red curves are obtained considering only the redshift-space distortions generated by the Kaiser and Doppler effects (KD) but $\mathcal{M} = 1$. The yellow ones (which basically coincide with the blue ones) also consider magnification bias due to weak gravitational lensing. All spectra are averaged in bandpowers with $\Delta l = 20$. The bottom panels highlight the relative difference of the KD and kKD models with respect to the GR signal.

latitude larger than 30 degrees ($f_{\text{sky}} = 0.36$). Low-resolution spectroscopy in the near infrared will be used to measure galaxy redshifts in the range $0.7 < z < 2.0$.

The specifics of the Euclid redshift survey depend on the poorly known properties of emission-line galaxies at moderate redshifts. In order to calculate the redshift distribution of the galaxies as well as $Q(z)$ and $\mathcal{E}(z)$ we use the redshift-dependent luminosity function by Pozzetti et al. (2016, model two) and assume a limiting line flux of 3.0×10^{-16} erg cm $^{-2}$ s $^{-1}$. Further, we use the linear fit for the galaxy bias $b_1(z)$ given in Pozzetti et al. (2016). Our results are summarised in fig. 4.5.

Angular power spectra

We split each of the 165 Euclid mocks into four redshift bins (with boundaries 0.7, 0.86, 1.06, 1.35, 2.0) that on average contain the same number of galaxies ($\sim 1.6 \times 10^7$). We then compute the auto- and cross-power spectra among all bins. To reduce noise we do not resolve individual multipoles and use ten bandpowers with $\Delta l = 20$. Figure 4.6 shows $C_l^{(44)}$ (left-hand panel) and $C_l^{(14)}$ (right-hand panel), where the indices 1 and 4 indicate the lowest and highest redshift bin, respectively. The blue curves correspond to the mean power spectra extracted from the mock catalogues that include all redshift-space effects (hereafter GR). Note that the auto-spectrum is more than ten times larger than the cross-spectrum. The shaded regions indicate the standard deviation of the spectra over the 165 realisations in the Euclid-like (cross pattern) and in the full-sky (light blue).

It is interesting to analyse the different contributions to the spectra. The most commonly considered source of redshift-space distortions is the so-called Kaiser effect due to the gradient of the galaxy radial peculiar velocities, i.e. the first term on the right-hand side in eq. (4.26). In our approach, this correction

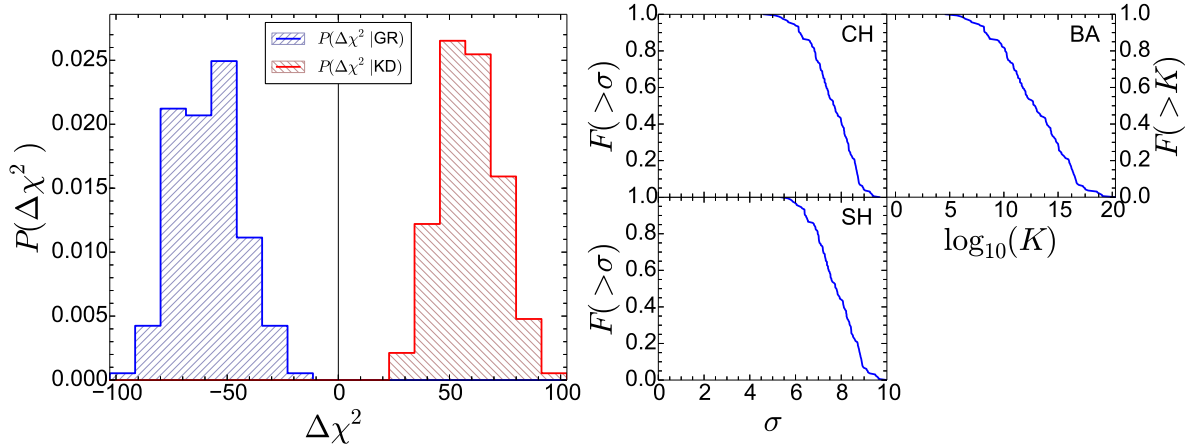


Figure 4.7: In order to explain the origin of the clustering signal, we consider two sets of Euclid-like mock catalogues (each one containing the same 165 skies) in which we arbitrarily switch on and off some effects. In the first group, redshift-space distortions are only generated by galaxy radial peculiar velocities (KD) whereas the second suite includes general-relativistic effects to linear order in the perturbations (GR). We fit the angular power spectra $C_l^{(ij)}$ extracted from each mock catalogue with two models that have been obtained averaging the clustering signal within each series of catalogues. We then compute the change in χ^2 for every sample. In the left-hand panel, we compare the histogram of $P(\Delta\chi^2|\text{GR})$ (on the left) versus $P(\Delta\chi^2|\text{KD})$ (on the right). The fact that the histograms are widely separated and do not overlap implies that an Euclid-like survey will clearly detect redshift-space distortions that are not included in the KD model. This is quantified in the right-hand panel where we plot the fraction $F(> x)$ of the GR mocks within which the KD model is rejected at a confidence level higher than x using different statistical tests (for further details see section 4.3.3).

derives from the $(n_s^i v_i)_e$ terms in the particle shift and is always mixed with the Doppler contribution. In order to evaluate the relative importance of the velocity-induced shift, we build a new set of Euclid mock catalogues (based on the same N-body simulations as the GR ones) in which we replace eqs. (4.8), (4.9) and (4.12) with $\delta\chi = -(n_s^i v_i)_e / \mathcal{H}$, $\delta x^i = 0$ and $\mathcal{M} = 1$, respectively (this is the standard way to implement redshift-space distortions in simulations and omits the terms proportional to Q in α). We dub these light cones KD, a short for ‘Kaiser and Doppler’. The red curves in fig. 4.6 show the mean clustering signal extracted from the KD mocks (which from now on we refer to as the KD model for the auto- and cross-spectra). The lack of power with respect to the GR results is evident: $C_l^{(44)}$ is underestimated by ~ 3 per cent and $C_l^{(14)}$ oscillates around zero. In the left-hand panel of fig. 4.7, we demonstrate that these differences are highly significant. The histogram on the left-hand side displays the distribution of $\Delta\chi^2 = \chi_{\text{GR}}^2 - \chi_{\text{KD}}^2$ obtained fitting all the $C_l^{(ij)}$ from the 165 GR mocks with the GR and the KD models, respectively. Similarly, the histogram on the right-hand side shows the corresponding distribution for the KD mocks. Based on the fact that the histograms are well separated, we conclude that an Euclid-like survey should be able to detect the signature of redshift-space distortions that are not included in the KD model. To better quantify how inaccurately the KD model fits the mock GR data, we apply the statistical tests we have introduced in section 4.3.3. The cumulative distribution over the 165 GR mocks of the significance with which the KD model is rejected is shown in the right-hand panel of fig. 4.7. Typically the data disfavour the simpler model with 8σ confidence or a Bayes factor of 10^{13} . The precise statistical significance of this result is very sensitive to the assumed $Q(z)$. For instance, it increases to 14σ if we use model 3 from Pozzetti et al. (2016).

This result is not surprising. It is well known that weak gravitational lensing alters the observed clustering signal in deep magnitude-limited surveys (E. L. Turner, 1980). The influence of lensing is

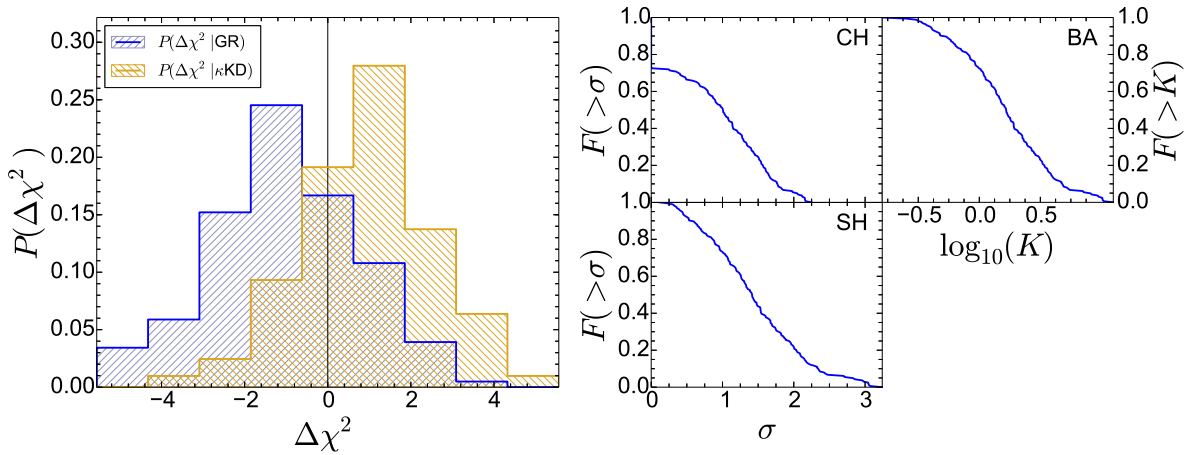


Figure 4.8: The same as fig. 4.7, but for the κKD model, i.e. including the effect of the convergence. For the CML test, 28 per cent of the GR mocks have $\Delta\chi^2 > 0$ and therefore favour the κKD model.

twofold: (i) the actual magnitude limit of the survey fluctuates on the sky and with redshift; (ii) the surface density of galaxies on the sky (and thus their volumetric density in redshift space) is changed. The last two terms in eq. (4.17) and the Q -dependent term in eq. (4.19) summarise the net effect on the galaxy overdensity field. Following some early detections (Bartelmann and P. Schneider, 1994; Norman and Williams, 2000), the weak-lensing effect on clustering has been measured with high statistical significance (8σ) by cross correlating samples of distant quasars and background galaxies in the Sloan Digital Sky Survey (Scranton et al., 2005). Given this premise, we build a third set of mock light cones (labelled κKD) in which we account for the redshift-space distortions due to both the peculiar velocities and weak lensing assuming that the convergence is the only source of magnification, i.e. $\mathcal{M} = 1 + 2\kappa$. To account for both magnification bias and the volume corrections due to lensing, we simply weigh the N-body particles proportionally to $[\mathcal{M}(\hat{\mathbf{n}}_s, z)]^{Q(z)-1}$ (instead of the standard $[\mathcal{M}(\hat{\mathbf{n}}_s, z)]^{Q(z)}$) and use the same shifts as in the KD mocks.⁵ The resulting spectra (yellow lines in fig. 4.6 which are barely distinguishable by eye from the blue ones) provide an excellent fit to the $C_l^{(ij)}$ derived from the GR mocks. This suggests that the measurable differences between the full signal and the KD model are due to gravitational-lensing convergence.

In order to make a quantitative analysis and investigate whether other (more subtle and interesting) light-cone effects (e.g. Doppler lensing and potential terms) might be detectable with a Euclid-like survey, we once again resort to statistics. Figure 4.8 shows that, in almost all mock GR realizations, the null hypothesis that the data are generated under the κKD model cannot be rejected to any meaningful confidence level. Although only few of the skies presents deviations larger than 3σ , fig. 4.8 indicates that the GR mocks contain an additional signal (most likely due to Doppler lensing) which is however comparable than the noise. We thus conclude that no additional sources of redshift-space distortions beyond the Kaiser effect, Doppler contributions and magnification bias can be detected from the angular clustering of all galaxies with spectroscopic redshifts in a Euclid-like survey divided in four equally-populated redshift bins. This, of course, does not prevent the development of dedicated probes to isolate additional contributions, in particular combining photometric and spectroscopic data to define multiple tracers of the large-scale structure along the lines of the forthcoming discussion in section 4.3.6.

⁵ The additional \mathcal{M}^{-1} results from a volume distortion due to lensing. To test the consistency of our code, we evaluate this effect in two ways. In the GR mocks the change of volume is realized by the particle shift. Alternatively, we weigh particles proportionally to \mathcal{M}^{-1} in the KD mocks. We find the same result.

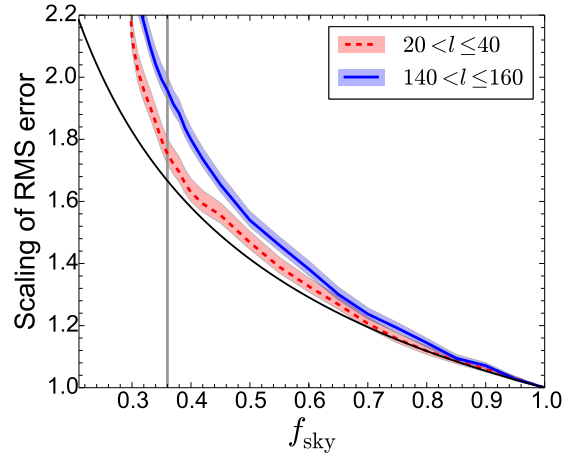


Figure 4.9: The average RMS statistical error of $\hat{C}_l^{(ij)}$ over the 165 Euclid mocks and 10 angular power spectra is plotted as a function of the covered sky fraction (all curves are normalized to unity for $f_{\text{sky}} = 1$). The thick dashed and solid lines refer to two multipole bins centred at $l = 30$ and $l = 150$, respectively. The shaded areas highlight the corresponding uncertainty obtained bootstrapping the mock light cones. The black curve shows the scaling $\propto f_{\text{sky}}^{-1/2}$ expected in the Gaussian approximation. The vertical grey line indicates the planned sky coverage of the Euclid redshift survey.

4.3.5 Estimating covariances with LIGER

Mock catalogues provide a direct way to estimate the covariance matrix of observables and test the range of validity of idealised theoretical models for the statistical errors and their correlations. The covariance matrix of the power spectrum on large scales is often described in terms of the Gaussian approximation,

$$\Sigma_{lm}^{(ik)(jh)} = \delta_{lm} \frac{C_l^{(ik)} C_l^{(jh)} + C_l^{(ih)} C_l^{(jk)}}{(2l+1)f_{\text{sky}}}, \quad (4.33)$$

where δ_{lm} denotes the Kronecker symbol and we have restored the superscripts for the redshift bins, for clarity. As a byproduct of the study presented in the previous section, we use the Euclid mock catalogues to assess the accuracy of the Gaussian approximation. Overall, our numerical estimates are compatible with the diagonal structure of $\Sigma_{lm}^{(ik)(jh)}$. The diagonal elements obtained from the full-sky mocks are in excellent agreement with eq. (4.33). However, we find that the expected scaling with respect to f_{sky} holds true only for low multipoles. Figure 4.9 shows how the average standard deviation of $C_l^{(ij)}$ in the mocks varies as a function of f_{sky} . The thick blue line corresponds to the multipole interval $20 < l \leq 40$, while the dashed line represents the bin $140 < l \leq 160$. Both curves have been normalised by the corresponding standard deviations measured in the full-sky mocks. The hatched area indicates the error on the ratio estimated bootstrapping the realisations. The black line highlights the theoretical scaling proportional to $f_{\text{sky}}^{-1/2}$. Note that the statistical error for $C_l^{(ij)}$ at $l \sim 30$ follows this curve for $f_{\text{sky}} > 0.35$ but rapidly departs from it for smaller sky fractions. Basically, the data cannot optimally constrain the large-scale power when the footprint of the survey covers too small a fraction of the sky. Higher multipoles deviate from the ideal relation for even larger values of f_{sky} . For an Euclid-like survey, the statistical error on $C_l^{(ij)}$ at $l \sim 150$ is on average 17 per cent larger than expected using the $f_{\text{sky}}^{-1/2}$ scaling. All this exemplifies the usefulness of LIGER (and mock catalogues in general) to estimate the size of measurement errors in clustering statistics and warns against using simple approximations outside the range within which they have been accurately tested.

4.3.6 Detectability of Doppler terms at low redshift

The question we want to address in this section is whether forthcoming probes of the large-scale structure will be able to provide evidence for additional sources of redshift-space distortions beyond the classic Kaiser effect and magnification bias. Although the term proportional to α in eq. (4.26) has been almost invariably neglected in past studies of galaxy clustering, it might become detectable using data from future wide-angle surveys. Recent work based on analytical calculations has concluded that the Doppler terms should leave a measurable imprint on the cross correlations between two galaxy populations (McDonald, 2009; Yoo, Hamaus et al., 2012; Bonvin, Hui and Gaztañaga, 2014) and, possibly, also on the angular clustering of a single population (Raccanelli, Bertacca, Jeong et al., 2016). Here we re-examine this case using LIGER to build mock catalogues for the SKA2 survey.

Simulating a galaxy redshift survey with the SKA2

The SKA is an unprecedentedly large and powerful array of radio telescopes that will be built in Australia and South Africa by an international collaboration. The construction will be split into two phases: 10 per cent of the collective area should be in place by 2023 (SKA1) while the full array should follow by 2030 (SKA2). The ‘billion galaxy survey’ conducted with the SKA2 will measure $\sim 10^9$ individual galaxy redshifts over $30,000 \text{ deg}^2$ using the 21-cm line emission from neutral atomic hydrogen (R. Maartens et al., 2015). In many senses, this will be the ultimate ground-based redshift survey for cosmology.

We build 125 mock light-cones with the expected characteristics of the billion-galaxy survey. Proceeding as described in sections 4.2.3 and 4.3.1, we populate our N-body simulations with galaxies making sure to reproduce the forecasts for the galaxy number counts presented in Yahya et al. (2015). At low redshifts ($z \lesssim 0.2$) and for flux⁶ limits below $10 \mu\text{Jy}$, their predictions for \bar{n}_g depend very little on the limiting flux of the survey (implying that $Q \simeq 0$). This might possibly reflect a shortcoming of their fitting formula (which covers a broad redshift range), an imperfection in the HI modeling, or the finite mass resolution of the N-body simulations used to make the forecasts (i.e. fainter galaxies might reside within unresolved dark-matter haloes). Indeed, Yahya et al. (2015) note that observed HI mass functions at low redshifts contain more low-mass objects than found in the forecasts for SKA2. To play safe, we avoid this region of parameter space. We thus use a conservative flux limit of $23 \mu\text{Jy}$ to define our main sample (Yahya et al., 2015, use $5.3 \mu\text{Jy}$ for their realistic forecasts and $23 \mu\text{Jy}$ for the pessimistic ones) and also consider a second galaxy population (the bright sample) with fluxes above $60 \mu\text{Jy}$. We derive the corresponding values for $Q(z)$ and $\mathcal{E}(z)$ after fitting the cumulative number density presented in Yahya et al. (2015) with a third-order polynomial. This is the same approach followed by S. Camera, M. G. Santos and R. Maartens (2015) and yields consistent results with their revised analysis⁷ (S. Camera, M. G. Santos and R. Maartens, 2017). The outcome of our calculations is shown in fig. 4.5 together with the functions $b_1(z)$ which we take directly from Yahya et al. (2015).

To test the impact of the Doppler terms on the clustering of SKA2 galaxies, we build and contrast two sets of mock catalogues. The first includes relativistic effects while the second drops the Doppler terms that are proportional to \mathcal{E} and Q . We omit Doppler magnification by simply ignoring the velocity-dependent terms in eq. (4.12). Further, we neglect the term proportional to \mathcal{E} in eq. (4.22) so that the weight $w_g(\bar{z})$ in the second line of eq. (4.25) is replaced with $w_g(z)$. We use the label DS (Doppler

⁶ Although Jy is a unit of flux density for simplicity we refer to it as a flux.

⁷ In a flux limited survey, Q cannot assume negative values as it would imply that less galaxies are detected when a fainter limiting flux is considered (the presence of an additional bright cut or another selection criterion are necessary to drive $Q < 0$). Due to an unfortunate mishap, the original fitting functions presented in S. Camera, M. G. Santos and R. Maartens (2015) yield $Q < 0$ for faint galaxies at low redshifts. Although this mistake does not affect their conclusions, the negative magnification biases have been used by many authors to make forecasts for the SKA2 survey

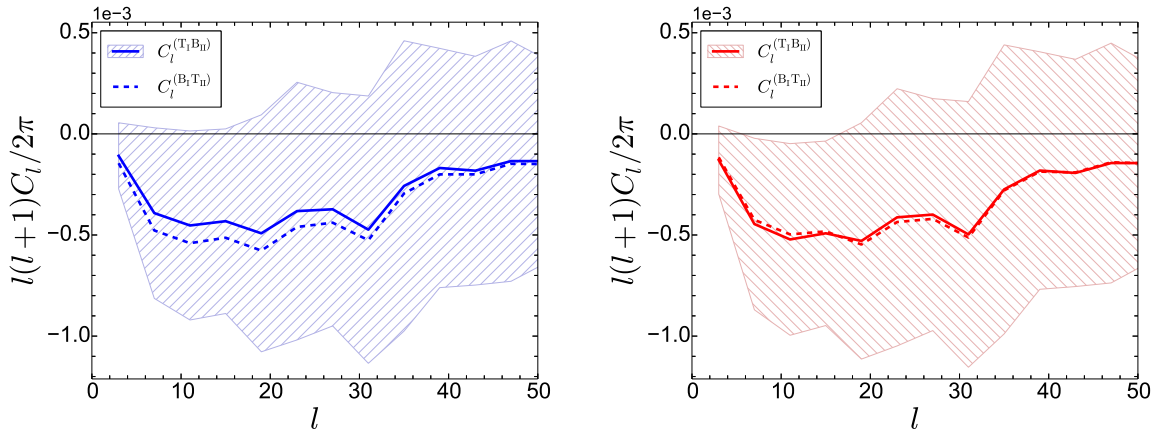


Figure 4.10: Forecasts for the billion-galaxy survey that will be conducted with the SKA2. We consider two galaxy populations (the total sample (T) characterised by observed flux above $23 \mu\text{Jy}$ and the bright sub-sample (B) corresponding to a flux limit of $60 \mu\text{Jy}$) sampled within two narrow and consecutive redshift bins (I: $0.15 < z < 0.2$ and II: $0.2 < z < 0.25$). The average cross-spectra $\hat{C}_l^{(T_1 B_{II})}$ (solid thick line) and $\hat{C}_l^{(B_I T_{II})}$ (dashed thick line) extracted from the full GR mocks are shown in the left-hand panel. The hatched area denotes the standard deviation of the noise for $\hat{C}_l^{(T_1 B_{II})}$. The corresponding quantities computed from the DS mock catalogues are displayed in the right-hand panel.

suppressed) to indicate the light cones constructed in this way, since it is impossible to isolate the remaining Doppler effects.

Cross spectra and results

General relativistic corrections alter galaxy clustering on large scales with respect to the predictions of the ‘standard model’ including a linear bias and the Kaiser distortions. In particular, they break the symmetry of two-point statistics under the exchange of particles in the pairs. In the distant-observer approximation, the relativistic effects generate odd multipoles in the redshift-space cross-correlation function between two galaxy populations or, equivalently, an imaginary part in the cross spectrum (McDonald, 2009; Yoo, Hamaus et al., 2012; Croft, 2013; Bonvin, Hui and Gaztañaga, 2014; Bonvin, 2014; Raccanelli, Bertacca, Doré et al., 2014). In terms of the comoving wavenumber of the perturbations k , relativistic corrections to the cross spectra due to Doppler effect and gravitational redshifts are suppressed by a factor \mathcal{H}/k with respect to the leading standard-model terms (McDonald, 2009). Additional corrections (due to the gravitational potential, the integrated Sachs-Wolfe effect and the Shapiro time delay) are instead suppressed by a factor $(\mathcal{H}/k)^2$. Measurements of galaxy clustering on scales comparable with the Hubble radius are therefore necessary to detect them. There is a complication, however. In the standard model, the time evolution of the galaxy populations and wide-angle effects due to the fact we observe on our past light-cone give rise to several anti-symmetric terms with similar amplitudes to the relativistic corrections (Bonvin, Hui and Gaztañaga, 2014). Moreover, dust extinction can further introduce spurious anti-symmetric terms in the galaxy correlation functions (Fang et al., 2011). Finally, from the observational point of view, it is challenging to keep the photometry stable and measure weak clustering signals on very large scales. Therefore, it is still an open question whether the Doppler contribution can be seen. In the rest of this section, we will employ our SKA2 mock light cones to address this issue. In doing this, we will neglect systematic effects due to observational limitations and dust and focus on the feasibility of the experiment from a theoretical point of view.

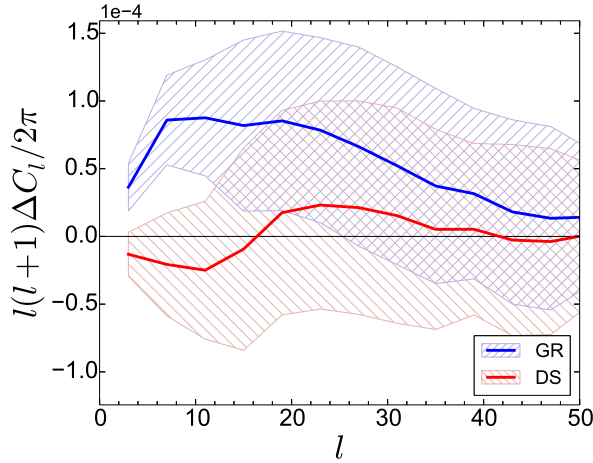


Figure 4.11: The observable $\Delta\hat{C}_l$ averaged over the GR (blue line) and DS (red line) mock catalogues. Hatched areas indicate the standard deviation of the estimates over the realisations.

In order to maximise the chances for a successful outcome, it is important to carefully configure the test we want to perform. There are a few facts to take into consideration: (i) linear peculiar velocities grow bigger at lower redshifts; (ii) γ_0 in $\delta_{g,v}$ is divided by $\mathcal{H}\chi_s$; (iii) the galaxy number density of the samples rapidly decreases for $z \gtrsim 0.2$ thus producing a large evolutionary bias but also increasing noise; (iv) we need to cover enough comoving volume to reduce sample variance. Given all this, we end up considering the interval $0.15 < z < 0.25$ which we further divide into the bins I: $0.15 < z < 0.2$ and II: $0.2 < z < 0.25$. We also make use of the two galaxy populations introduced in section 4.3.6.

In order to access the scales that are sensitive to the Doppler contribution, we focus on galaxy pairs with very wide angular separations. We thus compute the cross angular power spectrum, $\hat{C}_l^{(T_I B_{II})}$, between the total galaxy sample within the lower redshift bin and the bright subsample within the highest redshift bin. Similarly, we measure $\hat{C}_l^{(B_I T_{II})}$ by considering the bright galaxies in bin I and the full population in bin II. Finally, we consider the difference between the cross spectra:

$$\Delta\hat{C}_l = \hat{C}_l^{(T_I B_{II})} - \hat{C}_l^{(B_I T_{II})}. \quad (4.34)$$

Average results over the SKA2 mock light cones are shown in fig. 4.10. The left-hand panel displays $\hat{C}_l^{(T_I B_{II})}$ (solid thick line) and $\hat{C}_l^{(B_I T_{II})}$ (dashed thick line) both sampled in bandpowers with $\Delta l = 4$. The same quantities derived from the DS mock catalogues are shown in the right-hand panel. The additional Doppler terms included in the GR light cones clearly enhance the difference between the cross spectra at low l . They boost $\hat{C}_l^{(B_I T_{II})}$ (i.e. make it more negative) and suppress $\hat{C}_l^{(T_I B_{II})}$. This can be explained as follows. The leading Doppler contribution to the cross spectra on large scales originates from correlating the term $b_1 \delta_{\text{sim}} - \mathcal{H}^{-1} \partial n_s^i v_i / \partial \chi_s$ with the Doppler term in eq. (4.26). Therefore, schematically, in terms of single Fourier modes,

$$\Delta\hat{C}_l \propto \left[(b_{T_I} + \mu_I^2 f_I) \alpha_{B_{II}} - (b_{B_I} + \mu_I^2 f_I) \alpha_{T_{II}} \right] \frac{\delta_I v_{II}}{\mathcal{H}_{II} \chi_{II}} + \left[(b_{B_{II}} + \mu_{II}^2 f_{II}) \alpha_{T_I} - (b_{T_{II}} + \mu_{II}^2 f_{II}) \alpha_{B_I} \right] \frac{\delta_{II} v_I}{\mathcal{H}_I \chi_I}, \quad (4.35)$$

where $f = d \ln D / d \ln a$ (with D the linear growth factor of matter perturbations) describes the evolution of the velocity field, while μ_I and μ_{II} are the cosines between the wavenumber and the two lines of sight

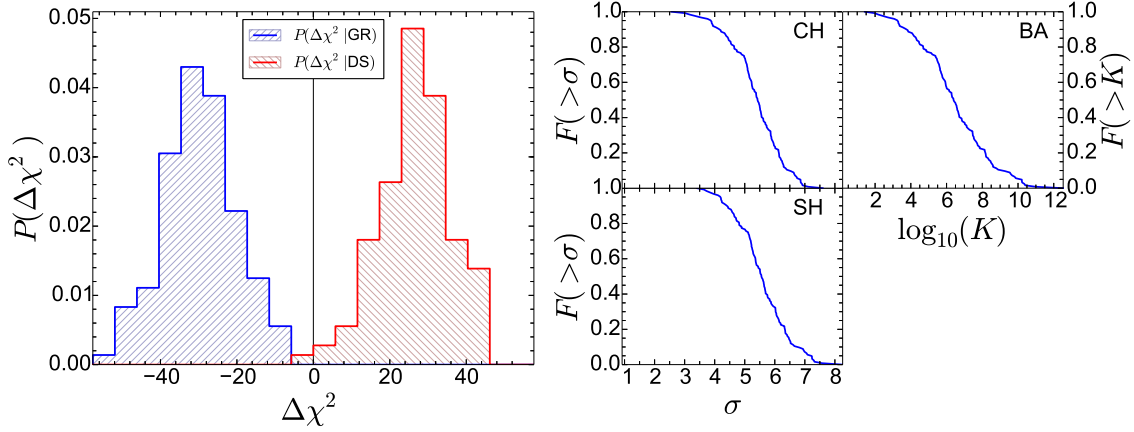


Figure 4.12: As in fig. 4.7 but for the 125 DS and GR mock catalogues for the billion-galaxy survey that will be conducted with the SKA2. We fit the first 25 multipoles of $\Delta\hat{C}_l$ defined in eq. (4.34). The fact that the histograms do not significantly overlap demonstrates that the SKA2 will be able to detect non-standard Doppler terms in the galaxy-clustering signal.

in the wide-angle configuration. A peculiarity of our samples is that $b_B(z) \simeq b_T(z) = b_l(z)$ to very good accuracy (this is different from Bonvin, Hui and Gaztañaga, 2014, which relies on different linear bias parameters and use three dimensional correlation functions) so that

$$\Delta\hat{C}_l \propto (\alpha_{B_{\text{II}}} - \alpha_{T_{\text{II}}}) (b_{\text{I}} + \mu_{\text{I}}^2 f_{\text{I}}) \frac{\delta_{\text{I}} v_{\text{II}}}{\mathcal{H}_{\text{II}} \chi_{\text{II}}} + (\alpha_{T_{\text{I}}} - \alpha_{B_{\text{I}}}) (b_{\text{II}} + \mu_{\text{II}}^2 f_{\text{II}}) \frac{\delta_{\text{II}} v_{\text{I}}}{\mathcal{H}_{\text{I}} \chi_{\text{I}}}. \quad (4.36)$$

Now, the DS mocks only include the geometric distortions and those generated by cosmic acceleration, i.e. $\alpha_{\text{DS}} = 2 + [1 - (3/2)\Omega_m(z)]\mathcal{H}\chi_s$ which is independent of the galaxy sample and only depends on the underlying cosmological model. Thus, $\Delta\hat{C}_l \simeq 0$ in the DS case. On the other hand, for the GR mocks we get $\alpha_{B_{\text{I}}} = -1.49$, $\alpha_{B_{\text{II}}} = -2.42$, $\alpha_{T_{\text{I}}} = 0.35$ and $\alpha_{T_{\text{II}}} = -0.38$ which combine to produce a positive signal. In this case \mathcal{Q} and \mathcal{E} give roughly equal contributions.

The shaded areas in fig. 4.10 indicate the standard deviation for $\hat{C}_l^{(T_{\text{I}} B_{\text{II}})}$ (the scatter for $\hat{C}_l^{(B_{\text{I}} T_{\text{II}})}$ is of comparable size). It is evident that the cross spectra extracted from the galaxy survey will be very noisy. In fig. 4.11 we show the mean and scatter of $\Delta\hat{C}_l$ for the full GR mocks (blue) and the DS ones (red). While the relative error on the single cross-spectra is very large, $\Delta\hat{C}_l$ can be measured with much better accuracy (especially for $l < 25$). Since both galaxy populations trace the same large-scale structure, most of the noise in the cross-spectra is correlated and thus does not appear in the difference. This exemplifies the advantage of using a multi-tracer approach (McDonald and Seljak, 2009).

We are now ready to investigate whether Doppler effects will be measurable with the SKA2. We first measure $\Delta\hat{C}_l$ from the 125 GR mocks and then fit the multipoles in the range $1 \leq l \leq 25$ using both the GR and the DS models (we recall that the models are obtained averaging the signal over all the mock light cones). The left-hand side histogram in the left panel of fig. 4.12 shows the distribution of the corresponding value for $\Delta\chi^2 = \chi_{\text{GR}}^2 - \chi_{\text{DS}}^2$. In parallel, we fit the $\Delta\hat{C}_l$ measurements extracted from the DS mocks and plot the corresponding histogram of $\Delta\chi^2$ on the right-hand side of the figure. The fact that the two histograms are well separated demonstrates that the SKA2 data should contain enough information to distinguish between the two models. To better quantify this, for each mock light cone we compute the statistical significance with which we can reject the null hypothesis that the GR data are generated by the DS model. The resulting cumulative distribution is plotted in the right panel

of fig. 4.12 using three different statistical tests (see section 4.3.3). In the vast majority of the mock catalogues, the DS model is ruled out at a confidence ranging between 4 and 7σ (or with a Bayes factor above 1000 corresponding to decisive evidence). We conclude that the SKA2 should be able to detect the non-standard Doppler contribution to galaxy clustering.

Our results heavily rely upon the multi-tracer technique for the suppression of the statistical noise. After repeating the analysis with a single tracer (using cross correlations between adjacent and narrow redshift bins), we find that only extreme values for the magnification and evolutionary biases (e.g. $Q \gtrsim 10$ and $|\mathcal{E}| \gtrsim 20$) could lead to a statistically significant detection.

4.4 Summary & conclusions

There are multiple reasons for which galaxy clustering requires a proper general relativistic description. (i) We observe events lying on our past light cone. (ii) The propagation of light is affected by the presence of inhomogeneities in the matter distribution. (iii) In consequence, galaxy observables (i.e. redshift, flux in some waveband and angular position on the sky) are influenced by the large-scale structure intervening between the source and the observer. However, when we interpret observations we use an unperturbed FRW model to translate redshifts and fluxes into distances and absolute luminosities. This leads to redshift-space distortions, i.e. the reconstructed galaxy density does not coincide with the actual one. The most important source of the discrepancy is the correction due to the peculiar velocity gradient (Kaiser, 1987) but it is long known that there are additional contributions and that they might become significant at large angular separations. Although no consensus has been reached yet, some recent studies based on analytical calculations and on the Fisher information matrix have concluded that signatures of these additional corrections should be detectable with the next generation of wide-angle surveys.

This chapter describes the LIGER method, a numerical technique to build mock galaxy catalogues including all general relativistic corrections at linear order in the cosmological perturbations. LIGER post processes the output of a Newtonian simulation and combines its snapshots at constant background time to build the galaxy distribution in comoving redshift space. The LIGER method is composed of three steps: (i) we shift the position of the simulated galaxies from real to redshift space; (ii) we evaluate the corresponding magnification due to gravitational lensing; (iii) we find the intersection of the modified world lines of the galaxies with the unperturbed backward light cone of the observer in redshift space. Steps (i) and (ii) include both local corrections and terms that have been integrated along the line of sight using the Born approximation. Note that standard mock galaxy catalogues generally include only the Kaiser effect for step (i) and do not account for lensing (with the exception of Guimarães, A. D. Myers and Shanks, 2005) although magnification maps are routinely built for weak-lensing studies (e.g. Wambsganss, Cen and Ostriker, 1998; Jain, Seljak and S. White, 2000; M. White and Hu, 2000; Vale and M. White, 2003; Fosalba, Gaztañaga, Castander and Manera, 2008; Fosalba, Gaztañaga, Castander and Crocce, 2015; Hilbert et al., 2009; Kiessling et al., 2011).

LIGER is characterized by the following features. (i) It can be applied to the output of any Newtonian simulation (N-body or hydrodynamic) independent of the code with which it has been run. (ii) It is fast to execute so that it is computationally feasible to produce very large numbers of mock catalogues for a given survey. (iii) A variant of the standard implementation has been specially designed to work with simulations that cover very large comoving volumes but do not resolve single galaxies. In this case, the galaxy density field is obtained by biasing the dark-matter distribution.

The main applications of LIGER are foreseen for forthcoming wide-angle spectroscopic surveys like

DESI⁸, Euclid⁹, HETDEX¹⁰, SKAII¹¹, SPHEREx¹², SuMiRe¹³ as well as photometric surveys like J-PAS¹⁴ and LSST¹⁵. Mock catalogues will be used as forecasting tools and to measure biases and covariance matrices of estimators for several statistics of the large-scale structure. As a proof of concept, we quantify the impact of magnification bias in the angular clustering of galaxies for a Euclid-like survey. Our results show that lensing convergence generates a non-negligible correction for the angular power spectra of galaxies in broad redshift bins and dominates cross-spectra between galaxies at widely separated redshifts (similar conclusions have been reached by Di Dio, Durrer et al., 2014; Montanari and Durrer, 2015, using analytical calculations). The convergence signal can be detected at 8σ significance and this provides the intriguing possibility to measure the lensing potential from the cross spectra (Montanari and Durrer, 2015).

Additional redshift-space distortions on top of the standard Kaiser correction and the weak-lensing convergence are generally small. Therefore, customised techniques need be developed in order to measure their signatures. It is foreseeable that LIGER-based mocks will be key to optimising the design of these probes. In anticipation of these future applications, we have investigated the detectability of several additional Doppler terms using the specifics of the planned ‘billion galaxy survey’ with the SKA2 telescope. Our results show that using two galaxy populations with different flux cuts (T: $f > 23 \mu\text{Jy}$ and B: $f > 60 \mu\text{Jy}$) and two consecutive redshift intervals (I: $0.15 < z < 0.2$ and II: $0.2 < z < 0.25$), it will be possible to measure a significant Doppler-induced signal. The statistic we use is the difference of the angular cross power spectra $\Delta C_l = C_l^{(T_1 B_{II})} - C_l^{(B_1 T_{II})}$. For multipoles $l \leq 25$, this quantity is dominated by the contribution of the Doppler terms and shows a strikingly reduced variance compared to each of the cross correlations due to the fact that both galaxy populations are biased tracers of the same underlying matter density. Based on our simulations, ΔC_l should be detectable with a signal-to-noise ratio of ~ 5.5 .

⁸ <http://desi.lbl.gov>

⁹ <http://www.euclid-ec.org>

¹⁰ <http://hetdex.org>

¹¹ <https://www.skatelescope.org>

¹² <http://spherex.caltech.edu>

¹³ <http://sumire.ipmu.jp/en/>

¹⁴ <http://j-pas.org>

¹⁵ <https://www.lsst.org>

Summary & conclusions

In the final chapter, we want to summarise and highlight the main results of this thesis. The investigation of a new model for gravitational collapse has improved our knowledge of how haloes form and has contributed to the understanding of their properties. Furthermore, we provide a tool to calculate mock observed distributions of galaxies including leading order general relativistic effects. This is particularly suited to predict observables on large scales for the upcoming surveys that will provide an unprecedented amount of data. In the following, we discuss these results also in a broader context.

5.1 A new paradigm for the formation of dark-matter haloes

The current picture of halo formation is mostly based on the ellipsoidal collapse model (BM96; Sheth, Mo and Tormen, 2001; dubbed ECS in chapter 2). One of the major successes of the ECS model is that it can explain why haloes of smaller mass originate on average from higher density regions in the initial density field (see e.g. fig. 2.9). Based on the spherical collapse model, the ECS additionally takes into account that surrounding structures break the spherical symmetry and induce an anisotropic external tidal field. The action of the tidal field distorts the initial sphere of the ECS and, as a consequence, the perturbation always collapses later compared to a vanishing tidal field. Since the mean strength of the tidal field increases for perturbations of lower mass, the ECS model predicts the density contrast δ_L to rise for lower mass haloes, which is in agreement with results from simulations.

However, simulations show a larger scatter in δ_L than estimated from the ECS model. Moreover, the distribution of the matter of a halo identified today in the initial density field (called protohalo) is not spherical, but better described by an ellipsoid. This is another effect of the tidal field: along a certain direction the gravitational force is enhanced, while it is reduced in another direction. Indeed, simulations reveal that the shape and orientation of protohaloes and their tidal field are correlated. Accordingly, we incorporate this into the collapse model by replacing the initial shape of the perturbation with an ellipsoid aligned with the tidal field (LBP14 and chapter 2; dubbed ECE). Interestingly, when this new model is applied to protohaloes from simulations, the required linear density contrast for perturbations to collapse today is approximately constant (see fig. 2.1). This common value for δ_L is close to δ_{sc} , indicating that the collapse of ellipsoidal perturbations in the presence of a tidal field proceeds similarly to the spherical collapse model.

Furthermore, following the collapse of the haloes in simulations, we found that many haloes of lower mass are already assembled prior to the time of their identification. In some cases this happens at times earlier than half of the age of the universe (see figs. 2.5 and 3.2). We give a prescription to estimate the

collapse time of haloes and show that if we require the perturbation in the ECE model to collapse at the very same time the model predictions match the results from simulations well (see fig. 2.8). In chapter 3 we study some example haloes and show that haloes which are located in prominent filaments of the cosmic web stop growing in mass. This behaviour is unexpected as we would suppose that haloes always grow.

Hence, we present a new paradigm of halo formation, where haloes evolve approximately following the expectations from the spherical collapse model. The tidal field reshapes the protohalo and eventually leads to the formation of a filament, which is able to quench the growth of the halo. Since haloes that collapse earlier originate from higher initial densities, this model can explain the observed trend of the linear density contrast at the sites of protohaloes as a function of their mass. Finally, we present a simple model that uses the ellipticity of the tidal field to predict the accretion history of haloes (see section 3.3.5).

5.2 A piece in the puzzle of understanding assembly bias

The fact that the amplitude of the two-point correlation function of haloes does not only depend on the halo mass but also on their age or other internal characteristics is called assembly bias. It has been argued that the suppressed accretion of a subset of low mass haloes would lead to assembly bias (e.g. H. Y. Wang, Mo and Jing, 2007; Dalal et al., 2008; Hahn, Porciani, Dekel et al., 2009; J. Wang et al., 2011). Although, a correlation between the growth of haloes and the strength of the tidal field has been noted (Hahn, Porciani, Dekel et al., 2009; J. Wang et al., 2011), the detailed physical mechanism was so far unclear. Within this thesis, in chapter 3, we describe how haloes embedded in prominent filaments become stalled, i.e. have no net growth in mass. From this explanation, it is clear that early and late collapsing haloes populate different regions of the cosmic web. This difference in the spatial distribution of the haloes is the origin of assembly bias. As very massive haloes source the filaments and have a large clustering amplitude, early collapsing smaller haloes follow their distribution and clustering properties. On the other side, accreting (or late collapsing) haloes avoid the close neighbourhood of filaments. Hence, their clustering amplitude is decreased. We find a consistent behaviour among all haloes within the sample we studied in fig. 3.3, classified using the collapse time. The strength of the bias found is among the largest reported in the literature.

Strong assembly bias has also been reported by Faltenbacher and S. D. White (2010) when splitting haloes by the velocity anisotropy parameter β (eq. 3.2). However, the reason of the correlation between the internal halo quantity β and the position in the cosmic web remained elusive. As we show in chapter 3, we can explain this as a characteristic imprint of the filament on stalled haloes. The prominent non-linear structure alters the accretion pattern of the collapsing patch and induces tangential orbits of the halo particles. Thus, early collapsing haloes carry a reduced value of β , as a characteristic signature, which indicates tangentially dominated particle orbits, as a consequence of the cosmic web (fig. 3.12). Hence, the model of halo formation presented here corroborates and connects different studies on halo clustering and contributes to the understanding of assembly bias.

5.3 The impact of General Relativity on the large-scale clustering of galaxies

Finally, in chapter 4 we present a novel method to build mock realisations of the observed galaxy number counts on large scales using numerical simulations. The next generation of galaxy redshift surveys will map galaxies over a large fraction of the sky up to high redshifts ($z \sim 1 - 2$). Thus, the correlation of

galaxies on large scales becomes observable. These correlations are effected by redshift-space distortions originating from the fact that we observe galaxies on the past light cone. We have developed and implemented a new algorithm to extract a light cone from a Newtonian simulation taking into account leading-order redshift-space distortions as predicted by the weak-field expansion of GR. The method is fast and can be used to produce many realisations, which is helpful to estimate the expected error on observables of galaxy clustering.

We name our method `LIGER` and illustrate its usage with two examples. First, we estimate the angular power spectra of the galaxy distribution for a Euclid-like survey. We find that the large-scale signal of the cross-correlation between galaxies in different redshift bins is dominated by magnification due to the weak lensing convergence. Second, we use the two-tracer approach to show that the SKA2 galaxy survey is in principle able to detect relativistic Doppler effects in the angular power spectrum of galaxies. The `LIGER` code is made publicly available¹.

5.4 Outlook

We present a model of halo formation which describes the evolution of our rather small number of randomly selected haloes well. Thus, it is desirable to test this model against a larger statistical sample of haloes. It is interesting to study whether the simple condition on e is sufficient to predict the appearance of filaments or further conditions e.g. on the prolateness p are necessary. Further, the implementation of this model into the excursion-set framework could improve predictions of the halo mass function in the future.

Another interesting question is whether early-collapsing haloes in filaments can accrete baryonic matter. Dark matter haloes are of special importance, because they are the sites where baryons accumulate and form galaxies. Hence, it is interesting to study what type of galaxies are harboured by early- and late collapsing haloes. This has already been investigated by the two follow-up papers of the ZOMG series (Romano-Díaz et al., 2017; Garaldi et al., 2017). Even though the gas accretion of stalled haloes is suppressed compared to accreting ones, in both halo types actively star-forming disk galaxies can develop. This makes it difficult to detect the assembly bias effect in galaxies. However, some characteristic differences between the galaxies are found, like the age of the stellar content and the thickness of the stellar disk. Although, it is currently computationally challenging, it would be desirable to study a larger galaxy sample in the future. This could help to determine whether a galaxy assembly bias signal is in principle observable.

Finally, we present `LIGER`, a tool to produce mock observations on large-scales including leading order general relativistic effects. This is particularly useful for the upcoming surveys, where `LIGER` can contribute to predict the expected large-scale clustering signal and it can be used to estimate the covariance matrix. Furthermore, `LIGER` can be used to identify observables which make it possible to measure the small signature of general-relativistic redshift-space distortions (beyond the known Kaiser and magnification effect). Thus, our new tool will be key to shape new probes and target novel large-scale clustering signals.

¹ www.astro.uni-bonn.de/~porciani/LIGER

Bibliography

- Adamek, J., R. Durrer and M. Kunz (2014), *N-body methods for relativistic cosmology*, Classical and Quantum Gravity **31**, 234006 234006, arXiv: 1408.3352 (cit. on p. 76).
- Adamek, J. et al. (2013), *General relativistic N-body simulations in the weak field limit*, Phys. Rev. D **88**, 103527 103527, arXiv: 1308.6524 (cit. on p. 76).
- (2016a), *General relativity and cosmic structure formation*, Nature Physics **12** 346, arXiv: 1509.01699 (cit. on p. 76).
- (2016b), *gevolution: a cosmological N-body code based on General Relativity*, J. Cosmology Astropart. Phys. **7**, 053 053, arXiv: 1604.06065 (cit. on p. 76).
- Adhikari, S., N. Dalal and R. T. Chamberlain (2014), *Splashback in accreting dark matter halos*, J. Cosmology Astropart. Phys. **11**, 019 019, arXiv: 1409.4482 (cit. on pp. 19, 54).
- Amanatides, J. and A. Woo (1987), “A Fast Voxel Traversal Algorithm for Ray Tracing”, *EG 1987-Technical Papers*, Eurographics Association (cit. on p. 81).
- Angrick, C. and M. Bartelmann (2010), *Triaxial collapse and virialisation of dark-matter haloes*, A&A **518** A38+, arXiv: 1001.4984 (cit. on pp. 28, 30).
- Angulo, R. E., C. M. Baugh and C. G. Lacey (2008), *The assembly bias of dark matter haloes to higher orders*, MNRAS **387** 921, arXiv: 0712.2280 (cit. on pp. 24, 47).
- Aragon-Calvo, M. A. and L. F. Yang (2014), *The hierarchical nature of the spin alignment of dark matter haloes in filaments*, MNRAS **440** L46, arXiv: 1303.1590 (cit. on p. 65).
- Aragón-Calvo, M. A. et al. (2007), *Spin Alignment of Dark Matter Halos in Filaments and Walls*, ApJ **655** L5, eprint: astro-ph/0610249 (cit. on pp. 47, 65).
- Aubert, D., C. Pichon and S. Colombi (2004), *The origin and implications of dark matter anisotropic cosmic infall on \tilde{L}_* haloes*, MNRAS **352** 376, eprint: astro-ph/0402405 (cit. on p. 65).
- Bailin, J. and M. Steinmetz (2005), *Internal and External Alignment of the Shapes and Angular Momenta of Λ CDM Halos*, ApJ **627** 647, eprint: astro-ph/0408163 (cit. on p. 65).
- Bardeen, J. M., J. R. Bond et al. (1986), *The statistics of peaks of Gaussian random fields*, ApJ **304** 15 (cit. on p. 27).
- Bardeen, J. M., P. J. Steinhardt and M. S. Turner (1983), *Spontaneous creation of almost scale-free density perturbations in an inflationary universe*, Phys. Rev. D **28** 679 (cit. on p. 9).
- Bartelmann, M. and P. Schneider (1994), *Large-scale correlations between QSOs and IRAS galaxies*, A&A **284** 1, eprint: astro-ph/9311008 (cit. on p. 92).
- Behroozi, P. S., R. H. Wechsler and C. Conroy (2013), *The Average Star Formation Histories of Galaxies in Dark Matter Halos from $z = 0-8$* , ApJ **770**, 57 57, arXiv: 1207.6105 (cit. on pp. 48, 52).
- Bentivegna, E. and M. Bruni (2016), *Effects of Nonlinear Inhomogeneity on the Cosmic Expansion with Numerical Relativity*, Physical Review Letters **116**, 251302 251302, arXiv: 1511.05124 (cit. on p. 76).

- Bertacca, D. (2015), *Observed galaxy number counts on the light cone up to second order: III. Magnification bias*, Classical and Quantum Gravity **32**, 195011 195011, arXiv: 1409.2024 (cit. on pp. 78, 80).
- Bertacca, D. et al. (2012), *Beyond the plane-parallel and Newtonian approach: wide-angle redshift distortions and convergence in general relativity*, J. Cosmology Astropart. Phys. **10**, 025 025, arXiv: 1205.5221 (cit. on pp. 76, 84).
- Bertschinger, E. and B. Jain (1994), *Gravitational instability of cold matter*, ApJ **431** 486, eprint: astro-ph/9307033 (cit. on p. 28).
- Bett, P. et al. (2007), *The spin and shape of dark matter haloes in the Millennium simulation of a Λ cold dark matter universe*, MNRAS **376** 215, eprint: arXiv:astro-ph/0608607 (cit. on pp. 24, 47).
- Blaizot, J. et al. (2005), *MoMaF: the Mock Map Facility*, MNRAS **360** 159, eprint: astro-ph/0309305 (cit. on pp. 75, 82).
- Bond, J. R., S. Cole et al. (1991), *Excursion set mass functions for hierarchical Gaussian fluctuations*, ApJ **379** 440 (cit. on pp. 20, 21, 28, 44, 49, 58, 67).
- Bond, J. R., L. Kofman and D. Pogosyan (1996), *How filaments of galaxies are woven into the cosmic web*, Nature **380** 603, eprint: astro-ph/9512141 (cit. on pp. 47, 68).
- Bond, J. R. and S. T. Myers (1996), *The Peak-Patch Picture of Cosmic Catalogs. I. Algorithms*, (BM96), ApJS **103** 1 (cit. on pp. 21, 28–30, 33, 42, 43, 45, 67, 69, 70, 101).
- Bonvin, C. (2014), *Isolating relativistic effects in large-scale structure*, Classical and Quantum Gravity **31**, 234002 234002, arXiv: 1409.2224 (cit. on p. 95).
- Bonvin, C. and R. Durrer (2011), *What galaxy surveys really measure*, Phys. Rev. D **84**, 063505 063505, arXiv: 1105.5280 (cit. on pp. 76, 79, 82).
- Bonvin, C., L. Hui and E. Gaztañaga (2014), *Asymmetric galaxy correlation functions*, Phys. Rev. D **89**, 083535 083535, arXiv: 1309.1321 (cit. on pp. 76, 94, 95, 97).
- (2016), *Optimising the measurement of relativistic distortions in large-scale structure*, J. Cosmology Astropart. Phys. **8**, 021 021, arXiv: 1512.03566 (cit. on p. 76).
- Borzyszkowski, M., D. Bertacca and C. Porciani (2017), *LIGER: mock relativistic light-cones from Newtonian simulations*, ArXiv e-prints, arXiv: 1703.03407 (cit. on p. 75).
- Borzyszkowski, M., A. D. Ludlow and C. Porciani (2014), *The formation of cold dark matter haloes - II. Collapse time and tides*, MNRAS **445** 4124, arXiv: 1405.7367 (cit. on p. 27).
- Borzyszkowski, M., C. Porciani et al. (2016), *ZOMG I: How the cosmic web inhibits halo growth and generates assembly bias*, ArXiv e-prints, arXiv: 1610.04231 (cit. on p. 47).
- Bosma, A. (1981), *21-cm line studies of spiral galaxies. II. The distribution and kinematics of neutral hydrogen in spiral galaxies of various morphological types.*, AJ **86** 1825 (cit. on p. 6).
- Bruni, M., D. B. Thomas and D. Wands (2014), *Computing general-relativistic effects from Newtonian N-body simulations: Frame dragging in the post-Friedmann approach*, Phys. Rev. D **89**, 044010 044010, arXiv: 1306.1562 (cit. on p. 76).
- Camera, S., M. G. Santos and R. Maartens (2015), *Probing primordial non-Gaussianity with SKA galaxy redshift surveys: a fully relativistic analysis*, MNRAS **448** 1035, arXiv: 1409.8286 (cit. on p. 94).
- Camera, S., M. G. Santos and R. Maartens (2017), *Erratum: Probing primordial non-Gaussianity with SKA galaxy redshift surveys: a fully relativistic analysis*, MNRAS **467** 1505 (cit. on p. 94).
- Cardona, W. et al. (2016), *Lensing convergence and the neutrino mass scale in galaxy redshift surveys*, Phys. Rev. D **94**, 043007 043007, arXiv: 1603.06481 (cit. on p. 76).
- Carlberg, R. G. et al. (1997), *The Average Mass Profile of Galaxy Clusters*, ApJ **485** L13, eprint: astro-ph/9703107 (cit. on p. 66).
- Carlson, J. and M. White (2010), *Embedding Realistic Surveys in Simulations Through Volume Remapping*, ApJS **190** 311, arXiv: 1003.3178 (cit. on p. 75).

- Carron, J. (2013), *On the assumption of Gaussianity for cosmological two-point statistics and parameter dependent covariance matrices*, A&A **551**, A88 A88, arXiv: 1204.4724 (cit. on p. 88).
- Catelan, P. et al. (1998), *The bias field of dark matter haloes*, MNRAS **297** 692, eprint: astro-ph/9708067 (cit. on p. 73).
- Cautun, M. et al. (2014), *Evolution of the cosmic web*, MNRAS **441** 2923, arXiv: 1401.7866 (cit. on p. 47).
- Challinor, A. and A. Lewis (2011), *Linear power spectrum of observed source number counts*, Phys. Rev. D **84**, 043516 043516, arXiv: 1105.5292 (cit. on pp. 76, 79, 80, 82, 83).
- Chisari, N. E. and M. Zaldarriaga (2011), *Connection between Newtonian simulations and general relativity*, Phys. Rev. D **83**, 123505 123505, arXiv: 1101.3555 (cit. on pp. 76, 80).
- Clowe, D. et al. (2006), *A Direct Empirical Proof of the Existence of Dark Matter*, ApJ **648** L109, eprint: astro-ph/0608407 (cit. on p. 6).
- Codis, S. et al. (2012), *Connecting the cosmic web to the spin of dark haloes: implications for galaxy formation*, MNRAS **427** 3320, arXiv: 1201.5794 (cit. on p. 65).
- Cole, S., S. Hatton et al. (1998), *Mock 2dF and SDSS galaxy redshift surveys*, MNRAS **300** 945, eprint: astro-ph/9801250 (cit. on p. 75).
- Cole, S. and C. Lacey (1996), *The structure of dark matter haloes in hierarchical clustering models*, MNRAS **281** 716, eprint: arXiv:astro-ph/9510147 (cit. on p. 66).
- Croft, R. A. (2013), *Gravitational redshifts from large-scale structure*, MNRAS **434** 3008, arXiv: 1304.4124 (cit. on p. 95).
- Cuesta, A. J. et al. (2008), *The virialized mass of dark matter haloes*, MNRAS **389** 385, arXiv: 0710.5520 (cit. on p. 38).
- Dalal, N. et al. (2008), *Halo Assembly Bias in Hierarchical Structure Formation*, ApJ **687** 12, arXiv: 0803.3453 (cit. on pp. 48, 102).
- Davis, M., G. Efstathiou et al. (1985), *The evolution of large-scale structure in a universe dominated by cold dark matter*, ApJ **292** 371 (cit. on pp. 18, 24).
- Davis, M., J. Huchra et al. (1982), *A survey of galaxy redshifts. II - The large scale space distribution*, ApJ **253** 423 (cit. on p. 22).
- Del Popolo, A. (2002), *On the evolution of aspherical perturbations in the universe: An analytical model*, A&A **387** 759, eprint: astro-ph/0202436 (cit. on p. 29).
- (2014), *Nonbaryonic Dark Matter in Cosmology*, International Journal of Modern Physics D **23**, 1430005 1430005, arXiv: 1305.0456 (cit. on p. 5).
- Desjacques, V., D. Jeong and F. Schmidt (2016), *Large-Scale Galaxy Bias*, ArXiv e-prints, arXiv: 1611.09787 (cit. on p. 22).
- Despali, G., G. Tormen and R. K. Sheth (2013), *Ellipsoidal halo finders and implications for models of triaxial halo formation*, MNRAS **431** 1143, arXiv: 1212.4157 (cit. on pp. 28, 70).
- Di Dio, E., R. Durrer et al. (2014), *Galaxy number counts to second order and their bispectrum*, J. Cosmology Astropart. Phys. **12**, 017 017, arXiv: 1407.0376 (cit. on pp. 89, 99).
- Di Dio, E., F. Montanari, R. Durrer et al. (2014), *Cosmological parameter estimation with large scale structure observations*, J. Cosmology Astropart. Phys. **1**, 042 042, arXiv: 1308.6186 (cit. on p. 76).
- Di Dio, E., F. Montanari, J. Lesgourgues et al. (2013), *The CLASSgal code for relativistic cosmological large scale structure*, J. Cosmology Astropart. Phys. **11**, 044 044, arXiv: 1307.1459 (cit. on p. 76).
- Di Dio, E., F. Montanari, A. Raccanelli et al. (2016), *Curvature constraints from large scale structure*, J. Cosmology Astropart. Phys. **6**, 013 013, arXiv: 1603.09073 (cit. on p. 76).
- Diaferio, A., S. Schindler and K. Dolag (2008), *Clusters of Galaxies: Setting the Stage*, Space Sci. Rev. **134** 7, arXiv: 0801.0968 (cit. on p. 5).

- Diemand, J., M. Kuhlen and P. Madau (2007), *Formation and Evolution of Galaxy Dark Matter Halos and Their Substructure*, ApJ **667** 859, eprint: astro-ph/0703337 (cit. on pp. 38, 48, 50).
- Diemand, J., B. Moore and J. Stadel (2005), *Earth-mass dark-matter haloes as the first structures in the early Universe*, Nature **433** 389, eprint: astro-ph/0501589 (cit. on p. 47).
- Diemer, B. and A. V. Kravtsov (2014), *Dependence of the Outer Density Profiles of Halos on Their Mass Accretion Rate*, ApJ **789**, 1 1, arXiv: 1401.1216 (cit. on pp. 19, 54).
- Diemer, B., S. More and A. V. Kravtsov (2013), *The Pseudo-evolution of Halo Mass*, ApJ **766**, 25 25, arXiv: 1207.0816 (cit. on pp. 38, 56).
- Doroshkevich, A. G. (1970), *The space structure of perturbations and the origin of rotation of galaxies in the theory of fluctuation.*, Astrofizika **6** 581 (cit. on pp. 34, 67).
- Dwek, E. et al. (1998), *The COBE Diffuse Infrared Background Experiment Search for the Cosmic Infrared Background. IV. Cosmological Implications*, ApJ **508** 106, eprint: astro-ph/9806129 (cit. on p. 8).
- Dyson, F. W., A. S. Eddington and C. Davidson (1920), *A Determination of the Deflection of Light by the Sun's Gravitational Field, from Observations Made at the Total Eclipse of May 29, 1919*, Philosophical Transactions of the Royal Society of London Series A **220** 291 (cit. on p. 3).
- Efstathiou, G. et al. (1988), *Gravitational clustering from scale-free initial conditions*, MNRAS **235** 715 (cit. on p. 27).
- Einstein, A. (1917), *Kosmologische Betrachtungen zur allgemeinen Relativitätstheorie*, Sitzungsberichte der Königlich Preussischen Akademie der Wissenschaften (Berlin), Seite 142-152. (cit. on p. 8).
- Eisenstein, D. J. and W. Hu (1998), *Baryonic Features in the Matter Transfer Function*, ApJ **496** 605, eprint: astro-ph/9709112 (cit. on p. 49).
- Eisenstein, D. J. and A. Loeb (1995), *An analytical model for the triaxial collapse of cosmological perturbations*, ApJ **439** 520, eprint: arXiv:astro-ph/9405012 (cit. on p. 28).
- Eke, V. R., S. Cole and C. S. Frenk (1996), *Cluster evolution as a diagnostic for Omega*, MNRAS **282** 263, eprint: arXiv:astro-ph/9601088 (cit. on p. 27).
- Elia, A., A. D. Ludlow and C. Porciani (2012), *The spatial and velocity bias of linear density peaks and protohaloes in the Λ cold dark matter cosmology*, MNRAS **421** 3472, arXiv: 1111.4211 (cit. on pp. 28, 46, 70).
- Fabricant, D., M. Lecar and P. Gorenstein (1980), *X-ray measurements of the mass of M87*, ApJ **241** 552 (cit. on p. 5).
- Faltenbacher, A. and S. D. White (2010), *Assembly Bias and the Dynamical Structure of Dark Matter Halos*, ApJ **708** 469, arXiv: 0909.4302 (cit. on pp. 24, 47, 49, 64, 65, 72, 102).
- Fang, W. et al. (2011), *Anisotropic extinction distortion of the galaxy correlation function*, Phys. Rev. D **84**, 063012 063012, arXiv: 1105.3421 (cit. on p. 95).
- Fidler, C., C. Rampf et al. (2015), *General relativistic corrections to N -body simulations and the Zel'dovich approximation*, Phys. Rev. D **92**, 123517 123517, arXiv: 1505.04756 (cit. on p. 76).
- Fidler, C., T. Tram et al. (2016), *Relativistic interpretation of Newtonian simulations for cosmic structure formation*, J. Cosmology Astropart. Phys. **9**, 031 031, arXiv: 1606.05588 (cit. on p. 76).
- Fosalba, P., E. Gaztañaga, F. J. Castander and M. Crocce (2015), *The MICE Grand Challenge light-cone simulation - III. Galaxy lensing mocks from all-sky lensing maps*, MNRAS **447** 1319, arXiv: 1312.2947 (cit. on pp. 80, 81, 98).
- Fosalba, P., E. Gaztañaga, F. J. Castander and M. Manera (2008), *The onion universe: all sky lightcone simulations in spherical shells*, MNRAS **391** 435, arXiv: 0711.1540 (cit. on pp. 80, 81, 98).
- Friedmann, A. (1922), *Über die Krümmung des Raumes*, Zeitschrift für Physik **10** 377 (cit. on p. 2).
- Gao, L., V. Springel and S. D. White (2005), *The age dependence of halo clustering*, MNRAS **363** L66, eprint: arXiv:astro-ph/0506510 (cit. on pp. 24, 45, 47, 52).

- Gao, L. and S. D. White (2007), *Assembly bias in the clustering of dark matter haloes*, MNRAS **377** L5, eprint: arXiv:astro-ph/0611921 (cit. on pp. 24, 47).
- Garaldi, E. et al. (2017), *ZOMG III*: MNRAS submitted, eprint: arXiv:astro-ph (cit. on pp. 48, 103).
- Gaztañaga, E., C. Bonvin and L. Hui (2017), *Measurement of the dipole in the cross-correlation function of galaxies*, J. Cosmology Astropart. Phys. **1**, 032 032, arXiv: 1512.03918 (cit. on p. 76).
- Giblin, J. T., J. B. Mertens and G. D. Starkman (2016), *Departures from the Friedmann-Lemaître-Robertson-Walker Cosmological Model in an Inhomogeneous Universe: A Numerical Examination*, Physical Review Letters **116**, 251301 251301, arXiv: 1511.01105 (cit. on p. 76).
- Gill, S. P., A. Knebe and B. K. Gibson (2004), *The evolution of substructure - I. A new identification method*, MNRAS **351** 399, eprint: astro-ph/0404258 (cit. on p. 49).
- Górski, K. M. et al. (2005), *HEALPix: A Framework for High-Resolution Discretization and Fast Analysis of Data Distributed on the Sphere*, ApJ **622** 759, eprint: astro-ph/0409513 (cit. on p. 87).
- Gott III, J. R. and M. J. Rees (1975), *A theory of galaxy formation and clustering*, A&A **45** 365 (cit. on p. 27).
- Green, S. R. and R. M. Wald (2012), *Newtonian and relativistic cosmologies*, Phys. Rev. D **85**, 063512 063512, arXiv: 1111.2997 (cit. on p. 80).
- Guimarães, A. C., A. D. Myers and T. Shanks (2005), *QSO lensing magnification associated with galaxy groups*, MNRAS **362** 657, eprint: astro-ph/0409484 (cit. on p. 98).
- Gunn, J. E. and J. R. Gott III (1972), *On the Infall of Matter Into Clusters of Galaxies and Some Effects on Their Evolution*, ApJ **176** 1 (cit. on pp. 12, 27).
- Gursky, H. et al. (1972), *X-Ray Emission from Rich Clusters of Galaxies*, ApJ **173** L99 (cit. on p. 5).
- Hahn, O. and T. Abel (2011), *Multi-scale initial conditions for cosmological simulations*, MNRAS **415** 2101, arXiv: 1103.6031 (cit. on pp. 17, 49, 52).
- Hahn, O., C. M. Carollo et al. (2007), *The evolution of dark matter halo properties in clusters, filaments, sheets and voids*, MNRAS **381** 41, arXiv: 0704.2595 (cit. on p. 47).
- Hahn, O. and A. Paranjape (2014), *The locations of halo formation and the peaks formalism*, MNRAS **438** 878, arXiv: 1308.4142 (cit. on pp. 29, 48, 70).
- Hahn, O., C. Porciani, C. M. Carollo et al. (2007), *Properties of dark matter haloes in clusters, filaments, sheets and voids*, MNRAS **375** 489, eprint: astro-ph/0610280 (cit. on pp. 47, 65).
- Hahn, O., C. Porciani, A. Dekel et al. (2009), *Tidal effects and the environment dependence of halo assembly*, MNRAS **398** 1742, arXiv: 0803.4211 (cit. on pp. 35, 45, 48, 52, 61–63, 102).
- Hamilton, A. J. (1998), “Linear Redshift Distortions: a Review”, *The Evolving Universe*, ed. by D. Hamilton, vol. 231, Astrophysics and Space Science Library 185, eprint: astro-ph/9708102 (cit. on pp. 75, 84).
- Han, E. et al. (2014), *Exoplanet Orbit Database. II. Updates to Exoplanets.org*, PASP **126** 827, arXiv: 1409.7709 (cit. on p. 1).
- Hansen, S. H. and B. Moore (2006), *A universal density slope Velocity anisotropy relation for relaxed structures*, New A **11** 333, eprint: astro-ph/0411473 (cit. on pp. 66, 67, 72).
- Harker, G. et al. (2006), *A marked correlation function analysis of halo formation times in the Millennium Simulation*, MNRAS **367** 1039, eprint: astro-ph/0510488 (cit. on p. 47).
- Haugg, T., S. Hofmann and M. Kopp (2012), *Newtonian N-body simulations are compatible with cosmological perturbation theory*, ArXiv e-prints, arXiv: 1211.0011 (cit. on p. 76).
- Hawking, S. W. (1982), *The development of irregularities in a single bubble inflationary universe*, Physics Letters B **115** 295 (cit. on p. 9).
- Hearin, A. P., D. F. Watson and F. C. van den Bosch (2015), *Beyond halo mass: galactic conformity as a smoking gun of central galaxy assembly bias*, MNRAS **452** 1958, arXiv: 1404.6524 (cit. on p. 47).

- Hearin, A. P., A. R. Zentner et al. (2016), *Introducing decorated HODs: modelling assembly bias in the galaxy-halo connection*, MNRAS **460** 2552, arXiv: 1512.03050 (cit. on p. 47).
- Hilbert, S. et al. (2009), *Ray-tracing through the Millennium Simulation: Born corrections and lens-lens coupling in cosmic shear and galaxy-galaxy lensing*, A&A **499** 31, arXiv: 0809.5035 (cit. on p. 98).
- Hinshaw, G. et al. (2013), *Nine-year Wilkinson Microwave Anisotropy Probe (WMAP) Observations: Cosmological Parameter Results*, ApJS **208**, 19 19, arXiv: 1212.5226 (cit. on p. 8).
- Hivon, E. et al. (2002), *MASTER of the Cosmic Microwave Background Anisotropy Power Spectrum: A Fast Method for Statistical Analysis of Large and Complex Cosmic Microwave Background Data Sets*, ApJ **567** 2, eprint: astro-ph/0105302 (cit. on p. 87).
- Hockney, R. W. and J. W. Eastwood (1988), *Computer simulation using particles*, Adam Hilger (cit. on pp. 15, 32, 80).
- Hoffman, Y. (1986), *The dynamics of superclusters - The effect of shear*, ApJ **308** 493 (cit. on p. 28).
- Howlett, C., M. Manera and W. J. Percival (2015), *L-PICOLA: A parallel code for fast dark matter simulation*, Astronomy and Computing **12** 109, arXiv: 1506.03737 (cit. on p. 85).
- Hubble, E. (1929), *A Relation between Distance and Radial Velocity among Extra-Galactic Nebulae*, Proceedings of the National Academy of Science **15** 168 (cit. on pp. 2, 4).
- Huchra, J. et al. (1983), *A survey of galaxy redshifts. IV - The data*, ApJS **52** 89 (cit. on p. 24).
- Humason, M. L. (1927), *Radial Velocities in Two Nebulae*, PASP **39** 317 (cit. on p. 2).
- Icke, V. (1973), *Formation of Galaxies inside Clusters*, A&A **27** 1 (cit. on p. 28).
- Jackson, J. C. (1972), *A critique of Rees's theory of primordial gravitational radiation*, MNRAS **156** 1P, arXiv: 0810.3908 (cit. on p. 78).
- Jain, B., U. Seljak and S. White (2000), *Ray-tracing Simulations of Weak Lensing by Large-Scale Structure*, ApJ **530** 547, eprint: astro-ph/9901191 (cit. on p. 98).
- Jenkins, A. et al. (2001), *The mass function of dark matter haloes*, MNRAS **321** 372, eprint: astro-ph/0005260 (cit. on pp. 20, 21).
- Jeong, D., F. Schmidt and C. M. Hirata (2012), *Large-scale clustering of galaxies in general relativity*, Phys. Rev. D **85**, 023504 023504, arXiv: 1107.5427 (cit. on pp. 76, 79, 83).
- Jing, Y. P., Y. Suto and H. J. Mo (2007), *The Dependence of Dark Halo Clustering on Formation Epoch and Concentration Parameter*, ApJ **657** 664, eprint: astro-ph/0610099 (cit. on pp. 24, 47).
- Jung, I., J. Lee and S. K. Yi (2014), *Effects of Large-scale Environment on the Assembly History of Central Galaxies*, ApJ **794**, 74 74, arXiv: 1409.0860 (cit. on p. 47).
- Kaiser, N. (1984), *On the spatial correlations of Abell clusters*, ApJ **284** L9 (cit. on pp. 24, 27).
- (1987), *Clustering in real space and in redshift space*, MNRAS **227** 1 (cit. on pp. 75, 84, 98).
- (1992), *Weak gravitational lensing of distant galaxies*, ApJ **388** 272 (cit. on p. 80).
- Kiessling, A. et al. (2011), *SUNGLASS: a new weak-lensing simulation pipeline*, MNRAS **414** 2235, arXiv: 1011.1476 (cit. on pp. 81, 98).
- Kitzbichler, M. G. and S. D. White (2007), *The high-redshift galaxy population in hierarchical galaxy formation models*, MNRAS **376** 2, eprint: astro-ph/0609636 (cit. on p. 75).
- Knollmann, S. R. and A. Knebe (2009), *AHF: Amiga's Halo Finder*, ApJS **182** 608, arXiv: 0904.3662 (cit. on pp. 49, 53).
- Komatsu, E. et al. (2009), *Five-Year Wilkinson Microwave Anisotropy Probe Observations: Cosmological Interpretation*, ApJS **180** 330, arXiv: 0803.0547 (cit. on p. 30).
- Lacey, C. and S. Cole (1993), *Merger rates in hierarchical models of galaxy formation*, MNRAS **262** 627 (cit. on p. 53).
- Lahav, O. et al. (1991), *Dynamical effects of the cosmological constant*, MNRAS **251** 128 (cit. on p. 27).
- Laigle, C. et al. (2015), *Swirling around filaments: are large-scale structure vortices spinning up dark haloes?*, MNRAS **446** 2744, arXiv: 1310.3801 (cit. on p. 65).

- Laureijs, R. et al. (2011), *Euclid Definition Study Report*, astro-ph.CO 1110.3193, arXiv: 1110.3193 (cit. on pp. 8, 75).
- Lee, J. and U. Pen (2000), *Cosmic Shear from Galaxy Spins*, ApJ **532** L5, eprint: arXiv:astro-ph/9911328 (cit. on pp. 28, 70).
- Lemaître, G. (1927), *Un Univers homogène de masse constante et de rayon croissant rendant compte de la vitesse radiale des nébuleuses extra-galactiques*, Annales de la Société Scientifique de Bruxelles **47** 49 (cit. on p. 2).
- Lemze, D. et al. (2012), *Profiles of Dark Matter Velocity Anisotropy in Simulated Clusters*, ApJ **752**, 141 141, arXiv: 1106.6048 (cit. on p. 66).
- Levi, M. et al. (2013), *The DESI Experiment, a whitepaper for Snowmass 2013*, astro-ph.CO 1308.0847, arXiv: 1308.0847 (cit. on p. 75).
- Lewis, A. and A. Challinor (2011), *CAMB: Code for Anisotropies in the Microwave Background*, Astrophysics Source Code Library 2026 (cit. on p. 11).
- Li, R. et al. (2013), *Assembly bias of dwarf-sized dark matter haloes*, MNRAS **435** 3592, arXiv: 1308.4204 (cit. on pp. 24, 47).
- Li, Y., H. J. Mo and L. Gao (2008), *On halo formation times and assembly bias*, MNRAS **389** 1419, arXiv: 0803.2250 (cit. on pp. 47, 53).
- Libeskind, N. I., Y. Hoffman and S. Gottlöber (2014), *The velocity shear and vorticity across redshifts and non-linear scales*, MNRAS **441** 1974, arXiv: 1310.5706 (cit. on p. 65).
- Libeskind, N. I., Y. Hoffman, M. Steinmetz et al. (2013), *Cosmic Vorticity and the Origin Halo Spins*, ApJ **766**, L15 L15, arXiv: 1212.1454 (cit. on p. 65).
- Lin, C. C., L. Mestel and F. H. Shu (1965), *The Gravitational Collapse of a Uniform Spheroid.*, ApJ **142** 1431 (cit. on p. 28).
- Lin, Y.-T. et al. (2016), *On Detecting Halo Assembly Bias with Galaxy Populations*, ApJ **819**, 119 119, arXiv: 1504.07632 (cit. on p. 48).
- Ludlow, A. D., M. Borzyszkowski and C. Porciani (2014), *The formation of CDM haloes - I. Collapse thresholds and the ellipsoidal collapse model*, (LBP14), MNRAS **445** 4110 (cit. on pp. 28–31, 35–37, 43, 45, 48, 64, 67, 68, 70, 101).
- Ludlow, A. D., J. F. Navarro et al. (2011), *The density and pseudo-phase-space density profiles of cold dark matter haloes*, MNRAS **415** 3895, arXiv: 1102.0002 (cit. on p. 66).
- Ludlow, A. D. and C. Porciani (2011), *The peaks formalism and the formation of cold dark matter haloes*, MNRAS **413** 1961, arXiv: 1011.2493 (cit. on p. 19).
- Lynden-Bell, D. (1964), *On Large-Scale Instabilities during Gravitational Collapse and the Evolution of Shrinking Maclaurin Spheroids.*, ApJ **139** 1195 (cit. on p. 28).
- Maartens, R. et al. (2015), *Cosmology with the SKA – overview*, astro-ph 1501.04076, arXiv: 1501.04076 (cit. on pp. 75, 94).
- Matsubara, T. (2000), *The Gravitational Lensing in Redshift-Space Correlation Functions of Galaxies and Quasars*, ApJ **537** L77, eprint: astro-ph/0004392 (cit. on p. 75).
- McDonald, P. (2009), *Gravitational redshift and other redshift-space distortions of the imaginary part of the power spectrum*, J. Cosmology Astropart. Phys. **11**, 026 026, arXiv: 0907.5220 (cit. on pp. 76, 84, 94, 95).
- McDonald, P. and U. Seljak (2009), *How to evade the sample variance limit on measurements of redshift-space distortions*, J. Cosmology Astropart. Phys. **10**, 007 007, arXiv: 0810.0323 (cit. on p. 97).
- Merson, A. I. et al. (2013), *Lightcone mock catalogues from semi-analytic models of galaxy formation - I. Construction and application to the BzK colour selection*, MNRAS **429** 556, arXiv: 1206.4049 (cit. on p. 75).

- Milillo, I. et al. (2015), *Missing link: A nonlinear post-Friedmann framework for small and large scales*, Phys. Rev. D **92**, 023519 023519, arXiv: 1502.02985 (cit. on p. 76).
- Mo, H. J. and S. D. White (1996), *An analytic model for the spatial clustering of dark matter haloes*, MNRAS **282** 347, eprint: astro-ph/9512127 (cit. on p. 73).
- Montanari, F. and R. Durrer (2015), *Measuring the lensing potential with tomographic galaxy number counts*, J. Cosmology Astropart. Phys. **10**, 070 070, arXiv: 1506.01369 (cit. on pp. 76, 89, 99).
- More, S., B. Diemer and A. V. Kravtsov (2015), *The Splashback Radius as a Physical Halo Boundary and the Growth of Halo Mass*, ApJ **810**, 36 36, arXiv: 1504.05591 (cit. on pp. 19, 54).
- More, S., A. V. Kravtsov et al. (2011), *The Overdensity and Masses of the Friends-of-friends Halos and Universality of Halo Mass Function*, ApJS **195**, 4 4, arXiv: 1103.0005 (cit. on p. 40).
- Moster, B. P., T. Naab and S. D. White (2013), *Galactic star formation and accretion histories from matching galaxies to dark matter haloes*, MNRAS **428** 3121, arXiv: 1205.5807 (cit. on pp. 48, 52).
- Navarro, J. F., C. S. Frenk and S. D. White (1997), *A Universal Density Profile from Hierarchical Clustering*, ApJ **490** 493, eprint: arXiv:astro-ph/9611107 (cit. on pp. 19, 53).
- Navarro, J. F., A. D. Ludlow et al. (2010), *The diversity and similarity of simulated cold dark matter haloes*, MNRAS **402** 21, arXiv: 0810.1522 (cit. on p. 66).
- Neto, A. F. et al. (2007), *The statistics of Lambda CDM halo concentrations*, MNRAS **381** 1450, arXiv: 0706.2919 (cit. on p. 63).
- Norman, D. J. and L. L. Williams (2000), *Weak Lensing-Induced Correlations between 1 JY QSOs and APM Galaxies on Angular Scales of a Degree*, AJ **119** 2060, eprint: astro-ph/9908177 (cit. on p. 92).
- Pápai, P. and I. Szapudi (2008), *Non-perturbative effects of geometry in wide-angle redshift distortions*, MNRAS **389** 292, arXiv: 0802.2940 (cit. on p. 85).
- Partridge, R. B. and P. J. Peebles (1967), *Are Young Galaxies Visible?*, ApJ **147** 868 (cit. on pp. 12, 27).
- Paz, D. J., F. Stasyszyn and N. D. Padilla (2008), *Angular momentum-large-scale structure alignments in Λ CDM models and the SDSS*, MNRAS **389** 1127, arXiv: 0804.4477 (cit. on p. 65).
- Peebles, P. J. (1967), *The Gravitational Instability of the Universe*, ApJ **147** 859 (cit. on pp. 12, 27).
- (1969), *Origin of the Angular Momentum of Galaxies*, ApJ **155** 393 (cit. on p. 53).
- (1973), *Statistical Analysis of Catalogs of Extragalactic Objects. I. Theory*, ApJ **185** 413 (cit. on p. 87).
- (1980), *The large-scale structure of the universe*, Princeton University Press (cit. on pp. 12, 27, 28, 67, 68).
- Perlmutter, S. et al. (1999), *Measurements of Ω and Λ from 42 High-Redshift Supernovae*, ApJ **517** 565, eprint: astro-ph/9812133 (cit. on p. 8).
- Pichon, C. and F. Bernardeau (1999), *Vorticity generation in large-scale structure caustics*, A&A **343** 663, eprint: astro-ph/9902142 (cit. on p. 65).
- Pichon, C., D. Pogosyan et al. (2011), *Rigging dark haloes: why is hierarchical galaxy formation consistent with the inside-out build-up of thin discs?*, MNRAS **418** 2493, arXiv: 1105.0210 (cit. on p. 65).
- Pillepich, A., C. Porciani and O. Hahn (2010), *Halo mass function and scale-dependent bias from N-body simulations with non-Gaussian initial conditions*, MNRAS **402** 191, arXiv: 0811.4176 (cit. on pp. 30, 31).
- Planck Collaboration et al. (2014a), *Planck 2013 results. XVI. Cosmological parameters*, A&A **571**, A16 A16, arXiv: 1303.5076 (cit. on pp. 4, 6, 8, 11, 12, 49).
- (2014b), *Planck 2013 results. XXIII. Isotropy and statistics of the CMB*, A&A **571**, A23 A23, arXiv: 1303.5083 (cit. on p. 11).

- Porciani, C., A. Dekel and Y. Hoffman (2002), *Testing tidal-torque theory - II. Alignment of inertia and shear and the characteristics of protohaloes*, MNRAS **332** 339, eprint: arXiv:astro-ph/0105165 (cit. on pp. 28, 29, 64, 70).
- Pound, R. V. and G. A. Rebka (1960), *Apparent Weight of Photons*, Physical Review Letters **4** 337 (cit. on p. 3).
- Pozzetti, L. et al. (2016), *Modelling the number density of H α emitters for future spectroscopic near-IR space missions*, A&A **590**, A3 A3, arXiv: 1603.01453 (cit. on pp. 90, 91).
- Prada, F. et al. (2006), *How Far Do They Go? The Outer Structure of Galactic Dark Matter Halos*, ApJ **645** 1001, eprint: astro-ph/0506432 (cit. on pp. 41, 48, 58).
- Press, W. H. and P. Schechter (1974), *Formation of Galaxies and Clusters of Galaxies by Self-Similar Gravitational Condensation*, ApJ **187** 425 (cit. on pp. 20, 21, 27, 58, 72, 73).
- Pueblas, S. and R. Scoccimarro (2009), *Generation of vorticity and velocity dispersion by orbit crossing*, Phys. Rev. D **80**, 043504 043504, arXiv: 0809.4606 (cit. on p. 65).
- Quinn, T. et al. (1997), *Time stepping N-body simulations*, ArXiv Astrophysics e-prints, eprint: arXiv:astro-ph/9710043 (cit. on p. 16).
- Raccanelli, A., D. Bertacca, O. Doré et al. (2014), *Large-scale 3D galaxy correlation function and non-Gaussianity*, J. Cosmology Astropart. Phys. **8**, 022 022, arXiv: 1306.6646 (cit. on p. 95).
- Raccanelli, A., D. Bertacca, D. Jeong et al. (2016), *Doppler term in the galaxy two-point correlation function: wide-angle, velocity, Doppler lensing and cosmic acceleration effects*, astrp-ph 1602.03186, arXiv: 1602.03186 (cit. on pp. 76, 84, 94).
- Raccanelli, A., D. Bertacca, R. Maartens et al. (2016), *Lensing and time-delay contributions to galaxy correlations*, General Relativity and Gravitation **48**, 84 84 (cit. on p. 76).
- Raccanelli, A., F. Montanari et al. (2016), *Cosmological measurements with general relativistic galaxy correlations*, J. Cosmology Astropart. Phys. **5**, 009 009, arXiv: 1505.06179 (cit. on p. 76).
- Raccanelli, A., L. Samushia and W. J. Percival (2010), *Simulating redshift-space distortions for galaxy pairs with wide angular separation*, MNRAS **409** 1525, arXiv: 1006.1652 (cit. on p. 85).
- Rasia, E., G. Tormen and L. Moscardini (2004), *A dynamical model for the distribution of dark matter and gas in galaxy clusters*, MNRAS **351** 237, eprint: astro-ph/0309405 (cit. on p. 66).
- Rees, M. J. and D. W. Sciama (1968), *Large-scale Density Inhomogeneities in the Universe*, Nature **217** 511 (cit. on p. 76).
- Rein, H. (2012), *A proposal for community driven and decentralized astronomical databases and the Open Exoplanet Catalogue*, ArXiv e-prints, arXiv: 1211.7121 (cit. on p. 1).
- Riess, A. G. et al. (1998), *Observational Evidence from Supernovae for an Accelerating Universe and a Cosmological Constant*, AJ **116** 1009, eprint: astro-ph/9805201 (cit. on p. 8).
- Rigopoulos, G. and W. Valkenburg (2015), *On the accuracy of N-body simulations at very large scales*, MNRAS **446** 677, arXiv: 1308.0057 (cit. on p. 76).
- Riotto, A. (2010), *Particle cosmology*, ArXiv e-prints, arXiv: 1010.2642 (cit. on p. 11).
- Robertson, B. E. et al. (2009), *Collapse Barriers and Halo Abundance: Testing the Excursion Set Ansatz*, ApJ **696** 636, arXiv: 0812.3148 (cit. on pp. 28, 46, 70).
- Robertson, H. P. (1935), *Kinematics and World-Structure*, ApJ **82** 284 (cit. on p. 3).
- Romano-Díaz, E. et al. (2017), *ZOMG II: Does the halo assembly history influence central galaxies and gas accretion?*, ArXiv e-prints, arXiv: 1701.02743 (cit. on pp. 48, 103).
- Rubin, V., N. Thonnard and W. K. Ford Jr. (1978), *Extended rotation curves of high-luminosity spiral galaxies. IV - Systematic dynamical properties, SA through SC*, ApJ **225** L107 (cit. on p. 6).
- Sachs, R. K. and A. M. Wolfe (1967), *Perturbations of a Cosmological Model and Angular Variations of the Microwave Background*, ApJ **147** 73 (cit. on pp. 3, 76).

- Salvador-Solé, E., J. M. Solanes and A. Manrique (1998), *Merger versus Accretion and the Structure of Dark Matter Halos*, ApJ **499** 542, eprint: astro-ph/9712080 (cit. on p. 57).
- Sargent, W. L. and E. L. Turner (1977), *A statistical method for determining the cosmological density parameter from the redshifts of a complete sample of galaxies*, ApJ **212** L3 (cit. on p. 78).
- Sasaki, M. (1987), *The magnitude-redshift relation in a perturbed Friedmann universe*, MNRAS **228** 653 (cit. on p. 75).
- Schäfer, J. and K. Strimmer (2005), *A Shrinkage Approach to Large-Scale Covariance Matrix Estimation and Implications for Functional Genomics*, Statistical Applications in Genetics and Molecular Biology **Vol. 4 [2005], No. 1** Article 32 (cit. on p. 89).
- Schmidt, F. et al. (2009), *Size Bias in Galaxy Surveys*, Physical Review Letters **103**, 051301 051301, arXiv: 0904.4702 (cit. on p. 83).
- Schneider, J. et al. (2011), *Defining and cataloging exoplanets: the exoplanet.eu database*, A&A **532**, A79 A79, arXiv: 1106.0586 (cit. on p. 1).
- Schneider, P. (2003), *Gravitational lensing as a probe of structure*, ArXiv Astrophysics e-prints, eprint: astro-ph/0306465 (cit. on pp. 3, 6).
- Scranton, R. et al. (2005), *Detection of Cosmic Magnification with the Sloan Digital Sky Survey*, ApJ **633** 589, eprint: astro-ph/0504510 (cit. on p. 92).
- Sheth, R. K., H. J. Mo and G. Tormen (2001), *Ellipsoidal collapse and an improved model for the number and spatial distribution of dark matter haloes*, MNRAS **323** 1, eprint: arXiv:astro-ph/9907024 (cit. on pp. 21, 28, 33, 45, 46, 69, 70, 73, 101).
- Sheth, R. K. and G. Tormen (1999), *Large-scale bias and the peak background split*, MNRAS **308** 119, eprint: arXiv:astro-ph/9901122 (cit. on p. 28).
- (2004), *On the environmental dependence of halo formation*, MNRAS **350** 1385, eprint: astro-ph/0402237 (cit. on p. 47).
- Singh, S. (2004), *Big Bang: the Origin of the Universe* (cit. on p. 1).
- Slipher, V. M. (1913), *The radial velocity of the Andromeda Nebula*, Lowell Observatory Bulletin **2** 56 (cit. on p. 2).
- (1915), *Spectrographic Observations of Nebulae*, Popular Astronomy **23** 21 (cit. on p. 2).
- Sofue, Y. and V. Rubin (2001), *Rotation Curves of Spiral Galaxies*, ARA&A **39** 137, eprint: astro-ph/0010594 (cit. on p. 6).
- Sousbie, T., H. Courtois et al. (2008), *MoLUSC: A Mock Local Universe Survey Constructor*, ApJ **678**, 569-577 569, eprint: astro-ph/0612166 (cit. on p. 75).
- Sousbie, T., C. Pichon et al. (2008), *The 3D skeleton: tracing the filamentary structure of the Universe*, MNRAS **383** 1655, arXiv: 0707.3123 (cit. on p. 65).
- Springel, V. (2005), *The cosmological simulation code GADGET-2*, MNRAS **364** 1105, eprint: astro-ph/0505010 (cit. on pp. 15, 30, 49).
- Springel, V., C. S. Frenk and S. D. White (2006), *The large-scale structure of the Universe*, Nature **440** 1137, eprint: astro-ph/0604561 (cit. on pp. 21, 22).
- Springel, V., S. D. White et al. (2005), *Simulations of the formation, evolution and clustering of galaxies and quasars*, Nature **435** 629, eprint: astro-ph/0504097 (cit. on pp. 20–22).
- Springel, V., N. Yoshida and S. D. White (2001), *GADGET: a code for collisionless and gasdynamical cosmological simulations*, New Astronomy **6** 79, eprint: astro-ph/0003162 (cit. on p. 30).
- Squires, G. et al. (1996), *The Dark Matter, Gas, and Galaxy Distributions in Abell 2218: A Weak Gravitational Lensing and X-Ray Analysis*, ApJ **461** 572, eprint: astro-ph/9507008 (cit. on p. 6).
- Sunayama, T. et al. (2016), *The scale-dependence of halo assembly bias*, MNRAS **458** 1510, arXiv: 1509.06417 (cit. on p. 47).

- Tassev, S., M. Zaldarriaga and D. J. Eisenstein (2013), *Solving large scale structure in ten easy steps with COLA*, J. Cosmology Astropart. Phys. **6**, 036 036, arXiv: 1301.0322 (cit. on p. 85).
- Thomas, D. B., M. Bruni and D. Wands (2015), *The fully non-linear post-Friedmann frame-dragging vector potential: magnitude and time evolution from N-body simulations*, MNRAS **452** 1727, arXiv: 1501.00799 (cit. on p. 76).
- Tinker, J. et al. (2008), *Toward a Halo Mass Function for Precision Cosmology: The Limits of Universality*, ApJ **688**, 709-728 709, arXiv: 0803.2706 (cit. on p. 21).
- Tissera, P. B. et al. (2010), *Dark matter response to galaxy formation*, MNRAS **406** 922, arXiv: 0911.2316 (cit. on p. 67).
- Tormen, G., F. R. Bouchet and S. D. White (1997), *The structure and dynamical evolution of dark matter haloes*, MNRAS **286** 865, eprint: astro-ph/9603132 (cit. on p. 20).
- Turner, E. L. (1980), *The effect of undetected gravitational lenses on statistical measures of quasar evolution*, ApJ **242** L135 (cit. on pp. 75, 91).
- Turner, E. L., J. P. Ostriker and J. R. Gott III (1984), *The statistics of gravitational lenses - The distributions of image angular separations and lens redshifts*, ApJ **284** 1 (cit. on p. 75).
- Vale, C. and M. White (2003), *Simulating Weak Lensing by Large-Scale Structure*, ApJ **592** 699, eprint: astro-ph/0303555 (cit. on p. 98).
- van der Kruit, P. C. and R. J. Allen (1978), *The kinematics of spiral and irregular galaxies*, ARA&A **16** 103 (cit. on p. 6).
- Walker, A. G. (1937), *On Milne's Theory of World-Structure*, Proceedings of the London Mathematical Society **s2-42** 90, eprint: <http://plms.oxfordjournals.org/content/s2-42/1/90.full.pdf+html> (cit. on p. 3).
- Wambsganss, J., R. Cen and J. P. Ostriker (1998), *Testing Cosmological Models by Gravitational Lensing. I. Method and First Applications*, ApJ **494** 29 (cit. on p. 98).
- Wandelt, B. D., E. Hivon and K. M. Górski (2001), *Cosmic microwave background anisotropy power spectrum statistics for high precision cosmology*, Phys. Rev. D **64**, 083003 083003, eprint: astro-ph/0008111 (cit. on p. 87).
- Wang, H. Y., H. J. Mo and Y. P. Jing (2007), *Environmental dependence of cold dark matter halo formation*, MNRAS **375** 633, eprint: astro-ph/0608690 (cit. on pp. 48, 52, 102).
- Wang, H. et al. (2011), *Internal properties and environments of dark matter haloes*, MNRAS **413** 1973, arXiv: 1007.0612 (cit. on p. 35).
- Wang, J. et al. (2011), *Assembly history and structure of galactic cold dark matter haloes*, MNRAS **413** 1373, arXiv: 1008.5114 (cit. on pp. 47, 48, 52, 57, 102).
- Wang, X. et al. (2014), *Kinematic Morphology of Large-scale Structure: Evolution from Potential to Rotational Flow*, ApJ **793**, 58 58, arXiv: 1309.5305 (cit. on p. 65).
- Wechsler, R. H., J. S. Bullock et al. (2002), *Concentrations of Dark Halos from Their Assembly Histories*, ApJ **568** 52, eprint: astro-ph/0108151 (cit. on p. 57).
- Wechsler, R. H., A. R. Zentner et al. (2006), *The Dependence of Halo Clustering on Halo Formation History, Concentration, and Occupation*, ApJ **652** 71, eprint: astro-ph/0512416 (cit. on pp. 24, 47).
- Weinberg, S. (1993), *The first three minutes : a modern view of the origin of the universe* (cit. on p. 1).
- White, M. and W. Hu (2000), *A New Algorithm for Computing Statistics of Weak Lensing by Large-Scale Structure*, ApJ **537** 1, eprint: astro-ph/9909165 (cit. on pp. 81, 98).
- White, S. D. and M. J. Rees (1978), *Core condensation in heavy halos - A two-stage theory for galaxy formation and clustering*, MNRAS **183** 341 (cit. on p. 19).
- White, S. D. and J. Silk (1979), *The growth of aspherical structure in the universe - Is the local supercluster an unusual system*, ApJ **231** 1 (cit. on p. 28).

- Yahya, S. et al. (2015), *Cosmological performance of SKA HI galaxy surveys*, MNRAS **450** 2251, arXiv: 1412.4700 (cit. on p. 94).
- Yoo, J. (2009), *Complete treatment of galaxy two-point statistics: Gravitational lensing effects and redshift-space distortions*, Phys. Rev. D **79**, 023517 023517, arXiv: 0808.3138 (cit. on pp. 76, 79, 82, 84).
- Yoo, J., A. L. Fitzpatrick and M. Zaldarriaga (2009), *New perspective on galaxy clustering as a cosmological probe: General relativistic effects*, Phys. Rev. D **80**, 083514 083514, arXiv: 0907.0707 (cit. on pp. 76, 79, 82).
- Yoo, J., N. Hamaus et al. (2012), *Going beyond the Kaiser redshift-space distortion formula: A full general relativistic account of the effects and their detectability in galaxy clustering*, Phys. Rev. D **86**, 063514 063514, arXiv: 1109.0998 (cit. on pp. 76, 94, 95).
- Yoo, J. and U. Seljak (2015), *Wide-angle effects in future galaxy surveys*, MNRAS **447** 1789, arXiv: 1308.1093 (cit. on p. 76).
- Zaroubi, S. and Y. Hoffman (1996), *Clustering in Redshift Space: Linear Theory*, ApJ **462** 25 (cit. on p. 84).
- Zel'Dovich, Y. B. (1970), *Gravitational instability: An approximate theory for large density perturbations.*, A&A **5** 84 (cit. on p. 28).
- Zemp, M. (2014), *On Physical Scales of Dark Matter Halos*, ApJ **792**, 124 124, arXiv: 1312.4629 (cit. on pp. 19, 38, 56).
- Zentner, A. R. (2007), *The Excursion Set Theory of Halo Mass Functions, Halo Clustering, and Halo Growth*, International Journal of Modern Physics D **16** 763, eprint: astro-ph/0611454 (cit. on pp. 49, 67).
- Zhang, Y. et al. (2009), *The Spin and Orientation of Dark Matter Halos Within Cosmic Filaments*, ApJ **706** 747, arXiv: 0906.1654 (cit. on p. 65).
- Zhao, D. H. et al. (2003), *Mass and Redshift Dependence of Dark Halo Structure*, ApJ **597** L9, eprint: astro-ph/0309375 (cit. on p. 57).
- Zhu, G. et al. (2006), *The Dependence of the Occupation of Galaxies on the Halo Formation Time*, ApJ **639** L5, eprint: astro-ph/0601120 (cit. on p. 47).
- Zwicky, F. (1933), *Die Rotverschiebung von extragalaktischen Nebeln*, Helvetica Physica Acta **6** 110 (cit. on p. 5).

Appendix

Collapse thresholds for SO-haloes

In order to test the sensitivity of our results to our adopted (FOF) halo definition, we have repeated the analysis on dark-matter haloes identified using a spherical overdensity (SO) algorithm. Our SO halo finder identifies local maxima in the evolved density field and grows spheres around them until a given density contrast, Δ_{SO} , is reached. For this analysis we have adopted three different overdensity values: $\Delta_{\text{SO}} = 100, 200$ and 500 . All aspects of the analysis were carried out as described in section 2.3.3, including modifications to the model freezing factor, f , required to match the ($z = 0$) SO-halo overdensities at $z = 0$.

In fig. A.1 we plot the resulting $\delta - \delta$ (for collapse at z_c rather than at $z = 0$). In general, we find that all conclusions drawn from our analysis of FOF haloes remains valid for SO haloes as well, suggesting that our interpretation should not be affected by halo definition.

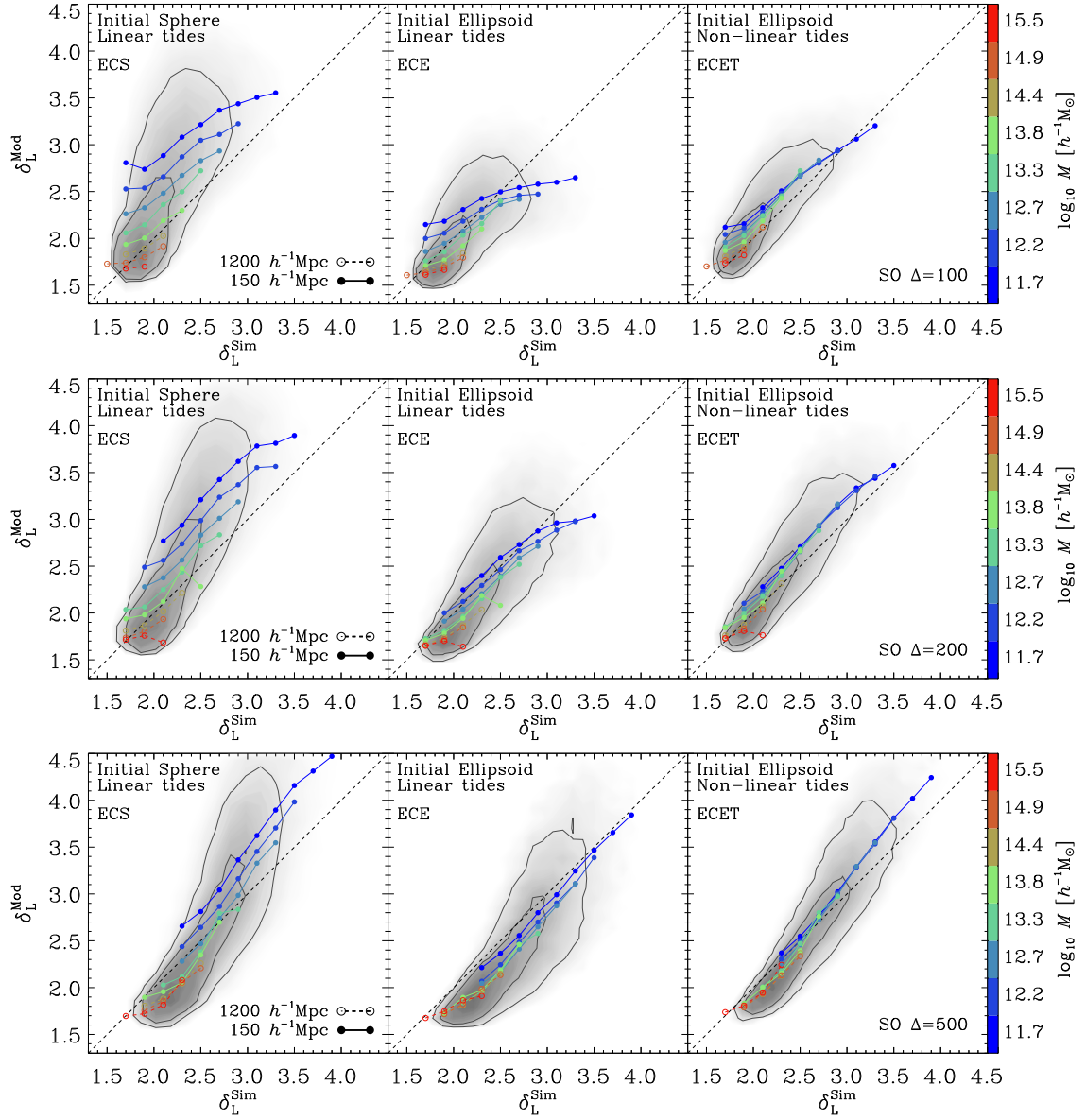


Figure A.1: Same as fig. 2.8 but for haloes identified using the spherical overdensity algorithm with density contrast thresholds of 100, 200 and 500.

Likelihood-ratio test

Let \mathbf{x} be a Gaussian data vector with mean \mathbf{m} and covariance matrix $\mathbf{\Sigma}$. Let \mathbf{M} be a perfect theoretical model for \mathbf{m} , i.e. $\mathbf{M} = \mathbf{m}$. The likelihood of \mathbf{M} given the data is proportional to the probability of observing the data under the hypothesis that \mathbf{M} is true, i.e. $\mathcal{L}(\mathbf{M}|\mathbf{x}) \propto \exp(-\chi^2/2)$ with $\chi^2 = (\mathbf{x} - \mathbf{M})^T \cdot \mathbf{\Sigma}^{-1} \cdot (\mathbf{x} - \mathbf{M})$. Let also consider an imperfect or incomplete model \mathbf{N} such that $\mathbf{m} - \mathbf{N} = \mathbf{B}$. The likelihood ratio between \mathbf{M} and \mathbf{N} is $\mathcal{L}(\mathbf{M}|\mathbf{x})/\mathcal{L}(\mathbf{N}|\mathbf{x}) = \exp(-\Delta\chi^2/2)$ with

$$\begin{aligned} \Delta\chi^2 &= (\mathbf{x} - \mathbf{N})^T \cdot \mathbf{\Sigma}^{-1} \cdot (\mathbf{x} - \mathbf{N}) - (\mathbf{x} - \mathbf{M})^T \cdot \mathbf{\Sigma}^{-1} \cdot (\mathbf{x} - \mathbf{M}) \\ &= (\mathbf{B} + \mathbf{e})^T \cdot \mathbf{\Sigma}^{-1} \cdot (\mathbf{B} + \mathbf{e}) - \mathbf{e}^T \cdot \mathbf{\Sigma}^{-1} \cdot \mathbf{e} \\ &= \mathbf{B}^T \cdot \mathbf{\Sigma}^{-1} \cdot \mathbf{B} + 2\mathbf{e}^T \cdot \mathbf{\Sigma}^{-1} \cdot \mathbf{B}, \end{aligned} \quad (\text{B.1})$$

where we have decomposed the data vector in the signal and noise components, $\mathbf{x} = \mathbf{m} + \mathbf{e} = \mathbf{M} + \mathbf{e}$, and used the symmetry of the covariance matrix. The fact that the difference in the log-likelihoods depends linearly on \mathbf{e} implies that $\Delta\chi^2$ follows a Gaussian distribution over an ensemble of realisations of the data vector. Its expectation is

$$\mu = E[\Delta\chi^2] = \mathbf{B}^T \cdot \mathbf{\Sigma}^{-1} \cdot \mathbf{B}. \quad (\text{B.2})$$

Similarly, its variance is

$$E[(\Delta\chi^2 - \mu)^2] = 4\mu. \quad (\text{B.3})$$

In a classic likelihood-ratio test for a simple hypothesis, the probability distribution of $\Delta\chi^2$ obtained under a model (i.e. assuming that this model perfectly describes \mathbf{m}) is compared against the corresponding distribution obtained under an alternative model. If the covariance matrix of the data does not depend on the model, the two $\Delta\chi^2$ distributions differ only in the sign of their mean values (in fact models M and N are switched in the alternative hypothesis and the sign of $\Delta\chi^2$ is reversed). The test rejects one of the models if the two distributions of $\Delta\chi^2$ are clearly separated with respect to their intrinsic dispersion. Since the distance between the averages is 2μ and the RMS value of each distribution is $2\sqrt{\mu}$, the ratio $2\mu/(2\sqrt{\mu}) = \sqrt{\mu}$ is commonly referred to as the signal-to-noise ratio S/N . If, however, the covariance matrix is model dependent, then the comparison should be done between two Gaussian distributions with different mean values $\mu_M = \mathbf{B}^T \cdot \mathbf{\Sigma}_M^{-1} \cdot \mathbf{B}$ and $\mu_N = -\mathbf{B}^T \cdot \mathbf{\Sigma}_N^{-1} \cdot \mathbf{B}$ as well as variances $4\mu_M$ and $4\mu_N$, respectively.

List of Figures

1.1	Observational evidence for dark matter.	6
1.2	Linear power spectrum of perturbations in the density field.	11
1.3	Evolution of radius and density of the spherical collapse model.	14
1.4	Slice through a simulation indicating density, with a zoom panel on a single halo. . . .	18
1.5	Standard deviation of smoothed linear density contrast as function of smoothing length.	20
1.6	Observed and simulated distribution of galaxies.	22
1.7	Two-point correlation function of matter and haloes of different mass from a simulation.	23
2.1	Linear density contrast predicted by the ellipsoidal collapse model versus measurements from simulations.	33
2.2	Evolution of the external tidal field acting on the haloes measured from simulations. .	34
2.3	Comparison of the measured linear density contrast at the sights of protohaloes with the prediction of the ellipsoidal collapse model including the non-linear evolution of the tidal field.	36
2.4	Median evolution of the occupied volumes of ellipsoids following the collapse of all particles of haloes at redshift zero.	37
2.5	Evolution of the volume of an ellipsoid enclosing the final mass of an example halo. The estimation of the collapse time is highlighted.	38
2.6	Dependence of the collapse and formation time on halo mass.	39
2.7	Median radial velocity profiles of haloes for different mass and initial density.	41
2.8	Comparison of the measured linear density contrast at the sights of protohaloes compared to the prediction of collapse models enforcing halo formation at the collapse time. . . .	42
2.9	Linear density contrast as a function of mass as measured in the simulations and predicted by the models.	43
2.10	Linear density contrast as a function of the size of the top-hat smoothing kernel for an example halo. The crossing of several collapse thresholds are indicated.	44
3.1	The volume of the collapsing patch of two example haloes simulated at different numerical resolutions is shown.	50
3.2	Probability distribution of the collapse time of haloes in a mass bin.	51
3.3	Two-point correlation function of haloes binned in collapse time.	51
3.4	Matter distribution of the D-ZOMG haloes at redshift zero.	54
3.5	Mass accretion histories of the D-ZOMG haloes at highest numerical resolution.	56
3.6	Mean mass enclosed by the splashback radius of accreting and stalled haloes as function of expansion factor.	56
3.7	Evolution of the volume of ellipsoids enclosing different masses centred on the patch of particles forming a halo today.	57

3.8	Radial phase-space diagram for two example haloes.	59
3.9	The distribution of particles around two example haloes at redshift zero and in the initial conditions of the simulations. Selected particles are highlighted to indicate the accretion pattern.	60
3.10	Particle distribution coloured according to the radial velocity around an accreting and stalled halo.	61
3.11	Indicators of the dynamical state of the D-ZOMG haloes.	63
3.12	Profiles of the tangential velocity variance and velocity anisotropy of the D-ZOMG haloes.	65
3.13	Velocity anisotropy versus the slope of the mass-density profile measured in different radial shells.	66
3.14	Map of the linear density field centred on the protohalo, shown for two example haloes.	67
3.15	Rendering of the linear density field around Supay.	68
3.16	Linear density contrast as function of the size of the top-hat smoothing kernel for the D-ZOMG haloes.	69
3.17	Ellipticity of the linear density field as function of the size of the top-hat smoothing kernel for the D-ZOMG haloes.	69
3.18	Predicted mass accretion histories for the D-ZOMG haloes from their excursion-set trajectories for different collapse barriers.	70
4.1	Schematic diagram illustrating the sequence of main processing steps in the LIGER method.	76
4.2	Schematic illustration of the real- and redshift-space position of an observed galaxy.	77
4.3	Schematic illustrating the shift of galaxies or N-body particles for the construction of the light cone.	81
4.4	Wedge plots extracted from a sample like cone.	86
4.5	Expected characteristics of the Euclid and SKA2 galaxy-redshift survey.	89
4.6	Angular power spectra for an Euclid-like survey.	90
4.7	Goodness of the fit of the approximate clustering signal from light cones only including the Kaiser and Doppler effect to the angular power spectrum constructed using the full LIGER method.	91
4.8	Goodness of the fit of the approximate clustering signal from light cones only including the Kaiser, Doppler and convergence effect to the angular power spectrum constructed using the full LIGER method.	92
4.9	The dependence of the RMS statistical error on the angular power spectrum as function of the sky coverage.	93
4.10	The angular cross-power spectra between two galaxy populations and two low redshift bins for the planned SKA2 survey.	95
4.11	The difference between the angular cross-power spectra $\Delta\hat{C}_l$ as an observable in case of the SKA2 survey.	96
4.12	Goodness of the fit of $\Delta\hat{C}_l$ between an approximate model excluding some Doppler effects to the signal constructed using the full LIGER method.	97
A.1	Same as fig. 2.8 but for haloes identified using the spherical overdensity algorithm with density contrast thresholds of 100, 200 and 500.	120

List of Tables

2.1	Parameters obtained from the linear fit of the collapse time to the logarithm of halo mass for different halo identification schemes.	40
3.1	Properties of the D-ZOMG haloes from the highest resolution simulation.	53

Acknowledgements

During the past years at the AIfA I received support from many people for which I am thankful. In particular, I show my gratitude to Prof. Cristiano Porciani for giving me the opportunity to work in his research group and for the continuous support throughout the time. I want to thank him for always having an open door and sharing his knowledge and expertise with me. It was Prof. Cristiano Porciani and Prof. Peter Schneider who attracted me to the field of cosmology by their lectures, triggered my interest and led me to conduct this fascinating research. No less I thank A. D. Ludlow, D. Bertacca and E. Romano-Díaz, as well as all members of the research group, for their help and all the valuable discussions we had.

Further, I thank my family and friends for their continuous support. In particular, I want to thank my wife for her positive mood backing me up and her patience especially during the final part of this thesis. I am very grateful to my parents who believe in me all the time and support me whenever necessary.

Last but not least, I acknowledge the financial support I received through the Trans-Regio 33 “The dark Universe” and a H2 grant from the Bonn-Cologne graduate school.